ISBN 978-82-471-1797-2 (printed ver.)
ISBN 978-82-471-1798-9 (electronic ver.)
ISSN 1503-8181

Kjersti Røkenes
Doctoral Thesis

Doctoral theses at NTNU, 2009:199

Kjersti Røkenes

Investigation of terrain effects with respect to wind farm siting

NTNU
Norwegian University of
Science and Technology

Thesis for the degree of
philosophiae doctor
Faculty of Engineering Science and Technology
Department of Energy and Process Engineering

NTNU
Norwegian University of
Science and Technology

Doctoral theses at NTNU, 2009:199
NTNU

Kjersti Røkenes

Investigation of terrain effects with respect to wind farm siting

Thesis for the degree of philosophiae doctor

Trondheim, October 2009

Norwegian University of
Science and Technology
Faculty of Engineering Science and Technology
Department of Energy and Process Engineering

NTNU
Norwegian University of
Science and Technology

NTNU
Norwegian University of Science and Technology

Thesis for the degree of philosophiae doctor

Faculty of Engineering Science and Technology
Department of Energy and Process Engineering

ISBN 978-82-471-1797-2 (printed ver.)
ISBN 978-82-471-1798-9 (electronic ver.)
ISSN 1503-8181

Doctoral Theses at NTNU, 2009:199

Printed by Tapir Uttrykk

Abstract

The turbulent flow above complex and generic terrain has been investigated in a wind tunnel. The objective was to generate a test case for numerical models, and to investigate flow above complex terrain with a view to wind turbine siting. The terrain model was inspired by locations in the mountainous terrain along the Norwegian coastline where wind farms existed or were planned. The model was split up into modules. Some of the modules could be studied both separately and together to cause an even more complex flow. The mean velocity, turbulence intensity and power spectrum in the simulated incoming atmospheric boundary layer was similar to wind in coastal areas. A large number of vertical velocity profiles were measured above the terrain model, using two-component Laser Doppler Anemometry. These were taken in regions where the flow was characterized by velocity speed-up, separation and flow recovery.

The flow above hills with sharp and rounded crests and various inclination angles, followed by a plateau, was compared. Results for a straight slope with a sharp crest was compared to a rounded hill with a similar slope, revealing large discrepancies. Flow above rounded hills was seen to be very advantageous for wind turbines, with increased mean velocities and reduced turbulence intensity, compared to the incoming flow. Separated flow occurred in the case with a sharp crest, resulting in highly increased levels of turbulence. Cases with two mountains of different heights combined were also studied. When the flow separated downstream of the first mountain, the flow above the second was affected to a varying extent, depending on the height of the upstream mountain compared to that downstream. One of the terrain modules was tested with three combinations of two different surface roughnesses in the inflow and on the model. The effect of different roughness in the inflow was seen to disappear only a short distance downstream of the leading edge of the model, and further downstream the flow conditions depended on the model surface roughness only.

The results were compared to several simple estimation methods, and the ESDU method was seen to give results which were in quite good accordance with the experimental data. The experimental results above the complex and generic terrain model has been used as a test case for one flow solver, and it was found to be a demanding test for the numerical tool.

Acknowledgements

This study has been carried out at the Department of Energy and Process Engineering at The Norwegian University of Science and Technology. It was a part of the Wind Energy Strategic Program 2003 - 2007, which aim was to support the development through a strengthening of the Norwegian wind energy competence. Thanks to all the other participants in the project for sharing the enthusiasm related to wind energy. I have spent six years doing this study, including 10 months relaxation during maternity leave. Three years were funded by The Research Council of Norway.

Professor Per-Åge Krogstad has been my supervisor throughout the study. I would like to thank him for always having the time to talk, for guiding me through various theoretical and practical questions, and for pushing me forward. I would also like to thank the two very skilled laboratory technicians John Krogstad and Arnt Egil Kolstad. In addition to solving every practical task very fast, solid and in a creative way, their company and good spirit cheered me up during numerous of hours in the laboratory. Thanks to Isabelle Roche-Cerasi, for giving me an introduction to Laser Doppler Anemometry. Also, thanks to all the other friendly and helpful colleagues at the Department of Energy and Process Engineering. Thanks to Jørgen Løvseth, for being inspiring in the field of wind energy throughout many years.

During the last two years of this study, I have been working at TrønderEnergi Kraft AS. This made it possible to complete this work from an economic point of view. Thanks to Stig Rolstadaas for encouraging me and enabling flexible working hours.

I would like to thank all my family and friends for always believing in me, and keeping in touch despite my lack of time. Most of all I would like to thank Stein for his endless patience and support, no matter what. Finishing this work would not have been possible without him. And finally, thanks to my dear daughter Leonore, for always smiling and making it easy to put things in perspective.

Kjersti Røkenes
Trondheim, October 2009

Contents

Nomenclature

Roman

A	Area	m^2
b_s	Base-length of spires	m
C_0	Constant in the logarithmic law	
C_p	Power coefficient	
c_p	Specific heat at constant pressure	kJ/kgK
d_0	Displacement height	m
E	Constant of LDA beam expander	
Ec	Eckert number	
E_{uu}	Spectral energy density	m^2/s
F	Focal length of the LDA probe	m
f	Frequency	s^{-1}
$F_{b,i}$	Mean body forces in the i^{th} direction	N/kg
$f_{b,i}$	Body forces in the i^{th} direction	N/kg
f_C	Coriolis parameter	rad/s
Fr	Densimetric Froude number	
g	Acceleration due to gravity	m/s^2
H	Hill height	m
h	Local boundary layer height in the ESDU method	
h_i	Height of internal boundary layer	m
H_1	Height of the plateau in Case I and II	m
h_s	Height of spires	m
H_2	Height of the plateau in Case III and IV	m
H_{ws}	Height of the working section in the wind tunnel	m
I_u	Turbulence intensity in the streamwise direction	
Je	Jensen number	
L	Horizontal length of ascending hill	m
l	Thickness of the inner layer	m
L_{Harris}	Length scale in Harris' model	m
$L_{H/2}$	Half-length of a hill	m
L_{Kaimal}	Length scale in Kaimal's model	m
L_{Karman}	Length scale in von Karman's model	m
L_P	Plateau length	m
${}^xL_u$	Integral length scale	m
L_u	Horizontal length of the upwind slope in the ESDU method	m
m	Mass	kg

N	Number of samples	
p'	Fluctuating part of the pressure	Pa
P	Length of the plateau in the ESDU method	m
P	Mean pressure	Pa
p	Pressure	Pa
Pr	Prandtl number	
Re	Reynolds number	
Ro	Rossby number	
Re_*	Roughness Reynolds number	
R_{uu}	Autocorrelation function	
s	Parameter in the ESDU method	
T	Time periode	s
t	Time	s
T_u	Integral time scale	s
T	Temperature	$^\circ C$
TKE	Turbulent kinetic energy	m^2/s^2
u'	Fluctuating part of the streamwise velocity	m/s
u_i'	Fluctuating part of the velocity in the i^{th} direction	m/s
U	Mean streamwise velocity	m/s
u	Streamwise velocity	m/s
U_e	Freestream velocity	m/s
u_*	Friction velocity	m/s
U_H	Velocity at the height H	m/s
U_i	Mean velocity in the i^{th} direction	m/s
u_i	Velocity component in the i^{th} direction	m/s
U_0	Mean velocity in the inflow	m/s
U_r	Reference velocity used for scaling	m/s
U_{ref}	Reference velocity in the power law	m/s
V	Mean spanwise velocity	m/s
v	Spanwise velocity	m/s
v'	Fluctuating part of the spanwise velocity	m/s
w'	Fluctuating part of the vertical velocity	m/s
W	Mean vertical velocity	m/s
w	Vertical velocity	m/s
x	Spatial coordinate in the streamwise direction	m
x_i	Spatial coordinate in the i^{th} direction	m
x_m	Model coordinate	m
y	Spatial coordinate in the spanwise direction	m
y_m	Model coordinate	m
Z	Spatial coordinate in the vertical direction from the tunnel floor	m
z	Spatial coordinate in the vertical direction from the local surface	m
z_0	Roughness length	m
z_r	Reference height used for scaling	m
z_{ref}	Reference height in power law	m
Z_z	Height above zero level in the logarithmic law	m

Greek letters

α	Exponent in the power law	
α_{mean}	Mean slope of a hill	$^\circ$
α_{max}	Maximum slope of a hill	$^\circ$
β	Tilt angle of the LDA probe	$^\circ$
δ	Boundary layer height	m
ΔS	Fractional speed-up ratio	
ΔU	Velocity increase	m/s
ΔU^+	Roughness function in the logarithmic law	
η_i	Weighting factor in statistical estimators	
Γ	Lapse rate	$^\circ C/m$
Γ_a	Adiabatic lapse rate	$^\circ C/m$
γ	Fractional reversed flow	
κ	von Karman's constant	
λ	Strength of the source/sink in potential flow theory	
μ	Dynamic viscosity	kg/ms
ν	Kinematic viscosity	m^2/s
Ω	The rate of rotation of the earth	rad/s
Φ	Velocity potential	
ϕ	Ratio of the hill height and the half-length of the hill	
ϕ_{max}	Effective maximum slope in the ESDU method	
ϕ_u	Characteristic hill slope in the ESDU method	
Φ_{uu}	Normalized spectral energy density	s
Ψ	Stream function	
ρ	Density	kg/m^3
σ_u	Standard deviation of velocities in the streamwise direction	m/s
σ_v	Standard deviation of velocities in the spanwise direction	m/s
σ_w	Standard deviation of velocities in the vertical direction	m/s
τ	Time lag	s
τ_{ij}	Reynolds stress tensor	N/m^2
τ_w	Wall shear stress	N/m^2
φ_{lat}	Latitude	$^\circ$
φ	Ratio of the hill height and the length of the hill	

Superscripts

$+$	Scaled in inner variables

Subscripts

max	Maximum
min	Minimum
0	The incoming flow
u	Related to the velocities in the streamwise direction
v	Related to the velocities in the spanwise direction
w	Related to the velocities in the vertical direction

Abbreviations

2D	Two-dimensional
3D	Three-dimensional
ABL	Atmospheric boundary layer
CTA	Constant Temperature Anemometry
ESDU	Engineering Sciences Data Unit
FFT	Fast Fourier Transform
IBL	Internal boundary layer
LDA	Laser Doppler Anemometry
LDA1	LDA channel measuring a component defined as u
LDA2	LDA channel measuring a component defined as v
LSD	Lemelin Surry Davenport
PSD	Power spectral density

List of Figures

List of Tables

Chapter 1

Introduction

Global winds are caused by the fact that some regions at the earth receives more solar energy than others, and this sets up large-scale convective currents in the lower layers of the atmosphere. It has been estimated that about $1-2$ % of the incoming solar energy is converted to wind energy. This daily wind energy input is about the amount of the worlds energy consumption one day. Hence the wind resources are very large.

The energy which can be extracted from the wind by a turbine depends on several parameters. The power output from a wind turbine generator is

$$P_{WTG} = C_p \frac{1}{2} \rho U^3 A \tag{1.1}$$

where ρ and U are the density and velocity of air, respectively. A is the area swept by the rotor. C_p is a dimensionless power coefficient which represents the fraction of the power in the wind that is extracted by the turbine. The maximum theoretical value is the Betz limit, $C_{p,max} = 16/27 = 0.59$. In practise the power coefficient is about $C_p = 0.5$ for modern turbines, meaning that about 50 % of the energy in the wind which approaches the wind turbine rotor can be extracted. It is seen that the power is proportional to the cube of the velocity, so site selection for wind turbines is crucial for the resulting energy production.

Norway was at the brink of a significant wind energy development at the start of this study. Many wind farms were planned, and still more are planned today. Only a few wind farms have been build in the meantime, mainly due to a lack of political will. The total capacity of wind power in Norway today is 429 MW, and the wind energy production in 2008 was 917 GWh (Jensen and Fossdal, 2009). Another 1256 MW has got a license, but are awaiting subsidies to be started. License is applied, or announced to be applied, for a capacity of 21935 MW. Several years ago The Norwegian parliament announced a goal of 3 TWh annual wind energy production, corresponding to about 1000 MW, within 2010. Recently, there has been much attention on EU's 20-20-20 target: 20 % cut in emissions of greenhouse gases by 2020, compared with 1990 levels; a 20 % increase in the share of renewables in the energy mix; and a 20 % cut in energy consumption. A consequence of this is increased focus on wind power in Norway. There has also been much focus on offshore wind the last years, but no offshore wind turbines have been erected in

Norway yet. Hywind, the world's first full-scale floating wind turbine, will be tested at a location near Karmøy over a two-year period from the autumn of 2009.

Most of the locations in Norway which are under consideration for wind energy are in complex terrain along the coastline, as illustrated by Havøygavlen wind farm in Figure 1.1. These are areas with high mean wind velocities and therefore have great potential for energy production. Unfortunately complex terrain like this may also cause negative effects due to high wind shear, flow separation and increased levels of turbulence generated by the terrain roughness. A consequence of this may be increased loads on the turbines, which can cause reduced lifetime for some parts of the turbine and total collapse as a worst case scenario. Other consequences might be reduced availability of the turbines and less energy production than expected.

Figure 1.1: Photo from Havøygavlen in Finmark, Norway. The turbines are Nordex N80, with a rotor diameter of 80 m and installed capacity of 2.5 MW. Source: Nordex GmbH.

1.1 Previous work

Considerable attention has been given to flow over hills the last four decades, and many wind tunnel investigations have been carried out. The motivation for studies like this can be to investigate the flow field with respect to wind power, dispersion of pollution, siting of airports and loads on structures. Some of the studies have been performed on models of real terrain, while most others have focused on some simple geometrical shapes with moderate slopes. Many models have been two-dimensional

hills. The effects of varying the hill slope, varying the surface roughness and combining similar hills, have been studied in several experimental investigations. In cases of three-dimensional terrain, the hills are often axisymmetrical. The thermal stratification is neutral in most wind tunnel experiments, unless when the experiments are specially created to study such effects. Detailed measurements of mean velocity and turbulence are commonly made in wind tunnel experiments with hills, and especially at the crest and in possible wake regions. The measurements are often compared to results from well-known analytical models, different estimation methods, or numerical simulations. The wind characteristics above moderately sloped terrain without any significant separation is generally well understood, but a continuous improvement in our understanding is still needed for wind above steeper and more complex terrain.

1.1.1 Analytical theory and estimation methods

Much effort has been put into developing simplified models for prediction of speed-up over hills. Estimation methods for calculating speed-up usually makes use of a characteristic slope based on simple length parameters. The terrain studied under development of such methods is usually symmetric and isolated with moderate slopes.

An analytical method for predicting the flow over hills was first developed by Jackson and Hunt (1975). They considered the linearized problem of turbulent flow over two-dimensional low, gentle and smooth hills. This work also postulated a two layer structure of the flow. The method of Jackson and Hunt has subsequently been extended by others. For example wind flow over three-dimensional hills has been included. This linearized theory has been criticized by some, but several laboratory and field experiments have shown that it can predict mean flow perturbations reasonably well, even for hills with moderate slopes. According to Lubitz and White (2007) the body of work based on Jackson and Hunt remains essentially the only satisfying analytical method of estimating speed-up over hills. The fractional speed-up ratio , ΔS, is the fraction of change in velocity above the terrain to the approaching undisturbed velocity. Kaimal and Finnigan (1994) reported some simple formulas for estimating the fractional speed-up ratio over small terrain features of different types at the height where ΔU_{max} attains its maximum. This is based on the analytical theory given by Jackson and Hunt. The Guidelines are a set of equations for estimation of fractional speed-up ratio at various heights over the crest of hills. The original Guidelines were developed by Taylor and Lee in 1984, as described in Lubitz and White (2007). The Guidelines were developed further by Weng et al. (2000), so that e.g. roughness effects and steeper slopes were included. Lemelin et al. (1988) developed a simple method for estimating the speed-up over escarpments, two-dimensional hills and three-dimensional hills. This set of equations for simple approximations, described as the LSD approach, was originally intended for implementation into building codes. The prediction formulas were derived from numerical simulations of the flow above an elliptical paraboloid hill with low to moderate slopes. Engineering Sciences Data Unit (ESDU, 1993)

provides formulas combined with look-up tables for estimating speed-up effects over an embankment equivalent to the actual hill. In contrast to the LSD approach, which mainly work well in the crest region, the ESDU method should be able to reproduce the decelerated wind speed upwind and downwind of the crest as well.

1.1.2 Wind tunnel experiments

2D and isolated terrain features

A wind tunnel simulation of neutral stratified flow normal to a rough, two-dimensional ridge was performed by Finnigan et al. (1990). The maximum slope of this ridge was only 9°, but flow characteristics were roughly similar to that above steeper hills. A pronounced wake region was formed behind the hill, despite the lack of separation. A decrease in the standard deviation of the velocity in the main flow direction was seen at all levels at the crest compared to the upwind profile, and a large increase was seen in the wake region. The mean velocity was slightly reduced at lower levels just upstream of the hill, increased at the crest and considerably reduced in the wake. Finnigan et al. compared the results with other wind tunnel models and data from real hills.

Experience from a measurement campaign in a real wind farm made it clear that the wind field was strongly affected by the slope of upwind escarpments, and led to the wind tunnel study performed by Imamura et al. (2003). They investigated the wind flow over two-dimensional forward facing escarpments with a cliff ($H : L = 1 : 0$), a $H : L = 1 : 1$ slope (45°), and a $H : L = 1 : 2$ slope (where H is the hill height and L its streamwise extent). The purpose of the study was to develop a method for the power curve measurement of wind turbine generator system in complex terrain. Reversed flow was observed downstream of the crest of the cliff, but not for the other models. A large region with highly increased turbulence intensity was seen for the cliff, and to some lesser extent for the 45° slope. For the most gentle slope accelerated velocity was observed near the surface, and no increase was seen in the turbulence intensity compared to the incoming flow. Low correlation was found between two points in the downwind direction in the reversed flow region. It was also seen that the peak of the energy spectrum above the 45° slope was shifted to higher frequencies compared to above a flat surface.

The primary objective in Arya et al. (1987), which was one in a series of studies by Arya et al., was to gain a better understanding of the effects of hill slope on flow and dispersion over low hills. The hills were two-dimensional, gentle and symmetrical, with maximum slopes in the range 10° to 26°. Arya et al. observed that the speed-up of flow on the hilltops were proportional to the average slope, which is consistent with several theories. The steepest hill induced separation on the lee side, and this was the most pronounced effects in the disturbance boundary layer. The fractional speed-up ratio above the crest of this hill was $\Delta S_{max} \approx 0.8$ near the ground. The most gentle hill did not induce any flow separation, while the hill with a maximum slope of 16° had drastic reduction in the mean velocity near the downwind base, indicating intermittent flow separation.

Wind tunnel measurements for a turbulent boundary layer flow over two-dimensional

embankments of trapezoidal shape with slope gradients of 45°, 27° and 14° were carried out by Shiau and Hsieh (2002). They analyzed the contributions of the stress components from four quadrants to the Reynolds stress, and concluded that both sweep and ejection events were the major contributors to the Reynolds stress for flow around the embankments. A similar study is described by Shiau and Hsu (2003), where the flow above a trapezoidal hill with slope 12.5° was investigated under different wind angles of attack. The fractional speed-up ratio was concluded to be in good agreement with other experimental results and the LSD approach for an angle of attack in the experiment of 30°.

2D and isolated terrain features with varying roughness

Cao and Tamura (2006) carried out wind tunnel experiments to study the effects of surface roughness. They compared two cases with turbulent boundary layer flow over a two-dimensional steep hill (maximum slope 32°), with roughness lengths of $z_0 = 0.004\ mm$ ("smooth") and $z_0 = 0.2\ mm$ ("rough"). Vertical profiles of the turbulence statistics over the hills were investigated, and compared with those for an incoming turbulent boundary layer over a flat surface covered by similar roughness. The measurements revealed that the fractional speed-up ratio on the crest depended on both the hill surface condition and the upstream surface condition. The separated shear layer of the rough hill was seen to be weaker than that of the smooth hill, while the separation region was seen to extend further downstream for the rough hill than the smooth hill. The hill in this study was steep enough to cause a steady separation, and the study focused mainly on the effects of roughness blocks on the separation and reattachment behavior. In another study Cao and Tamura (2007) did experiments to investigate the effects of roughness blocks on the flow over a two-dimensional low hill. The maximum slope of this hill was only 11.8°. Four cases were studied with/without a sudden roughness change in the main flow direction: a smooth hill in smooth flow, a rough hill in rough flow, a smooth hill in rough flow and a rough hill in smooth flow. Flow characteristics over the hill models were compared, with emphasis on speed-up and turbulence structure. It was seen that the velocity deficit was changed, and that a completely different turbulence structure was created in the wake, when roughness blocks were added or removed. A main conclusion from this study was that the turbulent boundary layer over a low hill is very sensitive to the surface conditions. As in their study of a steep hill (Cao and Tamura, 2006), it was seen that the speed-up depended on both the surface condition of the hill and the upstream surface condition, and that this dependence becomes stronger as the surface is approached. These results were also compared with the predictions obtained from linear models.

Ayotte and Hughes (2004) investigated flow, in the range from fully attached to strongly separated, over isolated ridges of varying steepness and roughness. A thorough discussion of linear theory was also presented by Ayotte and Hughes, especially regarding where linear models can be expected to work well, and where and how these models are likely to break down. The mean slopes of the ridges in this wind tunnel study were in the range $11° - 31°$, hence spanned from what can be explained by linear theory to slopes where nonlinear effects are significant.

The measurements showed that the linear theory over-predicted the speed-up at the crest in steep terrain, and that recovery in the lee of the steepest hills with strongly separated flow was delayed compared to the more gentle hills.

2D, isolated and subsequent, terrain features

The investigation of flow around two-dimensional hills with sinusoidal cross-section carried out by Ferreira et al. (1991), was motivated by an application related to the prediction of wind driven forest fires. Four steep hills with height to half-length ratios of 0.75, 1, 2 and 4 were investigated. The half-length is the horizontal distance from the crest to the upstream point where the height is half the maximum hill height. The results were presented as pressure and shear-stress distributions on each hill, as well as vertical velocity profiles on top of the hills. The general flow pattern around each of the four hills was also obtained visually. Lee separation was seen in all four cases, and the separation zone increased with increasing steepness as expected. Separation at the base of the uphill was only observed in the steepest case. The interaction between two identical hills was also studied for different distances, and the vicinity of a parallel hill was seen to mainly affect the flow above the downstream hill.

The interaction between hills was also studied by Carpenter and Locke (1999), who performed a wind tunnel investigation of flow above a variety of two-dimensional hill geometries. The scale was 1:1000, and the geometries included shallow sinusoidal hills, steep sinusoidal hills, consecutive hills and an irregularly shaped hill. The mean slope of the steep hill in the study was 26.6°, and the slope of the shallow hill was 14°. The mean speed and longitudinal turbulence were measured. The maximum fractional speed-up ratio at the crest for the steep hill was $\Delta S = 1.08$ occurring at a height 5 m above ground ($z/H = 0.025$), and the corresponding value 5 m above ground in the shallow case was $\Delta S = 1.13$. Additional measurements near the crests revealed that the maximum fractional speed-up ratio was found near the surface upwind of the crest for the steepest hill. The results were compared with predictions from a CFD model. The mean wind speed predicted showed reasonable agreement with the measurements for geometries with little flow separation, while the velocity standard deviation generally showed poor agreement with the experiments.

Athanassiadou and Castro (2001) carried out laboratory experiments with a series of 2D sinusoidal hills, also called wavy models. The flow was aerodynamically fully rough. Two sets of hills, with maximum slopes of 10° and 20°, were considered. Consistent with theory the flow did remain attached for the most gentle hills, while separation occurred for the steepest hills. Good agreement was seen between analytical theory and experimental results for the fractional speed-up ratio above the 10th crest. Good agreement between rapid distortion theory and the measured longitudinal stress was also observed, while the agreement for the vertical stress was at most qualitative.

An experimental and numerical investigation of flow over single hills and continuous double hills was performed by Kim et al. (1997). Both velocity profiles, turbulence characteristics, and pressure distributions were measured above four two-dimensional cosine shaped hills with two different heights and slopes of 16.7° and

26.6°. The flow was not fully rough. In non-separated flow conditions it was seen that a lower neighbouring hill did not change the mean velocity profile at the top of a higher hill, but the reverse was the case for a higher hill nearby a lower hill. In the case with the steepest and lowest hill upstream, the size of the separation zone on the lee side of the downstream hill was considerably decreased compared to the case with the single hill. This was considered to be due to the adverse pressure gradient and viscous dissipation in the separation region between the hills. The results were compared both with linear and numerical predictions, and showed good agreement.

2D and 3D, isolated, terrain features

The two-dimensional ridge and the axisymmetrical hill in the study of Gong and Ibbetson (1989) had maximum slopes of 14° and 16° respectively. Mean flow and turbulence were measured, and the results were compared to linear models and rapid distortion theory. Negative fractional speed-up ratios were seen above the ridge at the upwind hill foot and downstream of the top. The maximum fractional speed-up value of $\Delta S_{max} = 0.6$ was observed at $z/H = 0.16$ at the hill top. Vertical profiles of ΔS above the axisymmetrical hill showed a generally similar picture to the profiles over the ridge. A smaller speed-up would be expected over the top for the circular hill than the ridge, but in this study the opposite was observed. The main differences between the ridge and the circular hill was seen on the upwind and downwind slopes. The study showed that the linearized theory of Jackson and Hunt (1975) was adequate on the upwind side and at the top of the hill of moderate slope, but failed in the wake region on the lee side. It was especially successful in predicting the mean flow at high levels on the upwind side. In this area the mean flow was insensible to the way the turbulence was modelled, so the non-linearity was unimportant. Gong and Ibbetson also compared their results with rapid distortion theory, only showing acceptable agreement for certain components in certain regions. It was also concluded that axisymmetric rapid distortion theory did not offer any improvement compared to isotropic theory in the study. Both isotropic rapid distortion theory and axisymmetric rapid distortion theory has been applied to the flow over hills by several investigators, and the results have shown both to disagree and agree with experimental results.

3D terrain features

The turbulent flow over a circular hill with a maximum slope of about 32° was investigated by Ishihara et al. (1999). The undisturbed boundary layer was representative of the flow above a grass or heather covered surface. The flow was not completely aerodynamically rough, and the model scale was 1:1000. The profiles of the means and variances for all three velocity components were measured at the centreline of the hill, downstream of the hill, and at various positions at the side of the hill. The maximum fractional speed-up ratio of $\Delta S_{max} = 0.5$ was observed at the top of the hill at $z/H = 0.125$ (the lowest measurement point). Speed-up also occurred at the midway slope on the sides of the hill. The boundary layer separated at the crest, and reattached just at the lee foot of the hill. The maximum velocity

variance was seen at the same level as the hill, corresponding to the separation zone downstream of the crest.

Lubitz and White (2007) performed measurements of the flow above hills in an atmospheric boundary layer wind tunnel, and determined velocity profiles and speed-up factors for several model hills. All these hills had the same height and sinusoidal cross-sections. One was axisymmetric, one elliptical and one two-dimensional (length-to-width aspect ratios of one, four and infinity respectively). Five measurements were taken at similar positions for all models; at the base and half-way up/down both uphill and downhill, and at the top. Each of the three models were tested with varying approaching wind directions, from 0° to 90°, in 15° increments. It was observed that speed-up can vary significantly depending on the approaching wind direction. Maximum fractional speed-up ratios of about $\Delta S_{max} \approx 0.7$ at the top of the two-dimensional hill (with a mean and maximum uphill slope of about 15° and 23° respectively) were found at the lowest measurement point ($z/H = 0.13$). A comparison of the speed-up for four different hill aspect ratios (i.e. the ratio of half-length in y-direction to the half-length in the x-direction) was also done. The speed-up above the two-dimensional hill was generally somewhat greater than the observed values above the elliptical hill.

Investigations including real terrain

Miller and Davenport (1998) carried out a wind tunnel study of boundary layer flow above a number of two-dimensional complex surfaces to see the effect of upstream topography. The first part of the study consisted of twelve successive sinusoidal ridges. This case was also tested with two different surface roughnesses. In the second part of the study, they investigated three different complex surfaces based on real terrain. Speed-ups in complex terrain were found to be reduced compared to those above isolated features, and significantly increased levels of turbulence were seen. Miller and Davenport compared the observed maximum speed-ups to the results from the method given by Lemelin et al. (1988), and to results from a linear model. It was concluded that the models tended to overpredict the speed-ups.

Glanville and Kwok (1997) studied speed-up and separation from a nearly two-dimensional steep escarpment, and compared it to results from field measurements. The blocking in the wind tunnel due to the model was 25 %, but this was accounted for by installing a special ceiling in the wind tunnel, minimizing the effects of blocking. Good agreement was found between profiles from field measurements and wind tunnel simulation, and the speed-up values were also seen to agree well. The wind speed gradient was approximately constant in the region $z/H = 0.14 - 1$. The turbulence intensity was reduced over the crest outside areas of flow separation, as a result of both reduced turbulence and increased mean velocity. The turbulence intensity at lower elevation beyond the crest was seen to increase dramatically due to separated flow. The results between $z/H = 0.11$ and $z/H = 1$ were also compared to potential flow theory with a uniform incoming velocity profile. This approach was considered permissible as a first order estimate since the flow remained relatively inviscid in this range.

Sierputowski et al. (1995) analyzed both two- and three-dimensional simplified hill-valley configurations, with a main goal to study the ground level flow for given geometries and for further application to the modelling of diffusion. One model had a straight configuration, with the flow approaching normal to the valley. An oblique configuration was also tested, with the flow approaching from both sides, hence constituting two models with valley shaped as "<" and ">" respectively. The oblique models were tested in order to show the three-dimensional effects introduced in such cases. The oblique configurations altered the mean flow direction, and produced a weaker and more chaotic reversed flow in the separation zone compared to the straight configuration. An initial drop in the turbulence intensity was seen in all three cases, as a result of the acceleration at the leading edge of the hill. Rapid increase in the turbulence intensity then displayed the effect of separation at the lee side. A velocity field analysis was also done for the model of a real valley, and the qualitative similarity with the simplified models was obvious. Three-dimensional effects of real geometry influenced the scales of mean flow deformation. There was not a regular recirculation zone, but relatively smaller scale reversed flow occurred in the valley.

Neff and Meroney (1998) briefly reported from a three phase research program. The first part of the study was a literature review of the effects of trees and forests. Wind tunnel measurements of velocity profiles at crests as a function of surface roughness, hill shape, and hill slope constituted the second part. The combinations resulted in a total of 96 different run conditions. A substantially increase in the velocities near the ground was seen when even small areas with threes were cut. This kind of clear cutting only provided marginal velocity gain for the steeper hills. The turbulence intensity was seen to be mainly affected by the height of the upwind trees. The third part of the research program was a study of the flow above a proposed wind energy site. The flow above isolated ridges mirrored the previous results above generic ridges. Flow above three-dimensional features showed less speed-up compared to the corresponding two-dimensional features. A conclusion of this study was that a "crew cut" approach can be recommended for most forested ridges and hills if increased wind velocities are pursued.

Effects of thermal stability

Even if there has been many investigations on the flow above complex terrain, there are few studies considering the thermal stability. The effects of stable, neutral and unstable atmospheric boundary layers was the main focus in the study by Takahashi et al. (2005). They investigated the turbulent flow over a three-dimensional hill. The objective was to obtain data needed for validation of a prediction model developed for the mountainous and steep terrains in Japan. It was seen that the mean velocity did not vary at the crest of the hill, despite the different atmospheric conditions. At the back of the hill, the peak values for the turbulence level in the longitudinal and vertical directions ($\sqrt{\overline{u'^2}}/U_H$ and $\sqrt{\overline{w'^2}}/U_H$) became largest for the stable case and smallest for the unstable case. The peak value of $\sqrt{\overline{u'w'}}/U_H^2$ was also observed to be largest in the stable case and smallest in the unstable case, while $\sqrt{\overline{u'v'}}/U_H^2$ and

$\sqrt{\overline{v'w'}}/U_H^2$ was seen not to vary greatly with atmospheric stability.

1.1.3 Numerical modelling

Ayotte (2008) gives a brief history of computational modelling and methodology for wind resource assessment used in the wind industry. As the computational power has increased, the models in this field has changed from linear to nonlinear and the treatment of the surface boundary conditions has improved. This has led to more accurate estimates of wind resources, but Ayotte concludes that a number of challenges still exists when it comes to modelling scales of turbulent motion that are near those of the main topographic features.

1.2 Objective

This study has been a part of the Wind Energy Strategic Program 2003 - 2007, which later on has been extended until 2009. The aim of the project was to support the development through a strengthening of the Norwegian wind energy competence. The current study is a wind tunnel study of a generic terrain model, and it was involved in a task with a goal to develop and verify micro-scale wind flow models for providing improved design criteria for wind farms in complex terrain. Full-scale measurements are expensive and time-consuming, so numerical simulations are frequently used tools when wind farms are planned. However, there is always a need for data to verify the predictions. Accurate full-scale data are extremely difficult to obtain at the level of detail necessary to verify predictions. With the added problems of complex terrain, detailed wind tunnel data provides much more reliable data for verification, since boundary conditions may be accurately described.

The objective of the current study was to generate a test case for numerical models, and to study effects of complex terrain on the wind field at potential turbine sites. The terrain features are typical for the mountainous terrain along the Norwegian coastline, and the slopes of the hills are steeper than in most other corresponding studies. Some of the cases in the current study are relatively simple, but where combined in other cases to generate an even more complex terrain. This gradual increase of complexity is an advantage for numerical models using the experimental data for validation and calibration. Another advantage is that this is a comprehensive study with different terrain cases, allowing for a comparison with experimental data for many types of terrain which are obtained under equal conditions.

1.3 Overview of thesis

In this chapter, a review of other wind tunnel studies relevant for the current study has been presented. Chapter two presents governing equations of fluid flow. Chapter three deals with boundary layer theory. This includes boundary layer structure, mean velocity profiles, some turbulent quantities, and power spectra. Typical flow fields above complex terrain, and different estimation methods for speed-up over

hills, are presented in chapter four. Chapter five contains an overview of similarity parameters and other criteria for wind tunnel modelling. Chapter six introduces general principles of Laser Doppler Anemometry and details of the setup applied in the current study. The subject of chapter seven is the experimental setup and procedures. The terrain model, measurement positions, measuring methods, data collection, scaling of the data and data quality are also presented. Chapter eight contains an overview of all the main results, detailed discussions of these and comparisons with other methods. The thesis ends with conclusions and suggestions for further work. The process of generating the incoming boundary layer is presented in Appendix A. The quality of the experimental data is discussed in more detail in Appendix B. Separate papers are included in Appendix C.

Chapter 2

Governing equations of fluid flow

This chapter briefly presents some of the governing equations of fluid flow. The most basic set of equations are the widely applied Navier-Stokes equations. The Reynolds averaged Navier-Stokes equations are time averaged equations for fluid flow, and are primarily used in the field of turbulent flows. Reynolds decomposition is utilized to derive this, and the concept of Reynolds stresses is a result. The third equation presented in this chapter describes the transport of Reynolds stresses.

2.1 Navier-Stokes equations

The equations of motion for a Newtonian fluid with constant density and viscosity are

$$\frac{\partial u_i}{\partial t} + u_j \frac{\partial u_i}{\partial x_j} = -\frac{1}{\rho}\frac{\partial p}{\partial x_i} + f_{b,i} + \nu \frac{\partial^2 u_i}{\partial x_j^2} \tag{2.1}$$

$$\frac{\partial u_i}{\partial x_i} = 0 \tag{2.2}$$

where repeated indices in any term indicates a summation over all values of the index. u_i is the instantaneous velocity component in the i^{th} direction. The time t and the three spatial coordinates x_1, x_2 and x_3 (which corresponds to x, y and z) are the independent variables. p is the pressure. f_b are the body forces, i.e. due to gravitation and the Coriolis effect. $\nu = \mu/\rho$ is the kinematic viscosity. Equation 2.1 are the Navier-Stokes equations representing conservation of momentum and Equation 2.2 is the continuity equation. Note that there are four equations and four unknowns (u, v, w and p) if the density ρ and the dynamic viscosity μ are known.

2.2 Reynolds decomposition

In turbulent flows, the velocity and pressure are rapidly varying functions of time and space. The instantaneous values can be split up into a mean value and a fluctuating part

$$u = U + u' \qquad v = V + v' \qquad w = W + w' \qquad p = P + p' \tag{2.3}$$

where the mean value is defined as

$$U = \frac{1}{T}\int_{t=t_0}^{t=t_0+T} u dt \tag{2.4}$$

It follows from the definitions in Equation 2.3 that the mean value of the fluctuations are zero. The mean square of the fluctuations, the variance, on the other hand are non-zero and defined by

$$\overline{u'^2} = \frac{1}{T}\int_{t=t_0}^{t=t_0+T} (u-U)^2 dt = \frac{1}{T}\int_{t=t_0}^{t=t_0+T} u'^2 dt \tag{2.5}$$

The standard deviation, also called the root mean square (rms) value, is $\sigma_u = \sqrt{\overline{u'^2}}$.

2.3 Reynolds averaged Navier-Stokes equations and Reynolds stresses

Substituting the sum of the mean value and a fluctuating part for the instantaneous values in Equation 2.1, and then time-average the equations as defined in Equation 2.4, produces the Reynolds averaged Navier-Stokes (RANS) equations.

$$\frac{\partial U_i}{\partial t} + U_j\frac{\partial U_i}{\partial x_j} = -\frac{1}{\rho}\frac{\partial P}{\partial x_i} + F_{b,i} + \nu\frac{\partial^2 U_i}{\partial x_j^2} - \frac{\partial\left(\overline{u_i' u_j'}\right)}{\partial x_j} \tag{2.6}$$

$$\frac{\partial U_i}{\partial x_i} = 0 \tag{2.7}$$

Equation 2.6 for the mean velocity is very similar to Equation 2.1 for the instantaneous velocities, except for the addition of the turbulence term at the end. This can also be written as $\frac{1}{\rho}\frac{\partial \tau_{ij}}{\partial x_j}$ and represents the influence of turbulent stresses on the mean motions. The correlations of fluctuating velocities are also called Reynolds stresses. These are not really stresses, but are named stresses because they appear next to the laminar stress terms and have the same dimensions. Reynolds stresses can be represented as a symmetric tensor $\tau_{ij} = -\rho\overline{u_i' u_j'}$. The diagonal of the tensor τ_{ij} contain the normal stresses. The off-diagonal elements of the tensor are shear stresses, and are of major importance when it comes to turbulent transport of mean momentum. As in Section 2.1 the number of equations is still four, but six new unknown quantities (the Reynolds stresses) are now added.

2.4 Transport equation for Reynolds stresses

An equation describing the transport of Reynolds stresses can be derived by multiplying the moment equation for u_i by u_j', averaging, and then adding it to the mirror equation in which the indices i and j are interchanged. k is the repeated index in the following transport equation for Reynolds stresses

$$\frac{\partial\left(\overline{u_i'u_j'}\right)}{\partial t}+U_k\frac{\partial\left(\overline{u_i'u_j'}\right)}{\partial x_k}= \tag{2.8}$$

$$\underbrace{-\left(\overline{u_i'u_k'}\frac{\partial U_j}{\partial x_k}+\overline{u_j'u_k'}\frac{\partial U_i}{\partial x_k}\right)}_{P_{ij}}\underbrace{+\left(\overline{f_{b,i}'u_j'}+\overline{f_{b,i}'u_i'}\right)/\rho}_{G_{ij}}\underbrace{+\overline{\frac{p'}{\rho}\left(\frac{\partial u_i'}{\partial x_j}+\frac{\partial u_j'}{\partial x_i}\right)}}_{\phi_{ij}} \tag{2.9}$$

$$\underbrace{+\frac{\partial}{\partial x_k}\left(\overline{u_i'u_j'u_k'}+\overline{\frac{p'}{\rho}u_j'}\delta_{ik}+\overline{\frac{p'}{\rho}u_i'}\delta_{jk}-\nu\frac{\partial\left(\overline{u_i'u_j'}\right)}{\partial x_k}\right)}_{d_{ij}}\underbrace{-2\nu\overline{\frac{\partial u_i'}{\partial x_k}\frac{\partial u_j'}{\partial x_k}}}_{\epsilon_{ij}} \tag{2.10}$$

The left side of the equation gives the rate of change of Reynolds stresses, determined by the terms on the right side. P_{ij} is production of $\overline{u_i'u_j'}$ due to mean strain, and G_{ij} is production due to body forces. ϕ_{ij} is correlation between fluctuating pressure and fluctuating strain, which arranges redistribution of energy among the normal stress components. d_{ij} is diffusion, i.e. spatial redistribution of $\overline{u_i'u_j'}$. ϵ_{ij} is dissipation, representing the destruction rate of $\overline{u_i'u_j'}$ by viscous action.

2.5 Turbulent kinetic energy

Kinetic energy is usually defined as $KE=\frac{1}{2}mU^2$, where m is mass. Mean turbulent kinetic energy per unit mass can then be defined as

$$TKE=\frac{1}{2}\left(\overline{u'^2}+\overline{v'^2}+\overline{w'^2}\right) \tag{2.11}$$

Note that this is half the trace of the Reynolds stress tensor. The turbulent kinetic energy is one of the most important quantities used to study the boundary layer (Stull, 1988).

Chapter 3

Boundary layer theory

Boundary layers exist for viscous fluids like air due to the no-slip condition at surfaces. The mean velocity in the streamwise direction above a flat surface increases from zero at the surface to its maximum value at the top of the boundary layer. The maximum velocity is usually named freestream velocity in laboratory flows and gradient velocity in atmospheric flows, and the depth of the boundary layer is denoted by δ. Turbulence is an effective mechanism for transferring momentum in the vertical direction in such a boundary layer.

3.1 Boundary layer structure

Several models for the structure of turbulent boundary layers have been proposed over the years. These are based on experimental investigations and theoretical considerations. The classical model consist of two main layers and an overlap layer, but three and four layer structures have also been proposed. Different processes dominate the flow in the different layers. The well-known model with shear flows divided into an inner and an outer layer will be presented here. The two layers are overlapping, and the inner layer is usually also divided further into thinner layers.

The region from the surface and outwards to $z \approx 0.1 - 0.2\delta$ is called the inner layer. The vertical variation of total shear stress is negligible in the inner layer, and the flow in this layer is normally considered independent of Reynolds number. The inner layer contains a very thin sublayer closest to the surface named "viscous sublayer", or "roughness sublayer", dependent on whether the surface is smooth or rough. Viscous shear stress dominates in the viscous sublayer, with values an order of magnitude greater than the turbulent shear stress. Hence, the shear stress closest to the wall, τ_w, is dominated by the viscous stress. The friction velocity is defined as $u_* = \sqrt{\tau_w/\rho}$, where ρ is the density of air. This is a characteristic velocity, and not a flow velocity, but it is named velocity since it has dimensions LT^{-1}. A surface is aerodynamically smooth if the disturbances on the surface are small enough for a viscous sublayer to exist. The viscous sublayer covers the disturbances, and measurements in laboratories have shown that the thickness of this layer is about $5\nu/u_*$ (Arya, 1988). The velocity profile in a viscous sublayer is linear, $U^+ = U/u_* = zu_*/\nu = z^+$, from the surface and outwards to $z^+ = 5$ (White, 1991). A surface is

said to be aerodynamically rough if the disturbances are large enough to prevent a viscous sublayer from appearing. Some surfaces are neither smooth nor rough, resulting in a category called a transitional roughness regime.

Above the inner layer, typically at distances from the surface of $0.15 \leq z/\delta \leq 1$, is a layer called the outer layer. It is also commonly called the wake region. The turbulent stresses dominate in the outer layer, hence inertia is important. In the outer layer the distribution of shear stress is the opposite as in the viscous sublayer, the turbulent shear stress is two or three orders of magnitude greater than the viscous shear stress. The velocity-defect law (Section 3.3.2) can be used to describe the mean velocity in this layer. The structure of the outer layer is essentially the same for flow above smooth and rough surfaces. Closer to the surface the characteristics and the proper length scales of the flow depend on whether the surface is smooth or rough.

An overlap region is assumed to exist between the thin sublayer and the outer layer. Both viscous and turbulent shear are important in this region. The well known logarithmic velocity profile (Section 3.3.2) forms the link between the flow near the surface and the outer layer of the boundary layer. The logarithmic part has both been observed in laboratory experiments and in the atmospheric boundary layer.

3.1.1 The atmospheric boundary layer

The lowest region of the atmosphere, where the flow is affected by the surface friction, is known as the planetary or atmospheric boundary layer (ABL). As opposed to small-scale laboratory experiments, the flow in the ABL is significantly affected by the rotation of the earth. This phenomenon is known as the Coriolis force and has the effect of turning the mean wind direction towards the right with increasing altitude (on the Northern Hemisphere). For neutral thermal stability in the ABL the wind direction typically turns about 10° for smooth surfaces and up to about 35° for very rough surfaces (Arya, 1988). The Coriolis force starts to influence the wind above the lower 10 % of the ABL. The Coriolis parameter is $f_C = 2\Omega \sin \varphi_{lat}$. The rate of rotation of the earth calculated from the average rotation period is $\Omega = 7.292 \cdot 10^{-5}\ rad/s$. The latitudes in Norway are from $\varphi_{lat} = 58°N$ at Lindesnes in the south, to $\varphi_{lat} = 71°N$ at Nordkapp in the north. Hence, the Coriolis parameter in Norway is in the range $f_C = 1.24 - 1.38\ rad/s$. The latitude of Trondheim in Central Norway is about $\varphi_{lat} = 63°N$, corresponding to a Coriolis parameter of $f_C = 1.3\ rad/s$.

The ABL has a two layer structure which roughly parallels the inner and outer layers previously described. The inner layer is often named the surface layer. In this region the Coriolis force can be considered negligible, the shear stress is approximately constant in the vertical direction and the wind structure is mainly determined by the vertical temperature gradient and the surface friction. The thickness of the viscous sublayer, $5\nu/u_*$, is about 1 mm or less for atmospheric flows. Most natural surfaces has disturbances of height above 1 mm, so almost all surfaces in nature are consequently completely rough. Some exceptions can be flow above smooth ice, mud flats and water surfaces when the wind is weak enough not to cause significant waves

(i.e. $U_{10m} < 2.5\ m/s$) (Arya, 1988). Flow in the transitional roughness regime may occur above lakes and oceans during periods with moderate wind velocities, typically $2.5 < U_{10m} < 7.5\ m/s$. The outer layer in the ABL is called the Ekman layer. The wind direction turns significantly with height, forming the Ekman spiral, since the wind is affected by the Coriolis force in addition to the temperature gradient and friction. The Coriolis force increases with height in this layer, while the shear stress decreases with height until it becomes zero at the gradient height.

The distinction between the ABL, and the much smoother and non-turbulent flow in the free atmosphere above, is quite clear. The height above ground where this boundary exists is highly variable. It depends upon several factors, like the surface roughness, orography, the rate of heating and cooling of the surface, temperature, large-scale vertical motion, horizontal advection of heat and moisture, and the wind speed. Heights from 20 m to 5 km has been observed, but values in the range $100 - 2000\ m$ are more common. Heights as low as 100 m can be seen during stable thermal conditions and low wind speeds, while the depth can be up to 2000 m during unstable thermal conditions above rough terrain. Strong diurnal variations are common, with typically thickest ABL in the afternoon and thinnest at night, due to heating through the day and cooling through night respectively. Other influencing factors may also exhibit diurnal variations. A rule of thumb, according to meteorologists, is that the ABL is 1000 m above ground, and 300 m above sea. An estimate of the depth of a neutral ABL is (Kaimal and Finnigan, 1994)

$$z_{ABL} = C\left(\frac{u_*}{f_C}\right) \tag{3.1}$$

C is an empirical constant, with a value of $C = 0.25$ corresponding to typically observed daytime height. u_* is the friction velocity, and f_C is the Coriolis parameter.

3.1.2 Thermal stability

An important characteristic of the atmospheric boundary layer is the thermal stability. It describes the suppressing of vertical motion in the atmosphere, and depends on the vertical temperature distribution. The lapse rate, Γ, is defined as the negative of the temperature gradient.

$$\Gamma = -\left(\frac{dT}{dz}\right) \tag{3.2}$$

The change in temperature for a fluid element of air transferred vertically in a gravitational field, when considering the air as a dry ideal gas and assuming that the process is adiabatic, is

$$\Gamma_a = \frac{g}{c_p} \approx \frac{1°C}{100\ m} \tag{3.3}$$

where g is the acceleration due to gravity and c_p is the specific heat at constant pressure. A measure of the thermal stability of the atmosphere is given by a comparison of the actual lapse rate in the atmosphere to the dry adiabatic lapse rate given in Equation 3.3. Three thermal stability states are conventionally defined as

- $\Gamma < \Gamma_a$: stable
- $\Gamma \approx \Gamma_a$: neutral
- $\Gamma > \Gamma_a$: unstable

The effect of thermal stability can be illustrated by a parcel of air being lifted to a higher elevation, while it is cooled at the dry adiabatic lapse rate which is $1°C/100\ m$. If this parcel is cooled faster than the surroundings, it will be more dense compared to the surrounding air, and hence tend to return to its original level. The atmosphere is then stable, contrary to if the density of the air parcel became lower than the density of surrounding air and continued to raise. Hence vertical movements of air are suppressed in a stable atmosphere, and enhanced in an unstable atmosphere. A strictly neutral atmosphere is uncommon, but the atmospheric boundary layer can be near-neutral when it is cloudy and during periods with strong winds.

3.2 Self-similarity

The term self-similarity, or self-preservation, is the idea that for a given geometry, any measured statistical turbulent quantity measured at different facilities and Reynolds numbers will collapse onto a single universal profile if properly scaled. Different length and velocity scales are used close to the surface, and away from it. Many suggestions for scaling have been given, but none have so far been successful in representing all the experimental data for turbulent flow. Such a non-dimensionalization is much more than a simple coordinate transform, and should be chosen based on the physics of the problem (Buschmann and Gad–el–Hak, 2007).

The quantity ν/u_* is called the viscous length scale. For a smooth surface this is the proper length scale in the inner layer, while u_* is the proper velocity scale. The superscript $^+$ is commonly used for lengths non-dimensionalized with ν/u_*, and velocities non-dimensionalized with u_*. For a rough surface additional length scales which characterize the roughness are proper for scaling. The velocity defect $(U_e - U)$, where U_e is the freestream velocity, or u_* are proper velocity scales in the outer layer. δ is the proper length scale in this layer.

3.3 Mean velocity profiles

3.3.1 Power law

The vertical wind profile for the streamwise mean velocities in the atmospheric boundary layer is in micrometeorology often described by a power law

$$\frac{U(z)}{U(z_{ref})} = \left(\frac{z}{z_{ref}}\right)^{\alpha} \tag{3.4}$$

z_{ref} is a chosen reference height, where any height can be used in principle. It is common to standardize by using 10 m or gradient height as reference height. Since

there often is an uncertainty related to what is the gradient height in the atmospheric boundary layer, $z_{ref} = 10\ m$ can be the best choice.

The exponent, α, is Reynolds number dependent for aerodynamically smooth surfaces, while it mainly depends on the roughness for aerodynamically rough surfaces. The exponent α has also been seen to depend on the stability (Arya, 1988). Turbulent velocity profiles are generally well approximated by the power law. There is no physical basis for the use of a power law, unlike the logarithmic law (Section 3.3.2) for which there is a theoretical basis. The power law has been seen to give a better fit in a wider range of velocities, and for high wind speeds, compared to the logarithmic law. The flow closest to the ground is on the contrary usually not well represented by the power law.

3.3.2 Logarithmic law

The logarithmic law describes the vertical mean velocity profile in the main flow direction in a turbulent boundary layer. It is generally derived by asymptotical fitting, requiring that the velocity profile in the sublayer should match the velocity profile in the outer layer (velocity-defect law) in an overlap region. The logarithmic law can also be derived in other ways, using mixing length arguments and dimensional reasoning. All these methods are well known, and more or less physically based.

The logarithmic law represents the flow over an uniform surface, and is strictly valid only for neutral stability. It is universal for smooth surfaces, and shifted downwards for rough surfaces. The logarithmic law can be written in two ways:

$$\frac{U}{u_*} = \frac{1}{\kappa}\ln\left(\frac{Z_z u_*}{\nu}\right) + C_0 - \frac{\Delta U}{u_*} \tag{3.5}$$

$$\frac{U}{u_*} = \frac{1}{\kappa}\ln\left(\frac{Z_z}{z_0}\right) \tag{3.6}$$

The validity of the logarithmic law can easily be seen by plotting Equation 3.5 as a function of the inner variables $U^+ = U/u_*$ and $Z_z^+ = Z_z u_*/\nu$ in a semi-logarithmic plot. $\kappa = 0.41$ is von Karman's constant, z_0 is the roughness length, u_* the friction velocity, $C_0 \approx 5.2$ and $\Delta U^+ = \Delta U/u_*$ is called the roughness function. $\Delta U^+ = 0$ for smooth surfaces. The roughness function increases for rougher surfaces, resulting in a downwards shift in the smooth logarithmic law. The roughness function for sand-grain roughness in a fully rough flow is given by (Raupach et al., 1991)

$$\Delta U^+ = -8.5 + C_0 + \frac{1}{\kappa}\ln\left(k_s^+\right) \tag{3.7}$$

where $k_s^+ = k_s u_*/\nu$ and k_s is representative for the height of the roughness.

For very rough surfaces the ground is not always the best zero level for the height. It can be argued that an appropriate zero level is located in between the ground and the top of the roughness elements. The zero level is in practise found from wind measurements in the surface layer. It can be defined by $Z_z = z - d_0$, where z is the height above ground and Z_z is the height above the new zero level. d_0 is

called displacement height, and is expected to be between 0 and the average height of the roughness elements, dependent on the density and shape of the elements. d_0 is typically $70-80$ % of the height of large roughness elements like trees and houses.

The roughness length z_0 is a surface parameter characterizing the terrain. It is the constant of integration in Equation 3.6, and the height where U becomes zero when extrapolated towards the surface. Results from laboratory experiments have indicated that z_0 is about $1/30-1/10$ of the height of the roughness elements. According to Wang et al. (1996) the roughness length is 8 % of the average real roughness. A comparison of Equation 3.5 with $\Delta U^+ = 0$, and Equation 3.6 for a smooth surface, gives the relation

$$z_0 \approx 0.12\frac{\nu}{u_*} \tag{3.8}$$

with the values $C_0 = 0.52$ and $\kappa = 0.41$. This indicate that the roughness length decreases with increasing friction velocity for smooth flow. For an aerodynamically rough surface, the roughness length is assumed to be constant and independent of u_* (Arya, 1988). Table 3.1 gives an overview of typical terrain types and corresponding roughness lengths.

Type of terrain	z_0 [m]	α
Ice, mud flats	10^{-5} - $3 \cdot 10^{-5}$	
Calm open sea	10^{-4}	
Sand, flat desert	$2 \cdot 10^{-4}$ - 10^{-3}	0.10
Off-sea wind in coastal areas	10^{-3}	
Snow surface	10^{-3} - $6 \cdot 10^{-3}$	
Fairly level grass plains	$6 \cdot 10^{-3}$ - $2 \cdot 10^{-2}$	
Farmland	$2 \cdot 10^{-2}$ - 10^{-1}	0.19
Forest and woodland	10^{-1} - 1	
Suburb	1 - 2	0.32
City	1 - 4	

Table 3.1: Typical values of the roughness length z_0 and the exponent in the power law α for various types of terrain (Counihan, 1975; Arya, 1988; Freris, 1990).

Equation 3.6 is favoured by people in the field of meteorology and wind engineering describing the velocity profile in the atmospheric boundary layer. Equating 3.5 with 3.6 gives a relation between the roughness function ΔU^+ and $Re_* = z_0 u_*/\nu$.

$$\Delta U^+ = C_0 + \frac{1}{\kappa}\ln\left(Re_*\right) \tag{3.9}$$

Re_* is the roughness Reynolds number which will be discussed in Section 5.2.1. With the values for C_0 and κ given above, this gives a roughness Reynolds number for smooth flow ($\Delta U^+ = 0$) of $Re_* = 0.119$

The logarithmic law can be modified by expressing the mixing length as $l = \kappa(z + z_0)$ instead of assuming a smooth surface with $l = \kappa z$ (as Equation 3.6 is deduced

from). This is commonly done when mixing at the earth's surface in considered (Manwell et al., 2002). The modified logarithmic law becomes

$$\frac{U}{u_*} = \frac{1}{\kappa} \ln\left(\frac{z + z_0}{z_0}\right) \tag{3.10}$$

Wake-function

An equation which is valid both in the overlap region and the outer layer can be found by adding a term for the wake to the logarithmic law (Krogstad et al., 1992),

$$\frac{U}{u_*} = \frac{1}{\kappa} \ln\left(\frac{Z_z u_*}{\nu}\right) + C_0 - \frac{\Delta U}{u_*} + \frac{2\Pi}{\kappa}\omega\left(\eta\right) \tag{3.11}$$

where $\eta = Z_z/\delta$. The function $\omega\left(\eta\right)$ is normalized so that it is 0 at the surface and 1 at the top of the boundary layer (δ). The parameter Π is called Coles' wake parameter, and depends upon among other things on the pressure gradient in the main flow direction. It determines the strength of the wake function.

Velocity-defect law

The flow in the outer layer is independent of viscosity, and the deviation of the mean velocity from the freestream velocity is given by the velocity-defect law

$$\frac{U_e - U}{u_*} = G\left(\eta\right) \tag{3.12}$$

where $\eta = Z_z/\delta$. The logarithmic law with the wake function included (Equation 3.11) results in the velocity-defect law expressed as

$$\frac{U_e - U}{u_*} = -\frac{1}{\kappa} \ln\left(\eta\right) + \frac{2\Pi}{\kappa}\left[\omega\left(1\right) - \omega\left(\eta\right)\right] \tag{3.13}$$

A common formulation of the velocity-defect law for boundary layers with zero pressure gradient is (Perry et al., 1987)

$$\frac{U_e - U}{u_*} = -\frac{1}{\kappa} \ln\left(\eta\right) + 2.309 \qquad 0 \leq \eta \leq 0.15 \tag{3.14}$$

$$\frac{U_e - U}{u_*} = 9.6(1 - \eta)^2 \qquad 0.15 \leq \eta \leq 1 \tag{3.15}$$

The Coriolis force has to be considered when studying the outer layer of the atmospheric boundary layer. The corresponding laws for the velocity deficit from the geostrophic wind velocity in a neutrally stratified atmospheric boundary layer are (Arya et al., 1987)

$$\frac{U_g - U}{u_*} = G_u\left(\frac{f_C Z_z}{u_*}\right) \tag{3.16}$$

$$\frac{V_g - V}{u_*} = G_v\left(\frac{f_C Z_z}{u_*}\right) \tag{3.17}$$

While the velocity-defect law in non-rotating flows is well confirmed by laboratory measurements, the corresponding expressions for the atmospheric boundary layer are almost impossible to prove empirically. This is due to lack of measurements, since neutral thermal stability in the atmosphere is very rare. Measurements from slightly stable and slightly unstable conditions, and also laboratory experiments of rotating flows, seem to follow Equation 3.16-3.17.

3.3.3 Change in surface roughness

A step change in the surface roughness length normal to the main flow direction, from z_{01} to z_{02}, will cause the friction velocity to change from u_{*1} to u_{*2}. An internal boundary layer (IBL) with height $h_i(x)$ will be developed from the roughness change and grow within the approaching boundary layer further downstream (Arya, 1988). This process is illustrated in Figure 3.1. Above the IBL the characteristics of the flow are similar to the approaching boundary layer. These characteristics can be expected to disappear at distances far enough downstream of the roughness change, where the IBL has grown to the equilibrium depth for the boundary layer above the new surface.

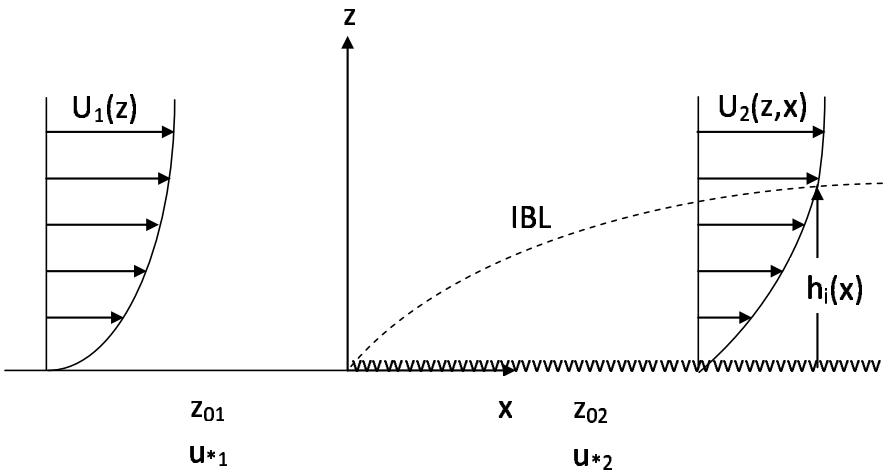

Figure 3.1: Illustration of a step change in the surface roughness length from z_{01} to z_{02}, with corresponding friction velocities u_{*1} and u_{*2}. The height of the created internal boundary layer (IBL) is denoted by $h_i(x)$.

Within the lowest $10 - 15$ % of the boundary layer in a neutral atmosphere the velocity profile can be approximated by (Arya, 1988)

$$U(z) = \frac{u_{*2}}{\kappa} \ln\left(\frac{z}{z_{02}}\right) \qquad z \leq h_i \tag{3.18}$$

$$U(z) = \frac{u_{*1}}{\kappa} \ln\left(\frac{z}{z_{01}}\right) \qquad z > h_i \tag{3.19}$$

The top of the IBL is naturally not as sharply defined as indicated by these equations, the velocity profiles change more gradually around $z = h_i$. There is also a question

about the validity of the logarithmic law in the lowest part, especially before the friction velocity u_{*2} has stabilized.

Several laboratory measurements and field studies under neutral conditions have revealed that the increasing thickness of the IBL after a step change in roughness seems to follow a power law (Arya, 1988)

$$\frac{h_i}{z_{02}} = a_i \left(\frac{x}{z_{02}} \right)^{0.8} \tag{3.20}$$

where the empirical constant has values $a_i = 0.35 - 0.75$. The value of a_i also depends upon how the top of the IBL is defined. Studies have shown that the value of the exponent is similar to the exponent in the classical approximate law for growth of a turbulent boundary layer above a flat plate parallel to the flow.

3.3.4 Fit of logarithmic law and power law

There are several ways to fit the logarithmic law to measured data. The method of trial and error is commonly applied, meaning that a combination of parameter values which gives the best fit in some way are selected. The method of least squares (Rice, 1995) can also be a part of the fitting procedure. As an alternative option the method given by Perry et al. (1987) can be used to find d_0 at first. It is also possible to measure u_* directly if a skin-friction balance is available. For measurements of flow above a smooth surface, the value of the parameters in the logarithmic law (Equation 3.5) can be found manually by inspecting the semilogarithmic plot of U^+ versus Z_z^+:

1. Due to uncertainty in positioning of the probe, d_0 might differ from 0. A straight line in the logarithmic area will indicate the right value of d_0. This will mainly alter the inner part of the profile in a plot like this.

2. Adjust u_* until as much as possible of the measured data coincides with the logarithmic law line for a smooth surface (with slope $1/\kappa$). This straight part is the logarithmic part of the profile. u_* is strictly speaking the only parameter possible to change.

3. C_0 can be altered slightly when u_* is roughly set. This will compensate for any possible irregularities of the surface. C_0 is usually in the range $5 - 5.5$.

Similarly, the parameters in Equation 3.5 for flow over a rough surface can also be found by inspecting the semilogarithmic plot of U^+ versus Z_z^+ and

1. Adjusting d_0 to make the logarithmic part a straight line.

2. Adjusting u_* roughly until the graph is parallel with the logarithmic law for a rough surface. This value of u_* can be compared to the value found by extrapolating the shear stress close to the wall (dependent on what is known about the pressure gradient).

3. Reading the value of ΔU^+ from the graph.

The power law can easily be fitted to the measured mean velocity profile by applying the method of least squares for a chosen reference height. The exponent is calculated by

$$\alpha = \frac{\sum_{i=1}^{i=N} \ln\left(z_i/z_{ref}\right) \ln\left(U_i/U_{ref}\right)}{\sum_{i=1}^{i=N} \left(\ln z_i/z_{ref}\right)^2} \tag{3.21}$$

where U_{ref} is the mean of the measured velocities at the reference height z_{ref}. This formula is derived to minimize the sum of the squared residuals, with the residuals defined as the deviation between the measured velocity and that given by the model at each height level. The height range included in this fit should be carefully selected, since the power law is considered to be less representative of the flow in the region closest to the wall compared to the flow further out in the boundary layer.

3.3.5 Relations between power law exponent, roughness length and turbulence intensity

Several relationships have been proposed to calculate the exponent α in the power law from the more physically correct logarithmic law. These approximations can be quite complicated, and reduce the directness and simplicity of the power law. Hence, it can be better just to accept the empirical nature of the power law and calculate α directly from the measured velocities. One of the proposed relations between the roughness length and the power coefficient is (Freris, 1990)

$$z_0 = 15.25e^{-1/\alpha} \tag{3.22}$$

The gustiness of the wind can be measured by the turbulence intensity, which is defined as the ratio of the standard deviation of the velocity to the mean velocity

$$I_u = \frac{\sigma_u}{U} \tag{3.23}$$

The variation of the turbulence intensity at 30 m height as a function of roughness length and that of the power law exponent as a function of roughness length obey the same law (Counihan, 1975).

$$\alpha = \left(\frac{\sigma_u}{U}\right)_{30m} = 0.096 log_{10} z_0 + 0.016 \left(log_{10} z_0\right)^2 + 0.24 \tag{3.24}$$

Hence, the turbulence intensity at 30 m above the ground is known if the power law exponent at a given location is known. The reference height of 30 m for turbulence intensity is chosen based on the fact that measurements at this height should be free from very local influences, at the same time as the measurements are representative of the local terrain. The commonly used reference height in meteorology of 10 m is too low at many locations, and for extremely rough conditions even 30 m can be too low.

Typical values for the streamwise standard deviation in the surface layer found by measurements is $\sigma_u \simeq 2.5u_*$. Combining this, Equation 3.6 (with $d_0 = 0$) and

Equation 3.23 gives the following expression for turbulence intensity as a function of the height above ground

$$I_u(z) = \frac{1}{\ln(z/z_0)} \tag{3.25}$$

With the relation in Equation 3.22 the dependence of the turbulence intensity with height can be written as

$$I_u(z) = \frac{\alpha}{1 + \alpha \ln z/15.25} \tag{3.26}$$

3.4 Integral length scale

The normalized autocorrelation function $R_{uu}(\tau)$ for a time series $u'(t)$ relates the fluctuation part of the velocity at the time t to the corresponding value at the time $t+\tau$, hence provides information about the correlation of the time series with itself for different time lags τ. It is given by (Freris, 1990; Manwell et al., 2002)

$$R_{uu}(\tau) = \frac{1}{\sigma^2 T} \int_{t=t_0}^{t=t_0+T} u(t)u(t+\tau)dt \tag{3.27}$$

This function has a maximum value at zero time lag, $R_{uu}(0) = 1$, and decreases to 0 as τ increases. The autocorrelation calculated from time series measured in a wind tunnel will finally fluctuate around 0, due to continuously small changes of the wind tunnel velocity.

The integral time scale is associated with the average eddy size of the turbulence. It is found by integrating the autocorrelation function from zero lag to the first zero crossing (Manwell et al., 2002)

$$T_u = \int_{\tau=0}^{\tau=\tau_{cross}} R_{uu}(\tau)\, d\tau \tag{3.28}$$

The integral length scale ${}^xL_u$ is the average size of the eddies in the streamwise direction, and it indicates the scales of the eddies containing the major part of the kinetic energy. At a given height it can be calculated by multiplying the integral time scale with the streamwise mean velocity.

$${}^xL_u = T_u U \tag{3.29}$$

The integral length scale in the atmospheric boundary layer decreases with increase of roughness, and it increases with increase of height up to $200 - 300\ m$. The length scale of the atmospheric turbulence at a height of $30\ m$ can be estimated by (Counihan, 1975)

$${}^xL_u = 108 \left(\frac{1}{z_0}\right)^{1/6} \tag{3.30}$$

ESDU recommend the following approximate relationship to estimate the integral length scale (Freris, 1990)

$${}^xL_u = 25 \frac{z^{0.35}}{z_0^{0.063}} \tag{3.31}$$

3.5 Power spectrum

The power spectral density, PSD, describes how the power (or variance) of a time series is distributed with frequency. Being power per unit of frequency, the dimensions are those of a power divided by Hz. When velocity time series are studied, the spectral energy density unit is m^2/s. Assuming that the spectral energy density can be integrated over all frequencies, it can be written as

$$\sigma_u^2 = \int_0^\infty E_{uu}(f)\, df \tag{3.32}$$

and the normalized power spectrum is

$$\Phi_{uu}(f) = \frac{E_{uu}(f)}{\sigma_u^2} \tag{3.33}$$

A common rewriting is

$$\int_0^\infty \Phi_{uu}(f)\, df = \int_0^\infty f\Phi_{uu}(f)\, d[\ln f] = 1 \tag{3.34}$$

When plotting Φ_{uu} versus f the total area under the curve equals 1, hence the area under the curve between any two frequencies corresponds to the fraction of the variance which is contained by that range of frequencies. Unfortunately such a plot will be useless since the wide range of values will compress the data to the axis. A much better alternative is plotting $f\Phi_{uu}$ versus $\ln f$. This conserves the characteristic related to the area under the curve, at the same time as the curve is made readable. A wide range of frequencies and spectral densities can also be displayed when plotting $\ln f\Phi_{uu}$ versus $\ln f$. The area under the curve is not equal to 1 when plotted this way, but the subrange part of the spectrum, which is proportional to $f^{-5/3}$, can be seen as a straight line with slope $-5/3$.

A commonly used model for the spectrum of the longitudinal component of turbulence, similar to one developed by von Karman for turbulence in wind tunnels, is

$$\frac{fE_{uu}(f)}{\sigma_u^2} = \frac{4X}{(1+70.8X^2)^{5/6}} \qquad X = \frac{fL_{Karman}}{U} \tag{3.35}$$

f is the frequency, L_{Karman} is identical to the integral length scale (${}^xL_u$) and U is the mean wind speed at the height of interest. This model will be referred to as "von Karman" throughout this thesis. The von Karman spectrum has been shown to represent wind tunnel turbulence well, and it has been suggested that it gives a good representation of atmospheric turbulence above about 150 m (Burton et al., 2001).

Harris proposed an improvement to an expression for the power spectra of the longitudinal gust component originally suggested by Davenport. This turned out to be identical in form to a formula previously proposed by von Karman for wind tunnel turbulence.

$$\frac{fE_{uu}(f)}{\sigma_u^2} = \frac{4X_H}{2.58^2\,(2+X_H^2)^{5/6}} \qquad X_H = \frac{fL_{Harris}}{U_{10m}} \tag{3.36}$$

where f is the frequency. L_{Harris} is an arbitrary length with a typical full-scale value of 1800 m and U_{10m} is the mean wind speed at 10 m, hence the model is independent of height above ground level.

Another model for longitudinal turbulence spectra, which differs from the two above, is Kaimal's model

$$\frac{fE_{uu}(f)}{\sigma_u^2} = \frac{4X}{(1+6X)^{5/3}} \qquad X = \frac{fL_{Kaimal}}{U} \tag{3.37}$$

where f is the frequency, L_{Kaimal} is a length scale and U is the mean wind speed at the height of interest. In order for Kaimal's model and von Karman's model to have the same high-frequency asymptotic limit, the length scale must be related to the von Karman length scale (i.e. the integral length scale) by $L_{Kaimal} = 2.329L_{Karman}$ (Burton et al., 2001). This spectrum has been seen to give a good fit to observations of atmospheric turbulence. Also, the Kaimal spectrum has a lower and broader peak than the von Karman spectrum.

Chapter 4

Wind above complex terrain

The term "complex terrain" is used for a wide range of terrain types in the literature. Some of the features which are called steep and complex in one case, can be gentle and simple compared to other cases. The term complex is sometimes used for steep hills, while in other cases used for terrain composed of several features. One criterion commonly used for defining the terrain as complex is that separation occurs. This chapter describes typical flows over complex terrain, mainly focusing on isolated terrain features. Well known theories and empirical estimation methods for speed-up effects are also presented.

4.1 Speed-up

An increase in velocity often occurs on the top of topographic features like escarpments and ridges, and this phenomenon is called speed-up. The velocity over the topography can be written as

$$U(x,z) = U_0(z) + \Delta U(x,z) \tag{4.1}$$

where $U_0(z)$ is the mean velocity of the incoming flow far upstream of the terrain feature. This is illustrated in Figure 4.1. The speed-up effect may be quantified by the fractional speed-up ratio, which is defined as the fraction of the change in velocity to the approaching undisturbed velocity at each height

$$\Delta S(x,z) = \frac{U(x,z) - U_0(z)}{U_0(z)} = \frac{\Delta U(x,z)}{U_0(z)} \tag{4.2}$$

The speed-up is typically highest close to the ground near the crest, and decreases with height and distance from the crest. According to Arya (1988) the largest speed-ups are observed over three-dimensional hills of moderate slope. A very general rule of thumb given by ESDU (1993) is that the speed-up vanishes at heights above $2L_u$ independent of position downstream of the crest. L_u is the horizontal length of the upwind slope of the equivalent embankment in the ESDU method as defined in Figure 4.2.

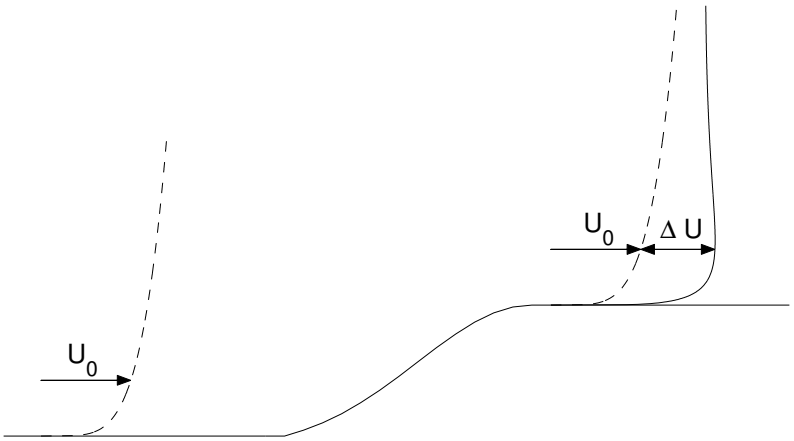

Figure 4.1: Illustration of speed-up.

4.2 Typical flow field

The mean flow approaching an isolated two-dimensional ridge at an approximately right angle under neutral thermal conditions is expected to behave according to the following description: The flow will decelerate slightly at the upwind foot of the hill, before it accelerates to the hilltop. This deceleration at the foot of the hill may cause a small separation bubble if the hill is steep enough. Maximum velocity occurs at the hilltop. According to ESDU (1993), the maximum speed-up is actually found just upwind of the highest point for rounded hills, and not exactly at the crest. The wind then decelerates again behind the hill. A wake region with a velocity deficit develops and lasts for several hill heights downstream of the hill. Similar features can be seen for flow over an axisymmetric hill, except that the upwind deceleration is absent. Instead the streamlines divide and pass on each side of the hill. This divergence decreases with height up along the centreline of the hill, and disappears at the crest. Studies of flows approaching several parallel ridges at a right angle to the ridge has shown that the speed-up is maximum for the first ridge, and that the flow above this ridge behaves as if the following ridges did not exist. After the flow has passed some more ridges, the speed-up approaches a constant and much lower value.

Separation above terrain features occurs due to high curvature and the accompanying adverse pressure gradient. Hence the flow will separate at the lee side of a hill if the downstream slope is steep enough. The velocity profile has zero gradient with respect to z close to the surface at the separation point, and the flow near the surface is reversed compared to the main flow at some region downstream of this point. Separation can also be provoked by sharp edged crests, where the separation point can easily be predicted. At such a sharp edge the velocity accelerates all the way to the separation point where the deceleration occurs. The lee-side hill wakes are characterized by reduced mean flow and enhanced turbulence. The maximum topographically induced perturbations to the flow in the near wake depend on the aspect ratio, slope and shape of the hill (Arya, 1988). Behind long steep ridges, the

wake region may extend up to ten hill heights in the downstream direction. The wake is at most a few hill heights long and frequently smaller for three-dimensional hills (Arya, 1988).

The roughness is of major importance for how steep a hill can be before separation occurs in the descending hill. It has been shown that both for smooth naturally shaped and triangularly shaped two-dimensional ridges, the critical angle for steady separation is 18° (Kaimal and Finnigan, 1994). For a corresponding very rough ridge, the critical angle is about 10°. For three-dimensional hills the critical angle for separation increases, while the separation bubbles decrease and are more dependent on the topography of the hills, compared to two-dimensional ridges. Reduction of surface roughness does also in this case result in a steeper critical slope needed for separation to occur. The onset of separation is in other words very dependent on the surface roughness, even when the hills are abrupt and topographical effects could be expected to dominate. Finnigan et al. (1990) refer to results which indicate that the critical slope angle for steady separation on the lee side of smooth, symmetrical and two-dimensional ridges is about 20°. Increased surface roughness is seen to promote separation, and "physically this can be explained as the increased roughness diminishes the wind momentum near the ground and thus reduces its capability to overcome the adverse pressure gradient" (Venås, 1998).

The onset of separation does not only affect the flow in the region of separation, but changes the wind field over the entire hill due to the large-scale pressure field that develops around the hill. Hence the terrain and the separation bubble appears as one single obstacle, making it necessary to consider separation before estimating the speed-up by formulas (Kaimal and Finnigan, 1994). This is taken into consideration by the ESDU method described in Section 4.3.3.

4.3 Speed-up estimates

As Miller and Davenport (1998) state, one of the most important questions about speed-ups in complex terrain is how the values calculated by commonly applied simple models coincide with observed values. Many codes of practice only consider a few simple features, and real terrain can not be represented by any of these separately. The situation is further complicated in cases where the terrain is steeper than the methods of estimation are designed for.

4.3.1 Linearized theory and simple estimates

The theory for flow over isolated, low and smooth hills in neutral stratification has become well-established. For hills like this, where separation is avoided, speed-up can be understood by applying ideas from linearized theory (i.e. linearized equations of motion). This kind of theory is strictly speaking only valid for hills with gentle slopes. The maximum recommended value of the hill slopes is typically 20°, or as low as 10° (Kaimal and Finnigan, 1994). Simple estimates based on linearized theory has frequently been applied to slopes out of the recommended range, and has shown to agree well with observations.

Jackson and Hunt (1975) separated the layer of air influenced by the terrain into an inner and an outer layer. The wind shear in the outer layer is small, the surface roughness is not important, turbulent exchange can be neglected, the Reynolds shear stress variation is negligible, the mean flow pattern is dominated by inertial forces, the mean flow can be treated as essentially inviscid, the disturbance due to the hill is almost irrotational, and only the size and shape of the terrain is significant, hence potential flow theory prevails. The surface roughness becomes more important below about $L_{H/2}/10$, so that potential theory is no longer applicable (Freris, 1990). $L_{H/2}$ is the half-length of the hill, defined as the horizontal distance from the crest to the upstream point where the height is half the maximum hill height (Figure 7.9). The inner layer is a region with large wind shear, where turbulent stress is important. It is influenced by the hill through turbulent exchange, and inertia and turbulence effects are dominant and balance each other. The thickness l of this layer depends on the roughness and size of the hill. The inner layer with height l is expected not to extend above the surface layer of the atmospheric boundary layer (Jackson and Hunt, 1975).

Over low hills where linearized theory apply, the very simple assumption that the hill constitutes only a small perturbation to an existing logarithmic velocity profile can be made, and this leads to the following definition of l (Kaimal and Finnigan, 1994):

$$\frac{l}{L_{H/2}} \ln\left(\frac{l}{z_0}\right) = c \tag{4.3}$$

where z_0 is the roughness length. This and other similar equations for l are discussed in the work by Pellegrini and Bodstein (2004). In the two layer theory of Jackson and Hunt the value stipulated for the constant was $c = 2\kappa^2$. κ is von Karman's constant. The fractional speed-up ratio is

$$\Delta S = \frac{\Delta U}{U_0} = O\left[\frac{H \ln^2\left(L_{H/2}/z_0\right)}{L_{H/2} \ln\left(z/z_0\right) \ln\left(l/z_0\right)}\right] \tag{4.4}$$

In this theory the thickness of the inner layer, l, is also the height where ΔU attains its maximum. The maximum of ΔS is at the top of the hill at a height $z \simeq l/10$ above the surface, but it varies quite slowly with height. In practice it is approximately $2H/L_{H/2}$ and hence proportional to the slope. This is twice the value that uniform potential flow over such a hill would give. The theory of Jackson and Hunt is developed with a view to two-dimensional symmetrical hills. It is valid in the limit as $L_{H/2}/z_0 \to \infty$ when $H/L_{H/2} < \frac{1}{8}\left(z_0/L_{H/2}\right)^{0.1}$ and $\delta/L_{H/2} \gg 2\kappa^2/\ln\left(\delta/z_0\right)$, where $L_{H/2}$ and H are the characteristic half-length and height of the hill, z_0 the roughness length and δ the boundary layer height. The height of the hill should be much smaller than the characteristic length scale. Cliffs are excluded since the slope of the hill is assumed to be of the order H/L everywhere.

Another, and much simpler, guideline for estimating the fractional speed-up ratio over small terrain features is given by Kaimal and Finnigan (1994). This is based on the ratio of the height to the half-length, $\phi = H/L_{H/2}$, of the axisymmetric hill, the two-dimensional escarpments or the two-dimensional ridge.

$$\begin{aligned} \Delta S_{\Delta U_{max}} &\simeq 1.6\phi \quad \text{axisymmetric hills} \\ \Delta S_{\Delta U_{max}} &\simeq 0.8\phi \quad \text{two-dimensional escarpments} \\ \Delta S_{\Delta U_{max}} &\simeq 2.0\phi \quad \text{two-dimensional ridges} \end{aligned} \tag{4.5}$$

$\Delta S_{\Delta U_{max}}$ is the value of ΔS where ΔU is maximum. Experiments in wind tunnels and field measurements have shown that this estimate is accurate to within ± 15 % (Kaimal and Finnigan, 1994), and even better when the studied feature fits the assumption of linear theory. Steady separation bubbles are formed when terrain features are steep enough, and the bubbles increase with increasing slope. In case of separation, it is the flow around the feature plus the separation bubble that should be considered and used to calculate $L_{H/2}$. This puts a limit to the fractional speed-up ratio of $\Delta S_{max} = 1.25$, a value attained for the feature resulting in the smallest separation bubble, which is found for an axisymmetric hill.

4.3.2 LSD approach

The LSD approach is a simple method to approximately determine the fractional speed-up ratio over several types of topography. It is mainly developed from numerical simulations of wind flow over various hills. The expression for two-dimensional escarpments/embankments will be given here. This and estimates for other terrain types are described by Lemelin et al. (1988). The approach is valid for near-neutral thermal stability. The local irregularities of the hill should be small compared to the overall dimensions of the hill, and the terrain surrounding the hill should be relatively flat. The LSD approach is independent of the surface roughness provided that $150 \leq L_{H/2}/z_0 \leq 100000$. The results for steep hills is more approximate, since separated flow might occur, and this again alters the effective shape of the hill. Speed-ups over embankments can be treated like escarpments when the horizontal downstream plateau is greater than $2L_{H/2}$, and the LSD approach for a two-dimensional escarpment is

$$\Delta S(x,z) = \Delta S_{max} \left(\frac{1}{1 + 3\left(x/nL_{H/2}\right)^p} \right)^2 \left(\frac{1}{1 + a\left(z/L_{H/2}\right)} \right)^2 \tag{4.6}$$

$$\Delta S_{max} = 1.3G \tag{4.7}$$

The parameter values are listed in Table 4.1. The maximum possible value $\Delta S = 1.3$ above an escarpment/embankment is found closest to the ground ($z \simeq 0$) at the very crest ($x = 0$) if $H/L_{H/2} > 1$. The second term on the right hand side in Equation 4.6 expresses how the fractional speed-up ratio decreases with distance from the crest, while the third term expresses how the fractional speed-up ratio decreases with height.

The LSD approach was kept relatively simple since it was intended for incorporation into building codes. According to Miller and Davenport (1998) the work of Lemelin et al. (1988) has been incorporated into the National Building Code of Canada.

$\phi = H/L_{H/2}$	G	$L_{H/2}$	a		n	p
≤ 1.0	ϕ	H/ϕ	2.0	$x \leq 0$	1.0	2.0
				$x > 0$	5.0	1.0
> 1.0	1.0	H	0.6	$x \leq 0$	0.5	2.0
				$x > 0$	10.0	1.0

Table 4.1: Values applied in the LSD approach. $x = 0$ at the crest. H is the hill height, and $L_{H/2}$ the half-length of the hill.

4.3.3 ESDU method

Engineering Sciences Data Unit (ESDU) provides validated design data, methods and software in the fields of aerospace, mechanical, process, and structural engineering. ESDU (1993) presents the method for estimating speed-up on the mean wind speed due to flow over topography. It is based on an equivalent embankment concept, which means that it is assumed that all topographical effects can be related to those occurring on a corresponding embankment. An embankment having the same hight and maximum slopes as the actual hill is superimposed. This embankment and relevant length parameters are illustrated in Figure 4.2. The method reported here is very simple, but is based on much more complex methods which solves the Navier-Stokes equations for flow over topography in a neutrally stratified atmospheric boundary layer.

For two-dimensional terrain the speed-up factor is given by

$$K_{L2d} = \frac{U(x,z)}{U_0(z)} = 1 + 2\phi_u s \tag{4.8}$$

where $\phi_u = H/L_u$ is the effective maximum upwind slope. The definition of ΔS in Section 4.1 yields $\Delta S = 2\phi_u s$. The variation of s with height is given as

$$\frac{s_z}{s_{z=0}} = \frac{1}{1 + a \mid s_{z=0} \mid (z/L_u)^{0.8}} \tag{4.9}$$

where the value $s_{z=0}$ has to be read from a graph ("Figure 1a Values of s for two-dimensional embankments at $z = 0$") given in ESDU (1993) for each horizontal position at the hill. The values of a depend on x_o/L_u and are

$$\begin{array}{rcccll} & x_o/L_u & \leq & -1 & : \quad a = & 12 \\ -1 \leq & x_o/L_u & < & 0.25 & : \quad a = & 5 - 7x_o/L_u \\ 0.25 \leq & x_o/L_u & \leq & P/L_u + 1 & : \quad a = & 5 + 7(x_o - P)/L_u \text{ or } 3.25 \\ & & & & & \text{(whichever is larger)} \end{array}$$

The extracted values for s have been derived for $H/h = 0.04$. The local boundary layer height is defined as $h = u_*/(6f_C)$, where u_* is the friction velocity and f_C the Coriolis parameter. In the case of very high hills ($H/h > 0.04$), an effective blocking appears and tends to increase the value of s. This is due to the fact that the top of the boundary layer does not react immediately to the change in the local

topography. s should then be multiplied by a correction factor $(1 + f_h)$, where f_h is approximated by

$$f_h = 1.25 \left(\frac{H}{h} \right)^{1/2} - 0.25 \tag{4.10}$$

When using this equation it is sufficiently accurate to assume that $h \approx 1500\ m$.

For steep slopes, $\phi_u > 0.4$, separation is assumed at the base of the hill upwind of the crest. This creates an effective maximum slope, which is approximately constant above a certain hill slope, so that $\phi_u = \phi_{max}$. The following limitation should then be introduced to the speed-up factor for $\phi_u > \phi_{max}$:

$$K_{L2d} = 1 + 2\phi_{max} s \tag{4.11}$$

where s is obtained as before.

$$\phi_{max} = \frac{\phi_{max,z=0}}{1 - (z/h)\,\phi_{max,z=0}} \tag{4.12}$$

where h is the local boundary layer height. For two-dimensional hills and embankments the value $\phi_{max,z=0} = 0.4$ can be assumed to apply. The value of ϕ_{max} increases with height, and this indicates that the effect of separation is of greatest importance in an inner region.

In addition to this simple method, ESDU (1993) gives a more detailed method which takes into consideration the actual profile of rounded hills. Methods for three-dimensional topography, for wind direction not normal to the ridge line, for irregularly shaped hills, and for multiple hills are also given in ESDU (1993) but not described or utilized here.

4.3.4 The Guidelines

The Guidelines (Weng et al., 2000) are a set of equations for estimation of the fractional speed-up ratio at various heights over the summit of hills. It is assumed that ΔS varies exponentially with height as

$$\Delta S = \Delta S_{max} \exp\left(-\frac{Az}{L_{H/2}}\right) \tag{4.13}$$

where the maximum fractional speed-up ratio, occurring closest to the surface, is given by

$$\Delta S_{max} = \frac{BH}{L_{H/2}} \tag{4.14}$$

The empirical constants A and B depend on the type of topographical feature and the surrounding terrain, and the recommended values are listed in Table 4.2. The terrain feature can either be isolated, or surrounded by regularly repeated similar features as in rolling terrain. The approaching wind profile is assumed to be logarithmic, and the atmospheric stability neutral. The Guidelines presented here are the original ones. These should be applied in cases of moderate to high wind speeds,

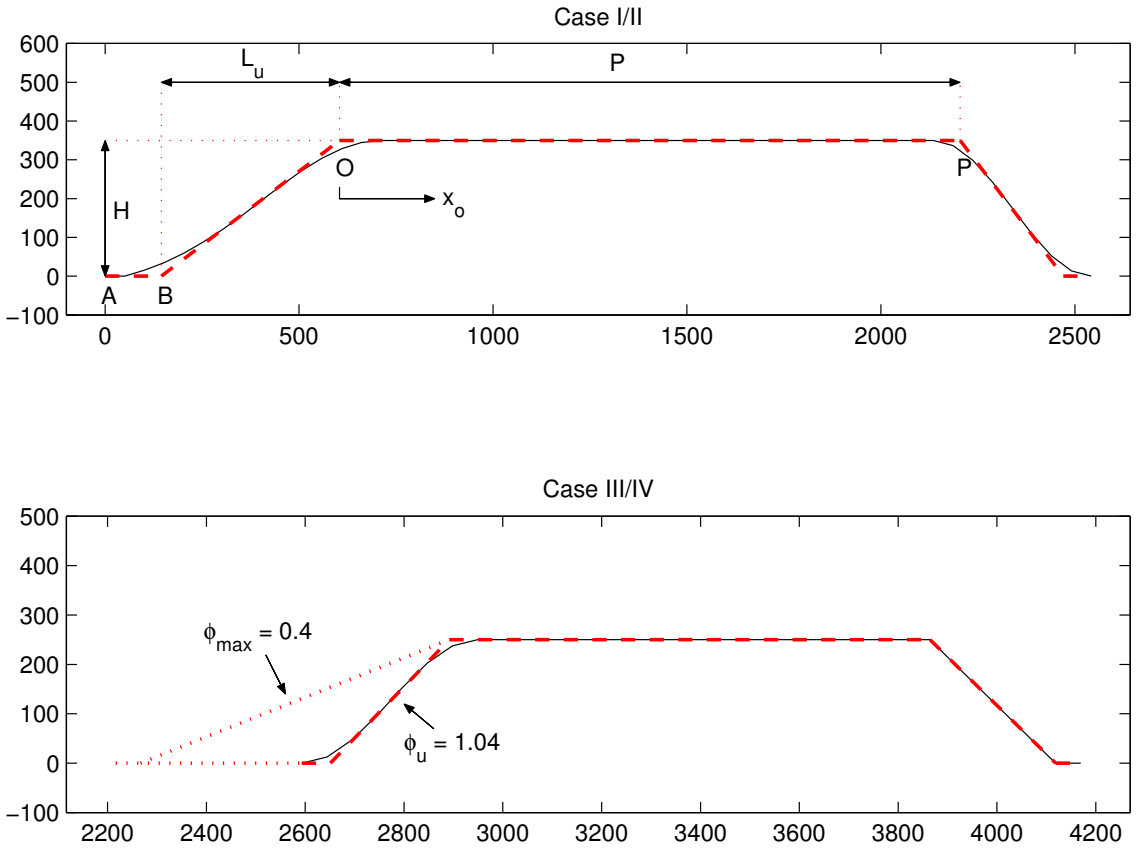

Figure 4.2: Equivalent embankment concept and length definitions for the ESDU method. The definitions are valid for wind from left to right in the upper part of the figure. The slope $\phi_{max} = 0.4$ is illustrated with a dotted line in the lower part of the figure.

Topography type	A	B
2D hills (ridges)	3.0	2.0
3D hills (axisymmetric hills)	4.0	1.6
2D escarpments	2.5	0.8
2D rolling terrain	3.5	1.55
3D rolling terrain	4.4	1.1
Flat terrain	0.0	0.0

Table 4.2: Constants for use with the original Guidelines.

maximum slopes < 0.3, $L_{H/2}/z_0 > 100$ and $L_{H/2} < 2000\ m$. The applicable height range is $z_0 \ll z < 150\ m$.

Nonlinear effects become important as the slope increases. Weng et al. (2000) presented a set of improved Guidelines which can be applied for slopes up to 0.5, instead of 0.3 as is the case for the original Guidelines presented above. The effect of surface roughness is also incorporated in the improved Guidelines. Compared to the original Guidelines the expression for ΔS_{max} is changed, and new empirical constants are given for different terrain types. Constants for escarpments are not given in the improved Guidelines.

4.3.5 Potential flow theory

The velocity potential Φ exists if the flow is irrotational, and all velocities derived from such a potential function always constitutes an irrotational flow.

$$\vec{V} = \nabla\Phi \tag{4.15}$$

A velocity potential can also be derived for a compressible fluid. Potential flow theory limited to incompressible fluids is often called ideal flow theory or hydrodynamics (Gerhart et al., 1992). If fluid viscosity is neglected, then an initially irrotational flow remains irrotational. The velocity potential fulfils Laplace's equation

$$\nabla^2\Phi = \frac{\partial^2\Phi}{\partial x^2} + \frac{\partial^2\Phi}{\partial y^2} + \frac{\partial^2\Phi}{\partial z^2} \tag{4.16}$$

If the flow under consideration is limited to be two-dimensional and two-directional, the velocity potential satisfies the two-dimensional Laplace equation. For two-dimensional flow a second scalar function, the stream function, can also be defined. It can be shown that the continuity equation both is a necessary and sufficient criterion for Ψ to exist, and velocity fields derived from Ψ automatically satisfies the continuity equation. Lines with $\Psi = constant$ are called streamlines, and hence are tangent to the velocity vector. Lines with $\Phi = constant$ are called equipotential lines, and are perpendicular to the streamlines. The velocity components can be derived from the velocity potential and the stream function by

$$u = \frac{\partial\Phi}{\partial x} = \frac{\partial\Psi}{\partial y} \tag{4.17}$$

$$v = \frac{\partial\Phi}{\partial y} = -\frac{\partial\Psi}{\partial x} \tag{4.18}$$

The stream function is constant on a solid surface, so a solid surface is a streamline. This implies that any streamline can be replaced by a solid surface, and the rest of the streamlines will represent the flow above this surface.

Finding the velocity potential function, the stream function or the velocity distribution for a specific geometry, is sufficient to find the two others. Potential flows can be calculated by either direct or indirect methods. Indirect methods include the method of complex variables, and the method of singularities. Singularities are

points where governing equations are not valid, and realistic mass-conserving irrotational flows can actually be generated by singularities. Two basic singularities are the source and the sink. Several singularities can be combined in the same plane. This is called superposition, and can be done since the velocity potential function and the stream function are linear. Hence, if Φ_1 and Φ_2 both are solutions to a problem, then $\Phi_1 + \Phi_2$ is also a solution.

A closed body can be created by adding a uniform flow parallel to the x-axis, a source and a sink with equal strength downstream. The sink located at $(+a, 0)$ ingests all the output from the source located at $(-a, 0)$. The resulting flow has a streamline surrounding the source-sink pair, which separates the flow introduced by the source and ingested by the sink from the main stream. This streamline can be replaced by a solid surface, which is called a Rankine oval. The streamlines outside the oval has $\Psi > 0$ and represents the flow around the Rankine oval. The streamlines inside the oval ($\Psi < 0$) are unrealistic. The stream function around a Rankine oval is (Gerhart et al., 1992)

$$\begin{aligned} \Psi &= \Psi_{uniform} + \Psi_{source} + \Psi_{sink} && (4.19)\\ &= U_\infty y + \frac{\lambda}{2\pi} \arctan\left(\frac{y}{x+a}\right) - \frac{\lambda}{2\pi} \arctan\left(\frac{y}{x-a}\right) && (4.20)\\ &= U_\infty y - \frac{\lambda}{2\pi} \arctan\left(\frac{2ay}{x^2+y^2-a^2}\right) && (4.21) \end{aligned}$$

And the corresponding velocities are

$$\begin{aligned} u &= \frac{\partial \Psi}{\partial y} = U_\infty + \frac{\lambda}{2\pi}\left[\frac{x+a}{(x+a)^2+y^2} - \frac{x-a}{(x-a)^2+y^2}\right] && (4.22)\\ v &= -\frac{\partial \Psi}{\partial x} = \frac{\lambda}{2\pi}\left[\frac{y}{(x+a)^2+y^2} - \frac{y}{(x-a)^2+y^2}\right] && (4.23) \end{aligned}$$

where λ is the flow rate, called the strength of the source/sink. The total velocity is $\sqrt{(u^2+v^2)}$. The maximum velocity is found where the Rankine oval has its maximum thickness. This thickness is given by

$$\frac{t}{a} = \cot \frac{t/a}{\lambda/(\pi U_0 a)} \qquad (4.24)$$

This type of calculations will be used later to compare the experimental observations of fractional speed-up ratio with potential flow estimates.

Chapter 5

Wind tunnel modelling

This chapter deals with possibilities, limitations and validity of wind tunnel modelling. Methods for generating atmospheric boundary layers in wind tunnels will also be presented.

5.1 Similarity parameters

Models studied in wind tunnels are typically much smaller than the corresponding full-scale objects, meaning that the model results do not necessarily correspond to full-scale conditions. Results from wind tunnel experiments are representative of full-scale flow if similarity parameters for the model and the full-scale object are equal. Similarity parameters can be obtained by non-dimensionalizing the equations of motion for fluid flow. These are the time-averaged equations for conservation of mass, conservation of momentum and conservation of energy. Some of the resulting dimensionless numbers are the (White et al., 2001)

- Reynolds number
- Rossby number
- Densimetric Froude number / Bulk Richardson number
- Prandtl number
- Eckert number

All these parameters should be matched for exact modelling, but this will be impossible. Hence those of the similarity parameters considered most critical for the validity of the experiment should be selected.

5.1.1 Reynolds number

The Reynolds number of a flow is

$$Re = \frac{UL}{\nu} \tag{5.1}$$

where U and L are characteristic velocity and length scales of the flow. $\nu = \mu/\rho$ is the kinematic viscosity, and the value for air at 1 atm and 20° is $\nu = 1.5 \cdot 10^{-5}$. The Reynolds number represents the ratio of inertial to viscous forces. The scale reduction usually necessary in wind tunnel experiments results in a Reynolds number that may be much smaller than in the full-scale case. It is hardly possible to create an orographic model with a Reynolds number identical to the full-scale, thus the viscous forces are more dominant in the experiments than in nature. No atmospheric flow could be modelled if strict adherence to the Reynolds number criterion was required. With the absence of thermal and Coriolis effects it has been shown that the scaled model flow will be dynamically similar to the full-scale case if the Reynolds number is larger than a minimum independence value. There exists a large amount of test results supporting this principle. The gross structure of turbulence is similar over a wide range of Reynolds numbers.

5.1.2 Rossby number

The Rossby number is defined by the ratio of advective acceleration to Coriolis acceleration

$$Ro = \frac{U}{L\Omega} \tag{5.2}$$

A large Rossby number indicates that Coriolis accelerations are small. The Rossby number of the flow in a non-rotating wind tunnel is large, while Coriolis forces affect levels above the surface layer in the atmospheric boundary layer. Hence the Rossby number can be ignored and the flow accurately modelled in the lowest $10 - 15$ % of the boundary layer in a non-rotating wind tunnel, while the Rossby number is small and so Coriolis effects become important to match at heights above this.

5.1.3 Densimetric Froude number

The Densimetric Froude number of a flow is

$$Fr = \frac{U}{\sqrt{(gL\Delta T/T)}} \tag{5.3}$$

where g is the acceleration due to gravity, T is the temperature of a neutral atmosphere, and ΔT is the deviation of temperature from T. The similarity parameter defined as $Ri = 1/Fr^2$ is called the Bulk Richardson number. The square of the Froude number indicates the ratio of inertial forces to gravitational forces. Inertial forces are dominant for values $Fr >> 1$, while thermal effects become important for values $Fr \leq 1$. In most wind tunnels there is no density gradient with height, hence Fr approaches infinity. This is similar to the Froude number for neutral thermal stability. It is also seen from the definition of the Froude number that increasing velocity and a decreasing characteristic length scale contribute to neutral thermal stability.

5.1.4 Prandtl number

The Prandtl number of a flow is

$$Pr = \frac{\rho c_p \nu}{\kappa_0} \tag{5.4}$$

where ρ is the density, κ_0 is the thermal diffusivity and c_p is the specific heat capacity at constant pressure. The Prandtl number of a wind tunnel flow and atmospheric flow is identical if the fluid is the same.

5.1.5 Eckert number

The Eckert number represents the relationship between a flow's kinetic energy and enthalpy.

$$Ec = \frac{U^2}{c_p \Delta T} \tag{5.5}$$

This criterion is only important in compressible flow, hence not relevant when modelling in low-speed wind tunnels.

5.2 Modelling of the atmospheric boundary layer

According to the similarity parameters presented in the previous section, some other conditions have to be fulfilled when simulating the atmospheric boundary layer with neutral thermal stability in a wind tunnel. The most important of these conditions are (White et al., 2001)

- The normalized mean velocity, turbulence intensity, and turbulent energy profiles
- The Roughness Reynolds number
- Jensens length scale criterion

The normalized mean velocity profile is easiest to match to full-scale. The turbulence intensity is more difficult to match, and the turbulence spectra are most difficult to simulate in a wind tunnel (Strataridakis et al., 1998).

5.2.1 Roughness Reynolds number

The roughness Reynolds number is defined as

$$Re_* = \frac{u_* z_0}{\nu} \tag{5.6}$$

where u_* is the friction velocity, z_0 is the roughness length and ν is the kinematic viscosity.

The atmospheric boundary layer is practically always fully rough. Hence, a minimum requirement for accurately reproducing the atmospheric boundary layer

in a wind tunnel is to ensure fully rough flow. Usually roughness elements are placed on the wind tunnel floor to create a rough surface, and the height of these elements has to be higher than the viscous sub-layer in order to trip the flow. The problem is that when terrain features like hills are scaled down to fit in a tunnel, the corresponding surface roughness (like grass, waves, threes and stones) is reduced too much to conserve aerodynamically rough flow. The alternatives are then to work with an aerodynamically smooth model, or to increase the surface roughness disproportionally to ensure fully rough flow. The consequence of the former is that the turbulence near the surface might be modelled incorrectly, hence also effects like separation which depends upon the turbulence level. The latter alternative could result in that the inner layer is occupied by roughness elements. Both ways produce measurements that only approximately represent the near surface properties of the atmospheric boundary layer.

Critical values for the roughness Reynolds number given in the literature are typically in the range from 2 to 5 (Kaimal and Finnigan, 1994). Snyder and Castro (2002) has done a study to identify how low the roughness Reynolds number can be before viscous effects become significant in the wall region of the flow. They assumed that the surface roughness consist of arrays of bluff elements. This is common in laboratory simulations of the atmospheric boundary layer. Snyder and Castro concluded that the limit seemed to be $Re_* = 1$, and perhaps as low as $Re_* = 0.5$ for certain surfaces. This result is very useful, as the criterion is less restrictive than values recommended in the literature.

5.2.2 Jensen's length scale criterion

Jensen and Franck (1963) concluded that the velocity profile in a wind tunnel must be similar to that in nature on the scale selected, meaning that the surface roughness in the wind tunnel must be on a scale with that in nature.

$$\frac{z_{0,full-scale}}{z_{0,model}} = \frac{d_{full-scale}}{d_{model}} \tag{5.7}$$

$z_{0,full-scale}$ is the roughness length in nature, $z_{0,model}$ is the roughness length in the wind tunnel, $d_{full-scale}$ and d_{model} is a measure of the object in nature and in the tunnel respectively. Hence geometrical similarity is preserved. The Jensen's length scale criterion is also called the model law based on the roughness parameter. A similarity parameter called the Jensen number (Wang et al., 1996) can correspondingly be formed:

$$Je = \frac{\delta}{z_0} \tag{5.8}$$

where δ is the height of the boundary layer. The Jensen number should be identical for the simulated boundary layer and nature.

5.2.3 Other constraints

Two other constraints also have to be met to simulate an atmospheric boundary layer. To match the zero pressure gradient found in the real world, the mean stream-

wise pressure gradient in the wind tunnel should be zero (Strataridakis et al., 1998). The other constraint is that the model should not block more than $10-15$ % of the wind tunnel cross-section area. The flow in a wind tunnel is naturally confined by the walls, roof and floor. A large model will obstruct the passage of air, and accelerate the velocity of the flow. Hence, if the model is too large the flow around it will not be representative of the flow around the full-scale version in nature. Below this limit of $10-15$ % local flow acceleration due to blocking is not expected to alter the longitudinal pressure gradient enough to affect the flow significantly. However, if the model blocks the tunnel more than this, the walls of the test section can generate a noticeable effect on the simulated flow past the model. The given limit is not an exact number, as the consequence of blocking depends on the type and design of the study performed.

5.2.4 Experimental techniques

Simulating an atmospheric boundary layer is of great importance in many wind tunnel studies. The length of the test sections are often too short to create a naturally growing boundary layer with required characteristics. Methods to accelerate the growth of such boundary layers, hence generating fully developed boundary layers within a shorter distance, are therefore necessary. Methods based on the early works by among others Armitt and Counihan (1968) and Counihan (1969) are recognized and commonly used in this field.

The system investigated by Armitt and Counihan (1968) was a simple barrier/wall placed across the floor of the tunnel, immediately followed by a set of triangular vortex generators. The vortex generators were at alternate incidences to aim for a total stream-wise vorticity of zero, and the distance between the vortex generators were similar to their heigh. The height of the boundary layer generated by this system was fractionally greater than the height of the vortex generators. The height of the barrier was 1/10 of the boundary layer thickness. "Lego" baseboards were placed at the floor downstream of the vortex generators to simulate surface roughness. This setup generated a velocity profile similar to the power law with an exponent $\alpha = 1/7$.

Counihan (1969) did a further investigation of the wake characteristics downstream of four different types of vortex generators. He gave a detailed presentation of the principles of two types, the triangular (as applied by Armitt and Counihan) and the elliptic wedge generators. A barrier wall was also present in this study, located upstream of the generators. "Lego" baseboards were located downstream of the generators to represent surface roughness. Both the spanwise variations and the streamwise variations in the area where the model would be during a test were found to be acceptable. The total length of test section required with this method was 4-5 boundary layer heights. It was concluded that the investigated system provided a suitable method for simulating a neutral atmospheric boundary layer in a wind tunnel considering all known important parameters, and that this boundary layer was comparable to a rough wall boundary layer.

Barbosa et al. (2002) also analyzed several types of thickening devices, with a

focus on how thick boundary layers can be generated in short wind tunnels. According to elliptic wedge generators, Barbosa et al. experimented with grids, trips and cylindrical rod generators. Using elliptic wedge generators did not give reasonable results in this investigation, hence prompting them to test other turbulence generators. The final conclusion of the work by Barbosa et al. was that the obtained results agreed reasonable well with both natural flow and what had been found by others in wind tunnel tests.

Irwin (1981) gave simple formulas for the design of spires used to generate an atmospheric boundary layer. Irwin considered flat triangular spires normal to the flow with a triangular splitter plate on the downwind side. Some of the results are also applicable to spires in general. According to Irwin the resulting flow is quite insensitive to the detailed design of the spires, as long as the shape is approximately triangular. In addition to the overall drag caused by the spires, characteristics of the generated boundary layer does also depend on the roughness added to the floor downstream of the spires. The spires are defined with a height h_s and a base-length b_s, and are evenly distributed with the centrelines at distances $h_s/2$. The study focused on the resulting boundary layer $6h_s$ downwind of the spires, since previous studies had shown that this was the distance needed to ensure lateral uniform flow. Based on the required height of the boundary layer, δ, and the required exponent in the power law, α, the height of the spires can be calculated from

$$h_s = 1.39\delta/(1+\alpha/2) \tag{5.9}$$

The base-to-height ratio should be

$$b_s/h_s = 0.5\left[\psi\left(H_{ws}/\delta\right)/\left(1+\psi\right)\right]\left(1+\alpha/2\right) \tag{5.10}$$

where

$$\psi = \beta\left\{\left[2/(1+2\alpha)\right]+\beta-\left[1.13\alpha/(1+\alpha)(1+\alpha/2)\right]\right\}/(1-\beta)^2 \tag{5.11}$$

$$\beta = (\delta/H_{ws})\alpha/(1+\alpha) \tag{5.12}$$

H_{ws} is the height of the working section. Applying Equation 5.9 yields a boundary layer thickness δ which is about 20 % lower than the height of the spires h_s. For elliptic wedge generators the height of the generated boundary layer is similar to the height of the turbulence generators, $\delta \approx h_s$ (Counihan, 1969).

Using devices like spires, wedges, rods, walls and roughness blocks is apparently a simple way to generate a boundary layer. In fact, the resulting flow is quite complicated. As a result of this, researchers often select the devices based on trial and error. Some end up with one type of turbulence generator, while others combine several types. Since different wind tunnels possess different dimensions and flow characteristics, a specific setup in one tunnel does not necessary produce a similar boundary layer if transferred to another tunnel.

Chapter 6

Laser Doppler Anemometry

Laser Doppler Anemometry (LDA) is a well-established optical technique which has been used for about four decades. It is based on the Doppler effect, and measures velocity in liquids and gases. One of the advantages of LDA is that it is non-intrusive, so the measurement equipment can be located outside the flow. LDA is indirect, as it measures the velocity of particles in the flow and not the flow itself. It has a very high accuracy, no calibration is needed, and it has a high spatial and temporal resolution. Another great advantage is that is can measure reversed flow due to the directional sensitivity.

6.1 Principles

The basic parts of an LDA configuration are

- a wave laser
- transmitting optics (including a beam splitter and a focusing lens)
- receiving optics (comprising a focusing lens, an interference filter, and a photodetector)
- a signal conditioner and a signal processor

Two parallel coherent beams are focused by the front lens of the probe. The beams intersect and with that form the measurement volume at a distance away from the probe equal to the focal length of the front lens. The measurement volume can be visualized as a pattern with bright and dark stripes due to interference between the laser beams. These stripes are often called fringes, and are illustrated in Figure 6.1. The fringe distance is determined by the wavelength of the laser (λ) and the angle between the beams (θ)

$$d_f = \frac{\lambda}{2\sin(\theta/2)} \tag{6.1}$$

The measurement volume is shaped as an ellipsoid with dimensions/diameters

$$\delta_x = \frac{4F\lambda}{\pi D\cos(\theta/2)} \tag{6.2}$$

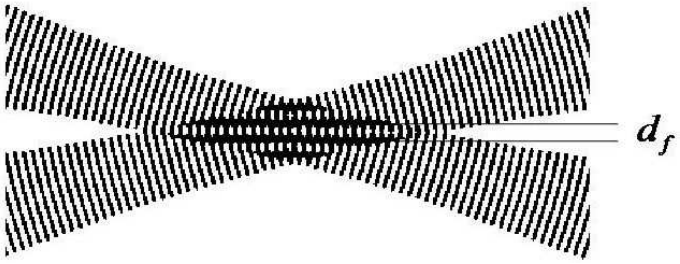

Figure 6.1: Illustration of fringes.

$$\delta_y = \frac{4F\lambda}{\pi D} \tag{6.3}$$

$$\delta_z = \frac{4F\lambda}{\pi D \sin(\theta/2)} \tag{6.4}$$

where D is the diameter of the laser beam and F the focal length as shown in Figure 6.2. The measurement volume has a Gaussian intensity distribution in all

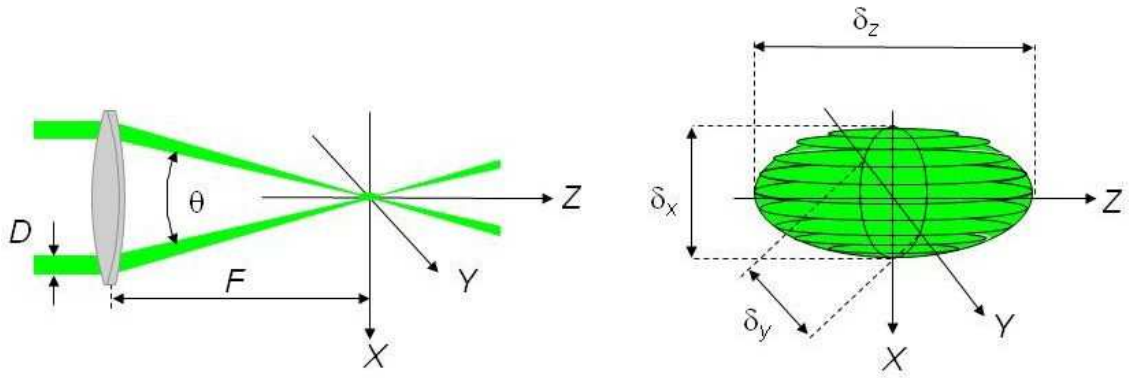

Figure 6.2: Laser beam intersection and measurement volume.

three directions.

Information about the flow velocity comes from light scattered by particles passing the measurement volume. The scattered light contains a Doppler shift which is proportional to the velocity component in the X-direction (Figure 6.2). This is collected by a receiver lens and focused on a photo detector. An interference filter is mounted before the photo-detector, so that only the required wavelengths are passed. The fluctuating light intensity is converted to an electrical signal at the photo-detector. This is the so-called Doppler-burst. This is filtered and amplified in the signal processor, and the Doppler frequency is determined for each particle. The velocity can then be found based on information about the distance travelled (d_f) during a known period of time (derived from the Doppler frequency).

The beam splitter often contains a Bragg cell. The input is one beam with frequency f_0, and the output is two beams of equal intensity where one has the

original frequency f_0 and the other a shifted frequency f_{shift}. Without a frequency shift of one of the two laser beams, the interference fringes would be stationary in space and the particles would produce identical signals/frequencies independent of direction. With the frequency shift from the Bragg cell the interference fringes appear to move at the shift frequency. The signal is then composed of the original Doppler signal and an additional shift frequency, allowing negative velocities to be distinguished.

Seeding of gases is usually necessary, while liquids often contain natural seeding. Since LDA is an indirect measurement method, it is important that the particles are small enough to follow the flow. At the same time the particles should be large enough to scatter sufficient light, so that the signal-to-noise is at an acceptable level. The size of the particles are typically in the range $1 - 10\ \mu m$.

To measure two velocity components, two extra beams can be added to the optics in a plane perpendicular to the first beams.

6.2 Details about the LDA equipment

The LDA system used in the current study was of type FiberFlow delivered by Dantec Dynamics. It could measure two velocity components simultaneously. A frequency shift allowed measurement of velocities without directional ambiguity. The laser was a 400 mW air cooled Ar-Ion laser. The wavelengths are given in Table 6.1. A beam expander was also available to increase the optical focal length. The beam

Color	Wavelength [nm]	Channel
Green	514.5	LDA1
Blue	488	LDA2

Table 6.1: Laser beam properties.

spacing with the beam expander was about twice the spacing without the expander, since the expander had a constant $E = 1.98$. The size of the lenses, measurement volumes and focal lengths are listed in Table 6.2. The system had a backscatter

Lens diameter	Beam spacing	Focal length	Measurement volume	
[mm]	[mm]	[mm]	Diameter [mm]	Length [mm]
60	38	300	0.15	2.3
112[a]	75.24	500	0.119	1.59

Table 6.2: Summary of probe and lens properties. [a]With beam expander (E=1.98).

configuration, so the probe contained both the transmitting and receiving optics.

Recognizing a good Doppler burst requires some experience. Two of the indicators were the data rate and the validation rate. The data rate is the number of validated bursts per second. The validation is the ratio of valid bursts to the total

amount of bursts (valid and invalid). These indicators could be optimized by e.g. adjusting the high voltage to the photo-multiplier, the signal gain etc. The corrects setting depended on factors like the laser power, the position of the measurement volume in the flow and the seeding.

6.3 Statistical estimators

The LDA system measures instantaneous velocities, and moments can be estimated by

$$U = \sum_{i=1}^{i=N} \eta_i u_i \tag{6.5}$$

$$\sigma_u^2 = \sum_{i=1}^{i=N} \eta_i (u_i - U)^2 \tag{6.6}$$

$$\overline{u'v'} = \sum_{i=1}^{i=N} \eta_i (u_i - U)(v_i - V) = \sum_{i=1}^{i=N} \eta_i u_i' v_i' \tag{6.7}$$

$$\tag{6.8}$$

where $u_i = U + u_i'$. Equation 6.5 is the time averaged mean velocity and 6.6 is the variance. The standard deviation is $\sigma_u = \sqrt{\sigma_u^2}$. This is also called the root-mean-square (rms) value since $\sigma_u = \sqrt{\overline{u'^2}}$. Equation 6.7 is the cross-moment. The weighting factor η_i in arithmetic weighting is

$$\eta_i = \frac{1}{N} \tag{6.9}$$

N is the number of velocity samples. Arithmetic weighting should only be used if the samples are independent. This is the case when the time between samples exceeds twice the integral time scale of the flow. If the time between the samples is shorter than this, the mean velocity will be biased towards higher velocities. A larger volume of fluid passes the measurement volume during periods of high velocity compared to periods with a lower velocity, hence a greater number of particles will be registered and result in a bias if arithmetic weighting is applied. Higher order moments will also be affected. The bias is avoided if transit time weighting is used. This non-uniform weighting factor is given by

$$\eta_i = \frac{\tau_i}{\sum_{j=1}^{N} \tau_j} \tag{6.10}$$

τ_i is the time used by the i'th seeding particle to pass the measurement volume. Transit time weighting was used in all the estimated moments in the current study.

Several measurements were done to see how confidence intervals and stabilizing of the estimated moments depended on different sampling times and number of samples. A selected sampling time of 45-60 seconds, and a sampling frequency of about 1000 Hz, were considered to be sufficient to estimate moments. It was not intended to calculate power spectra from these measurements, which would have required an even higher sampling frequency.

6.4 Probe position

Two velocity components were measured in all cases, and some profiles were measured a second time with the probe in a perpendicular position to obtain the third velocity component. The positioning of the probe in each case, and whether or not the expander was used, depended on a combination of

- The required positioning of the probe to achieve free sight to the measurement point
- The positioning of the probe to minimize the influence on the flow
- Minimizing the errors due to tilting of the probe
- Available locations of the traverse
- The strength of the traverse. The size and weight of the expander combined with the necessary fixing devices limited the alternatives in some cases
- Aiming at consistent measurements by mounting the probe similarly for the different velocity profiles

The probe was used with a beam expander in most of the positions, and mainly used without the beam expander when it was mounted vertically directly above the model ($F = 300\ mm$). The expander front lens had a focal length of $F = 500\ mm$, so the probe with expander was located further away from the measurement volume than the probe without an expander.

6.5 Tilting the probe

It is often necessary to tilt the LDA probe to measure the region closest to ground. This is illustrated in Figure 6.3. The probe is tilted at an angle β. w is the actual vertical velocity component and w_m is the measured component. Corrected quanti-

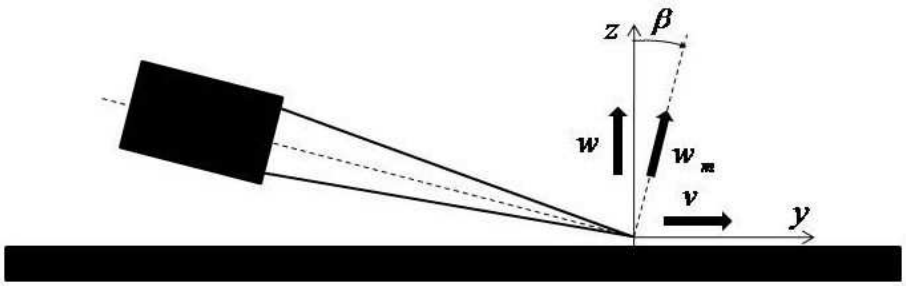

Figure 6.3: Tilted LDA probe.

ties for a tilted two-velocity component LDA system are (Albrecht et al., 2003)

$$w = \frac{1}{\cos\beta} w_m \tag{6.11}$$

$$\overline{u'w'} = \frac{1}{\cos\beta} \overline{u'_m w'_m} \tag{6.12}$$

$$\frac{w'}{w'_m} = \frac{1}{\cos\beta} \frac{1 - v'^2 \sin^2\beta}{\overline{w'^2}\cos^2\beta + \overline{v'^2}\sin^2\beta} \tag{6.13}$$

These relations are derived assuming a two-dimensional flow, so $V = \overline{u'v'} = \overline{v'w'} = 0$. If it is considered that the velocity component parallel to the probe deviates from zero, a part of this component is "seen" as if it is the vertical component, and yields the following relation

$$w = \frac{1}{\cos\beta} w_m - v \tan\beta \tag{6.14}$$

Equation 6.14 is plotted in Figure 6.4 for three different inclination angles. It is clearly seen that errors occurring when the flow along the probe is zero ($v = 0$) are insignificant compared to the errors caused by $v \neq 0$.

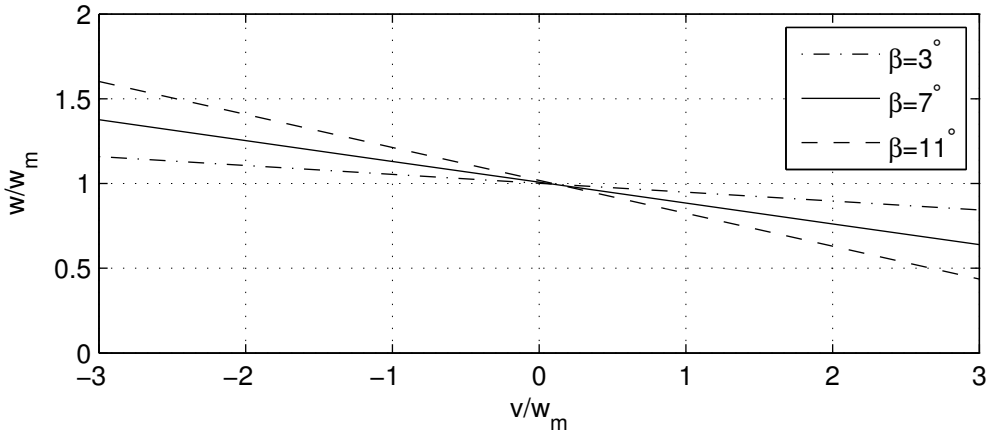

Figure 6.4: Errors introduced by tilting the LDA probe as a function of the velocity component along the probe.

In most of the measurements obtained with the probe from the side of the measurement volume, the probe was tilted approximately 7°. The mean flow in most of the cases in this study was approximately two-dimensional with a spanwise velocity $V \approx 0$, so the error introduced by tilting the probe are generally small as seen from Equation 6.11. In some positions, like in hill slopes, the probe also had to be tilted slightly in the horizontal plane. The spanwise velocity was only obtained in some of the measured positions, and large spanwise velocity components were only seen in a few measured positions, so the presented data in the current thesis has not been corrected.

6.6 Velocity transformation

When positioned to the side of a main flow direction from left to right, the probe could be mounted so that the channel LDA1 measured the velocity component defined as u and the channel LDA2 measured w. However, it is recommended that the measured velocity components are approximately equal to maximize the data rate. The main velocity component in each position (i.e. one vertical profile) was considered prior to measurements, and the probe was mounted accordingly. For most of the profiles this implied a rotation of the laser beams with 45 degrees compared to the wanted velocity components. The velocities were then transformed in the LDA software afterwards.

When the probe was directed towards a flow from left to right, the transformed coordinate system was rotated 45 degrees anticlockwise compared to the measured velocity components by

$$\begin{bmatrix} U \\ W \end{bmatrix} = \begin{bmatrix} \cos 45 & \sin 45 \\ -\sin 45 & \cos 45 \end{bmatrix} \begin{bmatrix} LDA1 \\ LDA2 \end{bmatrix} \tag{6.15}$$

When the probe was directed towards a flow from right to left, the transformed coordinate system was rotated 45 degrees clockwise compared to the measured velocity components by

$$\begin{bmatrix} U \\ W \end{bmatrix} = \begin{bmatrix} \sin 45 & \cos 45 \\ \cos 45 & -\sin 45 \end{bmatrix} \begin{bmatrix} LDA1 \\ LDA2 \end{bmatrix} \tag{6.16}$$

When u was measured directly, and the probe was directed towards a flow from right to left, then w was measured upside down. The following transformation was then done

$$\begin{bmatrix} U \\ W \end{bmatrix} = \begin{bmatrix} 1 & 0 \\ 0 & -1 \end{bmatrix} \begin{bmatrix} LDA1 \\ LDA2 \end{bmatrix} \tag{6.17}$$

Measurements were also carried out with the probe mounted above the flow in some positions. Transformation similar to Equation 6.15 was then utilized, but with w interchanged with v.

Chapter 7

Experimental setup and procedures

Principles of Laser Doppler Anemometry and details related to this was introduced in the previous chapter. This chapter describes the rest of the experimental facility and procedures. The wind tunnel and the flow field in the empty tunnel are presented in Section 7.1 and Section 7.2 respectively. The setup for generation of the incoming boundary layer is described in Section 7.3. The terrain model, the location of this in the wind tunnel and all measured cases and positions are presented in Sections 7.4, 7.5 and 7.6. Measuring methods are discussed in Section 7.7. The measuring procedure, collection of data, scaling of results and some comments on the quality of data are presented in Sections 7.8, 7.9, 7.10 and 7.11.

7.1 The wind tunnel

The study was carried out in a wind tunnel at NTNU, see Figure 7.1. The test section is 2.71 m wide and 11.2 m long. The roof in the test section has an adjustable height to enable manipulation of the pressure gradient in the direction of the flow. It is aimed to keep $dp/dx \approx 0$ in an empty tunnel, so the height of the roof is increased from 1.8 m at the start of the test section to 2.0 m at the end to counteract the displacement of mass flow in the boundary layers along the floor, walls and roof.

The wind tunnel is a closed circuit, with the flow return section on top of the test section. The flow is turned 180 degrees upstream of the test section. It then passes a honeycomb, a screen and a contraction to break down large scale turbulence and generate a more homogeneous flow field before entering the test section. The flow is generated downstream of the test section by an electric fan with an effect of 220 kW, and the wind speed is changed by adjusting the rotational speed of the fan.

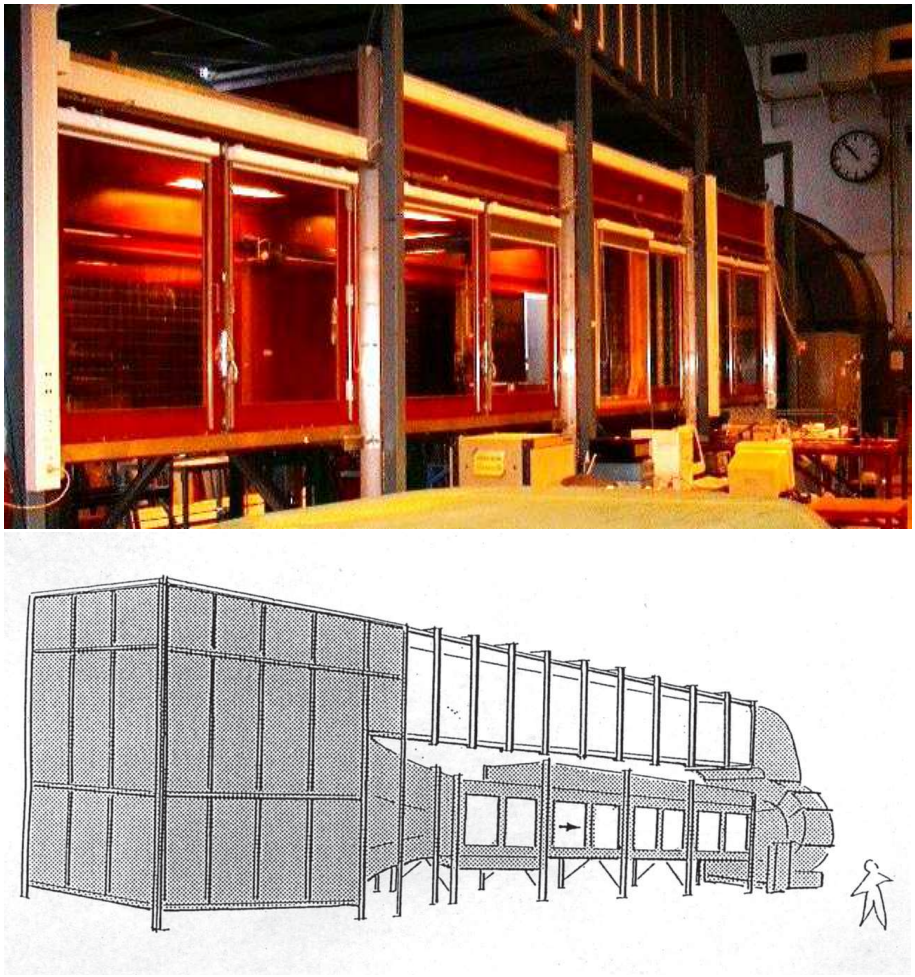

Figure 7.1: The wind tunnel.

7.2 Flow field in empty tunnel

The flow field across the test section was measured with a pitot tube 0.5 meters downstream of the entrance. The result is shown in Figure 7.2. It is clear that the heigh $z = 10\ mm$ with low velocities is within the boundary layer, while $z = 110\ mm$ is above. The boundary layer in the empty tunnel was measured in more detail 5 meters downstream of this cross section, where it can be assumed to be fully developed, and was found to bee about 12 cm thick. The flow field above the boundary layer at the start of the test section is not homogeneous. The largest spanwise differences are seen at the lowest measurement height, which is within the boundary layer. The measurements were taken with a horizontally moving probe which was mounted on a traverse, and the floor is not completely flat. Hence the measurement points at the level labelled $z = 10\ mm$ might be at different heights above the floor, so differences in velocities should be expected. The measurements at all the other levels were obtained at positions which were not affected by boundary layers at any surfaces, so the mean velocities should be approximately equal. The

mean velocity, minimum velocity, maximum velocity and the standard deviation of the velocities at each height are given in Table 7.1. The velocities increase up to the top of the boundary layer and then decreases slightly above this. The largest velocity deviations above $z = 10\ mm$ are seen in the lower right part of the incoming flow field, causing a standard deviation of 0.38 m/s at the height $z = 110\ mm$. If the measurement point with velocity 16.7 m/s is discarded, the standard deviations of the velocities at each height above the boundary layer are about 0.2 m/s, which is acceptable. A similar investigation was also carried out for the flow field at the entrance to an empty test section for a higher free stream velocity of about 19 m/s, and all the features discussed above were present and approximately equal.

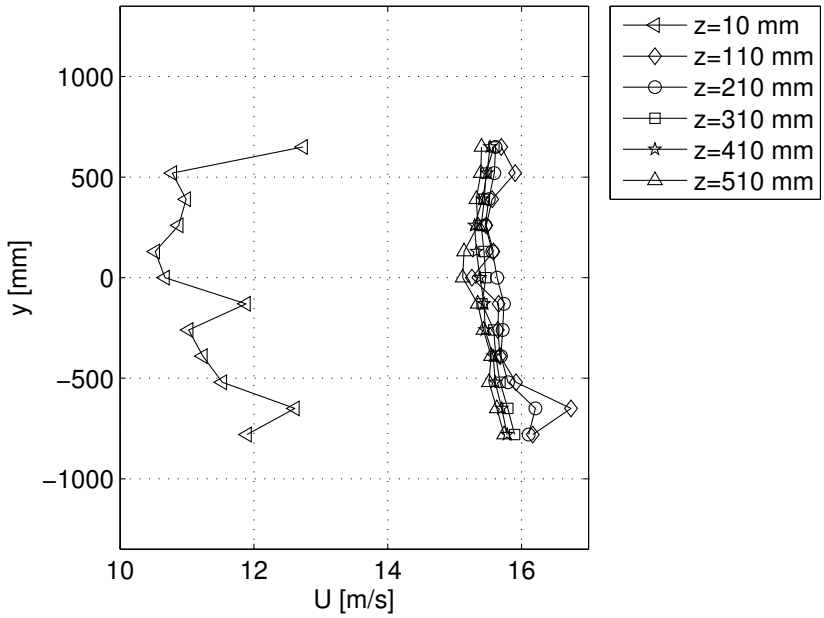

Figure 7.2: Flow field measured 0.5 meters downstream of the entrance to the empty test section.

$z\ [mm]$	$U_{mean}\ [m/s]$	$U_{min}\ [m/s]$	$U_{max}\ [m/s]$	$\sigma_U\ [m/s]$
10	11.4	10.5	12.7	0.74
110	15.8	15.3	16.7	0.38
210	15.7	15.5	16.2	0.22
310	15.6	15.4	15.9	0.16
410	15.5	15.3	15.8	0.15
510	15.4	15.1	15.7	0.18

Table 7.1: Characteristics of the mean velocities shown in Figure 7.2.

The turbulence intensity well outside the boundary layer in an empty test section is about 0.5 % at a mean velocity of 13.5 m/s.

7.3 Generation of artificial boundary layer

An overview of common practice for simulating an atmospheric boundary layer in wind tunnels is given in Section 5.2.4. The method of trial and error was the main method in the current work in the search for the best setup of turbulence generators, like in several other studies where atmospheric boundary layers have been generated. The experimental work of creating an incoming boundary layer started with the intention of generating a boundary layer with a power law exponent close to $\alpha = 0.11$, a depth of 350 mm and a turbulence level in accordance with this as in the atmospheric boundary layer.

A thorough investigation was carried out in the search for suitable turbulence generators, and this process is described in detail in Appendix A. Eight unevenly distributed wooden spires were eventually chosen. These were similar to the triangular spires considered by Irwin (1981), as presented in Section 5.2.4. The centre of the spires were positioned 44, 57, 70 and 83 cm away from the centreline of the test section at both sides. Hence the position of the spires were symmetrical around the centreline, but highly unevenly distributed. The position of the spires relative to the tunnel test section can be seen in Figure 7.3 and Figure 7.12, and photos of the spires are shown in Figure 7.4. According to these eight spires, one higher half-spire with base length $b_s/2 = 7.5$ cm was mounted slightly upstream of the other spires at each sidewall. Although the setup was not as expected beforehand, this final setup was the version resulting in the most homogeneous spanwise velocity field, at the same time as its mean velocity and turbulence characteristics were closest to what was intended in the beginning. The standard deviations of the mean velocities at the heights z =10, 110, 210, 310, 410 and 510 mm were 0.13, 0.13, 0.12, 0.13, 0.16 and 0.16 m/s respectively. These standard deviations are lower than the standard deviations observed at the entrance to an empty tunnel (see Table 7.1), and consequently acceptable. The height of the spires finally used was $h_s = 52$ cm, and the base-length $b_s = 9.5$ cm. This gives a ratio $b_s/h_s = 0.18$. According to Irwin's formulas this should correspond to a power law exponent of $\alpha > 0.5$, with $\delta/H_{ws} \approx 0.19$. Irwin assumed evenly distributed spires, with a centreline distance between the spires of $h_s/2$. Both the violation of this assumption, and the fact that the height δ in the current study is not actually the height where the velocity approaches a constant value, can explain why the formulas by Irwin are not applicable.

7.4 The terrain model

The terrain model is generic and was created based on locations in the mountainous terrain along the coastline where wind farms either existed or were planned. Typical slopes, terrain features, and combinations of these features served as an inspiration during the composition of the model. One of these wind farms was Hundhammerfjellet in Nord-Trøndelag, which is shown in Figure 7.5. This photo was taken during the erection of the wind farm with 17 wind turbines and a total power of 55 MW. Most of the turbines are located near the crest of the steep hill, and one of the main wind directions in this area is normal to this hill. Two of the turbines experienced

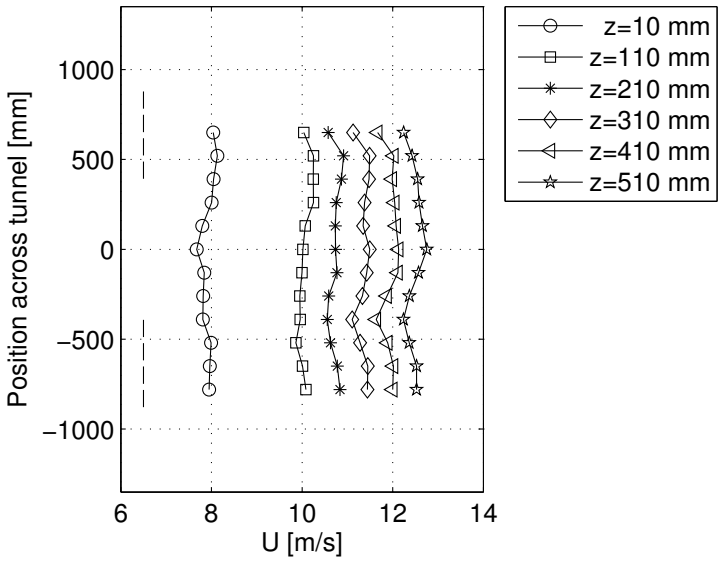

Figure 7.3: Mean velocities measured 6 meters downstream of the spires with a pitot tube. The positions of the spires are illustrated by the vertical lines to the left.

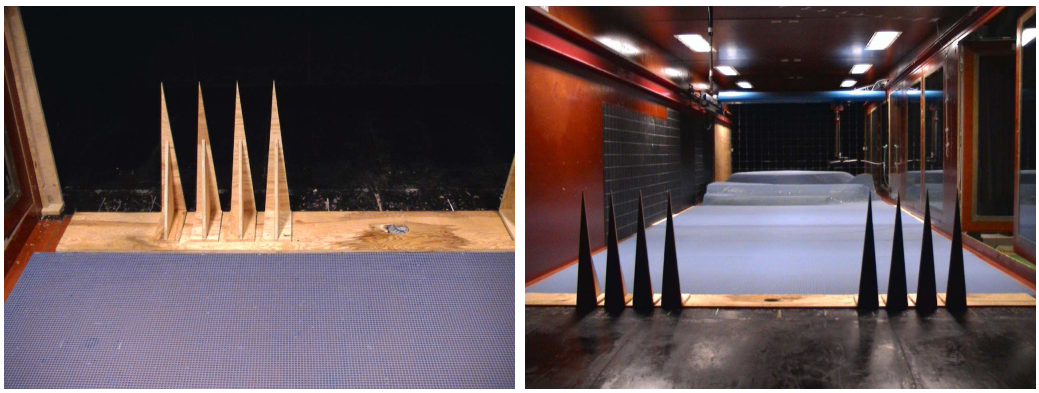

Figure 7.4: Configuration of spires.

a break down of turbine blades during periods of strong wind in 2005 and 2006, and the tip of one blade was cracked in 2009. Although this was probably caused by several factors, it illustrates the importance of gaining a better knowledge of wind in complex terrain. The mean slope of the steep hill seen in the photo, the quite sharp crest, and a depression with depth a third of the height of the mountain, were some of the features transferred to the generic model. Another wind farm which served as an inspiration was Havøygavlen, which is shown in Figure 1.1. The plateau, and the quite straight slope with a sharp crest were considered as especially interesting.

The base of the terrain model is about 4 $m \times 4$ m, and its maximum height is 0.35 m. It is milled out of Styrofoam with 5 mm contour intervals, then filled in and finally painted. This makes the surface quite smooth. A classification of typical

Figure 7.5: Photo of wind turbines Hundhammerfjellet wind farm in Nord-Trøndelag, Norway.

terrain features is given in Figure 7.6. Features represented in the generic model are for example escarpments with steep slopes followed by large plateaus, ridges, an axisymmetric hill and some fine scale terrain. An overview of the entire model is shown in Figure 7.7, and some photos are shown in Figure 7.8. A combination of mathematical functions and manual curve fittings were used to create the generic terrain. The upstream slope in Case I (the cases are described in Section 7.6) and the three-dimensional axisymmetric hill, were shaped as a Gaussian probability density function. The upstream slope in Cases II and III were constructed from cosine functions. The two ridges are second order polynomials.

The slopes and lengths of the hills in Case I to IV are given in Table 7.2. H is the hill height and L the horizontal distance from ground level to the hill crest. α_{max} is the maximum angle of the hill (located about half way up the hill in Cases I to III). α_{mean} is the mean angle calculated by

$$\alpha_{mean} = \tan^{-1} \varphi \tag{7.1}$$

where

$$\varphi = \frac{H}{L} \tag{7.2}$$

Another ratio, ϕ, is defined as

$$\phi = \frac{H}{L_{H/2}} \tag{7.3}$$

where H is the hill height and $L_{H/2}$ the horizontal length from the crest to the position at the upstream hill where the height equals half the maximum hill height. All these lengths are defined in Figure 7.9.

The model was too large to fit in the wind tunnel, so it was split into appropriate modules as shown in Figure 7.10. This division gave the opportunity to study some terrain features separately before modules were put together to produce an even more complex flow. Two examples can be seen by the photos in Figure 7.8, where Case V and Case IXb are shown mounted in the tunnel. The different cases will be presented in more detail in Section 7.6.

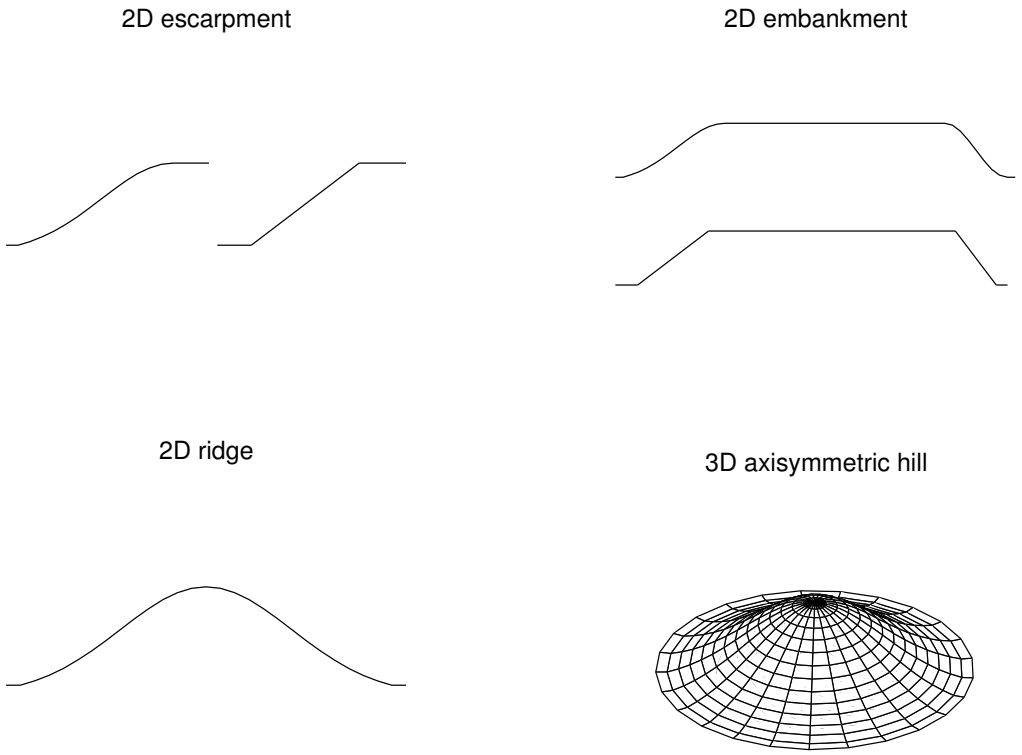

Figure 7.6: Definitions of terrain types.

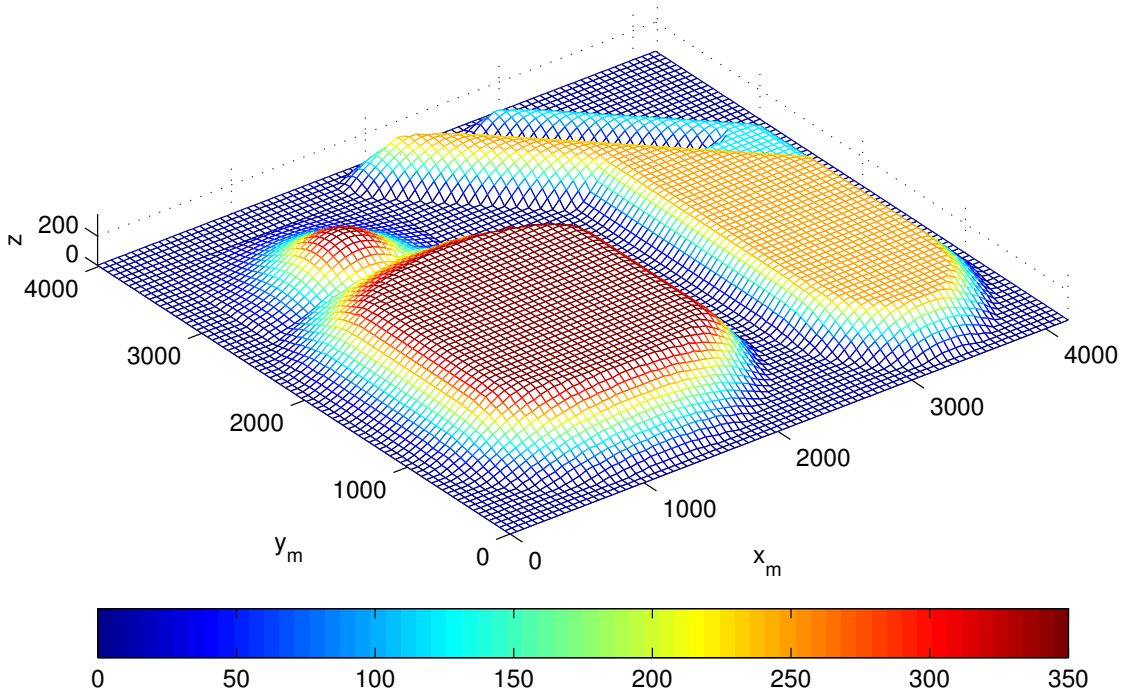

Figure 7.7: An overview of the entire terrain model. All the numbers are in mm.

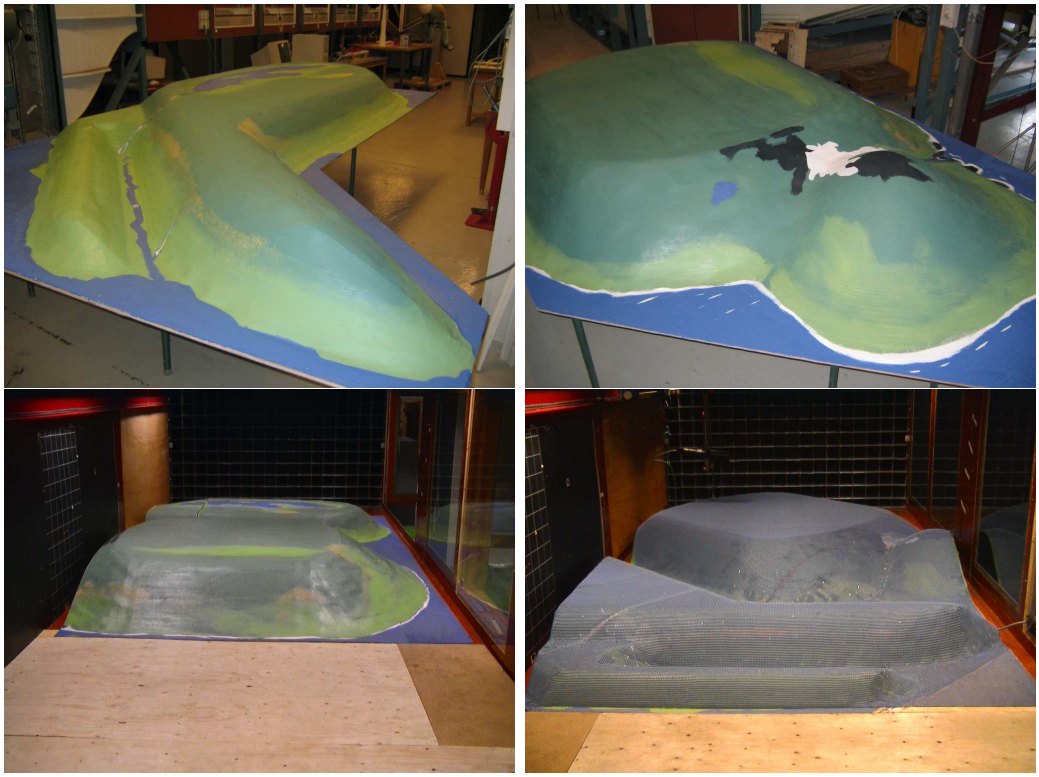

Figure 7.8: Photos of the terrain model.

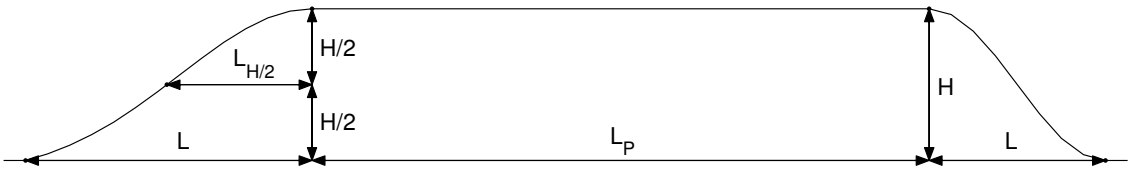

Figure 7.9: Definitions of the lengths given in Table 7.2

.

Case	I	II	III	IV
H [mm]	350	350	250	250
L [mm]	661	406.8	356	254.2
φ	0.53	0.86	0.70	0.98
$L_{H/2}$ [mm]	334.8	203.4	178	127.1
ϕ	1.05	1.72	1.40	1.97
α_{mean} [°]	27.9	40.7	35	44.5
α_{max} [°]	37.3	52.8	46.1	44.5
L_P [mm]	1423.7	1423.7	915.2	915.2

Table 7.2: Lengths and slopes for the hills in Case I-IV. Definitions are given in Figure 7.9

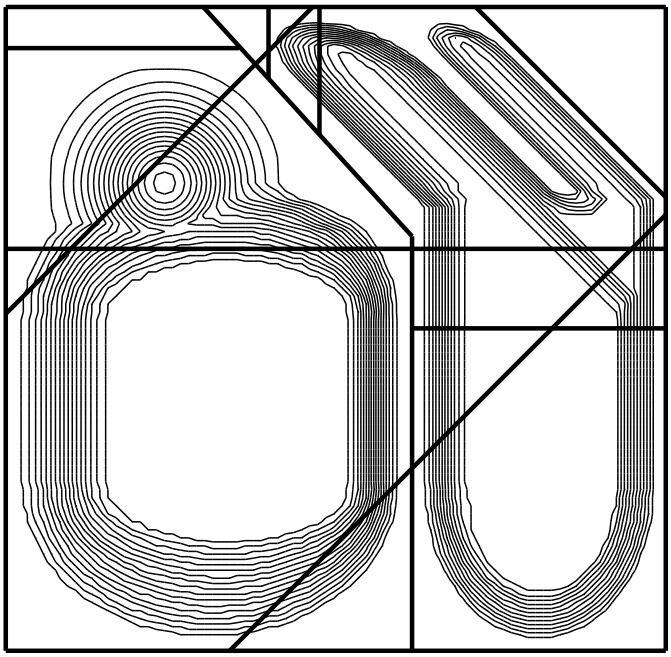

Figure 7.10: Division of the terrain model.

7.5 Total setup

The experimental setup in the tunnel test section is sketched in Figure 7.11. The distance from the spires to the leading edge of the model was 6 m. The reference plane of the model was 12 mm above the tunnel floor. To compensate for this, a plate was put on the floor and extended 2.4 m upstream of the model, and the passage from the floor to this level was shaped as a gentle ramp. The figure also

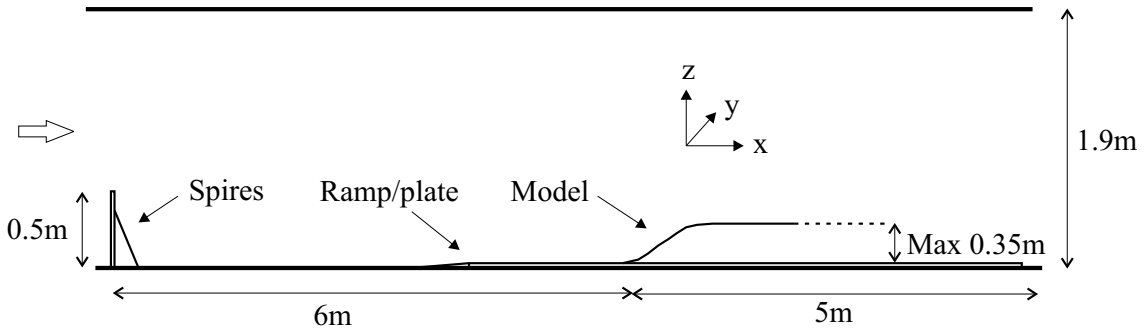

Figure 7.11: Sketch of wind tunnel test section with spires, plate and model.

illustrates the coordinate system used in the tunnel. x is the streamwise direction, y is the spanwise direction and z the vertical direction. The corresponding velocity components are u, v and w respectively. The height from the local surface is denoted by z, while Z will be used to represent the height from the tunnel floor.

The probe (LDA, hot-wire or pitot tube) was mounted on a three-dimensional traversing system. This system was remote-controlled from a computer located outside the tunnel.

The flow in the current study was seeded with fog particles during measurements with LDA. The fog was injected continuously through a hole in the floor in between the spires at the entrance to the test section, as can be seen in Figure 7.4. The amount of particles could be adjusted by a remote control.

7.6 Measured cases and positions

7.6.1 Inflow

Vertical profiles were measured 1 m upstream of the front edge of the model in all cases. It was expected that the presence of the model could influence the flow upstream of the model and possibly make it vary between the different cases. This was one of the reasons why one general inflow profile representative for the undisturbed inflow was sought. To find such a profile, 6 profiles positioned 0.3 m apart across the test section were measured with only spires and plates in the tunnel. These measurements were obtained about 6 m downstream of the spires, which was right in front of the leading edge of the model when it was present (Figure 7.11). The two outermost profiles were not included as a part of the general inflow profile. The four selected profiles were measured at a distance of ± 150 mm and ± 450 mm from the centreline of the tunnel, hence including the line of measurements in all cases by a large margin. The position of these four profiles are shown in Figure 7.12. The spatial average of the four profiles were taken to represent the general undisturbed inflow, and will consequently be used for comparison purposes with flow above the model in Cases I-IXa.

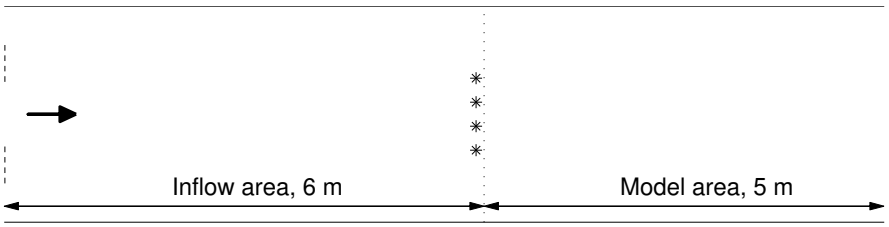

Figure 7.12: The test section seen from above. The dotted line indicates the leading edge of the model when present. Four markers (*) indicate the positions where the inflow profiles were measured in an empty tunnel. The eight short lines at the entrance to the test section illustrates the positions of the spires.

7.6.2 Smooth surface

As commented in Section 7.4, the terrain model had a smooth surface. A total of nine cases were studied with this model surface and an inflow profile generated as described in Section 7.3. These cases are named Case I-IX, and are shown in Figure 7.13. The 9 different cases are indicated by arrows in the direction of the flow, and positions where profiles were measured are marked by dots. A brief summary with reasons for the cases is given below.

Case I The terrain is an approximately two-dimensional embankment with rounded hills. The slope of the ascending hill was inspired by mountains considered for wind farms. This case with a moderate slope and a rounded crest represents terrain commonly considered as suitable for wind farms.

Case II The terrain is similar to Case I, but with a significant steeper slope. It was designed to study the effect of varying slopes by comparing it to Case I.

Case III The terrain is similar to Case I and II, with a mean slope in between Case I and Case II. The terrain module is approximately two-dimensional, and it is lower than in Case I and II.

Case IV The terrain was inspired by Havøygavlen wind farm, with a sharp crest and a plateau. It was designed to see the effect of a sharp crest by comparing it to Case III which has a similar slope and a rounded crest.

Case V The terrain was designed to see the effects of letting the flow pass a higher mountain and a valley before entering a lower mountain, as is often the case in mountainous terrain. It is identical to the terrain in Case I followed by Case III. This gave the possibility to study the effect of a mountain nearby on both the upstream and the downstream mountain, as the isolated cases were measured as well.

Case VI The terrain consists of Case IV followed by Case II. It is identical to Case V, but with the approaching flow from the opposite direction. Hence this case represents flow passing a lower mountain and a valley before entering a higher mountain.

Case VII The terrain consists of an axisymmetric hill, followed by a valley and a large plateau. The shape and relative heights were inspired by terrain features at Hundhammerfjellet wind farm. While the terrain in Case I-IV is approximately two-dimensional, Case VII is more three-dimensional.

Case VIII The terrain consists of a ridge upstream of a hill, both inclined compared to the main flow direction, and a following plateau. This case was designed to generate highly three-dimensional flow.

Case IX The first part of the terrain is two ridges orthogonal to the main flow direction. These two ridges are also a part of the terrain in Case VIII, and were inspired by terrain features at Hitra wind farm. Downstream of the ridges is a

large valley and a mountain with a curved ascending hill and a plateau. The ridges are approximately two-dimensional, while the downstream mountain and the surrounding terrain is three-dimensional.

In each case several profiles were measured along a line near centre of the test section. To avoid the effects of the boundary layers along the sidewalls, measurements were taken as close to the centreline of the test section as possible. The location of the measurement line relative to the centreline of the tunnel in Case I-VI was 154 *mm*. The gap between the line of measurements and the centreline in Case VII, VIII and IX was 203 *mm*, 100 *mm* and 90 *mm* respectively.

The number of profiles in the nine different cases varied, as can be seen from the dots in Figure 7.13. All the measurement positions are also listed in Tables 7.3, 7.4 and 7.5. The number of points measured in every vertical profile for these cases with a smooth surface was about 40.

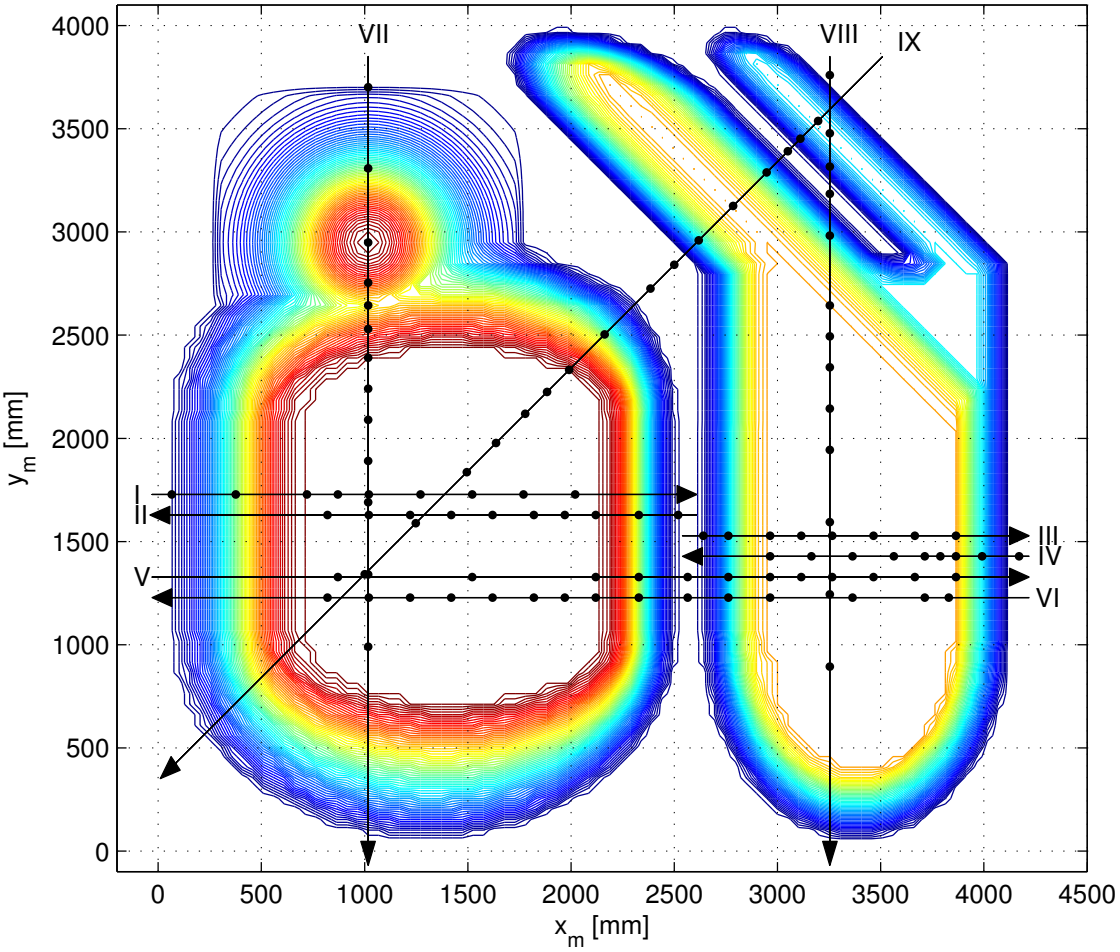

Figure 7.13: Top view of the terrain model with 5 *mm* elevation contours. Test cases are indicated by arrows in the direction of the flow. Positions where profiles were measured are marked by dots. Case I-VI are shown separately in this figure, but were all measured along the same line as Case IV.

Case I			Case III			Case V			Case VII		
x_m	y_m	x/H	x_m	y_m	x/H	x_m	y_m	x/H	x_m	y_m	x/H
66	1428	0.04	2640	1428	0.19	870	1428	2.34	1017	3701	0.00
376	1428	0.93	2764	1428	0.68	1521	1428	4.20	1017	3308	1.13
721	1428	1.91	2964	1428	1.48	2120	1428	5.91	1017	2949	2.15
870	1428	2.34	3115	1428	2.09	2328	1428	6.51	1017	2754	2.71
1020	1428	2.77	3265	1428	2.69	2565	1428	7.18	1017	2644	3.02
1271	1428	3.49	3465	1428	3.49	2762	1428	7.75	1017	2530	3.35
1521	1428	4.20	3665	1428	4.29	2964	1428	8.32	1017	2390	3.75
1770	1428	4.91	3864	1428	5.08	3115	1428	8.75	1017	2240	4.18
2020	1428	5.63				3265	1428	9.18	1017	2090	4.61
						3465	1428	9.75	1017	1890	5.18
						3665	1428	10.33	1017	1690	5.75
						3864	1428	10.89	1017	1340	6.75
									1017	990	7.75

Table 7.3: Overview of all measurement positions in Case I, III, V and VII. x_m and y_m are the model coordinates, as shown in Figure 7.13. x/H refers to the position in the streamwise direction in the tunnel, with $x/H = 0$ at the leading edge of the model in each case. H is the maximum height of the model in each case.

Case II			Case IV			Case VI			Case VIII		
x_m	y_m	x/H	x_m	y_m	x/H	x_m	y_m	x/H	x_m	y_m	x/H
2519	1428	0.07	4170	1428	-0.21	3830	1428	0.82	3254	3760	0.96
2328	1428	0.61	3991	1428	0.51	3714	1428	1.16	3254	3478	2.09
2120	1428	1.21	3864	1428	1.02	3364	1428	2.16	3254	2982	4.07
1970	1428	1.64	3789	1428	1.32	2964	1428	3.30	3254	2644	5.42
1820	1428	2.06	3714	1428	1.62	2762	1428	3.88	3254	2494	6.02
1620	1428	2.64	3564	1428	2.22	2565	1428	4.44	3254	2344	6.62
1420	1428	3.21	3364	1428	3.02	2328	1428	5.12	3254	2144	7.42
1221	1428	3.78	3164	1428	3.82	2120	1428	5.71	3254	1944	8.22
1020	1428	4.35	2964	1428	4.62	1970	1428	6.14	3254	1594	9.62
820	1428	4.92				1820	1428	6.57	3254	1244	11.02
						1620	1428	7.14	3254	894	12.42
						1420	1428	7.71			
						1221	1428	8.28			
						1020	1428	8.85			
						820	1428	9.42			

Table 7.4: Overview of all measurement positions in Case II, IV, VI and VIII. x_m and y_m are the model coordinates, as shown in Figure 7.13. x/H refers to the position in the streamwise direction in the tunnel, with $x/H = 0$ at the leading edge of the model in each case. H is the maximum height of the model in each case.

Case IXa			Case IXb			Case IXc		
x_m	y_m	x/H	x_m	y_m	x/H	x_m	y_m	x/H
3197	3538	0.41	3197	3538	0.41	3197	3538	0.41
3111	3452	0.82						
3050	3391	1.03						
2948	3289	1.44						
2785	2126	2.05	2785	2126	2.05	2785	2126	2.05
2619	2960	2.88	2619	2960	2.88	2619	2960	2.88
2500	2841	3.29						
2385	2726	3.70	2385	2726	3.70	2385	2726	3.70
2162	2503	4.73						
1990	2331	5.34	1990	2331	5.34	1990	2331	5.34
1884	2225	5.75	1884	2225	5.75	1884	2225	5.75
1778	2119	6.16						
1637	1978	6.78						
1495	1836	7.40						
1248	1589	8.42						
1000	1341	9.45	1000	1341	9.45	1000	1341	9.45

Table 7.5: Overview of all measurement positions in Case IXa-c. x_m and y_m are the model coordinates, as shown in Figure 7.13. x/H refers to the position in the streamwise direction in the tunnel, with $x/H = 0$ at the leading edge of the model. H is the maximum height of the model.

7.6.3 Added roughness

In addition to the nine cases shown in Figure 7.13, two more cases were studied. The terrain was equal to Case IX, but the model and the floor upstream of the model was in turn covered with mesh made of latex. The height of this mesh was approximately 3 mm, and the distance across the holes was about 5 mm (Figure 7.14). Introduction of this roughness resulted in 3 different roughness combinations with the terrain in Case IX:

Case IXa Inflow and model surface as described in Section 7.3 and 7.4. The surface of the flat area in the inflow and the surface of the model were quite smooth and similar.

Case IXb Inflow as described in Section 7.3 and model surface covered with the roughness. This introduced a change in surface roughness as the flow reached the model, as shown in Figure 7.15(a).

Case IXc Model surface and inflow covered with the roughness, as shown in Figure 7.15(b). There was no change in roughness as the flow reached the model in this case, but the incoming velocity profile was altered compared to Cases I-IXb.

The measurement positions in Cases IXa-IXc are given in Table 7.5.

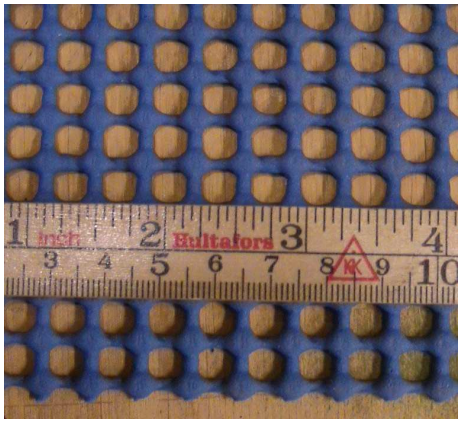

Figure 7.14: The roughness (latex mesh) added to inflow and model in Case IXb and IXc.

(a) (b)

Figure 7.15: Photos of Case IXb (a) and Case IXc (b).

7.7 Measuring methods

7.7.1 Techniques applied

Different measuring techniques were applied for different purposes in this study. The temperature in the test section was measured with thermocouples and a thermometer. The mean velocity across the entrance to the test section was measured by pressure holes in the walls at the inlet and outlet of the contraction and a pressure transducer, and the mean velocity in single points were measured by the use of a pitot tube and a pressure transducer. More detailed velocity measurements were obtained with hot-wire anemometry and LDA. The principles and details of LDA were presented in Chapter 6, and a short description of hot-wire anemometry will be given below.

Hot-wire

Hot-wire anemometers uses a fine wire which is heated up to a temperature above the ambient temperature. The wire is then cooled by the passing of the surrounding flow. Since the electrical resistance of such a wire is dependent upon temperature, a relation can be found between the resistance of the wire and the flow velocity. The principle of Constant Temperature Anemometry (CTA) is to keep the temperature, and thereby also the resistance, constant. The wire is connected to one arm of a Wheatstone bridge which is kept in balance, and the output of the CTA is the bridge voltage. Advantages of hot-wire anemometry are the very high frequency response and the continuous signal, which makes it very suitable for studies of turbulent flows.

Single hot-wires were made in-house. The wires were silver coated Platinum-10 % Rhodium with a diameter of 5 μm and a resistance of 5.7 Ω/mm. The wire length to diameter ratio was about 200. The frequency response of the hot-wire was always better than 15 kHz. The constant temperature anemometers were operated with an overheat ratio of 1.5. The anemometer signal was low-pass filtered and amplified to utilize the resolution of the 12 bit National Instruments PCI-6024E data acquisition card.

The system was calibrated by comparing the anemometer output to the reading of a pitot tube. A fit of a fourth degree polynomial to the output voltages and the corresponding velocities determined the calibration function. The pitot tube was located close to the hot-wire probe in the wind tunnel test section. The temperature in the wind tunnel increased quite a lot during the measurements. A rule of thumb is that a change of 3 $°C$ in the ambient temperature reduces the velocity with about 10 %. A temperature correction was therefore applied to all output voltages to compensate for this and bring the measurement outputs back to the calibration temperature.

$$E_c = \sqrt{\frac{T_w - T_0}{T_w - T_m}} E_m \tag{7.4}$$

where E_c is the corrected voltage, E_m the measured voltage, T_w the overheating temperature of the sensor, T_0 the calibration temperature and T_m the temperature during the measurement. The temperature in the tunnel was recorded by the use of thermocouples (type T). More information about hot-wire anemometry and its application may be found in e.g. Bruun (1995).

7.7.2 Considerations and comparisons

At the beginning of this experimental study, hot-wire anemometry was intended to be the main measuring technique. A large amount of time was spent to gain experience with hot-wire anemometry, and to compare it with pitot tube measurements. Pitot tubes are only suitable for measuring the mean velocity, due to the long response time of the system. Pitot tubes measures the velocity in one direction. Single hot-wire is also intended for one-dimensional flow. It is sensitive to all velocities in a plane normal to the wire, hence it is not possible to single out negative velocities. The terrain in the current study was composed to generate complex flow. Hence, separating between streamwise and vertical velocities, and between positive

and negative velocities, was of great importance. Other drawbacks with hot-wire anemometry were errors due to electrical noise, and drifting of the resulting velocities due to increasing temperature in the tunnel during measurements. The latter was a problem, despite the temperature corrections. The mean velocity results for the pitot tube were in general higher than for the hot-wire, and the deviation increased with increasing temperature. It was also a problem to measure near the ground at some positions with hot-wire and pitot tube, like halfway up the hill, due to the interference of the probe support with the model. It was therefore decided to use Laser Doppler Anemometry as the main measurement method throughout the experiments instead. All the disadvantages with single hot-wire were avoided by the use of LDA when it came to mean values. It was observed that both the mean values, the standard deviations and the resulting turbulence intensities were higher when measured with LDA compared to hot-wire anemometry. The velocities measured with hot-wire anemometry decreased with increasing temperature in the wind tunnel. Hence, these velocities were consequently too low, as the temperature in the wind tunnel was higher during measurements than during the calibration. Tests confirmed that using transit time weighting for the LDA data reduced the velocity bias towards higher velocities compared to using arithmetic weighting. Still, it might be a velocity bias in in the LDA results, caused by the estimation of moments or other biases in the LDA system (DeGraaff and Eaton, 2001).

Single hot-wire anemometry and pitot tube were used during the creation of the approaching boundary layer in the current study. Hot-wire anemometry was also later applied for spectrum measurements in the inflow profile. It was more suitable for this purpose than LDA, due to the required high sampling ratio. A pitot tube was always used to check the mean velocity at the entrance to the test section during the experiments. Case I was measured with hot-wire, pitot tube and LDA. All the measurements above the terrain model which are presented in this thesis were acquired by LDA.

7.8 Measuring procedure

A profile was measured 1 m upstream of the leading edge of the model in each case. This was along the line of measurements planned above the terrain model (Section 7.6). Profiles at two positions to each side of this was also measured in almost all cases. This was done to confirm the uniformity of the approaching boundary layer in the spanwise direction. Measurements were then obtained at all positions above the terrain model in each case. The vertical profile in each of these positions was measured by the following procedure.

1. The measurement volume was positioned in the required position without wind in the tunnel.

2. The wind tunnel was started, and the rotational speed of the fan was set to about 1000 rpm.

3. The reference velocity was then checked by measurements. A pitot tube was

mounted about 50 cm below the roof some meters downstream of the contraction. This was used to adjust the velocity during startup of the tunnel, and for monitoring the mean velocity during the measurements, to ensure a constant inflow velocity. The velocity at this location was 14.7 ± 0.1 m/s. If necessary the rotational speed of the fan was adjusted slightly to increase or decrease the velocity before the profile was measured. This velocity was only used as a reference to keep a constant wind speed in the tunnel for all measurement positions and cases, and should not be confused with the velocity at the top of the artificial boundary layer.

4. One vertical profile was obtained. Fog was inserted continuously throughout the measurements, and the reference velocity was checked at regular intervals. The lowest measurement point was about 3 mm above the surface. All profiles were measured from this point and then outwards to $z = 350$ mm, with a total of about 40 measurement points. The traversing system with the probe was moved in the vertical direction from outside the tunnel while the fan was running.

The time spent measuring one vertical profile, after adjusting the probe, was about one hour.

7.9 Data collection

The measurements were obtained with a FiberFlow optical system and processor from Dantec Dynamics. BSA Flow Software is a software package dedicated LDA measurements running under Windows, and was installed on a PC connected to the processor. The BSA Flow Software took care of communication with hardware, acquisition of data, and statistical processing of data. Settings could be adjusted prior to every measurement to ensure optimal signals, and the Doppler bursts were monitored in the software during measurements. Transformation of velocity vectors, as described in Section 6.6, were done before calculation of statistical quantities. An overview of the most important estimators were given in Section 6.3. Finally the estimated moments were exported from the BSA Flow Software to Excel-files. These data files were then imported into MATLAB for further analysis. In addition to the exported results the project file with raw data was saved for each profile, so that existing data could be imported into the software and re-analyzed if necessary.

7.10 Scaling of measured data

Scaling of the data in this thesis was a complicated task. Self-similarity requirements were presented in Section 3.2, but it was considered that this theory did not necessarily give the best presentation of the results. A typical quantity to use is U_e, i.e. the free stream velocity in the inflow. This is not constant in this study, since the velocity increases further above the top of the generated boundary layer (Section 7.3). The friction velocity u_* commonly used for scaling is calculated in

the inflow, and partly used for scaling in the presentation of the inflow profile. The surfaces in the inflow and on the model are not the same, even though both are quite smooth. Hence, the roughness of the model surface is unknown and hard to extract from the measured velocity profiles above the terrain model. Many different types of figures and comparisons between various cases are shown in this thesis. This also requires different scaling, to clarify the results.

To simplify the interpretation of the terrain effects, the reference velocity used to scale most of the data is kept constant at $U_r = 13.5\ m/s$, measured in the incoming profile at the maximum model elevation of $z_r = 350\ m$. The vertical and horizontal positions are scaled with H, which is taken to be the maximum height in each case. Hence, $H_1 = 350\ m$ (Case I, II, V, VI, VII and IX), and $H_2 = 250\ m$ (Case III, IV and VIII).

7.11 Quality of data

The Reynolds numbers in the present study are in the range 10^5 to $3 \cdot 10^5$, based on typical heights of the terrain and the corresponding incoming velocities at these heights. Reynolds numbers of the order of some hundred thousand are commonly assumed to be enough to compare experimental flows to real atmospheric flows. The roughness Reynolds number in this study indicates that the flow is close to smooth. Hence, the flow in this study differs from most atmospheric flows which are fully rough. The added roughness in Case IXc makes the flow fully rough. The results in this experiment are studied from the ground and to the top of the boundary layer, even if it is only recommended to study simulated atmospheric flows below 0.15δ (Section 5.1.2). However, the current study was carried out with the main perspective to create a test case for numerical simulations, and flow solvers can be set up to reproduce the experiment.

The maximum blocking of the tunnel cross section caused by any terrain module in the current study was 15 %. Hence, blocking is an important issue and will be considered in the discussion of the results.

The positioning of the measurement points was challenging, as described in detail in Section B.3. The positioning uncertainty of the measurement point in the vertical and spanwise direction was approximately $\pm 1\ mm$, and the corresponding uncertainty in the streamwise direction was approximately $\pm 2\ mm$. Tilting of the LDA probe introduces errors as described in Section 6.5. The importance of considering the velocity component along the tilted probe is illustrated by an example in Section B.4.

Chapter 8

Results and discussion

Descriptions of the tunnel, setup, generation of approaching boundary layer, measurement positions and measurement procedure were given in Chapter 7. The resulting flow fields will now be presented and discussed. First, an overview of the generated undisturbed boundary layer and the flow above the model in Case I-IX will be given. Comparisons between selected cases and a more detailed discussion of special effects are then presented. The results are successively compared to experimental results in similar studies, and they are also compared to results from a numerical simulation and several analytical methods at the end of the chapter.

8.1 Undisturbed incoming boundary layer

8.1.1 Characteristics of inflow profile

The arrangement and size of the spires was chosen to generate conditions similar to atmospheric wind in coastal areas with regard to the mean velocity profile, turbulence intensity and turbulence spectrum. Characteristics of the generated undisturbed boundary layer are shown in Figure 8.1. This is the mean of 4 profiles positioned 0.3 m apart across the test section with only spires and base plates in the tunnel. The measurements were taken about 6 m downstream of the spires. An overview of the main parameters fitted to the experimental data are listed in Table 8.1. The height denoted δ in the current study is not really the top of the boundary layer, but the maximum height level measured and which the fit is acceptable for.

d_0 [mm]	δ [mm]	$U(\delta)$ [m/s]	u_* [m/s]	z_0 [mm]	ΔU^+	Re_*
0.90	349.1	13.5	0.50	0.004	0.5	0.13

Table 8.1: Characteristics of simulated atmospheric boundary layer generated by spires. All values are at model scale.

The well-known logarithmic velocity profile was fitted to the experimental mean velocity in the lower part of the undisturbed boundary layer. The displacement

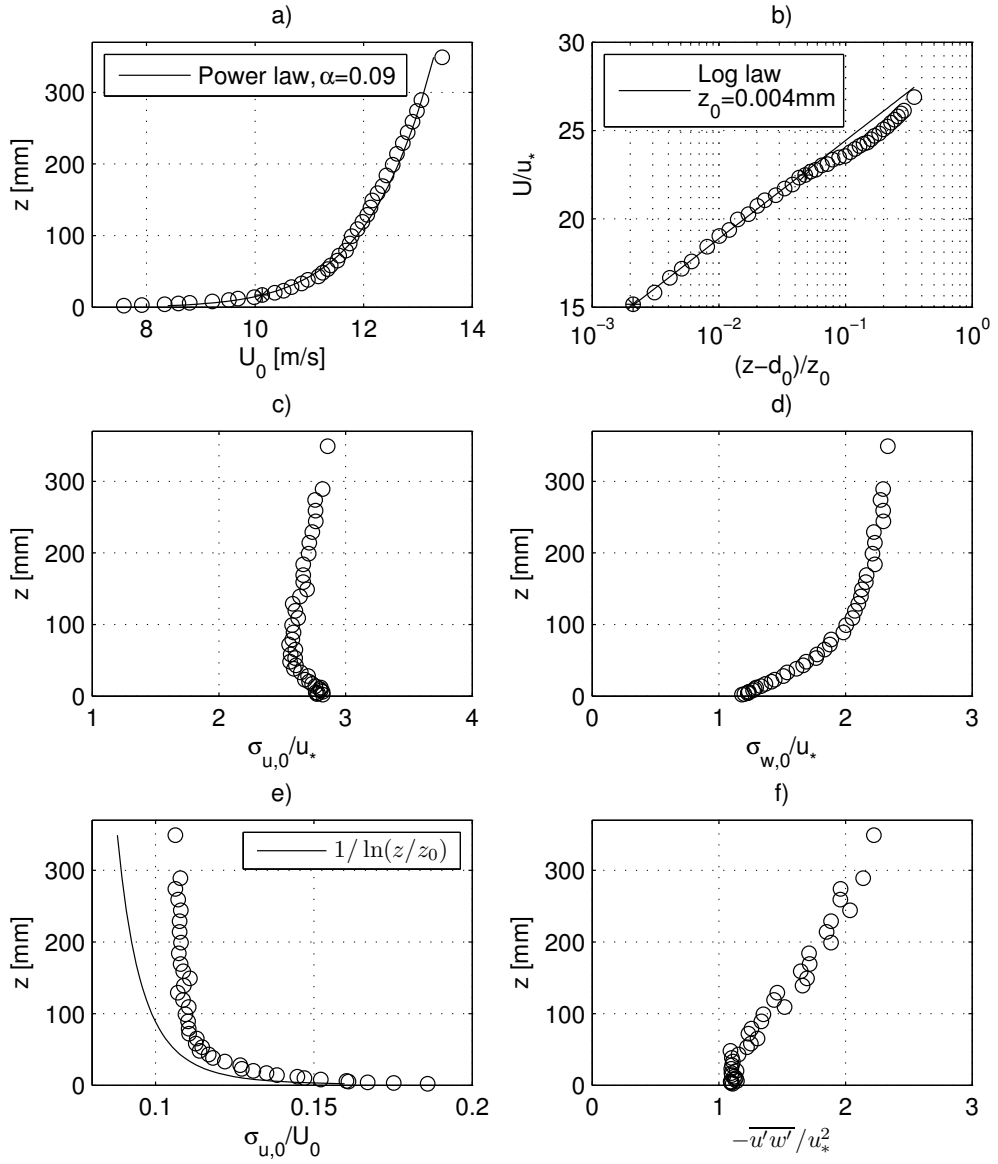

Figure 8.1: Incoming undisturbed turbulent boundary layer. The streamwise mean velocity profile is compared to the power law in a), and to the logarithmic law in b). The '*' in a) indicates the reference height, and '*' in b) indicates the outermost points of the range where the logarithmic law has been fit to the data. The index 0 shows that it is the incoming boundary layer.

height d_0 was found by a manual fit. It was adjusted to make the lower part of the profile as linear as possible in a plot of $\ln(z - d_0)u_*/\nu$ versus U/u_*. Note that the quantity d_0 is mainly used in this section, where it is related to the fit of the logarithmic law. The displacement height has not been subtracted from the measurement heights in the presentation of the results in subsequent chapters, as the surface is virtually smooth. The only exception is the presentation of the results related to the rough surface in Case IXb-c. The friction velocity, u_*, was also found manually by adjusting the value until the slope of the calculated line matched the slope of the experimental data in the lower region. Adding a roughness function of $\Delta U^+ = 0.5$, gave a very good fit to the data below $z/\delta = 0.15$. The value of the roughness length $z_0 = 0.0044$ was calculated by use of Equation 3.9. Another approach was also taken to find a roughness length representative of the measured data. The method of least squares was applied between $(z-d_0)/\delta = 0.0060$ and $(z-d_0)/\delta = 0.1378$, with the value $d_0 = 0.9\ mm$ determined previously. The resulting friction velocity was $u_* = 0.49\ m/s$, and the roughness length $z_0 = 0.0040\ mm$, hence quite similar to the results found by a manual fit. An adjustment of z_0 to fit the modified logarithmic law (Equation 3.10) to the measured inflow profile, gave a roughness length of about $z_0 = 0.0052\ mm$. The lowest part of the profile was not a straight line since d_0 was not subtracted, so the fit done this way was not especially good.

A fit of the power law to the experimental data was done by the method of least squares for a given reference height. The velocity profile in the undisturbed boundary layer can be reasonably represented by a power law with an exponent $\alpha = 0.09$ up to the height $z = 300\ mm$. If the lower part of the boundary layer is excluded from the fit, an exponent of $\alpha = 0.08 - 0.09$ is even better.

Converted from a model scale of 1:1000 to full-scale conditions, the roughness length in Table 8.1 corresponds to a value of $z_0 = 0.004\ m$. Typical heights of the atmospheric boundary layer was described in Section 3.1.1 and an overview of roughness categories was given in Table 3.1. Both the roughness length, the adapted α and a full-scale boundary layer height of 350 m are values typical for off sea wind in coastal areas. The mean velocity at the height corresponding to 30 m in full-scale was about 10.7 m/s.

A comparison of the turbulence intensity of the measured data and a theoretical expression (Equation 3.25) is shown in Figure 8.1e). The turbulence intensity does not decrease as much as expected with height. The slightly high values for the turbulence intensity profile is mostly due to the fact that the normal stress in the streamwise direction ($\sigma_{u,0}$) does not decrease with height as it should. It decreases up to 50 mm, is constant in the range 50 mm to 100 mm, and then increases to values similar to those close to the ground at the top of the boundary layer. It is worth noticing that these variations are in the range around 1.3 - 1.4 m/s, so $\sigma_{u,0}$ can be considered approximately constant throughout the boundary layer. According to Equation 3.24 the turbulence intensity at the height corresponding to 30 m and the power law coefficient (α) should be equal. The latter was found to be 0.08-0.1 dependent on the heights utilized in the power law fit. A full-scale roughness length of $z_0 = 0.004\ m$ results in $\alpha = 0.1$ from Equation 3.24. The measured turbulence

intensity at this height is 0.12-0.13, which is a bit high.

According to Gong and Ibbetson (1989) a lack of a constant stress layer near the surface is common in wind tunnel experiments. It often decreases almost linearly with height instead. This is not the case in the current study, where the shear stress $\overline{u'w'}$ is approximately constant up to 0.1δ, with a mean value in this region of $\overline{u'w'} = -0.278\ m^2/s^2$. The calculated friction velocity is $u_* = \sqrt{-\overline{u'w'}} = 0.53\ m/s$, hence corresponding satisfactory with the values of friction velocity found by the manual fit and the method of least squares to the logarithmic law. The differences are within typical uncertainties of the friction velocity, as implied by for instance Krogstad et al. (1992). In contrast to theory $\overline{u'w'}$ does increase with height above 0.1δ (see Figure 8.1f). Some measurements were also taken at heights above the outermost measurement point shown in Figure 8.1, and it was then confirmed that the trend is reversed. The Reynolds stresses decreases at heights above 350 mm. This unexpected tendency can be explained by the spires which generate the incoming boundary layer in the lower part of the wind tunnel. The height of 350 mm taken as the top of the boundary layer in this study is not really the height where the longitudinally velocity become constant, it actually increases even more further up.

The ratios of standard deviations to friction velocity near the surface in the streamwise and vertical directions are $\sigma_u/u_* = 2.8$ and $\sigma_w/u_* = 1.2$ respectively with $u_* = 0.5\ m/s$. If the friction velocity calculated from the shear stress is used instead, the ratios decreases to $\sigma_u/u_* = 2.64$ and $\sigma_w/u_* = 1.13$. Cao and Tamura (2007) reported values of $\sigma_u/u_* = 2.35$ and $\sigma_w/u_* = 1.1$ for flow above a smooth surface similar to the surface in the current study. The mean values derived from all the field data reviewed by Counihan (1975) were $\sigma_u/u_* = 2.5$ and $\sigma_w/u_* = 1.25$. Mochizuki and Nieuwstadt (1996) studied the maximum in the streamwise velocity fluctuations in wall turbulence and its dependence on Reynolds number. Data was collected from both numerical and experimental studies. They found that the most probable peak value for σ_u/u_* in a turbulent boundary layer under zero pressure gradient was 2.71 ± 0.14, and that it within statistical errors was independent of Reynolds number. Also, they did not find any significant difference in the magnitude of this peak value above rough and smooth surfaces. These data were obtained for walls which could be considered as smooth, but at lower Reynolds numbers than the current study. Mochizuki and Nieuwstadt stressed the fact that the accuracy in the method used to find the friction velocity is of great importance in this context. A choice has to be made for the constants when the logarithmic velocity profile is used to find u_*, which introduces significant errors to the friction velocity. Mochizuki and Nieuwstadt commented that an experiment in the atmospheric boundary layer could be a candidate for studying the near-wall turbulent flow at very large Reynolds numbers. Data for the atmospheric boundary layer has for instance been given by Panofsky and Dutton (1984), with a near surface value of $\sigma_u/u_* = 2.39$. As mentioned by Mochizuki and Nieuwstadt most atmospheric measurements are done at heights which are at least 10 meters above the surface. This could explain why the near surface values of normalized streamwise velocity fluctuations reported by for instance Panofsky and Dutton, and Counihan are lower than the results found

by Mochizuki and Nieuwstadt. Hutchins and Marusic (2007) stated that since the year 2000 it has been well-known that the inner-scaled peak in σ_u/u_* rises with Reynolds number. They gave a formula found by a curve fit to experimental and numerical data

$$\left(\frac{\sigma_u^2}{u_*^2}\right)_{peak} = 1.036 + 0.965 \ln\left(\frac{\delta u_*}{\nu}\right) \tag{8.1}$$

Applying this formula to the parameters in the present study yields $\sigma_u/u_* \approx 3.17$. While the referred results above indicated that the inner scaled streamwise standard deviation found in the present study was too high, these latter results indicate the opposite. σ_w/u_* was quite close to values reported in other studies. Hence, it can be concluded that the experimental values for the maximum in both the streamwise and spanwise velocity fluctuations agree well with corresponding field data and results reported from other wind tunnel experiments and numerical simulations.

The roughness Reynolds number of the flow, $u_* z_0/\nu$, is about 0.13. This is less than typical values of about 2.5 given to indicate fully rough flow (Snyder and Castro, 2002). A value of 0.13 indicates that the flow is actually close to the flow above a smooth surface. As pointed out earlier, the experiment was carried out with the main perspective to create a test case for numerical simulations. Therefore having a surface which is almost hydrodynamically smooth reduces the uncertainty in the numerical calculations, since the emulation of roughness effects introduces additional challenges.

8.1.2 Homogeneity across the flow

All the six profiles measured across the flow with only spires in the tunnel (see Section 7.6.1) are shown in Figure 8.2. A plane average of four of these were taken to represent the undisturbed incoming flow, as described above. Clearly, there were some differences in the flow conditions across the tunnel test section, but these were considered to be acceptable in view of how the inflow was generated. The introduction of spires to the original flow in the test section undoubtedly caused complex flow conditions, and the final setup of the spires were unconventional. The maximum deviation of U, σ_u, σ_w and $\overline{u'w'}$ at each height can be seen in Figure 8.2f. The maximum deviations for the streamwise mean velocity is about 5 % at all heights.

The inflow characteristics of the undisturbed boundary layer shown in Figure 8.1 were compared to the middle profile of the five profiles which were measured 1 m upstream of the model in Case I-IX (i.e. the profile measured along the line of measurements in each case). This was done as a check to see possible discrepancies and to get an idea of to which degree the inflow profile was influenced by the model. The most striking change in the inflow profile, was increased Reynolds stresses due to the blocking when models were inserted to the flow. The homogeneity across the flow upstream of the model in each case was also considered acceptable.

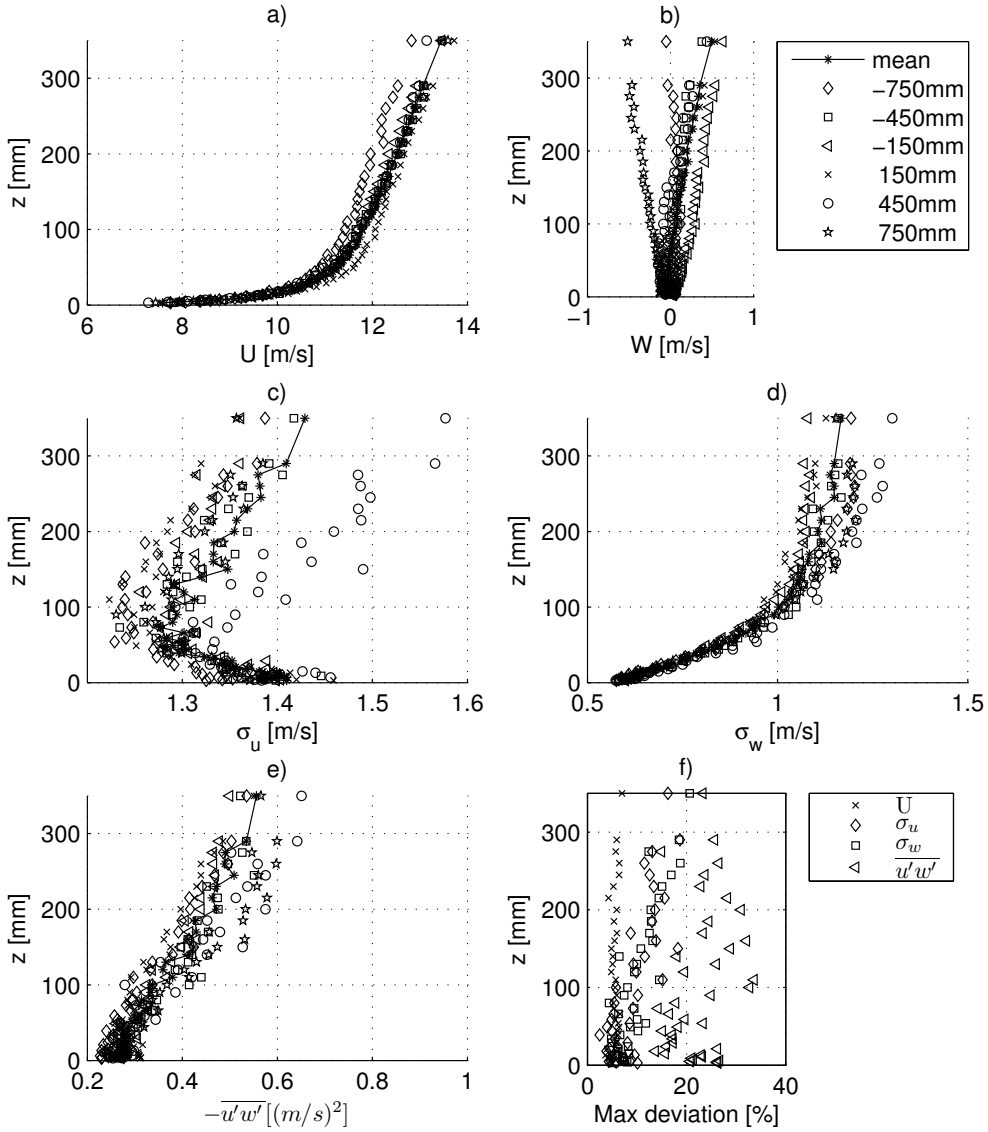

Figure 8.2: All six profiles measured in the incoming undisturbed turbulent boundary layer. "Mean" is identical to the data shown in Figure 8.1. Positions $\pm 150/450/750$ mm refer to spanwise distance from the centreline of the tunnel. "Max deviation" shown in f) is the maximum deviation between these six profiles at each height.

8.1.3 Power density spectra

Time series were measured with hot-wire to see if the experimental data were in agreement with atmospheric turbulence spectra and length scales. The measurements were taken in the centre of the tunnel 6 meters downstream of the spires at the four heights 10 mm, 30 mm, 100 mm and 300 mm. The sampling frequency used to acquire the four time series was 13.158 kHz, so the highest frequency in the spectra was $13158/2 = 6579$ Hz. The sampling time was close to 45 seconds.

The integral length scales at these four measurement heights were calculated from the velocity time series using Equation 3.29, and are listed in Table 8.2. The same values are plotted in Figure 8.3 with the recommended values by Counihan (1975) and ESDU (Freris, 1990) calculated from Equation 3.30 and 3.31 respectively. The experimental integral length scale increases with height. According to Counihan, the integral length scale in the atmospheric boundary layer increases with height up to 200-300 m. The calculated integral length scale at the highest level is smaller than the ESDU value at this height. The integral length scale at the height 30 m given by Counihan for a roughness length of $z_0 = 0.004$ m gives a full-scale value of 271 m, while the corresponding result recommended by ESDU is 116 m. Both these values are of the same order as the integral length scale found from the time series, which at full-scale is 164 m at the height 30 m. The results are consequently in agreement with a model scale of 1:1000. This is also confirmed by the length scale in Harris' spectrum model. The recommended value for atmospheric conditions is $L_{Harris} = 1800$ (Counihan, 1975), and the value $L_{Harris} = 1800/1000 = 1.8$ employed in the model results in good agreement with the measured data (not shown here). All this implies that the energy distribution in the generated boundary layer is similar to the one in the full-scale atmosphere.

Height [mm]	${}^xL_u$ [mm]
10	144.1
30	164.2
100	189.8
300	204.9

Table 8.2: Calculated integral length scales at four different heights in the incoming flow.

The power density spectrum was calculated from the time series using Fast Fourier Transform. The number of samples in each FFT window was 2^{14}, so the total number of windows used was 36. The size of the FFT windows was chosen so that it was low enough to give a clear spectrum at the high frequency end, and at the same time high enough to close the spectrum at the lowest frequencies (as seen when plotting $f\Phi_{uu}$). The results were also smoothed. In Figure 8.4, $f\Phi_{uu}$ is plotted as a function of the normalized frequency $X = f^xL_u/U$ on a semi-log axes, while the same is plotted on log-log axes in Figure 8.5. The experimental turbulence spectra are compared to von Karmans and Kaimals models for power density spectra in both figures. The length scales L_{Karman} used at the different heights in von

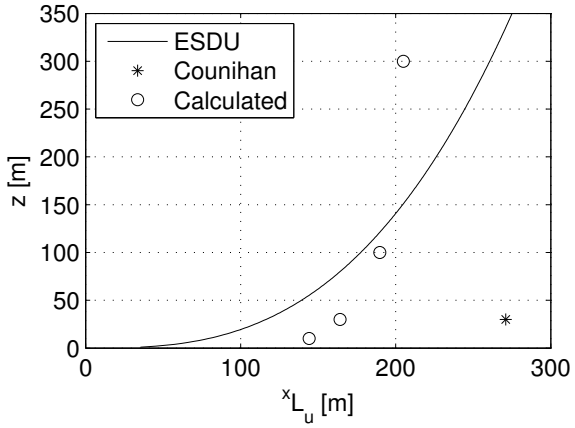

Figure 8.3: Integral length scales calculated from the experimental data. Recommended values given by Counihan (1975) and ESDU (Freris, 1990) are also plotted. All values are in full-scale, and the roughness length is $z_0 = 0.004\ m$.

Karman's model was the calculated integral length scales (^xL_u) which are listed in Table 8.2, hence not a length scale found by adjusting the model to the data. The length scale used in Kaimal's model is $L_{Kaimal} = 2.329 L_{Karman}$.

It can be shown that both models used for comparison will approximate to a straight line with slope $-5/3$ in the high frequency range when plotted on a log-log axes ($\Phi_{uu} \sim f^{-5/3}$). The positioning of this line depends on the mean velocity, the integral length scale and the standard deviation. It is seen from Figure 8.5 that the measured data have an identical slope. This is known as the inertial subrange, where energy is neither produced nor dissipated but handed down to smaller and smaller scales. The dissipation of turbulent kinetic energy into heat by viscous effects occurs at the highest frequencies. The area in between this, where the calculated values are higher than what the model predicts, is known as the pre-dissipative bump (Coantic and Lasserre, 1999). The pre-dissipative bump is less visible as the height increases, while the inertial subrange becomes broader.

Values higher than the model values can be seen at the top of the curves $f\Phi_{uu}$ in Figure 8.4 at the three highest of the four measured elevations. This top occurs where the physical frequency is about 7 Hz. The explanation for these high values might be that the measurement device was oscillating at this frequency. Since this is not the case at the lowest height, a more probable explanation is that the top is due to the way the boundary layer is set up.

The experimental data agrees very well with the von Karman power spectrum, and to some less extent with the Kaimal power spectrum. This could be expected, as the von Karman model is known to fit well with wind tunnel turbulence. The measured values are in least accordance with the models in the regions with the pre-dissipative bump and for the maximum experimental values of $f\Phi_{uu}$ as commented on above.

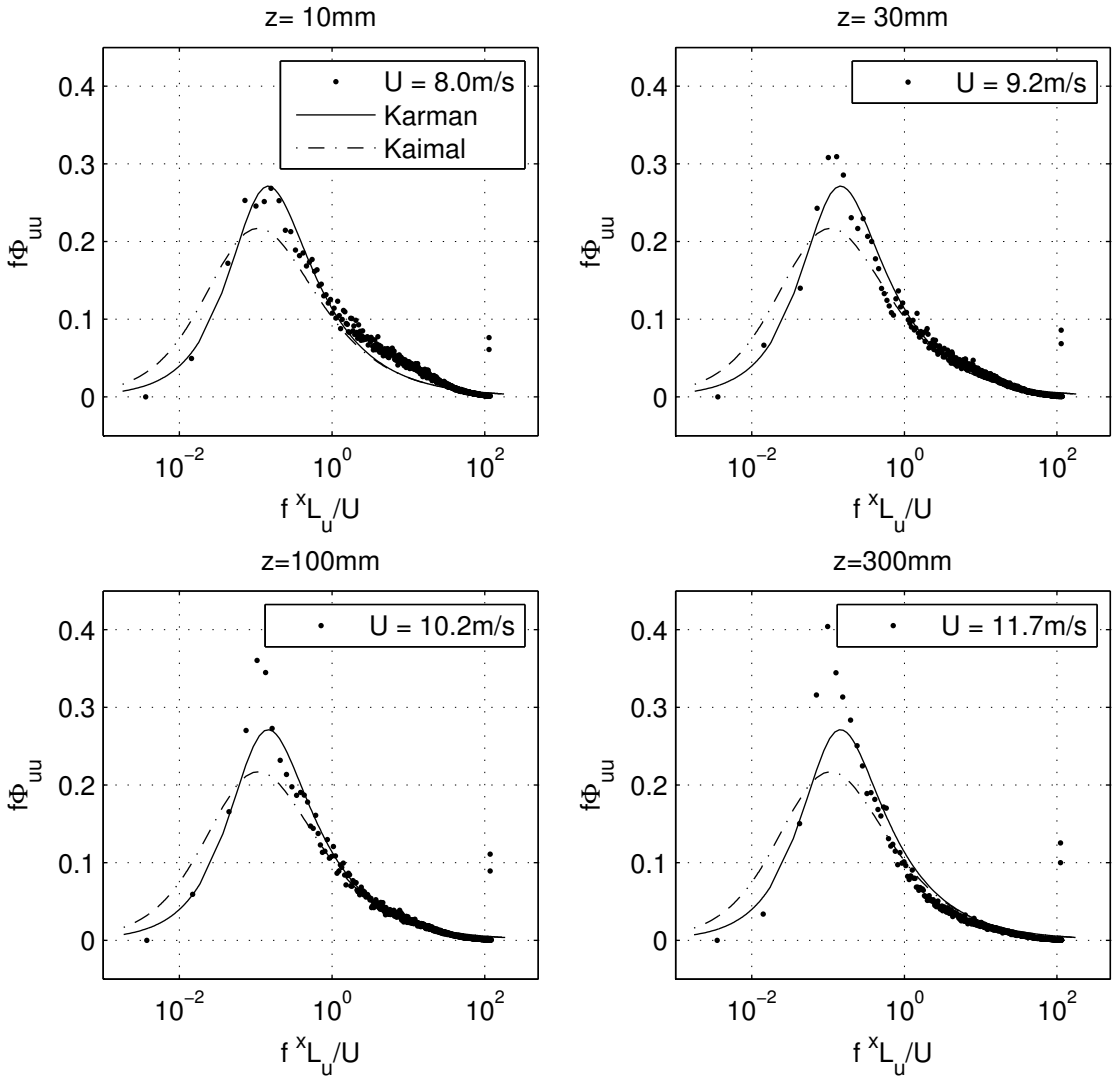

Figure 8.4: Power spectrum (plotted with semi-log axis) at 4 different heights in the inflow compared to von Karman's and Kaimal's model.

8.2 Flow above model - an overview

This section gives an overview of the main results in Case I-IXa.

8.2.1 Case I

Case I is the first of six cases (I-VI) which are approximately two-dimensional. This is the simplest of these cases, consisting of one mountain and the most gentle slope. The mean slope of the ascending hill is 27.9° and the maximum slope occurring about half way up the hill is 37.3°. The terrain and mean velocity vectors are shown in Figure 8.6. Some of the markers have been omitted to make the figure more readable. Results for all the measured positions are shown in more detail

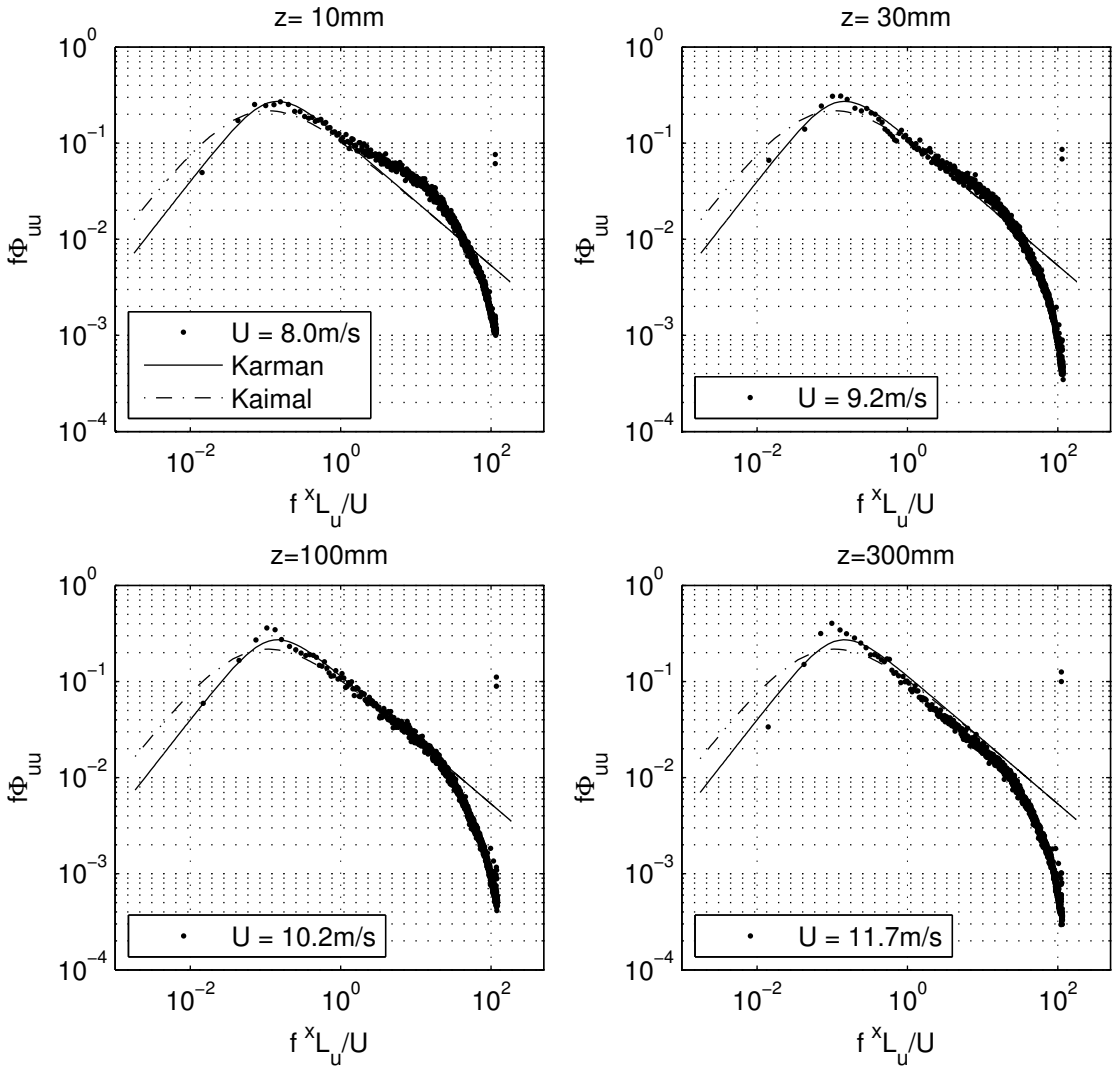

Figure 8.5: Power spectrum (plotted with log-log axis) at 4 different heights in the inflow compared to von Karman's and Kaimal's model.

in Figures 8.7 and 8.8. This includes moments and the fractional speed-up ratio $\Delta S(z/H_1)$.

At the base of the hill, $x/H_1 = 0.04$, the flow velocity has been reduced over the entire mountain height and by as much as 60 % near the ground. This is due to the blocking effect of the mountain on the flow. At the position of maximum slope (i.e. half way up the hill, $x/H_1 = 0.93$) the flow is still retarded below the top of the mountain ($z/H_1 = 0.5$). However, at the crest of the hill a significant velocity gain is evident for all heights (Figure 8.7). The mean velocity is doubled near the wall, and the fractional speed-up ratio then drops rapidly with increasing height up to about $z/H_1 = 0.2$. From $z/H_1 = 0.2$ to $z/H_1 = 1$ the velocity gain falls off more slowly from about 50 to 20 %. One of the ridges studied by Arya et al. (1987) had a maximum slope of 26°, which is approximately equal to the mean slope of the hill in

Case I. The maximum fractional speed-up ratio observed near the ground at the crest of this hill was $\Delta S_{max} = 0.8$, compared to $\Delta S_{max} = 1.02$ for the somewhat steeper hill in this case. Arya et al. observed that the speed-up of flow on the hilltops were proportional to the average slope, which is consistent with several theories. The results in the current study is also in reasonable agreement with this, as the speed-up increases further with increasing slope. Carpenter and Locke (1999) also studied steep ridges, and one of these had a mean slope of 26.6°, which is approximately equal to the slope in Case I. The maximum fractional speed-up ratio measured at the crest of this ridge was $\Delta S_{max} = 1.08$, occurring at a height $z/H = 0.025$. This is remarkably similar the value of $\Delta S_{max} = 1.02$ occurring at the height $z/H_1 = 0.02$ at the crest in Case I. Increased velocities compared to corresponding heights above ground in the inflow are actually seen in all the measured points above the plateau in Case I, even at the uppermost point at the end of the plateau ($x/H_1 = 5.63$) where $\Delta S \approx 0.19$.

A striking consequence of the speed-up is that the streamwise mean velocity is considerably more uniform with height than in the incoming boundary layer. The mean velocities are almost independent of height above $z/H_1 = 0.2$, except at the very crest where the velocity shows a stronger dependence on height up to $z/H_1 = 0.4$. This is very favorable for wind turbines, which then experience an approximately constant velocity over the entire rotor area.

The normal stresses in the streamwise direction are only altered in a thin layer close to the ground, typically below $z/H_1 = 0.1$. Here an enhanced turbulence production due to the increased mean shear causes an amplification in all stresses, as can be seen from the dominant turbulence production term, $-\overline{u'w'}\frac{\partial U}{\partial z}$. However, further from the surface a decreased turbulence at heights typical of the rotor plane, compared to the turbulence in the inflow, may be observed. This is due to a dominance of the second order production term $-\overline{u'^2}\frac{\partial U}{\partial x}$ which is negative and dominant in the outer layer where $\frac{\partial U}{\partial z}$ is small. Together with the speed-up, this results in a decreased turbulence intensity at heights of rotor planes compared to the turbulence intensity in the inflow. This is another beneficial result for wind turbines.

The mean velocity has a non-zero vertical component in the ascending hill and at the very crest. The velocity vector becomes approximately horizontal from the next measured profile and onwards. A slightly negative vertical velocity can be seen at the profile at the end part of the plateau, as the descending hill influences the approaching flow. The normal stresses in the vertical direction are slightly altered in the lowest region in the ascending hill, and near the crest. Like the vertical mean velocity, the normal stresses soon decay to the same level as in the inflow.

8.2.2 Case II

The terrain in Case II is similar to Case I, but the flow is approaching the terrain from the opposite direction. The terrain and mean velocity profiles are shown in Figure 8.9. Note that the x position is again measured from the model leading edge. Hence the coordinates given in Figures 8.9 and 8.6 do not refer to the same position on the model. The slope in this case is significantly steeper than in Case I, with

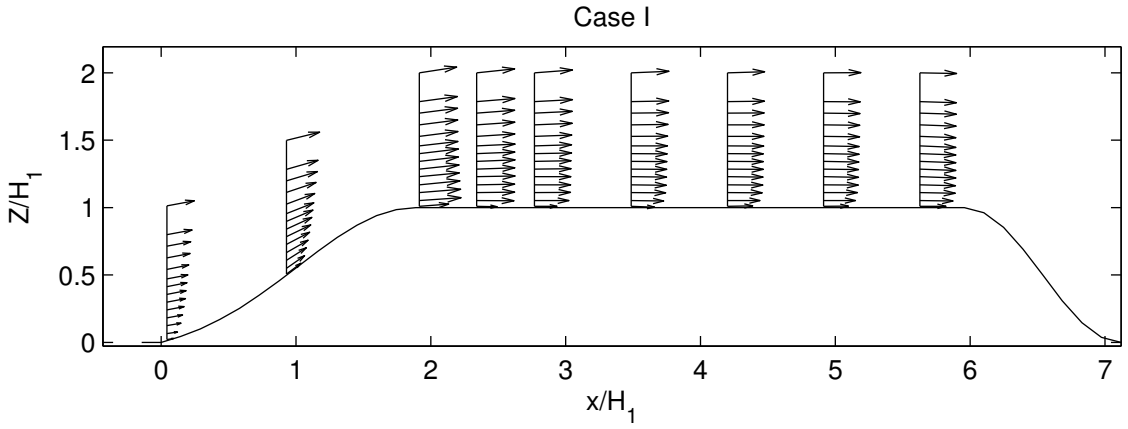

Figure 8.6: Terrain and mean velocity vectors at all measured positions in the xz-plane in Case I.

mean and maximum slopes of 40.7° and 52.8° respectively. More detailed results for U, W, σ_u, σ_w, $\overline{u'w'}$ and ΔS are shown in Figures 8.10 and 8.11. The results are very similar to Case I, except that both the vertical and longitudinal mean velocities near the crest are somewhat higher in this case. The maximum fractional speed-up ratio in Case II is close to 1.5, compared to $\Delta S_{max} = 1$ in Case I. Both maximum values occur near the ground at the very crest, as expected according to theory. Also it may be seen that the flow is very close to separating at the base of the hill, due to the more substantial blocking effect. The height to half-length ratio in Case II is 1.72. Ferreira et al. (1991) studied two-dimensional hills with height to half-length ratios of 0.75, 1, 2 and 4. They observed separation at the base of the uphill for the steepest case, but not for a height to half-length ratio of 2.

Compared to Case I, which has a more gentle slope, the streamwise normal stresses, σ_u, in Case II are somewhat higher closest to the ground, but slightly lower further out. The increased stresses near the ground are due to higher speed-up in Case II than I, hence a larger velocity gradient in this layer resulting in increased stresses. The slightly lower turbulence in Case II compared to Case I at heights $z/H_1 > 0.2$ is a consequence of the flow being more accelerated in Case II (max slope 52.8°) than Case I (maximum slope 37.3°).

The profiles measured at $x/H_1 = 3.21$, 3.78 and 4.35 are very similar. The streamwise velocities in positions upstream of this region are higher (decreasing from the crest) as a result of the speed-up. The streamwise velocities below $z/H_1 = 0.5$ at the very end of the plateau increases compared to the three upstream profiles as a consequence of the following descending hill.

8.2.3 Case III

The geometry and mean velocity vectors obtained for Case III are shown in Figure 8.12, and the data are presented in Figures 8.13 and 8.14. All results are quite similar to the two previous cases. The main difference between the terrain in these

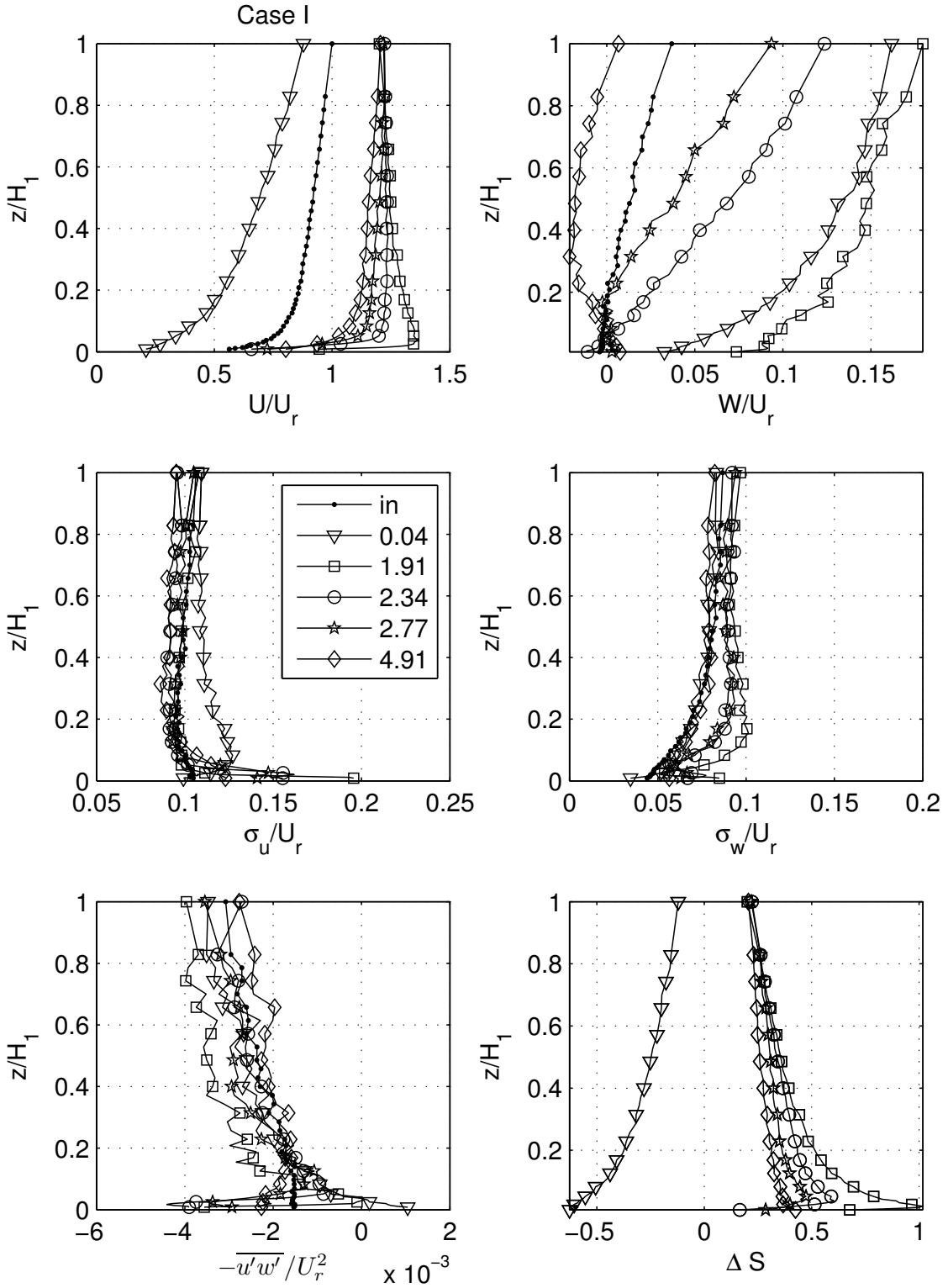

Figure 8.7: Selected profiles of streamwise mean velocity (U/U_r), vertical mean velocity (W/U_r), streamwise normal stress (σ_u/U_r), vertical normal stress (σ_w/U_r), shear stress ($-\overline{u'w'}/U_r^2$), and fractional speed-up ratio (ΔS) in Case I. "in" denotes the undisturbed boundary layer as shown in Figure 8.1. The positions x/H_1 refer to Figure 8.6.

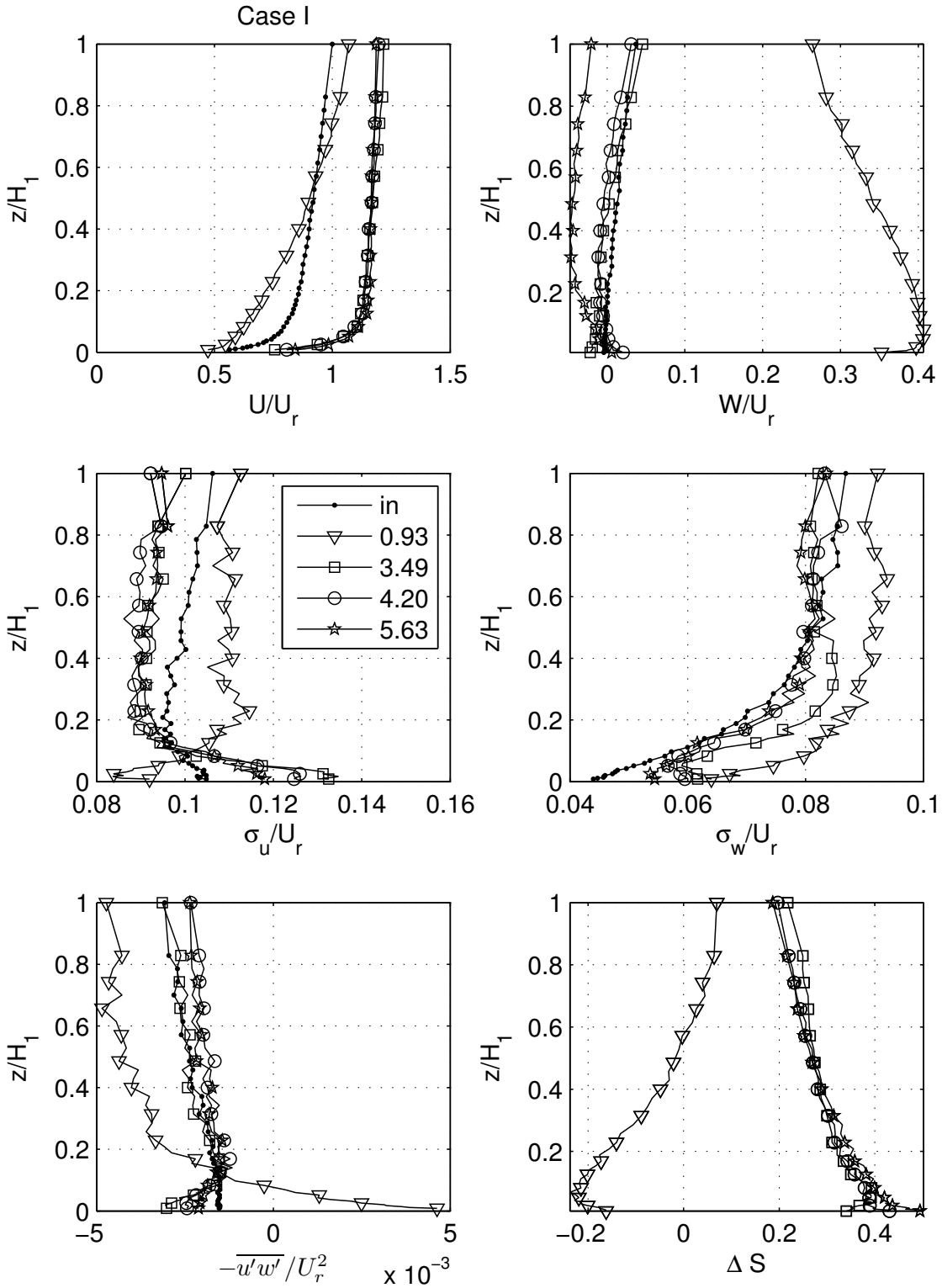

Figure 8.8: The rest of the measured profiles in Case I. The figure is similar to Figure 8.7.

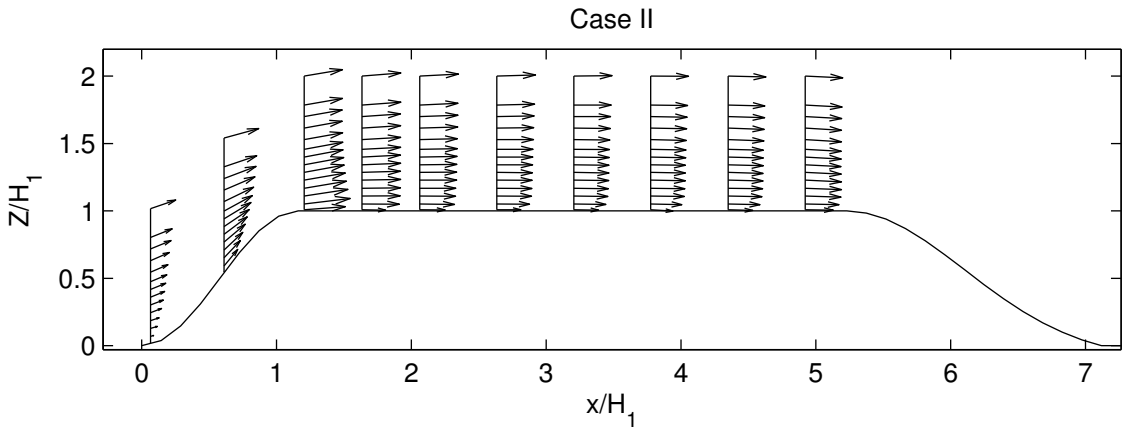

Figure 8.9: Terrain and mean velocity vectors at all measured positions in the xz-plane in Case II.

cases is that the plateau level in Case III is at 250 m, compared to 350 m in Case I and II. The mean and maximum slopes of 35° and 46.1° respectively, are steeper than Case I, but more gentle than Case II. Maximum fractional speed-up ratio found in this case is 1.35, which is between the results in Case I and II, as expected. A more detailed comparison of Case I-III is carried out in Section 8.3.

8.2.4 Case IV

The terrain in Case IV is the same as in Case III, except that the model is reversed. The mean velocity vectors above the terrain are shown in Figure 8.15. The hill in this case is a straight line with a slope of 44.5°. This results in the crest being a sharp edge, while the average slope angle is roughly the same as for Case III. The effect of a rounded versus a sharp edge is discussed more thoroughly in Section 8.4.

As in Case I to III, a distinct speed-up can be seen at the crest. The detailed results for the crest ($x/H_2 = 1.02$) and some of the other measured positions can be seen in Figure 8.16, while the rest of the measured profiles are plotted in Figure 8.17. Separation near the crest could be expected in this case, but negative longitudinal velocities were not recorded at any positions, possibly because the separated region was shorter than the distance between the first two measured positions at the plateau. One profile was measured at the very crest, and the next profile was positioned 0.3 hill heights downstream at $x/H_2 = 1.32$. The longitudinal velocity closest to the ground in the latter profile was very close to zero, and the fractional reversed flow at $z = 0.012H_2$ above ground is $\gamma = 44.3$ %. γ is defined as $\gamma = 100\ \% \frac{N_{reversed}}{N_{total}}$, where $N_{reversed}$ is the number of samples where $u < 0$ and N_{total} is the total number of samples. Even though the separation point, often defined as where $\gamma = 50$ %, was not measured, it is seen that the flow downstream of the crest behaves as if a relatively small separation bubble is present. Longitudinal velocities are close to zero in the lowest part of the profile, while it is quite similar to Case I to III further up. The normal stresses, especially in the streamwise direction, are much higher

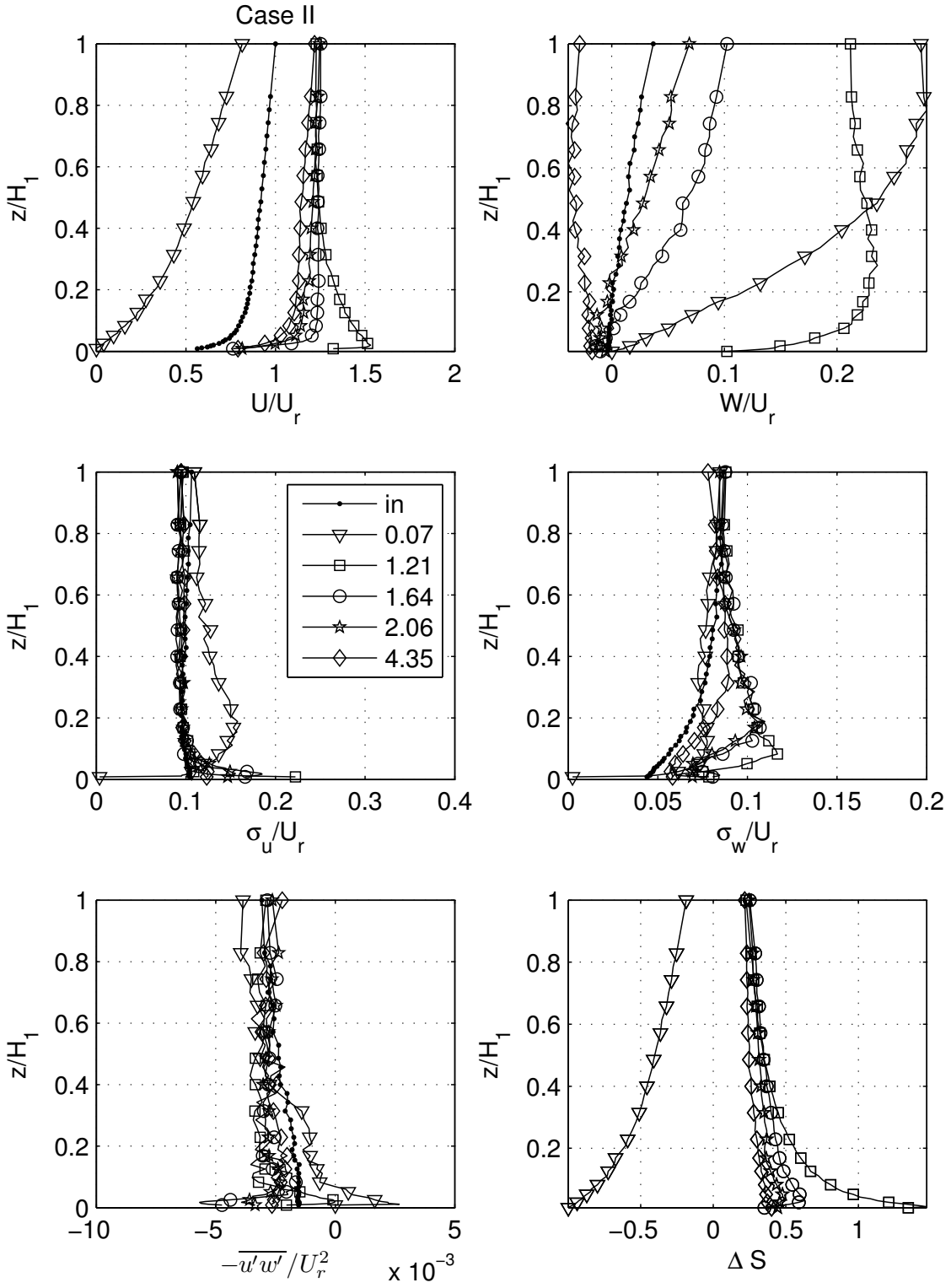

Figure 8.10: Selected profiles of streamwise mean velocity (U/U_r), vertical mean velocity (W/U_r), streamwise normal stress (σ_u/U_r), vertical normal stress (σ_w/U_r), shear stress ($-\overline{u'w'}/U_r^2$), and fractional speed-up ratio (ΔS) in Case II. "in" denotes the undisturbed boundary layer as shown in Figure 8.1. The positions x/H_1 refer to Figure 8.9.

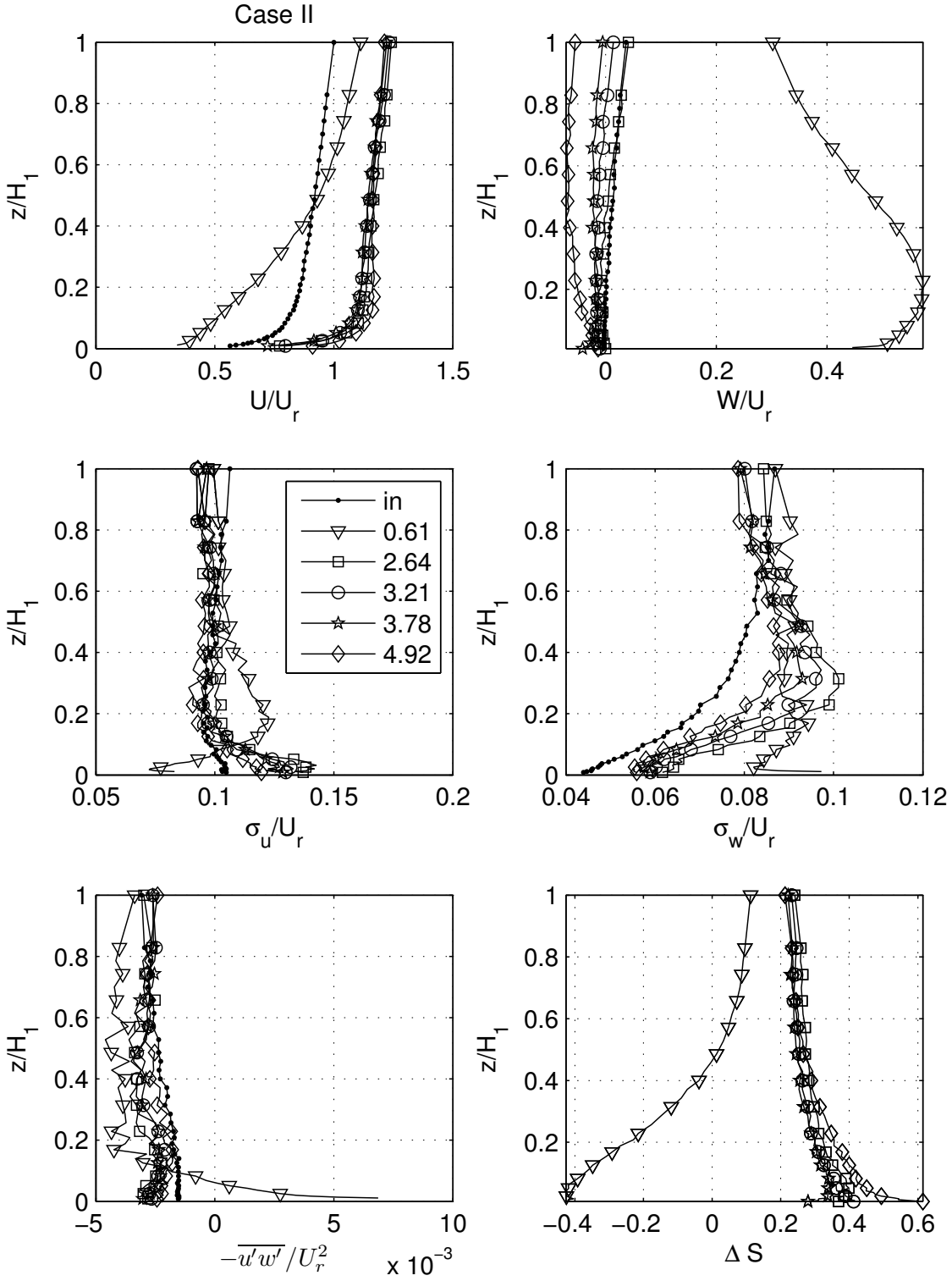

Figure 8.11: The rest of the measured profiles in Case II. The figure is similar to Figure 8.10.

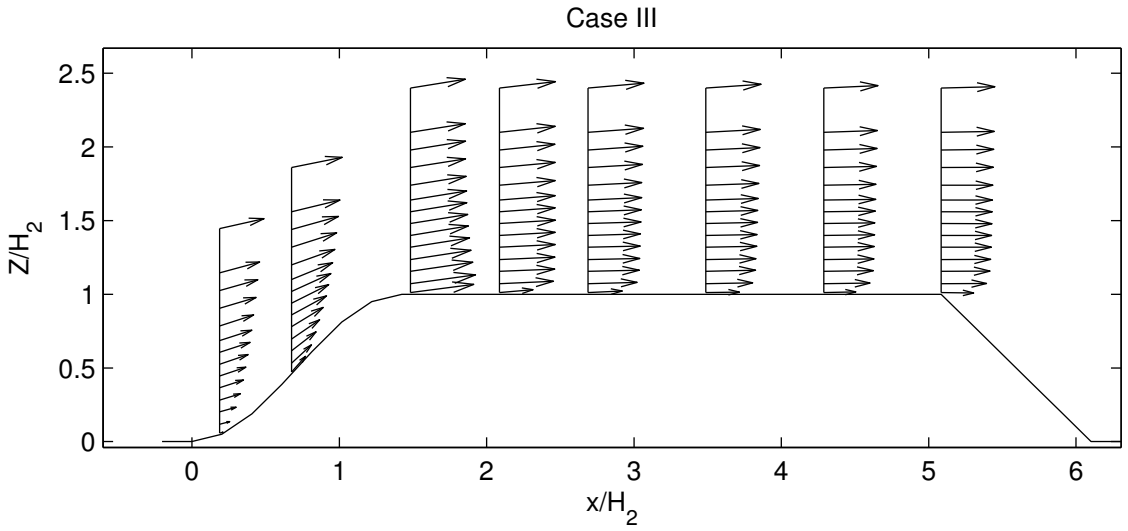

Figure 8.12: Terrain and mean velocity vectors at all measured positions in the xz-plane in Case III.

than in the inflow. Turbulence is increased considerably in the lowest part of the profile at the start of the plateau, but decreases gradually and spreads upwards as the flow proceeds along the plateau. Imamura et al. (2003) studied a straight slope of 45°. As in the current study, a region with highly increased turbulence intensity was observed in the region $\Delta x = 0.4H - 1.4H$ downstream of the crest. Separation was not observed in this region, but reversed flow occurred in 1 % of the total measuring time.

The maximum σ_u measured in Case IV is $0.58U_r$, which is 5.7 times higher than at the corresponding height in the inflow. This value was measured at the height $z = 0.06H_2$ at $x/H_2 = 1.32$, which is 0.3 hill heights downstream of the crest. The corresponding peak value at $\Delta x = 2H_2$ downstream of the crest ($x/H_2 = 3.02$, corresponds to the centre of the plateau) is $\sigma_u = 0.21U_r$ at the height $z = 0.136H_2$. At the very end of the plateau, $x/H_2 = 4.62$, which is 3.6 hill heights downstream of the crest, the turbulence level is higher than in the undisturbed inflow up to a height of $z = 0.68H_2$. The maximum value of $\sigma_u = 0.16U_r$ was obtained at the height $z = 0.16H_2$. As often found near separated regions, the normal stresses in the vertical direction, σ_w, resembles closely σ_u, even if σ_w is some smaller than in the streamwise direction.

The vertical mean velocity is significant at the very crest ($x/H_2 = 1.02$) and at the two following positions ($x/H_2 = 1.32$ and $x/H_2 = 1.62$). This introduces extra fatigue load on the turbines, since vertical wind causes a periodic load due to the rotation of the rotor (Manwell et al., 2002).

The terrain features in Case IV were inspired by Havøygavlen wind farm, which can partly be seen at the photo in Figure 1.1. This wind farm consists of 16 turbines, and has been in operation since October 2006. It has had problems with the gearing system, problems with blades and the entire nacelle at one turbine once fell down.

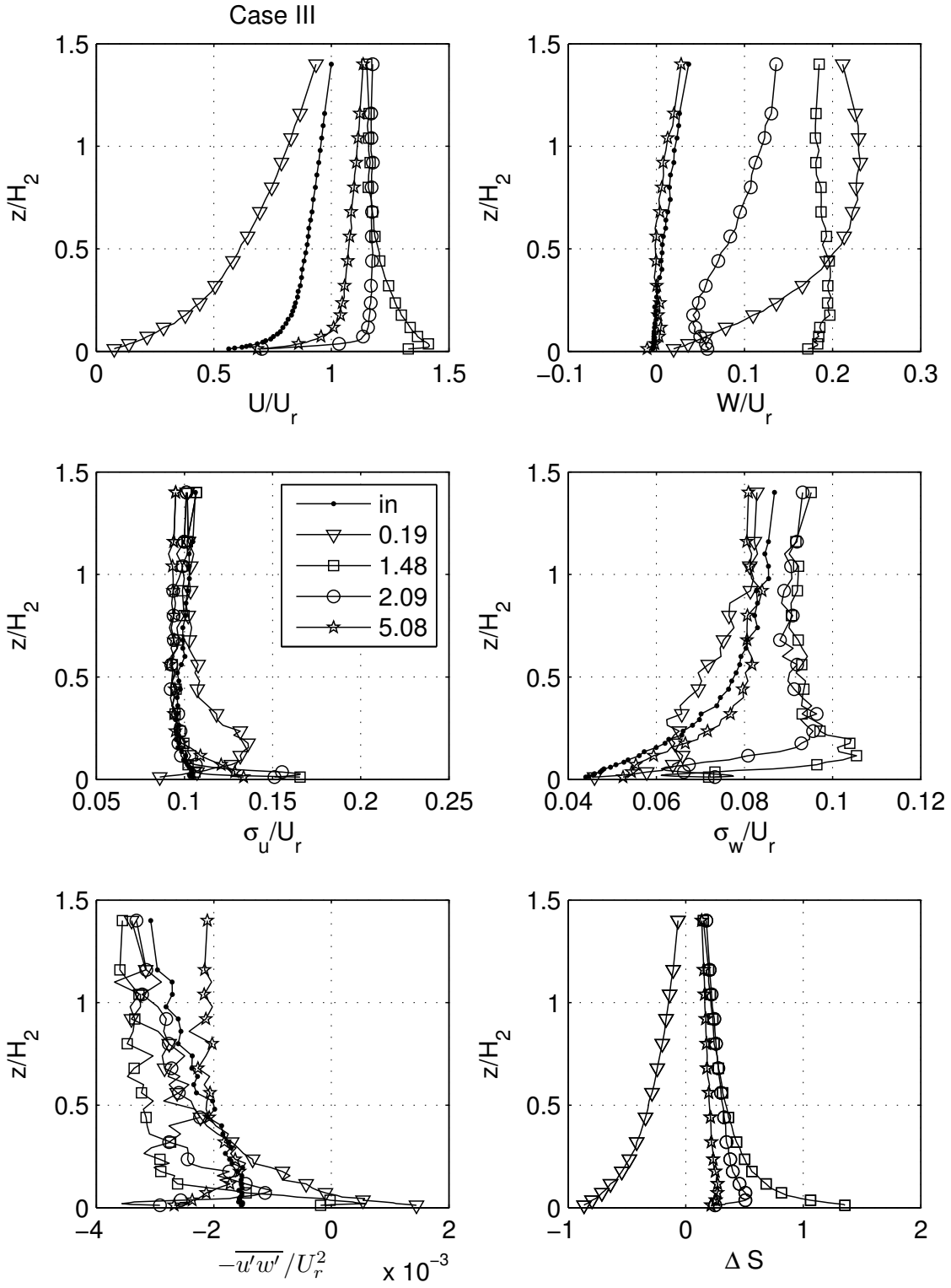

Figure 8.13: Selected profiles of streamwise mean velocity (U/U_r), vertical mean velocity (W/U_r), streamwise normal stress (σ_u/U_r), vertical normal stress (σ_w/U_r), shear stress ($-\overline{u'w'}/U_r^2$), and fractional speed-up ratio (ΔS) in Case III. "in" denotes the undisturbed boundary layer as shown in Figure 8.1. The positions x/H_2 refer to Figure 8.12.

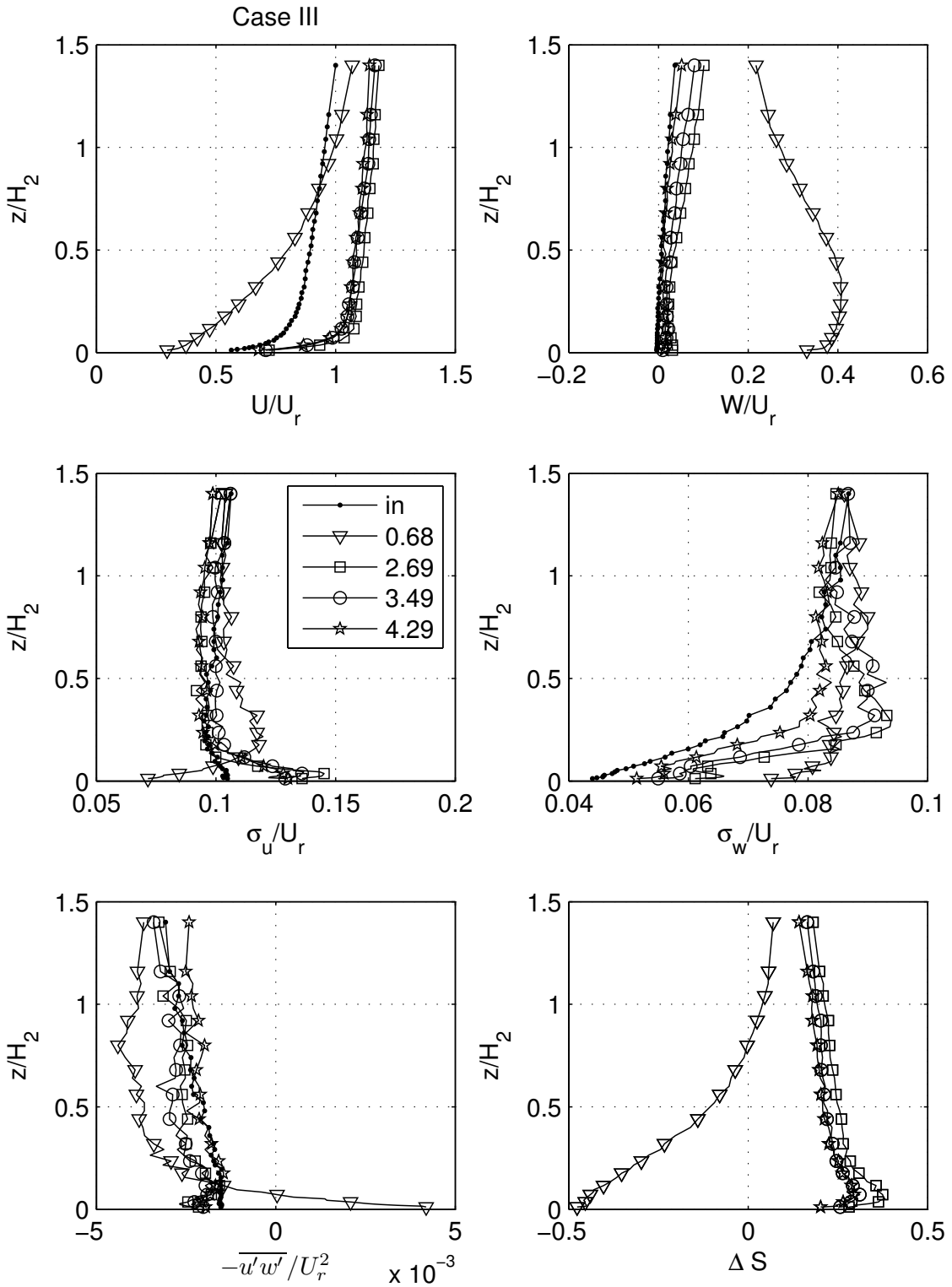

Figure 8.14: The rest of the measured profiles in Case III. The figure is similar to Figure 8.13.

The fraction of time the turbines are up and running in this wind farm is also said to be very low. The weather in this area is rough, and Havøygavlen has a high mean wind speed. Based on the results from Case IV it can be concluded that the terrain probably has caused a substantial part of the problems experienced in this wind farm.

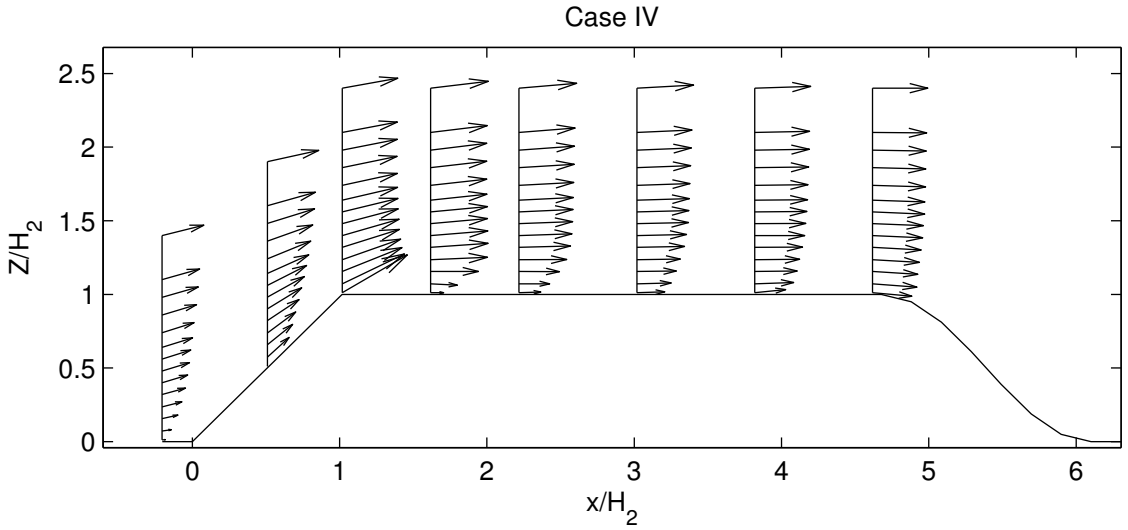

Figure 8.15: Terrain and mean velocity vectors in the xz-plane in Case IV. The profile measured at $x/H_2 = 1.32$ is omitted in this figure.

8.2.5 Case V

An overview of the terrain and the measured mean velocities in Case V is given in Figure 8.18. The effects of letting the flow pass a higher mountain and a valley before it enters a lower mountain can be seen in more detail in Figures 8.19 and 8.20. This terrain is identical to the terrain in Case I followed by Case III.

The flow measured above the first mountain was virtually unchanged from that reported for Case I and will therefore not be discussed here. This negligible influence of a lower downstream mountain on the upstream mountain is in accordance with the results found by Ferreira et al. (1991). They investigated the interaction between two identical hills for different distances, and concluded that the vicinity of a parallel hill mainly affected the flow above the downstream hill.

Separation is clearly seen in the valley at the downstream side of the highest mountain. The three mean velocity profiles measured in the valley between the two mountains indicate a large separation vortex filling the entire valley. Halfway between the mountains ($x/H_1 = 7.18$) negative mean velocities were recorded up to $z = 0.59H_1$, where H_1 is the height of the upstream plateau. As expected, the peak in the normal stresses in the streamwise direction appear close to the heights where the velocity gradient attains its maximum. For the first profile measured downstream of the first plateau (position $x/H_1 = 6.51$) this is slightly below the

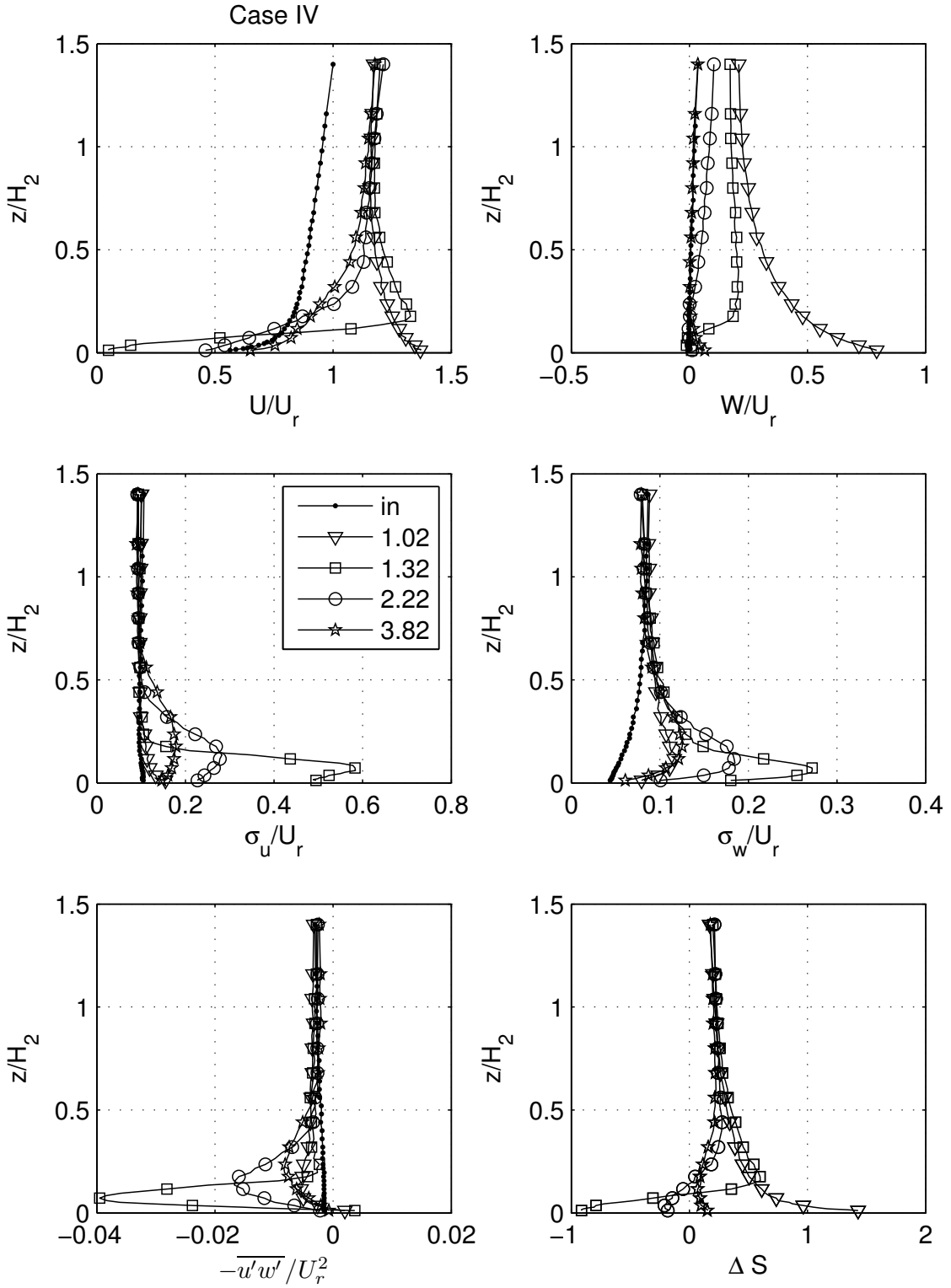

Figure 8.16: Selected profiles of streamwise mean velocity (U/U_r), vertical mean velocity (W/U_r), streamwise normal stress (σ_u/U_r), vertical normal stress (σ_w/U_r), shear stress ($-\overline{u'w'}/U_r^2$), and fractional speed-up ratio (ΔS) in Case IV. "in" denotes the undisturbed boundary layer as shown in Figure 8.1. The positions x/H_2 refer to Figure 8.15.

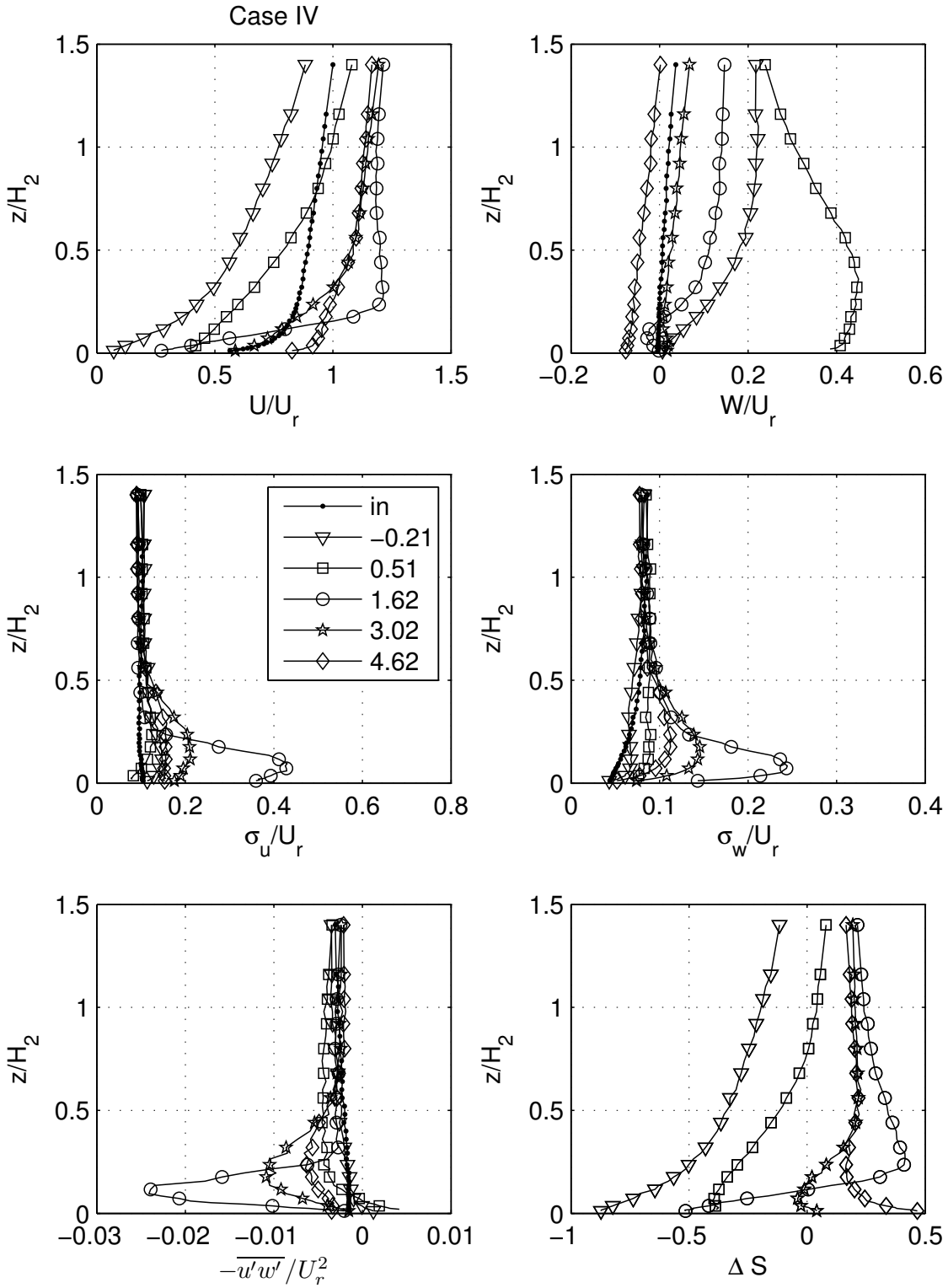

Figure 8.17: The rest of the measured profiles in Case IV. The figure is similar to Figure 8.16.

height of the plateau. The peak longitudinal normal stress is $\sigma_u = 0.3U_r$, which is three times higher than at the same height above ground in the undisturbed inflow. The maximum value of σ_u recorded at any position in Case V is found in the profile half way up the second uphill, $x/H_1 = 7.75$, and attains the value $\sigma_u = 0.38U_r$ at a height which is 10 % below the level of the upstream plateau. The mean velocities at the crest of the second mountain are lower than the undisturbed boundary layer in the lowest region, but this velocity deficit is reduced as the flow develops along the plateau. The separation downstream of the highest mountain causes highly increased levels of turbulence over the second plateau compared to the undisturbed boundary layer. The maximum normal stress at the crest (position $x/H_1 = 8.32$) is $\sigma_u = 0.33U_r$ at the height $z = 0.19H_1$ above ground. The increased turbulence is still present at the end of the plateau ($x/H_1 = 10.89$), even if it has diminished substantially. The maximum value of $\sigma_u = 0.16U_r$ in this position is found at $z = 0.4H_1$ above the surface, which is twice as high above ground as where the maximum value was found at the crest. It is worth noting that the maximum values for stresses occur at elevations where rotor blades might operate, hence increasing the dynamic loads on wind turbines considerably.

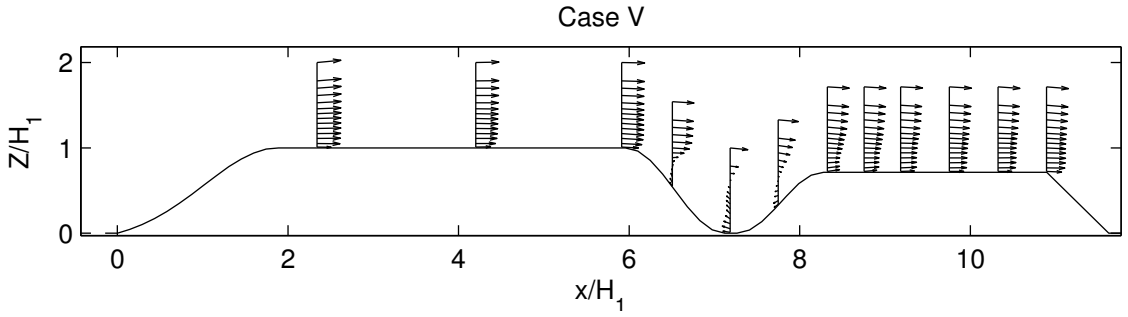

Figure 8.18: Terrain and mean velocity vectors at all measured positions in the xz-plane in Case V.

8.2.6 Case VI

The terrain in Case VI is identical to Case IV followed by Case II, and is shown in Figure 8.21. The effects of this terrain, where the flow passes a lower mountain and a valley before it enters a higher mountain, can be seen in Figures 8.22 and 8.23. Separation at the sharp crest in Case IV was again suspected. To confirm that separation really occurred, a profile was also measured at $\Delta x = 0.136H_1$ downstream of the crest, i.e. half way between the two first measured positions at the plateau in Case IV. Mean streamwise velocities down to about -2.7 m/s were measured closest to the ground, confirming the expected separation. The profile measured at position $x/H_1 = 1.16$ is virtually identical to the profile at this position in Case IV, confirming that the flow above the first part of the combined terrain is similar to Case IV alone. Despite the mountain upstream with separated flow at the start and in the valley, a speed-up effect is seen at all measured heights and positions above

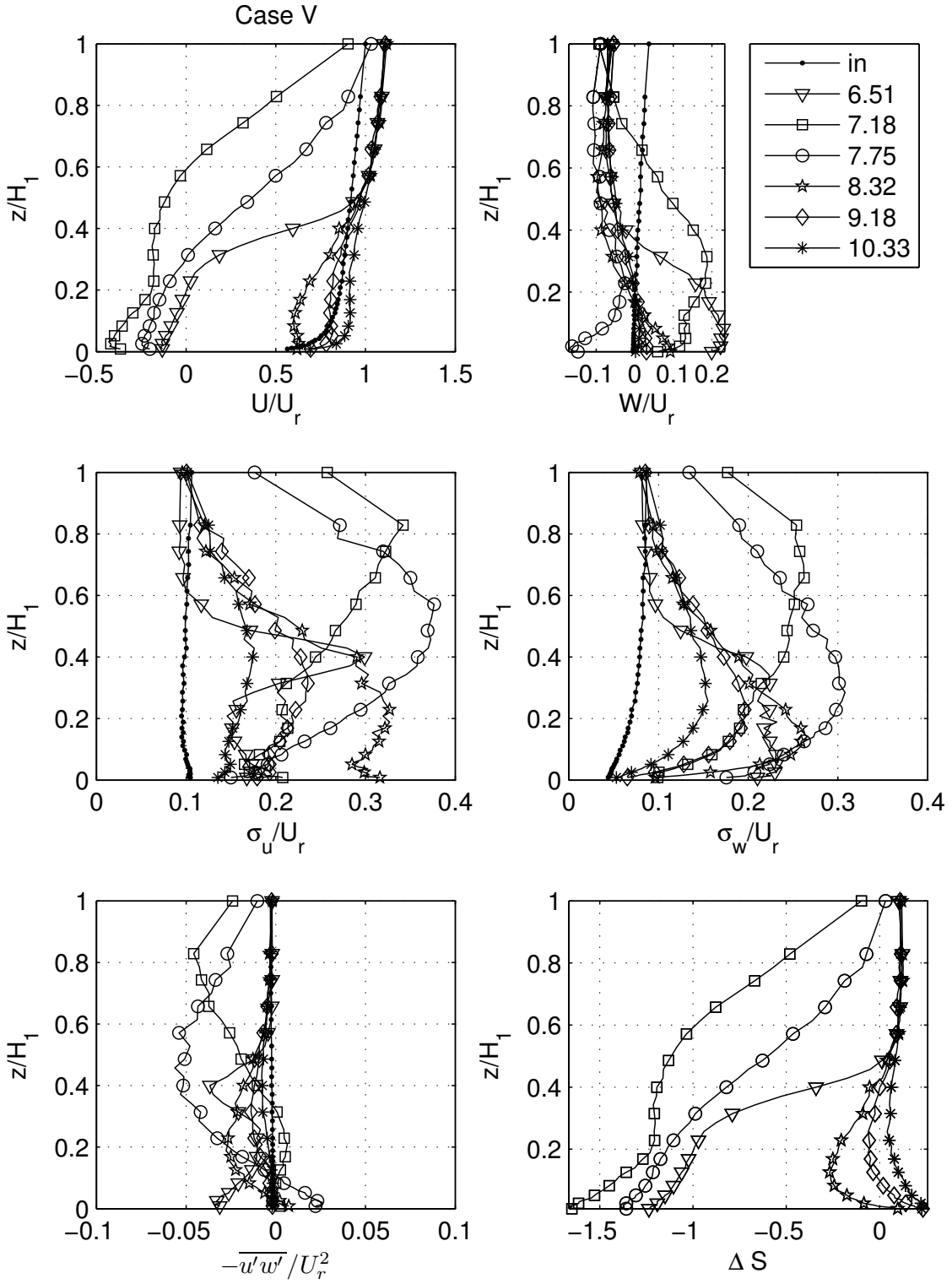

Figure 8.19: Selected profiles of streamwise mean velocity (U/U_r), vertical mean velocity (W/U_r), streamwise normal stress (σ_u/U_r), vertical normal stress (σ_w/U_r), shear stress ($-\overline{u'w'}/U_r^2$), and fractional speed-up ratio (ΔS) in Case V. "in" denotes the undisturbed boundary layer as shown in Figure 8.1. The positions x/H_1 refer to Figure 8.18.

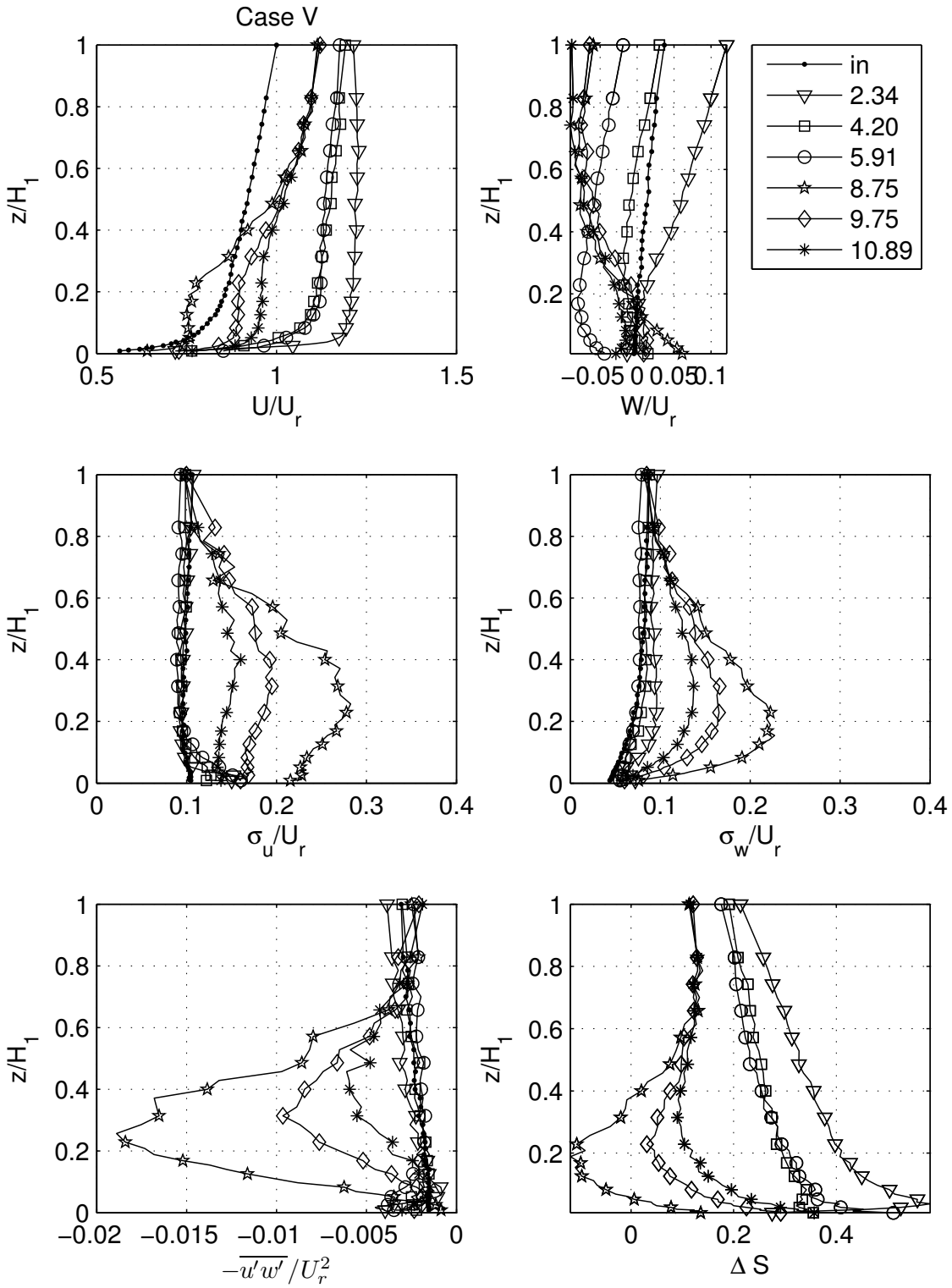

Figure 8.20: The rest of the measured profiles in Case V. The figure is similar to Figure 8.19.

the second and largest mountain. The maximum fractional speed-up ratio above this plateau is about 0.9. Like in isolated cases this maximum value was observed near the ground at the crest.

As in Case V, there is a separation vortex between the mountains, although less substantial in this case due to the reduced height of the upstream plateau. Negative velocities are apparent up to $z = 0.53H_1$ in the profile measured in the centre of the valley ($x/H_1 = 4.44$). Also, the maximum value for the streamwise normal stress half way down the first hill corresponds quite well with the maximum observed in $\frac{\partial U}{\partial z}$. The peak values found in the valley, at the positions $x/H_1 = 3.88$, 4.44 and 5.12, are all about $\sigma_u = 0.28U_r$. In the downhill ($x/H_1 = 3.88$), the maximum value is found at the same level as the upstream plateau. At the bottom of the valley the peak in σ_u occurs at an elevation 10 % higher than the upstream plateau level, while the maximum in the uphill is found at a position which is 20 % higher than the upstream plateau level. This increased height for the maximum stress is due to the fact that the flow passes towards a downstream mountain which is higher than the one upstream. The heights for maximum σ_u in the valley are still located well below the level of the downstream plateau. As a further consequence of this, the maximum value of $\sigma_u = 0.25U_r$ at the very crest of the downstream mountain is found closest to the ground.

Compared to the undisturbed inflow the normal stresses are increased above the entire downstream mountain to an elevation which is at least as high as the upstream mountain. At the very end of the plateau ($x/H_1 = 9.42$) the maximum value of $\sigma_u = 0.15U_r$ is found at $z = 0.66H_1$. Hence the stress decreases significantly and spreads outwards as the flow passes the plateau.

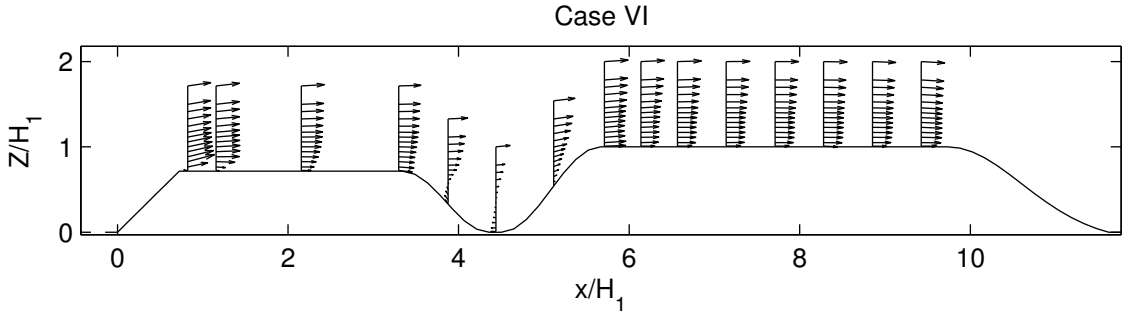

Figure 8.21: Terrain and mean velocity vectors at all measured positions in the xz-plane in Case VI.

8.2.7 Case VII

The terrain and mean velocity vectors in Case VII are shown in Figure 8.24. This is flow above an axisymmetric hill, followed by a depression as deep as 1/3 of the hill, and then an ascending hill followed by a very long plateau with equal hight as the axisymmetric hill. The terrain in this case is three-dimensional. The first hill is

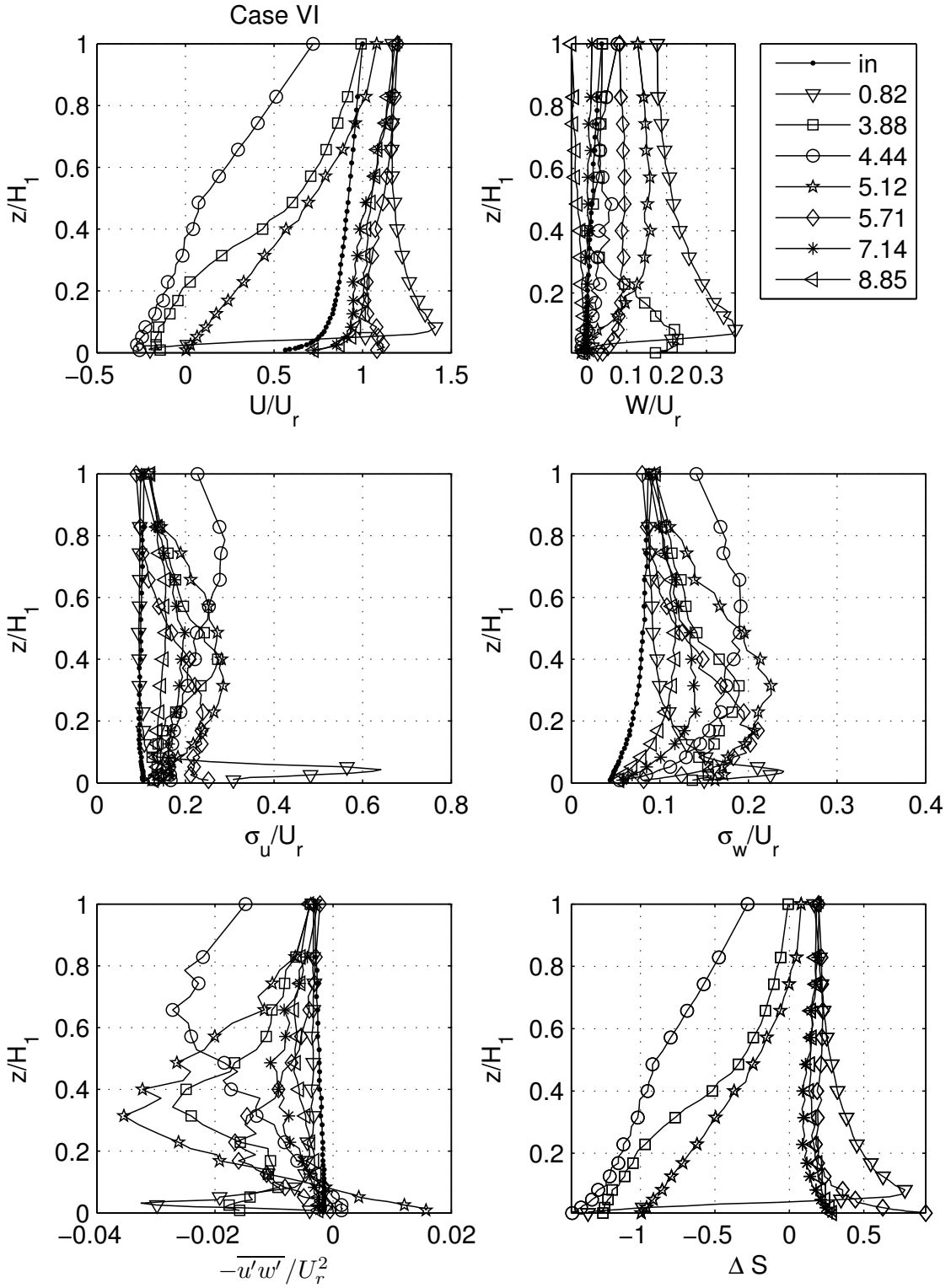

Figure 8.22: Selected profiles of streamwise mean velocity (U/U_r), vertical mean velocity (W/U_r), streamwise normal stress (σ_u/U_r), vertical normal stress (σ_w/U_r), shear stress ($-\overline{u'w'}/U_r^2$), and fractional speed-up ratio (ΔS) in Case VI. "in" denotes the undisturbed boundary layer as shown in Figure 8.1. The positions x/H_1 refer to Figure 8.21.

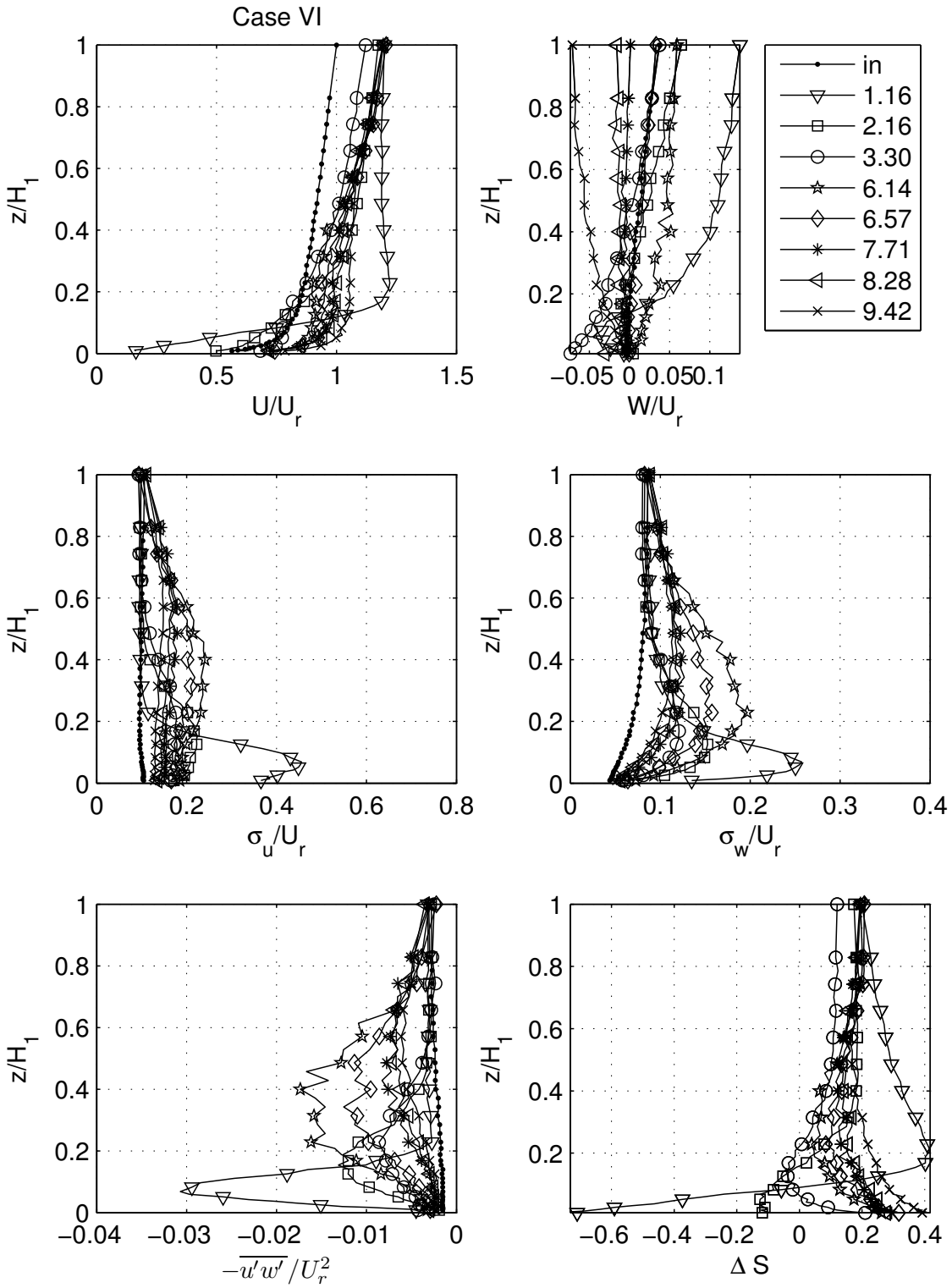

Figure 8.23: The rest of the measured profiles in Case VI. The figure is similar to Figure 8.22.

axisymmetric, but the downstream hill is neither two-dimensional nor axisymmetric, as can be seen from Figure 7.13.

Calculated moments and fractional speed-up ratios are plotted in Figures 8.25 and 8.26. Speed-up is seen above the first hill as expected, with a fractional speed-up ratio of 0.85 near the ground at the crest. The mean slope along the measurement line of this hill is 24.7°, and the maximum slope is 34.6°. A separation occurs in the depression downstream of the first hill. The maximum streamwise standard deviation is seen at the height $z/H_1 \approx 0.1$ above the surface, where the velocity shear is largest, in the position $x/H_1 = 2.71$. This is $Z/H_1 = 0.914$ above the flat ground, hence slightly lower than the top of the axisymmetric hill. Negative velocities are observed up to $z/H_1 = 0.075$ in the centre of the depression ($x/H_1 = 3.02$), and the velocities are reduced compared to the inflow at all heights up to $z/H_1 = 0.5$. Speed-up is also observed at the crest of the large mountain ($x/H_1 = 3.75$), and the maximum fractional speed-up ratio is 1.35. This is actually higher than what was seen above the axisymmetric hill, despite the separation upstream. Like in Case I-III the speed-up effect is present at all heights and positions measured above the plateau, and the fractional speed-up ratio decreases both with height and as the flow passes the plateau. The streamwise normal stress has a peak value in the centre of the depression, but this turbulence decays quickly. Slightly increased streamwise normal stresses were observed near the ground downstream, but these are lower than in the inflow at heights $z/H_1 > 0.2$ above the entire plateau.

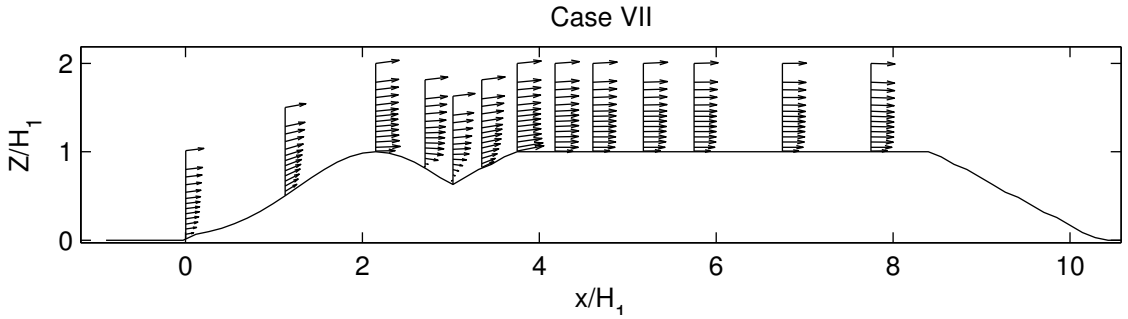

Figure 8.24: Terrain and mean velocity vectors at all measured positions in the xz-plane in Case VII.

8.2.8 Case VIII

The terrain and mean velocity vectors in the streamwise and vertical directions in Case VIII is shown in Figure 8.27. This is the case where the most striking three-dimensional effects can be expected, since the first ridge, the following valley and finally the hill leading up to the plateau are all located with an angle 45 degrees to the main flow direction. The contours of the terrain and the measured positions were shown in Figure 7.13. The LDA equipment used in this investigation can measure the velocity in two directions simultaneously. To acquire all three velocity components,

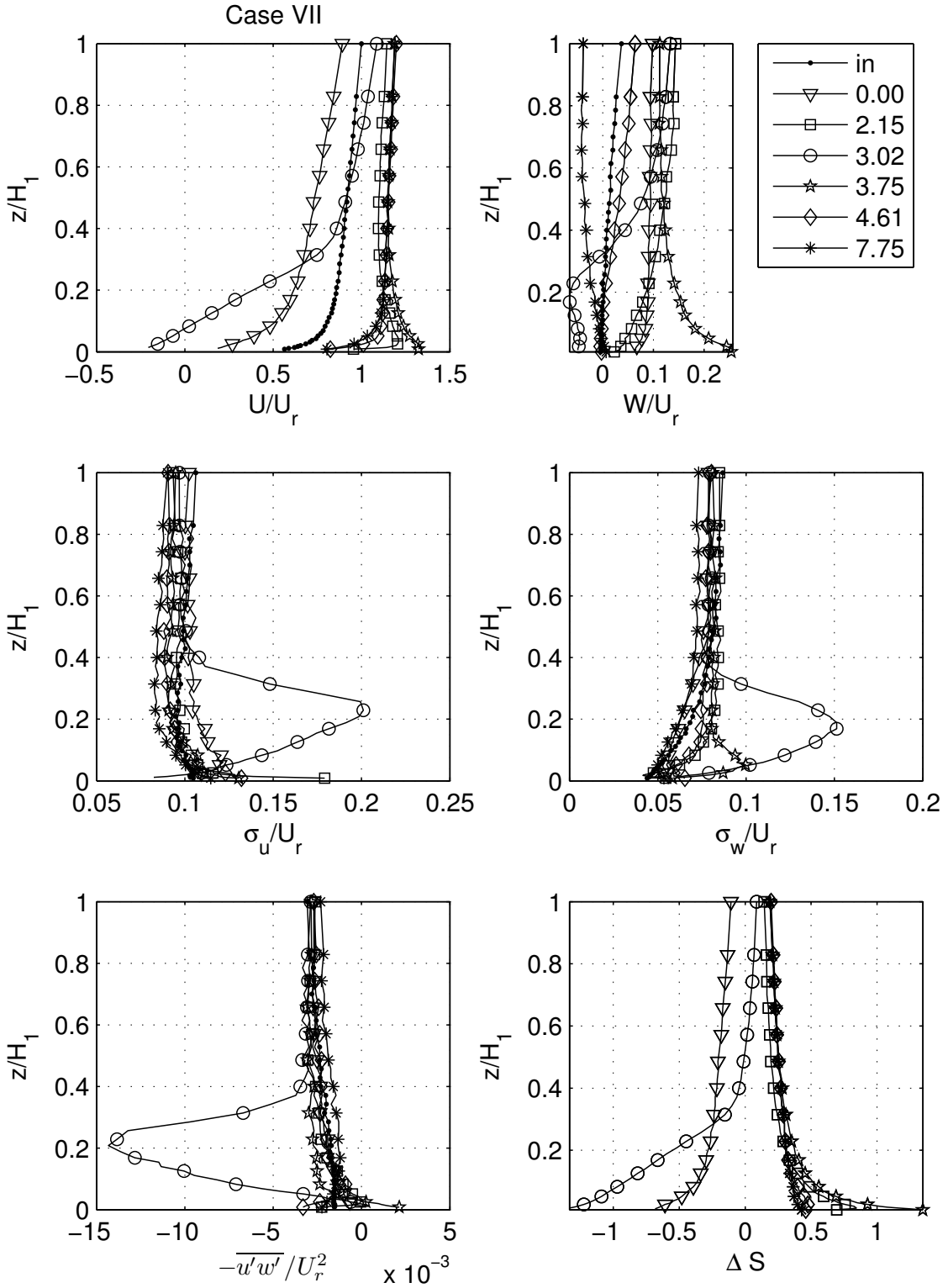

Figure 8.25: Selected profiles of streamwise mean velocity (U/U_r), vertical mean velocity (W/U_r), streamwise normal stress (σ_u/U_r), vertical normal stress (σ_w/U_r), shear stress ($-\overline{u'w'}/U_r^2$), and fractional speed-up ratio (ΔS) in Case VII. "in" denotes the undisturbed boundary layer as shown in Figure 8.1. The positions x/H_1 refer to Figure 8.24.

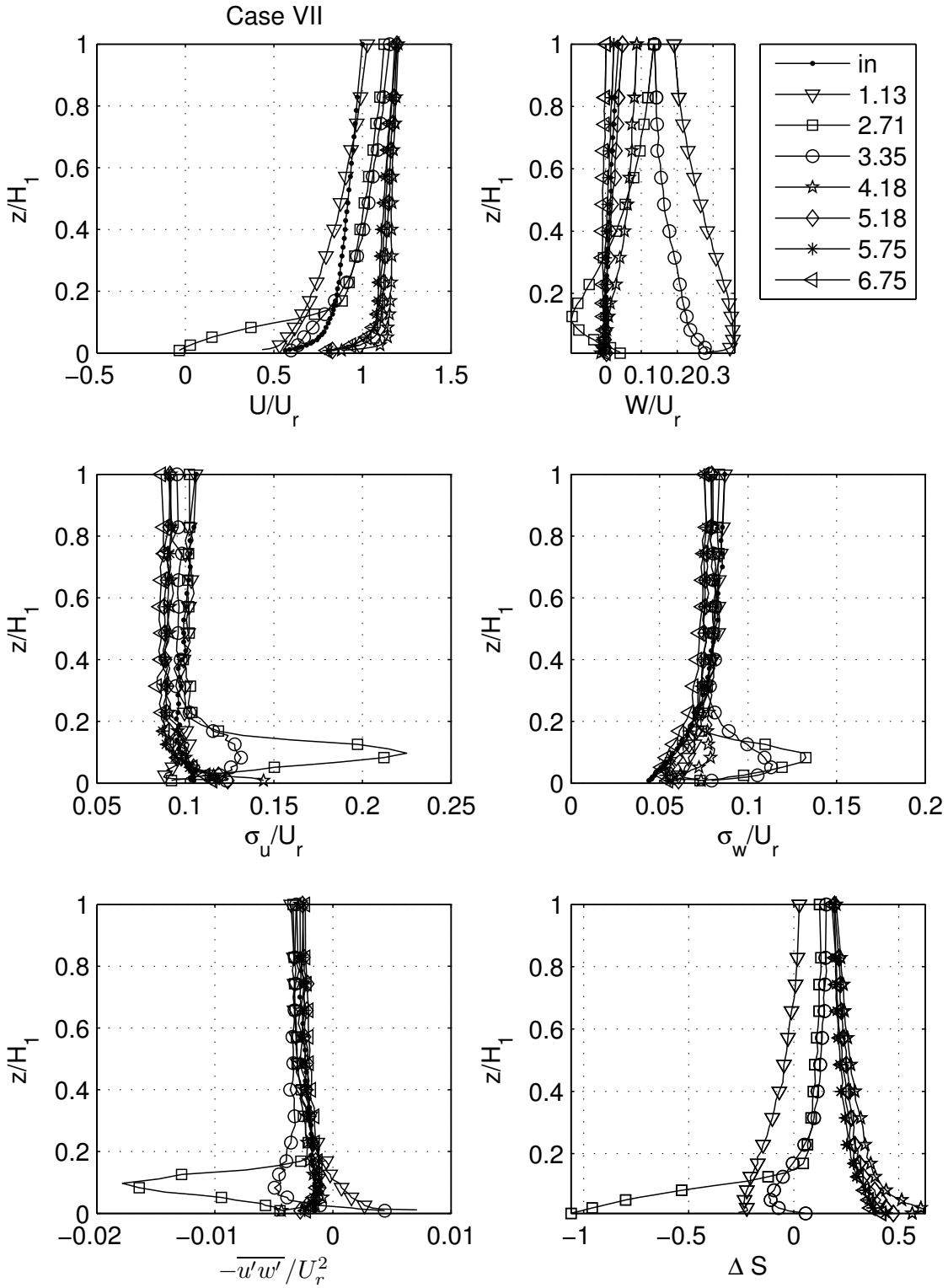

Figure 8.26: The rest of the measured profiles in Case VII. The figure is similar to Figure 8.25.

measurements were obtained twice in the same positions with the probe facing the flow from a side and from above. Hence, the streamwise velocity component shown in different plots for Case VIII is not always from the same series of measurement. A comparison can be done to confirm equal flow during the experiment for these profiles where one of the components has been measured twice. Similar results also indicates that the positions of the measurement volumes were approximately equal. The discrepancies between the same velocity component measured from two different sides were seen to be small.

All three velocity components were measured at seven positions in the area near the valley and the second crest. As discussed above, only two of the three components were measured simultaneously in each position. A part of the terrain in Case VIII and the three-dimensional mean velocity profiles are shown in Figure 8.28. The main flow direction is approximately equal to the direction of the vectors above the plateau, i.e. approaching from the lower left corner of the figure. It is clearly seen that the flow is forced along the valley near the ground, so the x- and y-component of the mean velocity are of the same order in the lowest part of the profile. A simple experiment was done to visualize the flow in this region. Fog was inserted to the valley through a hole in the floor, and it was not captioned in a stretched vortex along the valley as could be expected. It simply illustrated the reversed flow up the lee side of the first ridge combined with positive spanwise velocities, before it gradually turned into the main flow direction further up. The flow then continued following the main flow near the ground above the plateau, but without a significant spanwise velocity component.

Figure 8.29 gives an overview of the mean velocities (U, V, W) and standard deviations $(\sigma_u, \sigma_v, \sigma_w)$ in the positions were all the three velocity components were measured. In position $x/H_2 = 3.26$, which is in the centre of the valley, V is actually larger than U from the ground and up to $z/H_2 = 0.32$. The ridge upstream of the measured position has a height of $0.48H_2$. The velocities are easier to understand if seen in a coordinate system with one mean velocity component parallel to the valley (V'), and one mean velocity component normal to the ridge (U'). Closest to the ground in position $x/H_2 = 3.26$ $V' \approx 10\ m/s$ and $U' \approx -5\ m/s$. The mean velocities in position $x/H_2 = 3.26$ can be divided into three regions dependent on height, where the influence of the terrain is of different degrees of importance. Separation is present at the lowest part, and V is larger than U. The upper part is where the flow is no longer significantly effected by the valley, hence U is large and V is close to zero. This upper part starts at $z/H_2 = 0.6$, which is above the height of the ridge with height $0.48H_2$ causing the separation. The turbulence in the streamwise and spanwise direction is approximately equal at all heights, despite the large differences in the mean values. The middle part is a transition region, where U goes from low to high values while V does the opposite. These mean values cross at $z/H_2 = 0.32$, which is the top of the region with flow parallel to the valley.

Figures 8.30 and 8.31 shows calculated moments and fractional speed-up ratios in the xz-plane for 11 measured positions. The mean velocity in the streamwise direction, U, displays a speed-up near both the first and second crest ($x/H_2 = 2.09$ and $x/H_2 = 5.42$). The maximum values are $\Delta S = 0.25$ and $\Delta S = 0.45$

over respectively the first and second crest, which is quite low compared to speed-ups observed in the other cases with rounded crests. The highest speed-ups were observed closest to the ground. The fractional speed-up ratio found in position $x/H_2 = 6.02$ has a maximum value of $\Delta S = 0.28$. This maximum is not found closest to the ground, but slightly higher. Above the rest of the plateau the observed values of the fractional speed-up ratio are in the range 0.05-0.2. The maximum value in many of these positions are also found some higher than the lowest measurement point. This might be a consequence of the generated vortex in the valley upstream the plateau, which causes a spanwise velocity-component near the ground above the first part of the plateau.

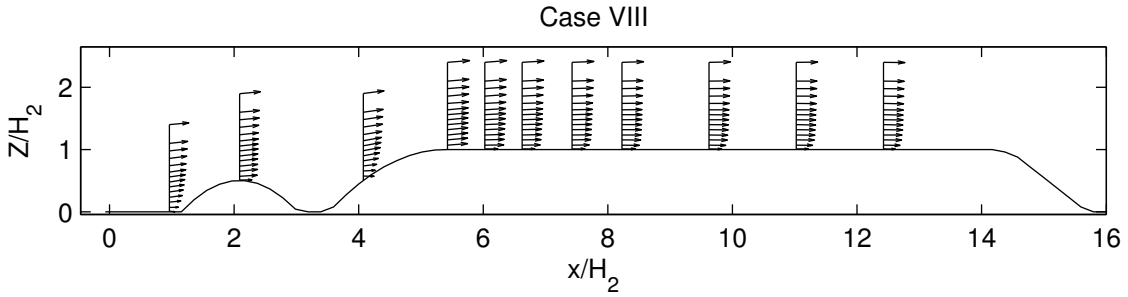

Figure 8.27: Terrain and mean velocity vectors in the xz-plane in Case VIII.

8.2.9 Case IXa

The measured positions in Case IX lies along a line normal to a ridge of height 125 mm. Close and parallel to this ridge is another ridge twice as high as the first one. The ridges are followed by a large valley and a three-dimensional hill leading up a to a plateau of height 350 mm. The terrain and mean velocity vectors in the xz-plane can be seen in Figure 8.32, and the terrain and measured positions are shown from above in Figure 8.33. Results for calculated moments and fractional speed-up ratio at all positions are plotted in Figures 8.34 and 8.35.

Separation occur downhill of both ridges, and the separation bubbles are seen most clearly in Figure 8.32. The shape of the resulting profiles of mean velocities and stresses in the separated flow regions are quite similar at corresponding positions near the two ridges, like half-way down the lee side of the ridges. Since the second ridge is twice as high as the first, the region of separation is naturally also more extended and the level of turbulence higher compared to the lower ridge. The peak of the streamwise normal stress half-way down the lee side of the first ridge is $\sigma_u/U_r = 0.26$ at $z/H_1 = 0.19$ above ground, while it is $\sigma_u/U_r = 0.38$ at $z/H_1 = 0.3$ above the second ridge. Hence, both the strength of turbulence and height where this occurs is about 50 % higher for the second ridge. The height of zero velocity and maximum streamwise normal stress in the valley (positions $x/H_1 = 1.03$ and $x/H_1 = 3.29$) also occur at heights about 50 % higher for the second and largest ridge compared to the first ridge.

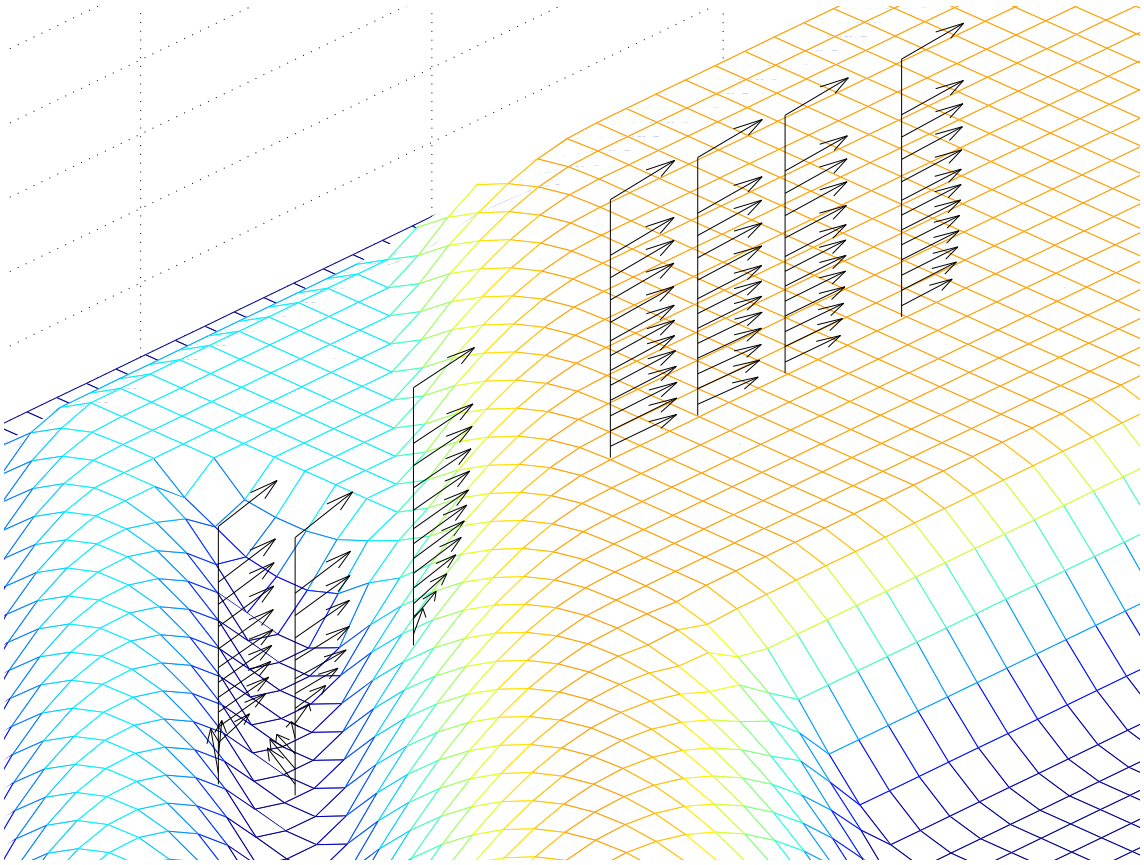

Figure 8.28: Mean velocity profiles (3D) at selected heights above a part of the terrain in Case VIII. Positions from left to right are $x/H_2 = 2.73, 3.26, 4.07, 5.42, 6.02, 6.62$ and 7.42.

The normal stresses, σ_u, in the streamwise direction in the second valley are also very large compared to the undisturbed boundary layer. The maximum values in the profile downhill the second ridge ($x/H_1 = 2.88$), and at the two positions in the following valley ($x/H_1 = 3.29$ and $x/H_1 = 3.70$) are four times larger than the corresponding values at the same heights in the inflow. The values of σ_u at the crest of the mountain range from twice as high as in the inflow closest to the ground, to values about the same size as in the inflow at the height H_1 above the surface. The increased values at the beginning of the plateau also gradually decay to values similar to those in the inflow at the end of the plateau, which is four hill heights downstream of the crest.

The vertical velocities downstream of the first ridge increases strikingly at height levels more than $0.3H_1$ above flat ground. The flow is quickly driven over the second ridge since the valley in between the ridges is quite narrow. This is not the case at such low heights downstream of the second ridge, since the following valley is much broader. On the contrary, negative vertical mean velocities are seen in this second valley. The vertical mean velocities are negative at all measured levels above $z/H_1 = 0.04$ in position $x/H_1 = 3.70$. Streamwise mean velocities at positions

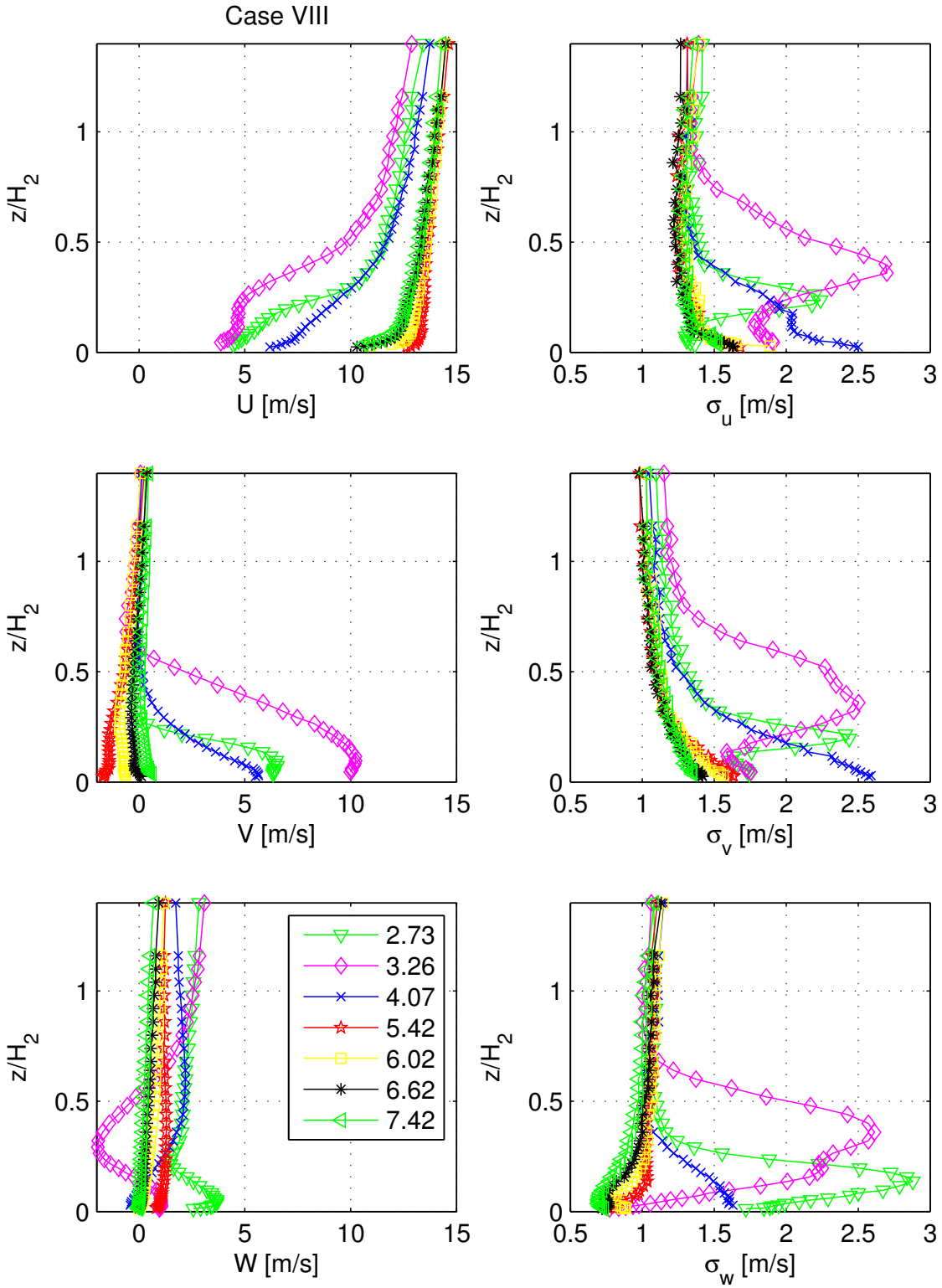

Figure 8.29: Mean velocity and standard deviation for all three velocity components in some positions in Case VIII.

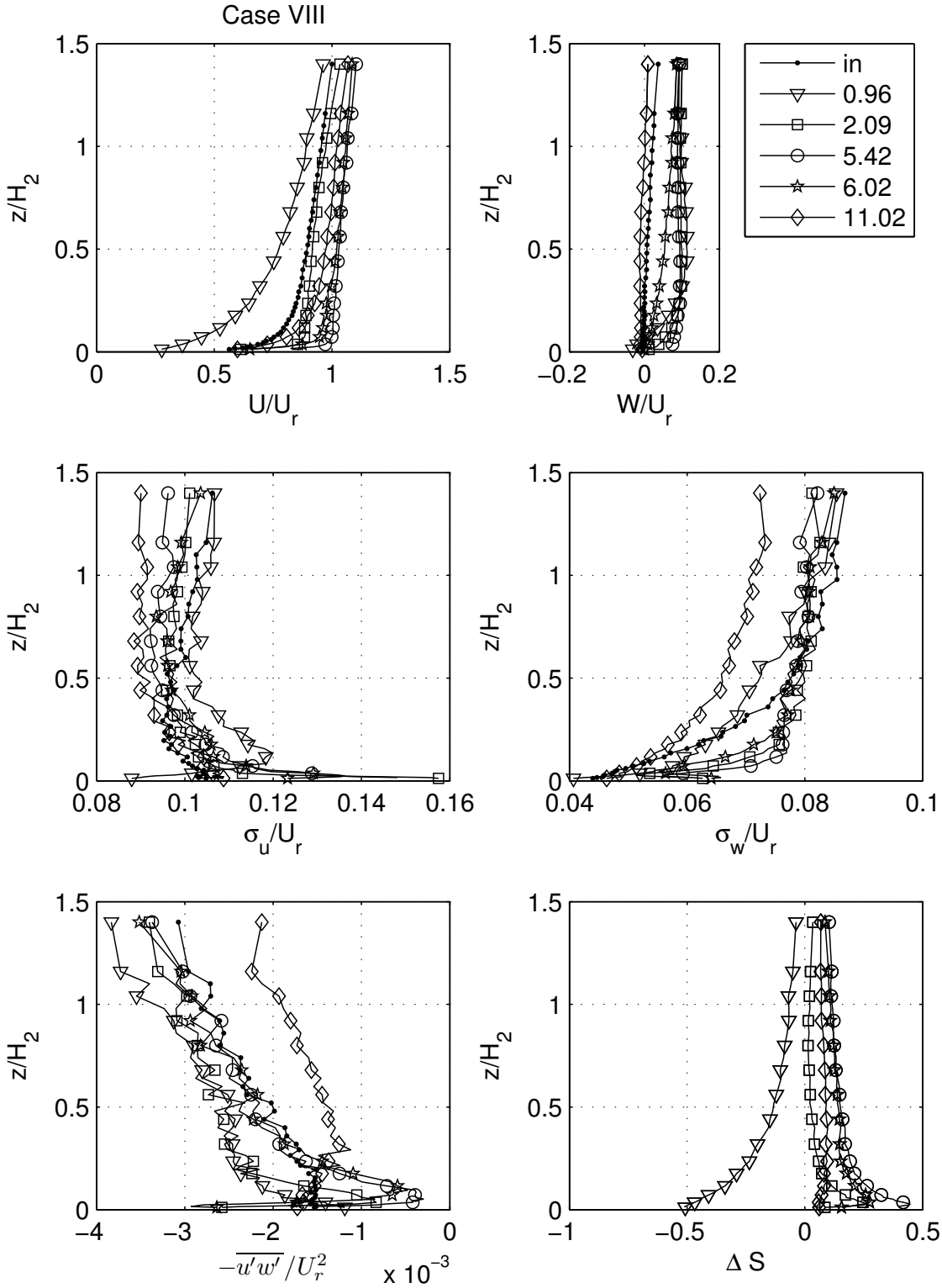

Figure 8.30: Selected profiles of streamwise mean velocity (U/U_r), vertical mean velocity (W/U_r), streamwise normal stress (σ_u/U_r), vertical normal stress (σ_w/U_r), shear stress ($-\overline{u'w'}/U_r^2$), and fractional speed-up ratio (ΔS) in Case VIII. "in" denotes the undisturbed boundary layer as shown in Figure 8.1. The positions x/H_2 refer to Figure 8.27.

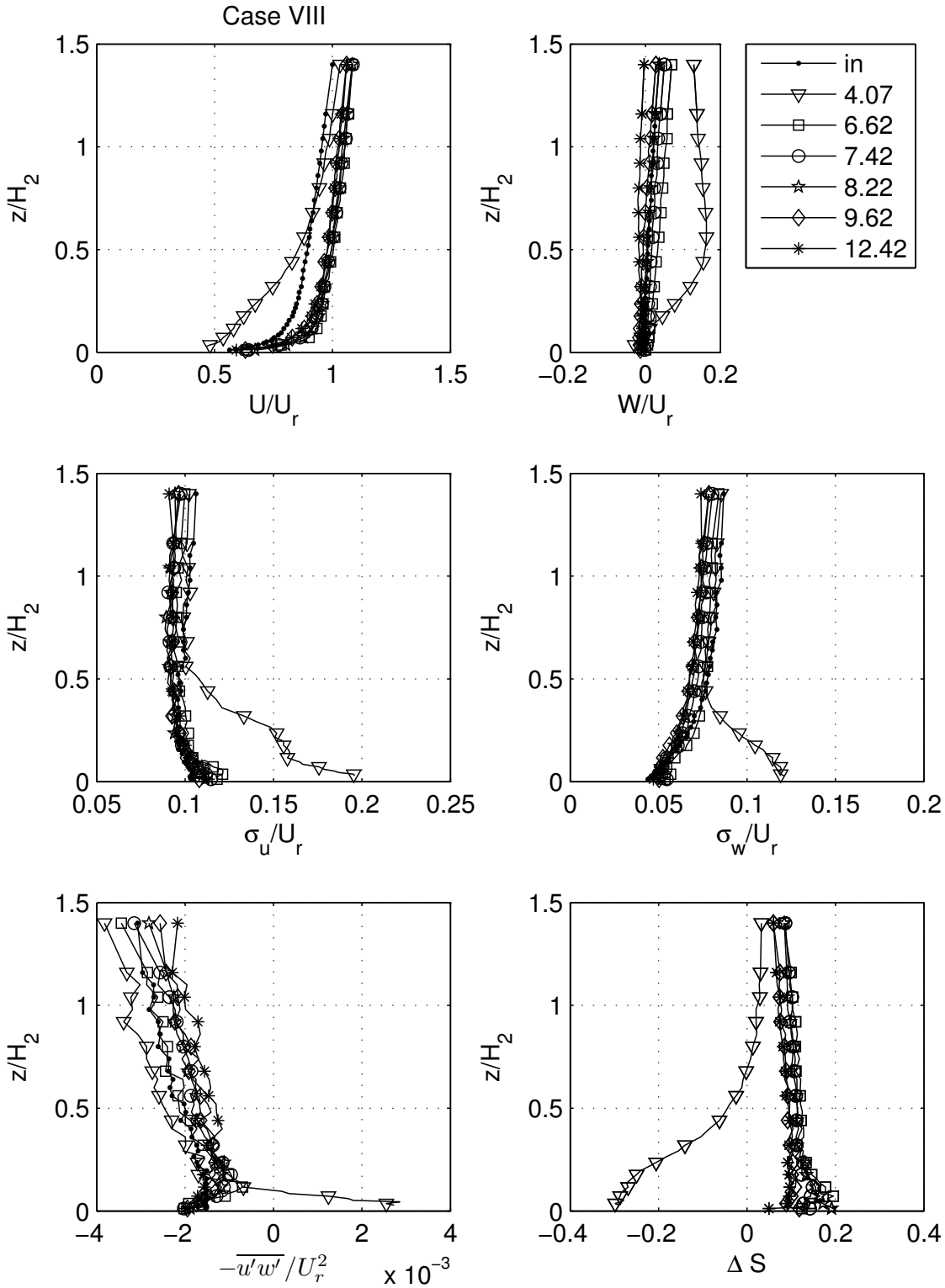

Figure 8.31: The rest of the measured profiles in Case VIII. The figure is similar to Figure 8.30.

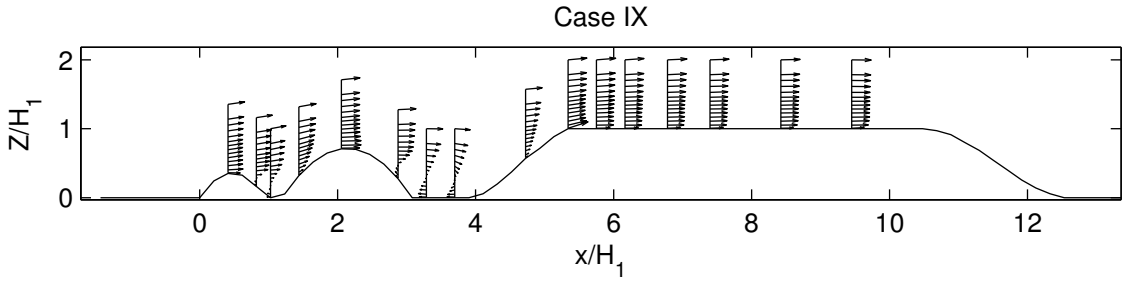

Figure 8.32: Terrain and mean velocity vectors at all measured positions in the xz-plane in Case IX.

$x/H_1 = 3.29$ and $x/H_1 = 3.70$ are negative up to about $z/H_1 = 0.5$. Positive vertical mean velocities are observed as expected at the crest, but also to some degree above the first part of the plateau. The flow is approximately parallel with the surface above the trailing half of the plateau.

Speed-up occur at the crest of both ridges, and the largest speed-up was observed at the second ridge, despite the valley upstream. Hence, the effect of the upstream ridge with the resulting separated flow is not significant at the second ridge, since the first ridge is only half the height as the second. At the very crest of the mountain ($x/H_1 = 5.34$) the fractional speed-up ratio is 1.2 closest to the ground, but has decayed to 0.3 already at the height $z/H_1 = 0.14$. The fractional speed-up ratio at all positions and all heights measured above the plateau downstream of the crest are in the range $0.2 - 0.5$.

Similar to in Case VIII all three velocity components were measured at some selected positions. The results are shown in Figure 8.36. The spanwise mean velocity, V, indicates a slightly turning of the flow to the left (positive V) compared to the inflow near the base of the mountain (position $x/H_1 = 3.70$). The flow at the crest of the mountain is approximately parallel to the walls in the test section, as in the undisturbed incoming boundary layer. Four hill heights downstream of the crest the flow has turned slightly further to the right (negative V). The reason for this is not clear, but most likely it is due to the complex valley and horizontally curved uphill upstream. A comparison of U measured with the probe facing the flow from the side (U_{side}) and from above (U_{above}) shows approximately similar results. The mean absolute error of the deviation between U_{side} and U_{above} in position $x/H_1 = 3.70$ is $0.58\ m/s$, while the mean absolute errors are $0.17\ m/s$ both in position $x/H_1 = 5.34$ and $x/H_1 = 9.45$ above the plateau. This indicates that the negative spanwise mean velocities at the end of the plateau is not due to a misaligned probe. The differences in the valley is probably higher due to the more complex flow in this region, with separation and increased turbulence levels. This complicates accurate measurements. The probe will be more unsteady, which affects both the measurements and the position of the measurement volume.

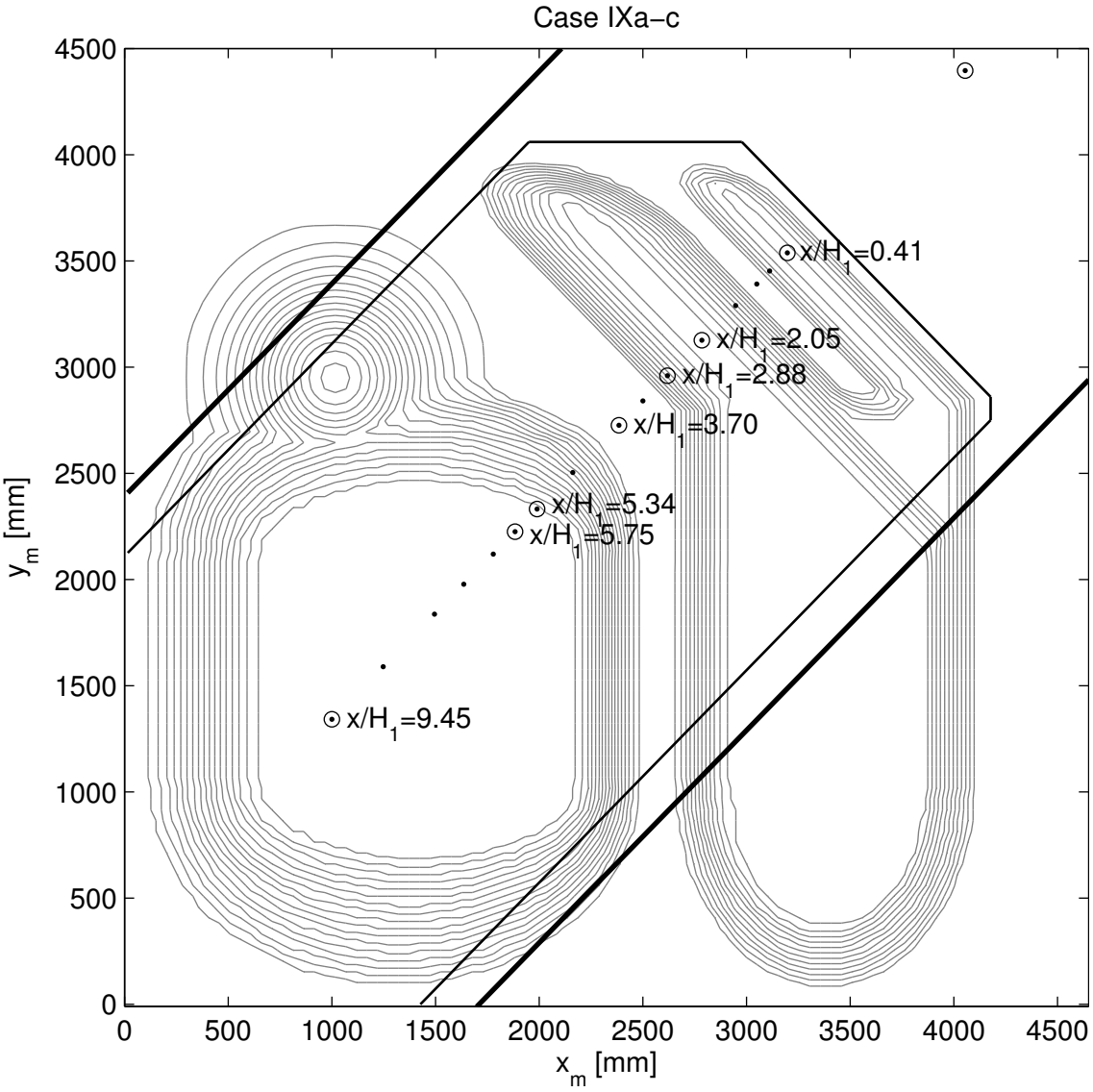

Figure 8.33: The thick black lines are the tunnel walls, the thin black lines surround the part of the terrain constituting Case IX, the black dots are the measured positions in Case IXa, and the dots with circles around are the positions which were measured for all the three roughness variants (Case IXa-c). The flow direction is from right to left, hence with decreasing x_m.

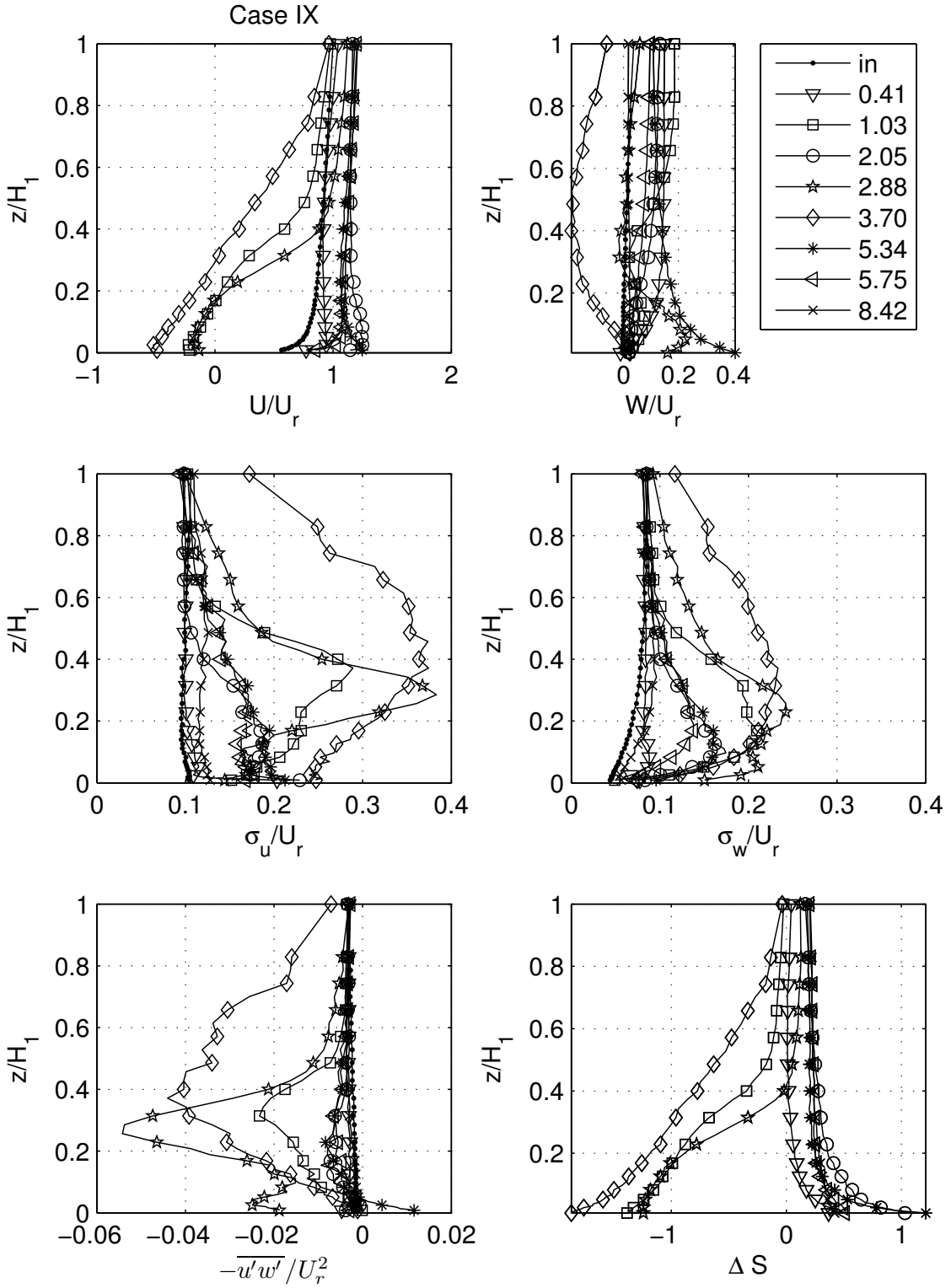

Figure 8.34: Selected profiles of streamwise mean velocity (U/U_r), vertical mean velocity (W/U_r), streamwise normal stress (σ_u/U_r), vertical normal stress (σ_w/U_r), shear stress ($-\overline{u'w'}/U_r^2$), and fractional speed-up ratio (ΔS) in Case IX. "in" denotes the undisturbed boundary layer as shown in Figure 8.1. The positions x/H_1 refer to Figure 8.32.

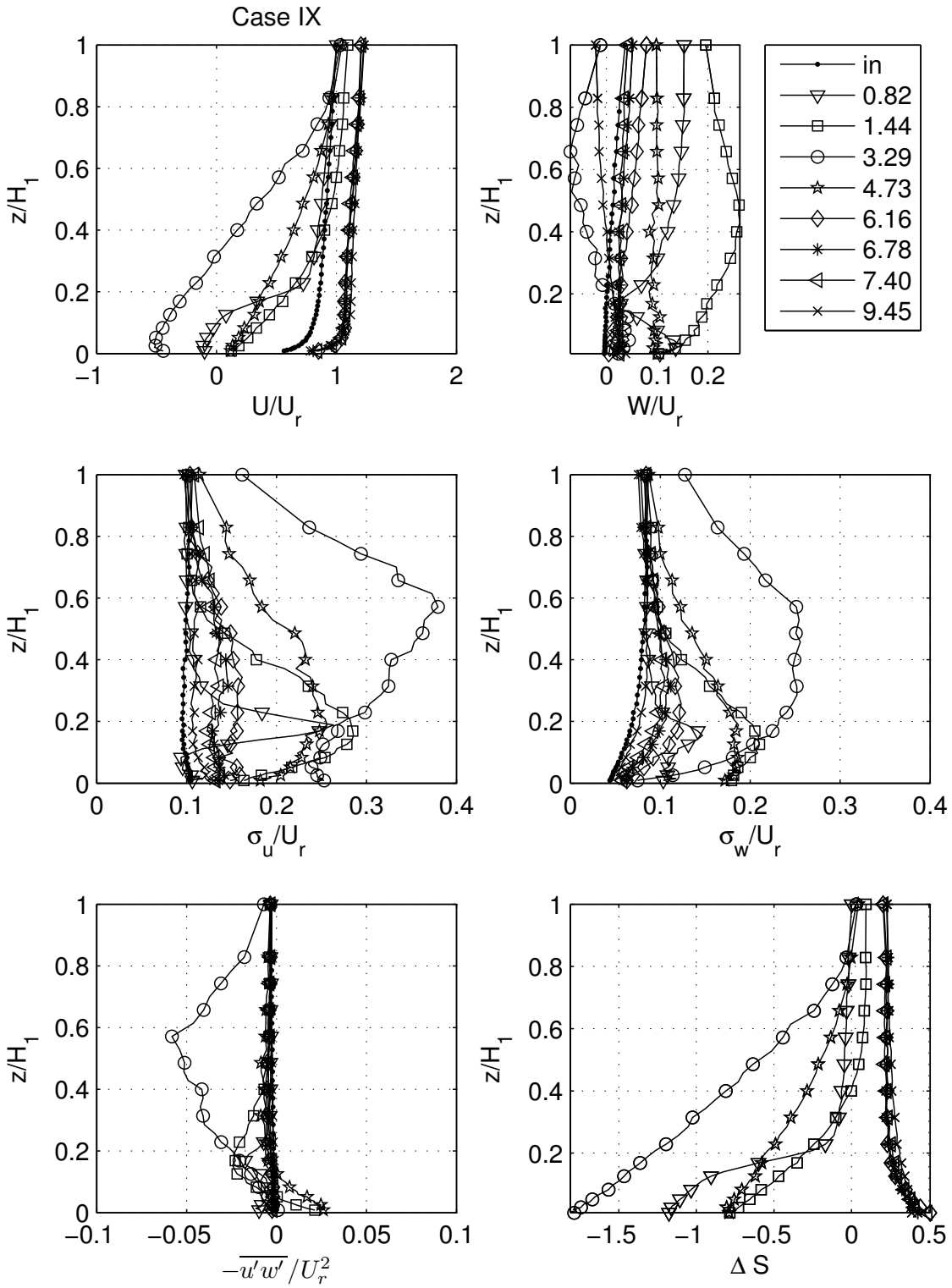

Figure 8.35: The rest of the measured profiles in Case IX. The figure is similar to Figure 8.34.

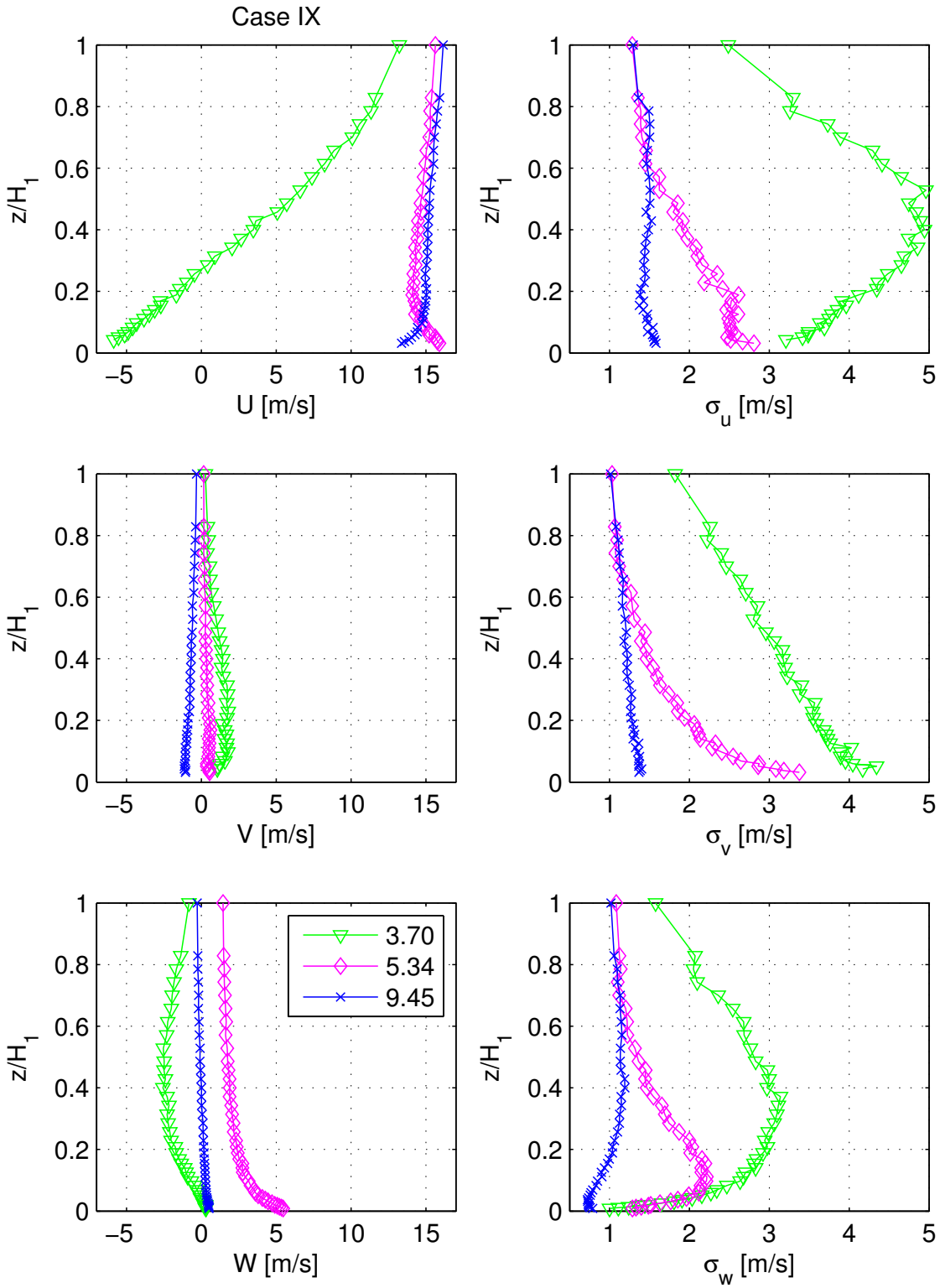

Figure 8.36: Mean velocities and standard deviations for all three velocity components for some positions in Case IXa.

8.3 Speed-up; Case I-III

Case I-III were designed to study the effects of slope angle. The hills were made with slightly different average slope angles, and the slopes start and end with a mild curvature before the flow enters the elevated plateau. For Case I the maximum slope angle is 37.3°, which is increased to 52.8° in Case II. The lower model in Case III ($H_2 = 250\ m$ versus $H_1 = 350\ m$ in Case I-II) has the same type of slope, with a maximum angle of 46.1°. The fractional speed-up ratios at three positions in each case are compared in Figure 8.37. The selected positions are approximately the same number of hill heights downstream of the crest. The hills in Case I-III are also shown in this figure.

The maximum fractional speed-up ratios at the very crests increase with increasing slope angles, and attain the values 1.02 (Case I), 1.35 (Case III) and 1.47 (Case II) near the ground. The fractional speed-up ratios above the crests in Case I-III are approximately equal at all measured levels above $z/H = 0.02$. The values downstream of the crest of the most gentle hill (Case I) and the steepest hill (Case II) are still very similar at the positions $x/H = 0.4$ and $x/H = 3.7$. Case III differs more and more from the two other cases as the flow passes along the plateau, with lower fractional speed-up ratio, despite that the slope in this case is in between the two other cases. The most significant difference between the terrain in Case II and the two others, is that the plateau in Case II is 250 m while it is 350 m in Case I and II. Also, the length of the plateau in Case I and II is 55 % longer than the plateau in Case III. The terrain in Case I and II occupies a larger part of the tunnel cross-section, so a part of the difference in speed-up occurring downstream of the crest might be caused by blocking. The terrain occupies 15 % of the tunnel cross-section in Case I and II, compared to 11.5 % in Case III. The extra blocking of 4.5 % is not enough to be the only explanation for the higher speed-up in Case I and II compared to Case III. A very simple calculation based on the principle of continuity, $u_1 A_1 = u_2 A_2$, was done to verify this. If it is assumed that the flow with the entire tunnel area (A_1) available is undisturbed, while the velocity above the model (u_2) with the area $A_2 = A_1 - A_{model}$ available is influenced by blocking, the velocities corrected for increased velocity due to blocking are $u_1 = u_2(1 - A_{model}/A_1)$. Hence, the mean velocities above the plateau of 350 m were decreased by a factor $1 - 0.15 = 0.85$, while the mean velocities above the plateau of 250 m were decreased by a factor $1 - 0.115 = 0.885$. The results implied that blocking is not the only answer to the diversity. At the position $x/H \approx 3.6 - 3.7$ the corrected velocities above the lowest plateau were still significantly lower than above the highest plateau outwards to $z/H = 0.6$. However, it is important to notice that this is a very simple approach. It corrects velocities at all heights by the same factor and does not consider the interaction with the boundary layer influenced by the terrain. Another factor which also excludes blocking as the main explanation, is that the difference in fractional speed-up ratio between the cases is largest near the terrain and decays outwards. It is expected that the effects of the terrain dominates closest to surface, while the effects of blocking are more conspicuous further away from the surface. Another significant difference between the fractional speed-up ratio in Case

III and Case I-II, is that the maximum values are observed higher above ground in Case III in the position $3.6H$ downstream of the crest.

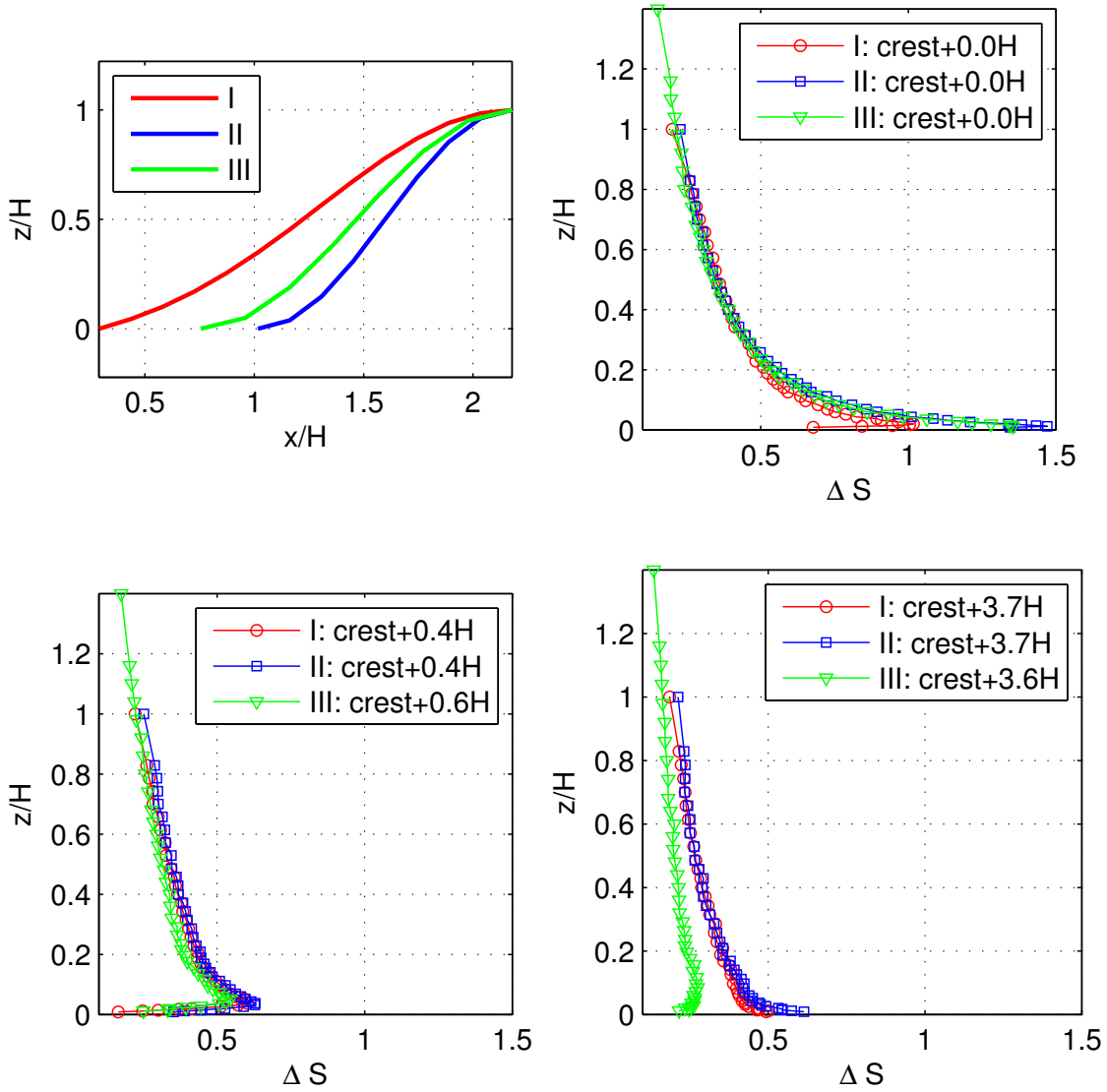

Figure 8.37: A comparison of the slopes and the fractional speed-up ratio at three different positions above the plateaus in Case I-III. The streamwise positions are given as distance from the crest. H_1 has been used to normalize Case I-II and H_2 is used for Case III.

8.4 Effect of rounded and sharp edge; Case III versus Case IV

The maximum slope in Case III occurs about half way up the hill and is 46.1°. This slope is quite similar to the angle of the straight hill in Case IV (44.5°), and

the similarity between the hills is illustrated in Figure 8.38. Case IV is identical to the terrain in Case III reversed, so the lengths and heights of the plateaus are equal. Hence, the main difference between these cases is that the base and crest are rounded in Case III while sharp in Case IV. The effect of this diversity is clearly seen in Figure 8.39. Wind turbines are also shown in the figure. The height of the mountain is 250 m in absolute numbers, and the drawn wind turbine rotor is in the range 30-140 meters above ground. A diameter of 110 m is a bit large compared to typical onshore turbines today. Moreover, this drawn turbine is supposed to illustrate typical heights which modern wind turbines ($2-3.5\ MW$) operates within.

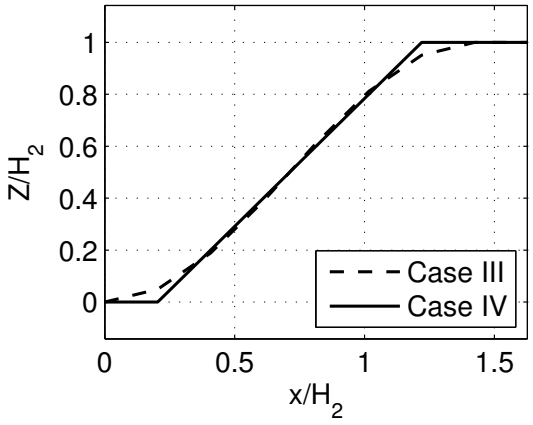

Figure 8.38: The hills in Case III and IV. The rounded hill has a mean slope of 35° and a maximum slope of 46.1°, while the straight side has a slope of 44.5°.

The profile of the fractional speed-up ratios at the crests are very similar in Case III and IV. Also, the maximum value in both cases is about 1.4 and observed closest to the ground. There is no measured separation upstream of the crests, and the flow does not seem to depend on the detailed shape of the hill at this position. However, a separation occurs right downstream of the crest in Case IV (this was confirmed as described in Section 8.2.6), and the effect of this dominates the flow field above the entire plateau. There is no separation downstream of the rounded crest in Case III, and this results in wind conditions which are more favorable for wind turbines as discussed in Section 8.2.3.

The fractional speed-up ratio 0.6 hill heights downstream of the sharp crest is severely reduced compared to at the very crest below $z/H_2 = 0.26$, but it is actually similar to the values observed at the crest above $z/H_2 = 0.26$. The flow at the corresponding position downstream of the rounded crest has a reduced speed-up compared to at the crest up to twice this height. Anyway, there is no doubt that Case III is more advantageous in the context of wind power than Case IV. While both the turbulence and the wind shear (see Section 8.2.3 and 8.2.4) are quite constant across the rotor area in Case III, large variations are seen across the rotor area in Case IV. The variations with height are also quite constant as the flow passes the plateau in Case III. The variations decay as the flow passes the plateau in Case

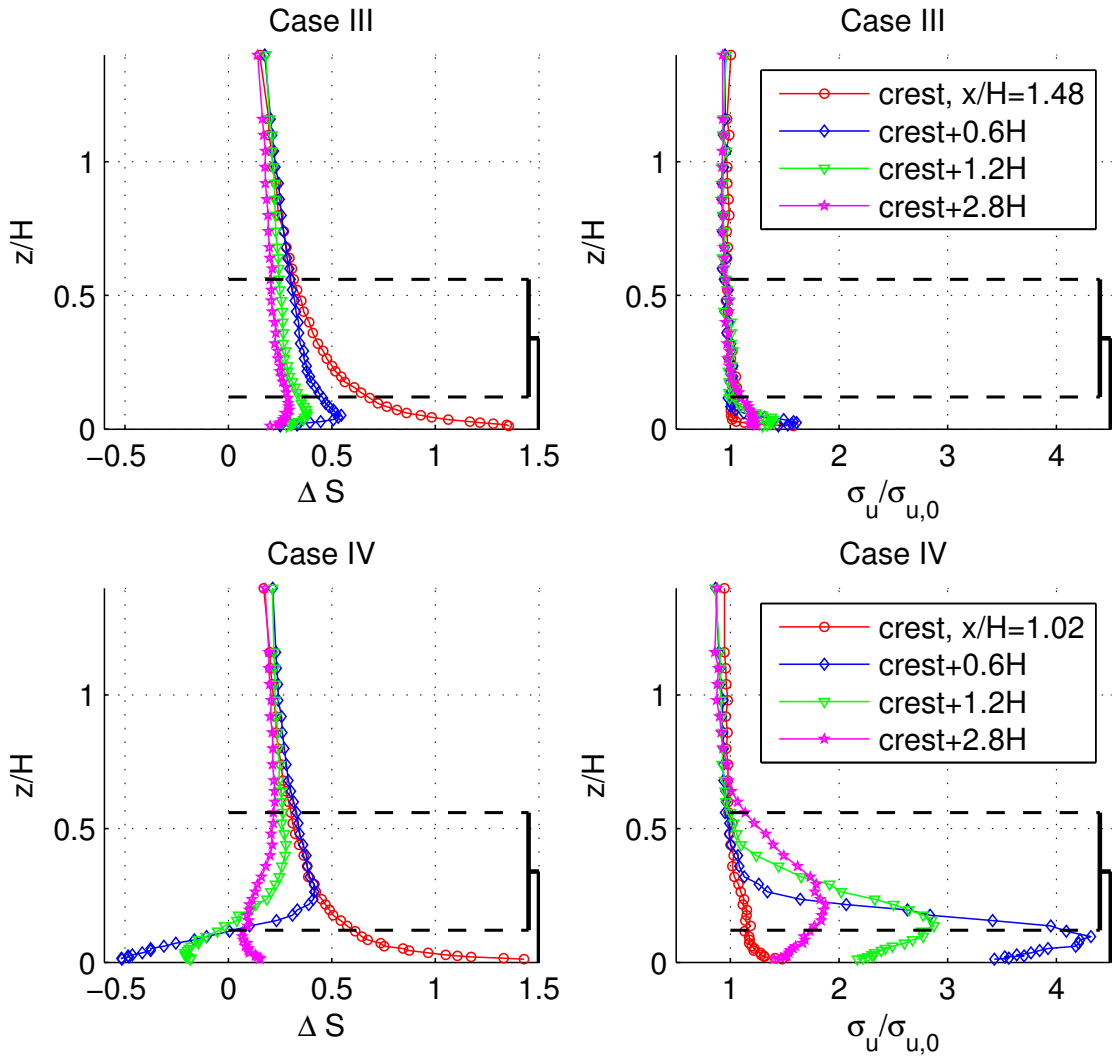

Figure 8.39: The fractional speed-up ratios and streamwise standard deviations at four selected positions in Case III and IV. The turbulence is normalized with the streamwise standard deviation in the undisturbed boundary layer (see Figure 8.1). H is the height of the plateau in Case III and IV, $H_2 = 250\ m$. The axis are identical for Case III and IV for comparison purposes.

IV, but at the same time the fluctuations spread outwards and affects an even larger part of the rotor area.

8.5 Consequence of large terrain features nearby; Case V-VI

The fractional speed-up ratio at three positions above an isolated mountain (Case IV) and above the same mountain with a larger mountain downstream (Case VI)

are compared in Figure 8.40. As commented on in Section 8.2.6 the flow in position $x/H_2 = 1.62$ (coordinates as in Case IV) at the start of the plateau is not affected by the mountain downstream. Deviations between Case IV and VI found below $z/H_2 = 0.2$ in this position are most probably not a consequence of the topography. These deviations are more likely caused by other factors, such as probe alignment, in this region with quickly varying flow conditions. The mean velocities in position $x/H_2 = 3.02$, which is about the centre of the first plateau, are slightly reduced compared to Case IV. This trend is continued to position $x/H_2 = 4.62$, which is at the very end of the first plateau. The deviations between Case IV and VI are quite large in this position, with reduced mean velocities at all measured heights in Case VI. Hence, it is clear that the flow above the first mountain in Case VI is variably effected by the downstream mountain. The flow above the start of the plateau of length $3.66H_2$ is similar to that of the isolated mountain. At the centre of the plateau a slight effect of the terrain downstream is seen, while the flow at the very end of the plateau is significantly affected by the larger mountain downstream. A similar trend can also be seen for the streamwise standard deviations, although less distinct, and with increasing values for Case VI. Only two corresponding positions were measured above the isolated mountain in Case I and the first mountain in Case V. Some small deviations were seen, but not a clear trend as described for Case IV and VI.

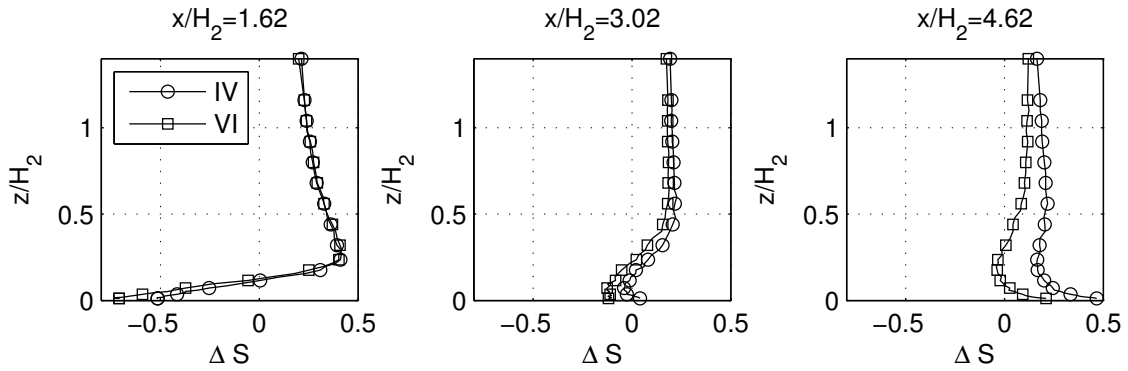

Figure 8.40: The fractional speed-up ratios above the isolated mountain in Case IV and above the upstream mountain in Case VI. The positions refer to Figure 8.15 for both cases.

The fractional speed-up ratios above the downstream mountain in Case V is compared to that above the corresponding isolated mountain in Figure 8.41. The mean velocity at the crest, $x/H_2 = 1.48$, is significantly affected by the higher mountain upstream. The positions refer to the isolated mountain in Case III (see Figure 8.12). In the isolated case the mean velocity is *increased* by 50 % at $z/H_2 = 0.2$ compared to the incoming flow, while the mean velocity at the corresponding position is *reduced* by 25 % when the mountain is located upstream. The fractional speed-up ratio at the crest is approximately equal in Case III and Case V at $z = 1.4H_2$ above ground. The discrepancies are reduced as the flow passes the plateau,

but are still present at $x/H_2 = 4.29$. The fractional speed-up ratios in both cases are within the range 0 to 0.3 at this most downstream position, and are much more uniform with height than at the crest. A comparison of the turbulence intensities is shown in Figure 8.43. It is seen that the turbulence intensity in Case III is considerably lower than in the inflow at all heights along the entire plateau. On the other hand, the turbulence intensity in Case V is higher than in the inflow below $z/H_2 = 0.6$ at the crest ($x/H_2 = 1.48$), and lower than in the inflow at all heights at the position $x/H_2 = 4.29$.

Despite the mountain upstream, with separated flow at the crest and in the valley between the two mountains, some speed-up effects are seen at all measured heights and positions above the second and largest mountain in Case VI. The maximum fractional speed-up ratio found near the ground at the crest is about 0.9 in this case, compared to almost 1.5 in Case II where the mountain is isolated. This is shown in Figure 8.42, where the fractional speed-up ratios above the second plateau in Case VI are compared to those above the plateau in Case II. Discrepancies are seen at all heights and positions, but these are considerably reduced from the crest ($x/H_2 = 1.21$) to $x/H_1 = 4.35$. The turbulence level is increased significantly at all heights compared to the isolated case, but the turbulence intensities, shown in Figure 8.44, are less than in the inflow at all positions ($x/H_1 = 1.21, 2.64$ and 4.35) both with and without a lower mountain upstream. However, the mean velocity is quite constant at heights typical for wind turbine rotors. Hence, the wind field across a typical rotor area in this case is relatively homogeneous. This is beneficial as turbine sizes increases, since the dynamic loads a turbine blade experiences during one rotation due to the vertical variation in the mean wind field, has become an increased concern.

Each of the Figures 8.41 and 8.42 illustrates the effect of a mountain upstream on the fractional speed-up ratio versus the flow above a corresponding isolated mountain. A comparison of these two figures also roughly indicates the differences between having a larger (Figure 8.41) versus a smaller (Figure 8.42) mountain upstream. The turbulence intensity can be compared in a similar way by studying Figures 8.43 and 8.44. The most striking feature is how much a larger mountain upstream increases the turbulence intensity on the downstream mountain, compared to the case with the smallest mountain upstream.

Miller and Davenport (1998) studied flow above complex terrain, and three of the conclusions from this work were

- A decrease of fractional speed-up ratios in complex terrain compared to those above isolated hills.
- Significant increase of turbulence levels in complex terrain compared to flat land with similar roughness.
- No allowance for a reduction in the local turbulence intensity, $\sigma_u(z)/U(z)$, should be made in estimates for flow above complex terrain.

The downstream mountains in Case V and Case VI can be defined as complex terrain, and most of the results are in accordance with the theses given by Miller

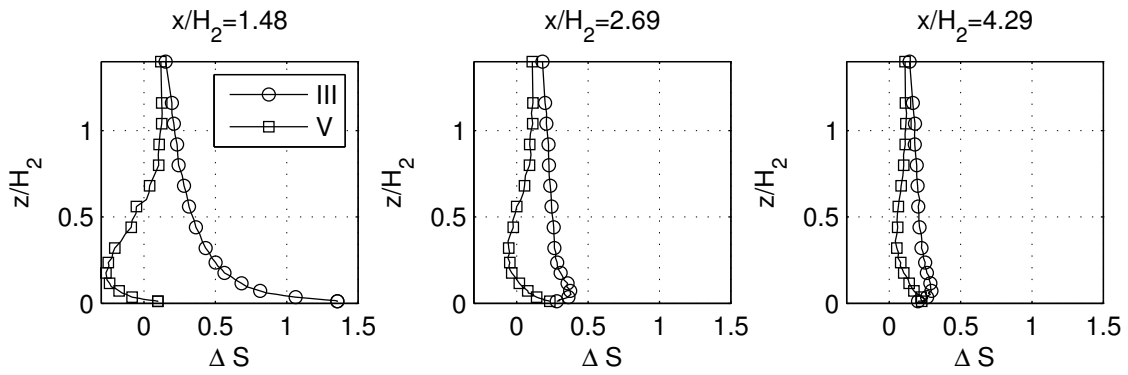

Figure 8.41: The fractional speed-up ratios above the isolated mountain in Case III and above the downstream mountain in Case V. The positions refer to Figure 8.12 for both cases.

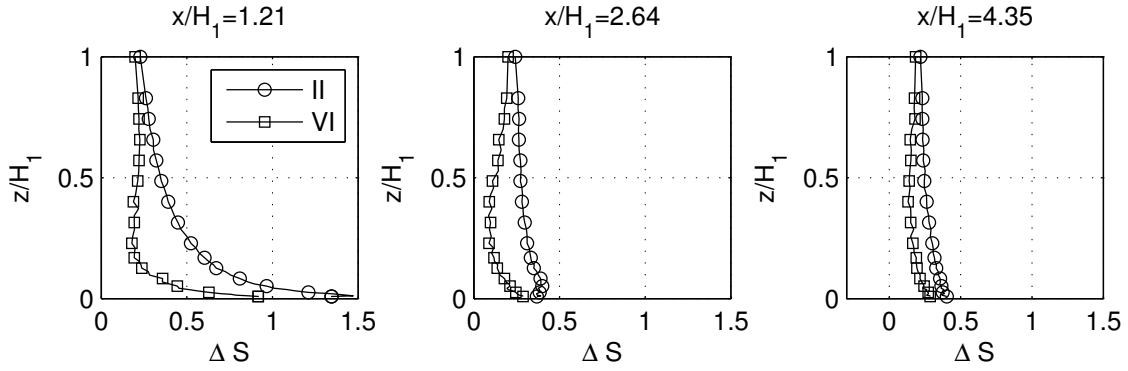

Figure 8.42: The fractional speed-up ratios above the isolated mountain in Case II and above the downstream mountain in Case VI. The positions refer to Figure 8.9 for both cases.

and Davenport. The only exception is the turbulence intensity in Case VI, which is reduced compared to the turbulence intensity in the approaching flow at all heights along the entire plateau (Figure 8.44). The turbulence levels above this plateau are increased compared to the approaching flow, but the speed-up effect is large enough to cause a reduced turbulence intensity. However, Miller and Davenport also observed that the speed-up depended significantly on the relative size of the feature compared to those immediately upstream, as the sheltering effect of larger features upstream reduces the speed-up above the terrain downstream. The importance of the size of the mountain upstream was also clearly seen in this study, and the turbulence intensity is not decreased in Case V where the flow passes the largest mountain first.

Enlarged versions of the terrain and mean velocity vectors near the valley in Case V and VI are shown in Figure 8.45. The velocities at the end of the first plateau in Case V are more constant with height than at the end of the plateau

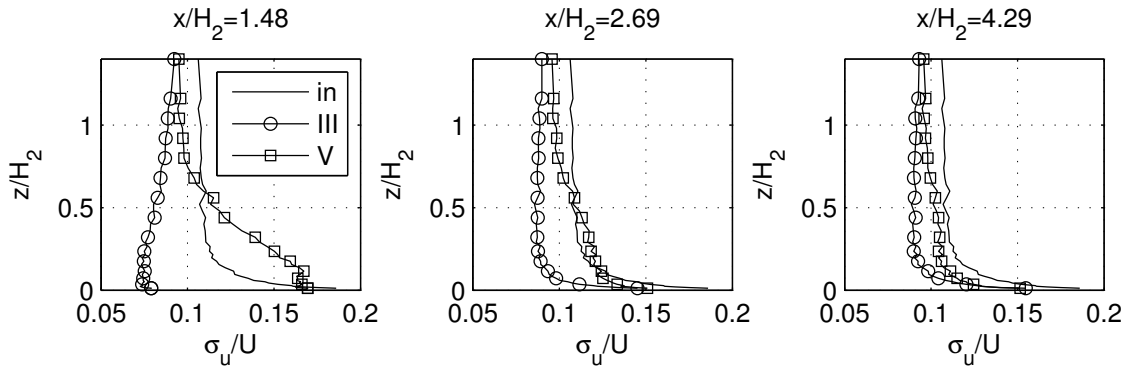

Figure 8.43: The streamwise turbulence intensity above the isolated mountain in Case III and above the downstream mountain in Case V. The positions refer to Figure 8.12 for both cases.

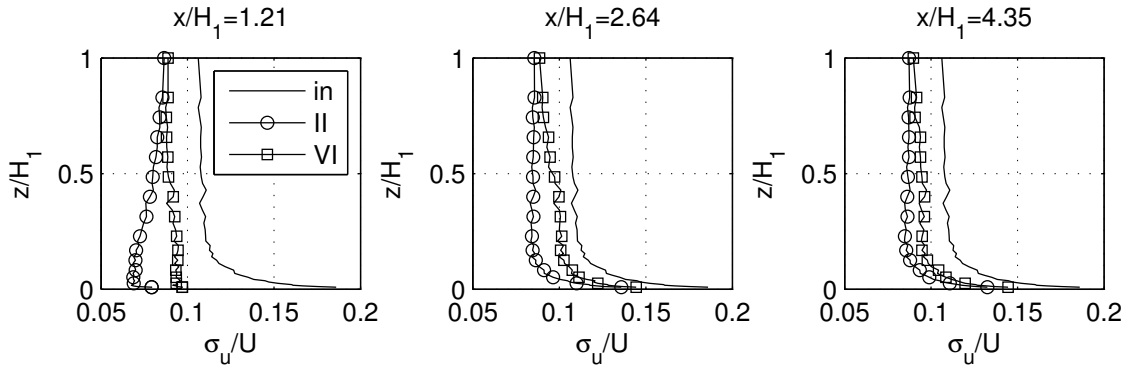

Figure 8.44: The streamwise turbulence intensity above the isolated mountain in Case II and above the downstream mountain in Case VI. The positions refer to Figure 8.9 for both cases.

in Case VI. This is an effect of the rounded edge upstream in Case V compared to the sharp crest in Case VI, as discussed above. The three velocity profiles in the valley clearly show that the separation bubble is significantly larger in Case V than VI, as a result of the height of the upstream plateau. Negative velocities are also seen half-way up the ascending hill of the downstream mountain in Case V. The effect of this deviation in size between the two separated regions is seen at the crest of the downstream mountain in each case, where the velocities in Case V are more influenced by the valley than in Case VI.

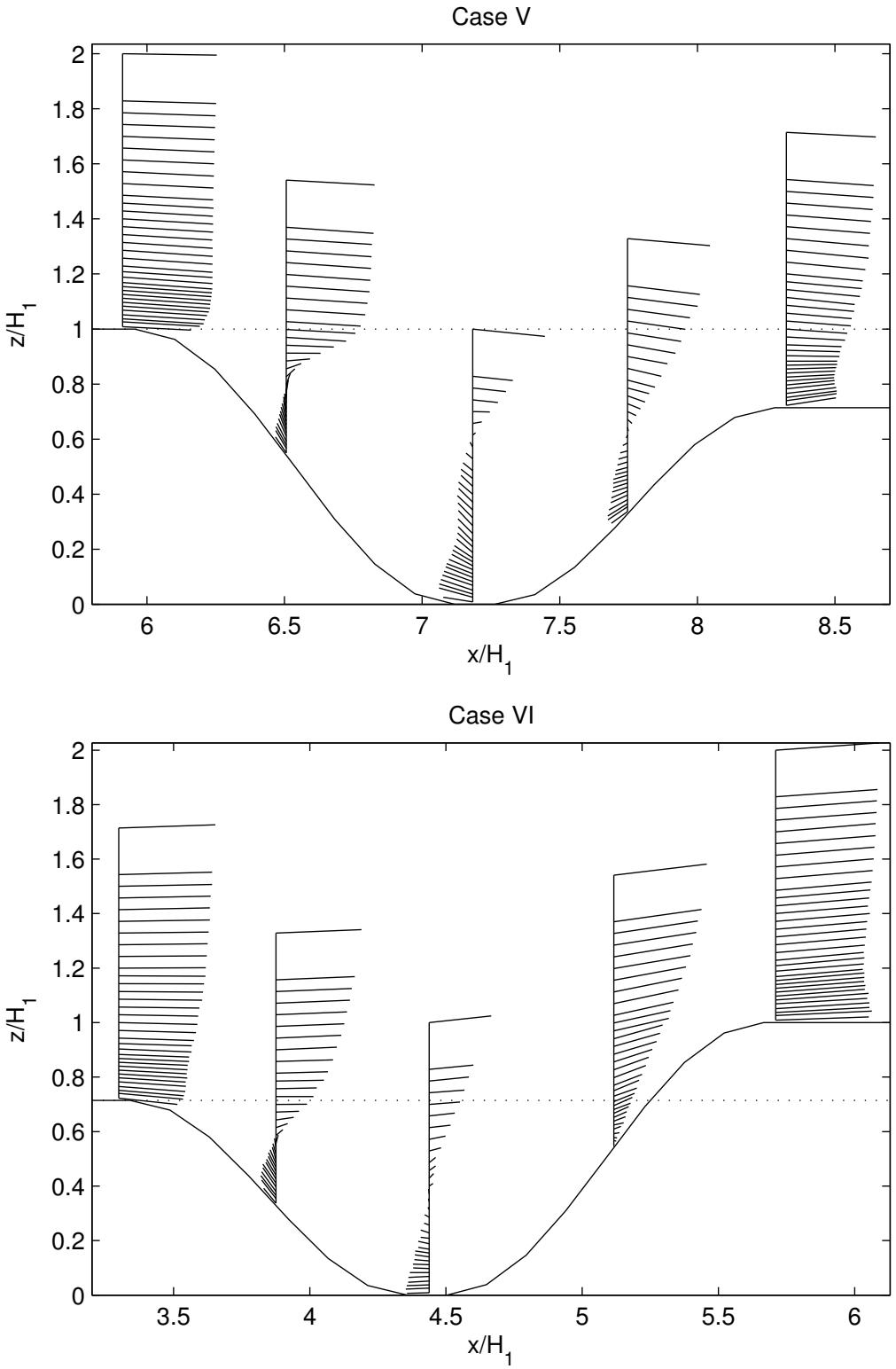

Figure 8.45: Terrain and mean velocity vectors (U and W) near the valley in Case V and VI. This is quite similar to Figures 8.18 and 8.21. The vertical lines indicate zero velocity, so that velocity vectors to the left of these are negative. The dotted horizontal lines illustrates the height of the upstream plateaus.

8.6 Effect of approaching flow direction; Case VIII and IX

The ridge which constitutes the first part of the terrain in Case VIII and Case IX is the same. The approaching flow direction is 45° in Case VIII and orthogonal to the ridgeline in Case IX. Measurements were obtained at the top of the ridge in both cases, so it is possible to see the effect of the direction of the approaching flow. The measurement above the following ridge in Case IX can also be compared to the flow above the second crest in Case VIII. The location of all these four measurement points can be seen in Figure 7.13.

The fractional speed-up ratios above the first and second crest in Case VIII and Case IX are shown in Figure 8.46. The fractional speed-up ratios above the first crest are identical for the two cases above $z/H_2 = 0.4$, and only small effects of the terrain are seen above this. At all heights below this level the fractional speed-up ratio is higher with the orthogonal approaching flow than for the flow with an angle of 45°. Clear discrepancies between the two cases are seen at all measured levels above the second crest. Maximum fractional speed-up ratio observed near the ground at the second crest is more than twice as high with flow orthogonal to the ridge compared to the main flow direction at an angle.

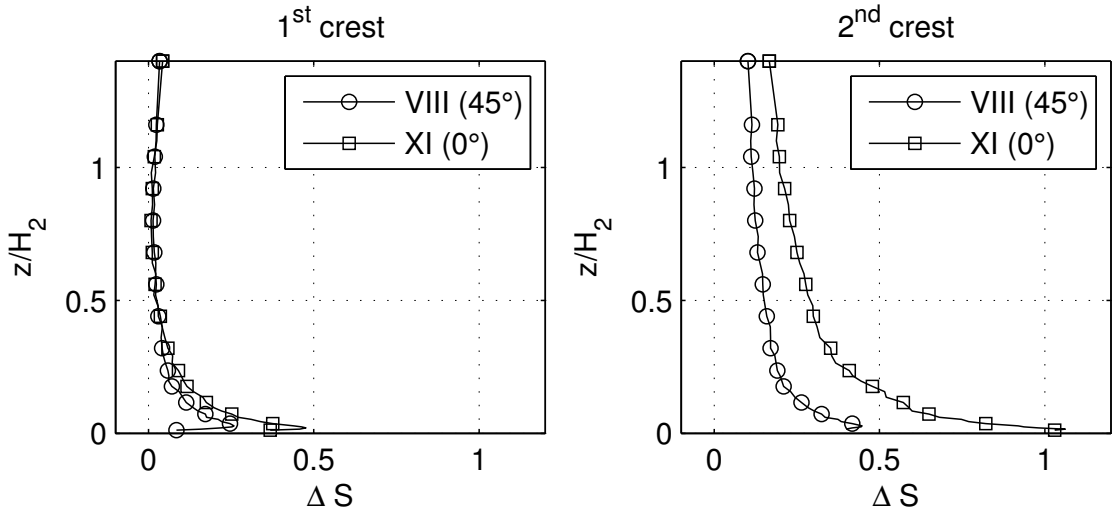

Figure 8.46: Fractional speed-up ratios above the first and the second crest in Case VIII and IX.

Lubitz and White (2007) studied the effect of approaching flow direction on a two-dimensional ridge. They tested flow angles from $0° - 90°$ with increments of 15°. The numbers are not directly comparable to the current study due to different slopes, shapes and roughness of the ridges, in addition to the fact that there also is surrounding terrain in the current study. But the experiments are similar enough to compare the relative effect of flow direction above the first ridge in this study to that above the isolated ridge investigated by Lubitz and White. Similar to the results in

the current study, Lubitz and White observed the highest fractional speed-up ratio at the top of the ridge for angles near 0°. The maximum fractional speed-up ratio above the first crest in this study decreases from 0.48 to 0.26 as the flow direction is changed from 0 to 45°. This is a decrease of 45 % as the angle increases to 45°. The corresponding values found by Lubitz and White are 0.68 and about 0.42 respectively, which corresponds to a decrease of 38 %.

8.7 Effect of roughness on model and in inflow; Case IXa-c

It has been shown by other investigations that the effect of roughness should be considered when the effects of topography are examined. The introduction in the work by Cao and Tamura (2007) gives a brief summary of studies in this context. The effect of surface roughness was also investigated for one selected case in the current study, as described in Section 7.6.3. Both the floor upstream of the model and the model in Case IXa have smooth surfaces, and the flow above this terrain was described in Section 8.2.9. Roughness was added to all surfaces in Case IXc. Case IXa is named "smooth" in the following text, while Case IXc is named "rough. Case IXb has a smooth surface in the inflow, while roughness is added to the model (named "smooth/rough"). The model in this study was created to simulate the mountainous terrain along the Norwegian coastline, and the approaching boundary layer is similar to flow in coastal areas. The roughness change between the flat area and the terrain in Case IXb is very relevant, as the surface roughness of mountains differ from that above the sea. However, the change of roughness in Case IXb is more abrupt than it would be in most cases in a real terrain. Such a roughness change was described in Section 3.3.3. An establishment of an internal boundary layer can not easily be seen in this case, since the abrupt roughness change occurs at the very base of the first hill. Effects due to the terrain are expected to dominate the flow structure, but the results should be analyzed with the roughness change in mind as well.

The approaching wind profiles measured above the smooth surface 1 meter upstream of the smooth model in Case IXa and 1 meter upstream of the rough model in Case IXb are very similar. Hence, the roughness on the model does not seem to influence the flow upstream. The profile in these two cases deviate from the inflow profile in Case IXc, where also the floor is covered with roughness. The approaching flow above the smooth and rough surface 1 m upstream of the model are shown in Figure 8.47, and the characteristics of these two are listed in Table 8.3. The mean velocities in the streamwise direction are equal at the height $z \approx 350$ mm, which is the maximum height of the terrain in Case IX. At all levels below this the velocities in the rough case are reduced compared to the smooth case. The standard deviations in both the streamwise and vertical directions are lower near the ground in the smooth than in the rough case. While the flow in Case IXa is similar to flow above sea, the flow in Case IXc corresponds to farmland and grassy plains. The flow in the former has a roughness length of $z_0 = 0.004$ mm and a roughness Reynolds

number of 0.13, which is close to the limit of a smooth surface. The latter is fully rough with a roughness length of $z_0 = 0.102\ mm$. The roughness Reynolds number is 4.74, which is greater than a typical limit of 2.5 given to be the lower limit of fully rough flow. Reynolds numbers in Case IX (calculated by maximum height of the terrain model and the approaching mean velocity at this height) is $3.2 \cdot 10^5$ for the completely smooth case, and $3.0 \cdot 10^5$ for the completely rough case. This difference is quite small, so it is not necessary to consider Reynolds number effects.

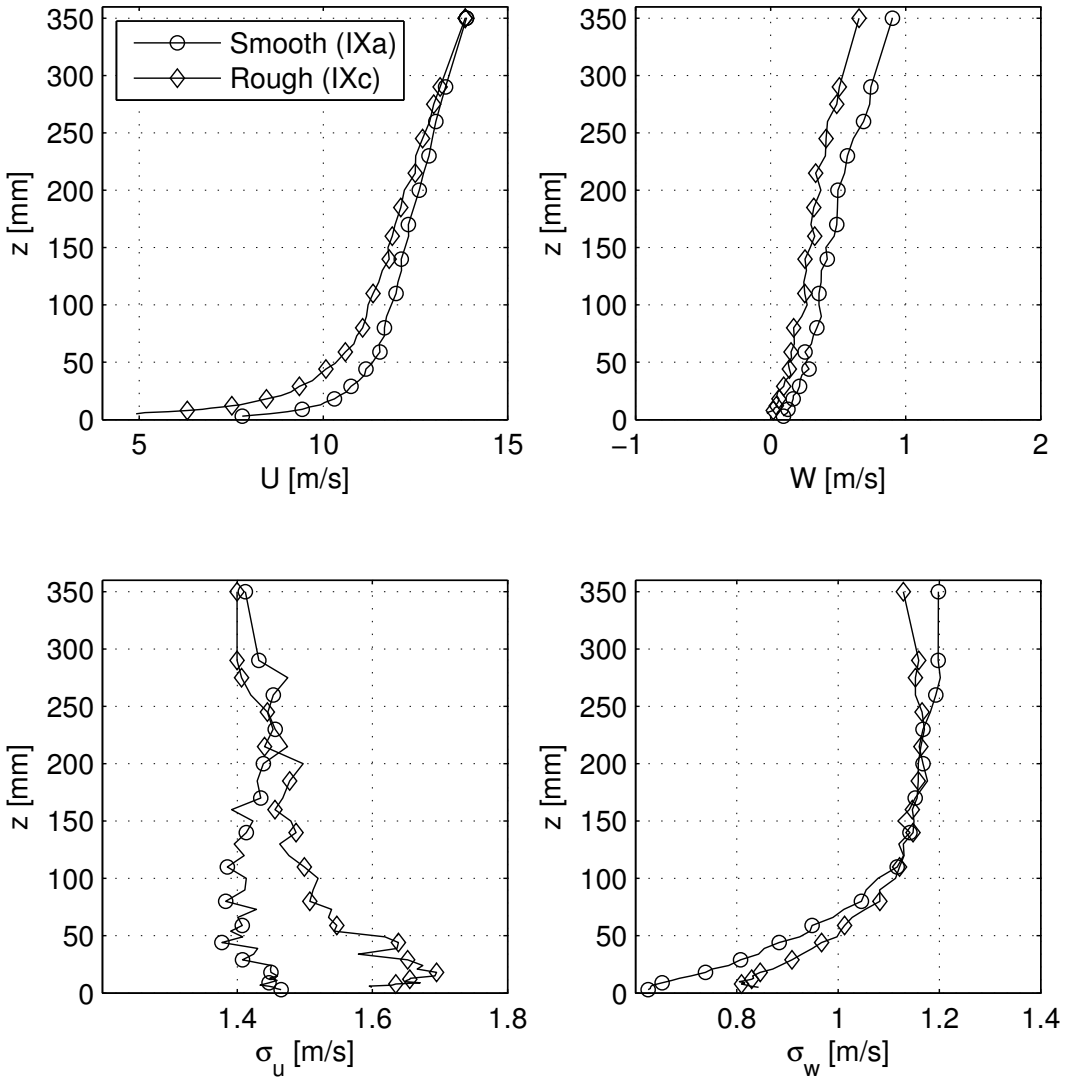

Figure 8.47: Incoming boundary layer 1 m upstream of the model (position a in Figure 8.48). Case IXa with no roughness compared to Case IX with roughness on all surfaces.

The measured positions common for all the three roughness combinations in Case IX were shown in Figure 8.33. A side view of the terrain and labeled measured positions (a-h) can be seen in Figure 8.48. Results for the mean streamwise velocities

	Case IXa	Case IXc
d_0 [mm]	0.80	3.90
δ [mm]	349.2	346.1
$U(\delta)$	13.9	13.9
u_* [m/s]	0.50	0.70
z_0 [mm]	0.004	0.102
ΔU^+	0	9.0
Re_*	0.13	4.74

Table 8.3: Characteristics of simulated atmospheric boundary layer observed 1 m upstream of the model in Case IXa and Case IXc. The parameters are found by manual fit, and all values are in model scale. δ is the maximum elevation measured for which the fit is acceptable for, and not the height of the real boundary layer in the tunnel.

(U) and the streamwise standard deviations (σ_u) in these positions are compared in Figure 8.49 and 8.50 respectively. It is seen that the general structures of the flow are quite similar for all the roughness combinations, even though there are some differences. This was also observed by Cao and Tamura (2006).

An interesting result displayed in Figure 8.49 is the effect of the inflow compared to the effect of the roughness on the model. The mean velocity in the inflow (a) is similar for the smooth and smooth/rough variant, as described above, while decreased in the rough case. The combined effect of inflow and roughness on the model can be seen on the first crest (b). In all following profiles the roughness effect of the inflow profile has vanished, so that the smooth/rough and rough profiles are approximately equal. Hence, the differences downstream of the first ridge are due to the roughness on the model only.

The mean velocities above the second ridge (c) are significantly higher in the lower region for the smooth case than for the two cases with a rough surface. The streamwise standard deviations in positions upstream of and on the second ridge (c) are lower than and approximately equal in the smooth case compared to the cases with a rough model surface. This is altered with onset of the separation at the lee side of the second ridge (d). The height of zero velocity in this region of separation is higher above ground for the rough than the smooth case. This has also been observed by Cao and Tamura (2006) and Song and Eaton (2002). The streamwise mean velocity is zero at a height $z/H = 0.17$ above ground in the smooth case, and $z/H = 0.22$ above ground in the rough case. The difference in height above ground where zero velocity occurs is 30 % from the smooth to the rough case. Even though the size of the separated flow region is largest in the two rough model cases, the resulting stresses are significantly higher above the smooth terrain. A stronger peak is developed for the smooth case than the rough case. The height of these maximum values for σ_u (and also σ_w and $-\overline{u'w'}$, which are not shown) coincides with the height of strongest wind shear dU/dz downstream of the second crest (d). The height of maximum value for σ_u and dU/dz is $z/H = 0.29$ for the smooth case, and $z/H = 0.37$ for the rough case. As for the height levels of zero velocity this

difference is also 30 %. All this indicates that the centre of the separated shear layer is higher, and thus that the flow separates further upstream, for the rough case than for the smooth case. This was also observed among others by Song and Eaton, who investigated the effects of wall roughness on the separated flow over a smoothly contoured ramp. They concluded that "the increase in skin friction and turbulence levels that would be expected to delay separation are overwhelmed by the increase in the boundary layer momentum thickness". Higher velocity, as for the smooth case, results in higher resistance to separation. The mean velocities in the centre of the valley (e) are quite similar for all the three cases. The highly increased streamwise standard deviations in the smooth case are even larger compared to the rough cases in this position, hence the separated shear layer is clearly stronger for the smooth than for the rough case. Cao and Tamura correspondingly observed that the streamwise velocity fluctuations were significantly larger downstream of a ridge with a smooth surface than a rough surface. The values in the smooth case are still slightly higher than the rough model cases at the crest of the plateau (f). The mean velocities are also marginally higher closest to the ground for the smooth case at the start of the plateau (f and g). Similarly, at the end of the plateau (h) the smooth case differs from the two others, having higher mean velocities up to $z = 0.5H$. At the end of the plateau the streamwise standard deviations have decayed, so that they are lower than the two rough cases closest to the ground, and equal to the other two cases further up.

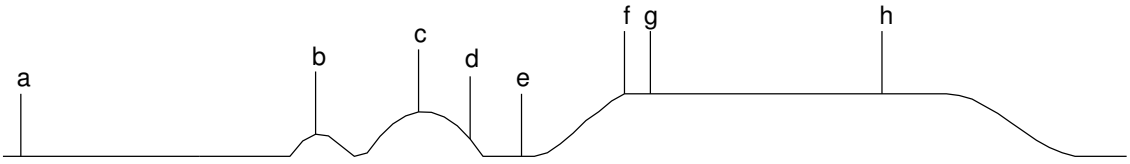

Figure 8.48: Labeled positions for use with Figures 8.49-8.52

The fractional speed-up ratios at the top of the first and second crest (positions b and c) are shown in Figure 8.51. The mean velocity profiles taken to be the undisturbed incoming flow in these calculations are the measurements 1 m upstream of the model in each case. It is seen that the fractional speed-up ratios are not affected by the roughness above $z/H_1 = 0.15$ at the first crest and above $z/H_1 = 0.4$ at the second crest. The maximum values observed at the first crest, with heights given as z/H_1, are

$$\begin{aligned} [\Delta S_{max}]_{smooth}\,(0.014) &= 0.44 \\ [\Delta S_{max}]_{smooth/rough}\,(0.051) &= 0.16 \\ [\Delta S_{max}]_{rough}\,(0.043) &= 0.34 \end{aligned}$$

while the maximum fractional speed-up ratios observed at the second crest are

$$\begin{aligned} [\Delta S_{max}]_{smooth}\,(0.011) &= 1.00 \\ [\Delta S_{max}]_{smooth/rough}\,(0.043) &= 0.36 \\ [\Delta S_{max}]_{rough}\,(0.043) &= 0.70 \end{aligned}$$

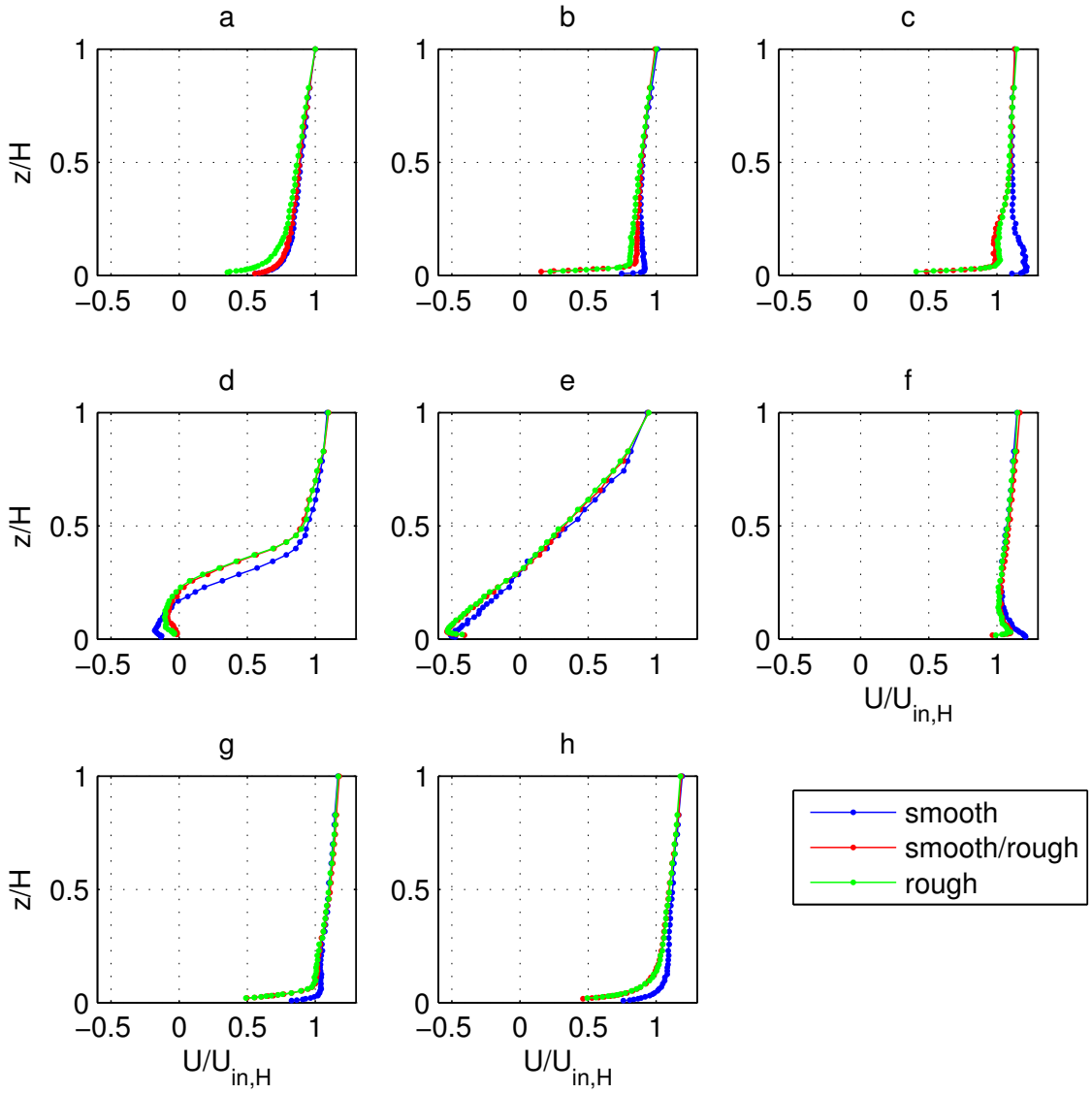

Figure 8.49: Mean streamwise velocities in Case IX with the three roughness combinations; Case IXa (smooth), Case IXb (smooth/rough) and Case IXc (rough). The velocities are normalized with the mean streamwise velocity at the height H in the corresponding inflow, while the heights are normalized with H. All axes are equal, and positions a-h are shown in Figure 8.48.

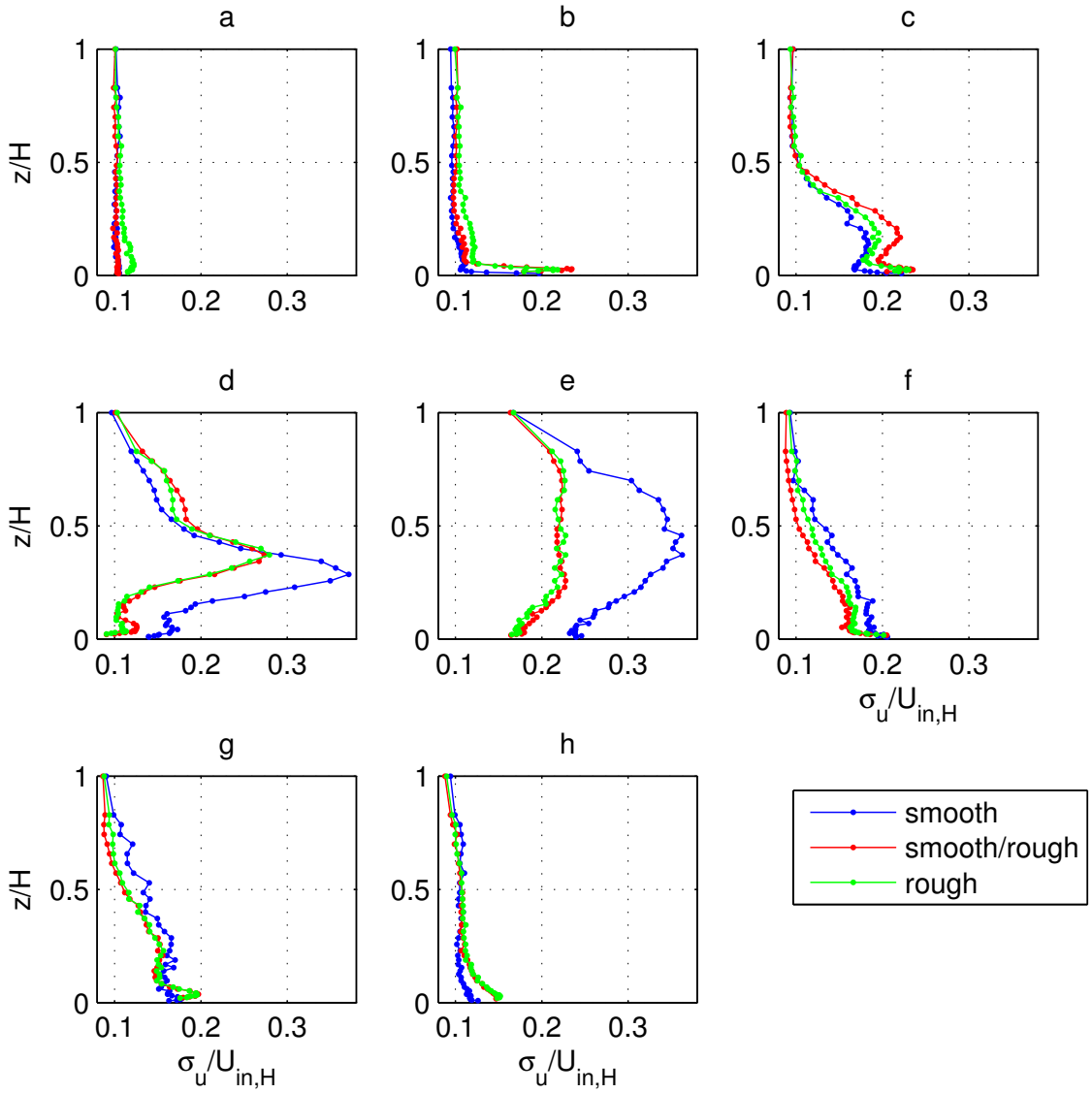

Figure 8.50: Streamwise standard deviations in Case IX with the three roughness combinations; Case IXa (smooth), Case IXb (smooth/rough) and Case IXc (rough). The standard deviations are normalized with the mean streamwise velocity at the height H in the corresponding inflow, while the heights are normalized with H. All axes are equal, and positions a-h are shown in Figure 8.48.

The highest maximum fractional speed-up ratio is observed for the completely smooth case at both these crests, followed by the completely rough case, and the lowest maximum fractional speed-up ratio is seen for the rough model with smooth inflow. The heights where these maximum values occur are approximately equal for IXb and IXc, which both have a rough model surface. The maximum values for the smooth surface (IXa) are found at a significantly lower level. Cao and Tamura (2006) also observed the lowest fractional speed-up ratio for a rough hill in smooth flow, but they observed a significant larger maximum fractional speed-up ratio for the rough than the smooth case for $z/H < 0.5$. However, if only the first crest in the current study is considered, and the heights are normalized with the height of this crest ($H = 125\ mm$), it is seen that $[\Delta S]_{rough} > [\Delta S]_{smooth}$ in the region $0.1 < z/H < 0.4$. Hence, the results found in the current study does not differ as much from the work by Cao and Tamura as it could seem at first. Due to the no-slip condition on the model surface there should be a height where the increase in velocity (ΔU) attains a maximum value. The height above ground where maximum speed-up occurs are higher for the two cases with a rough model surface than it is with a smooth model surface. Cao and Tamura predicted this based on that "the inner layer where the boundary layer is in local equilibrium becomes deeper on the crest of the rough hill". This height above the ground where the maximum increase in velocity occurs was clearly seen for all three cases at the top of both ridges in the current study, but Cao and Tamura could not detect it since the measurements did not reach close enough to the surface.

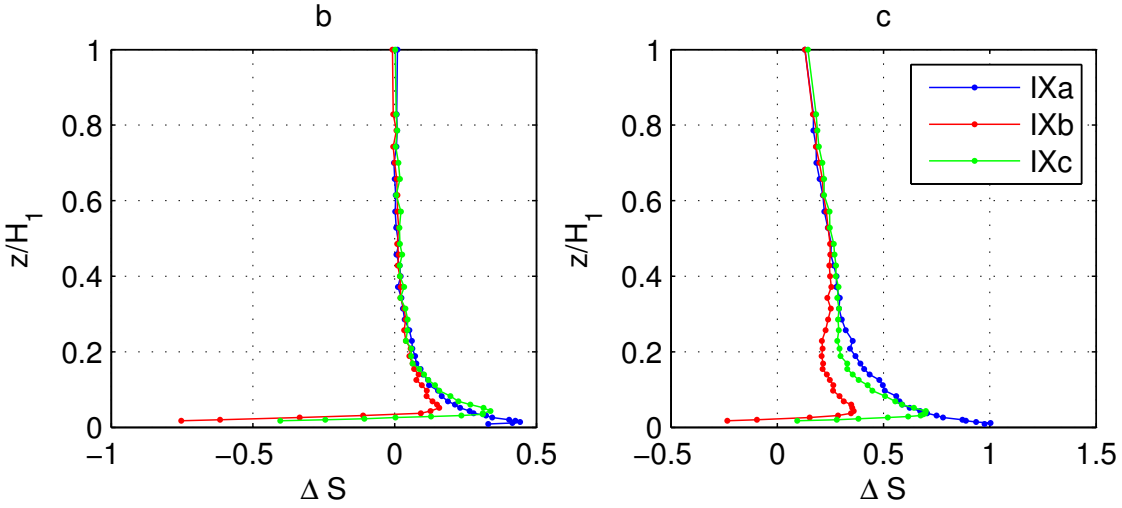

Figure 8.51: Fractional speed-up ratio in Case IXa (smooth), IXb (smooth/rough) and IXc (rough). Positions b and c are at the top of the first and second crest respectively, as shown in Figure 8.48

Measurements with the LDA probe aligned to measure (u, w) and (u, v), respectively, were done at three of the positions common for Case IXa-c. Hence, all three velocity components are available for these positions. Each frame in Figure 8.52 gives a comparison of all the standard deviations for a given position and roughness

case. The results shown in the first column in Figure 8.52 are measured in the second valley (e), the results in the middle column are measured at the very crest of the mountain (f), and results from the end of the plateau (h) are shown in the third column. The three rows represents the three roughness combinations (Case IXa-c). The horizontal velocities across the main flow were unfortunately not measured in the inflow profile in the three current cases, so a normalization with $\sigma_{v,in}$ is not possible. It is seen that the velocity fluctuations in position (e), (f) and (h) are virtually identical above the rough model surfaces, independent of the incoming flow field. The velocity fluctuations above the smooth surface in the valley (e) deviate from the rough cases, with much higher values in all three directions.

In the valley (e), $\sigma_w < \sigma_v < \sigma_u$ in general, except in the lowest part of the boundary layer. σ_v and σ_w are quite similar above $z/H = 0.4$ for the smooth case, while these velocity fluctuations are different at all heights for the two rough model cases. At the crest (f), $\sigma_v = \sigma_w$ for all cases, while the standard deviation in the streamwise direction is higher. The exception is a thin region near the ground. As in the valley, $\sigma_w < \sigma_u < \sigma_v$ at heights below about $z = 0.15H$ for all the roughness cases. At the end of the plateau (h), σ_u is higher than the standard deviation in the other two directions at all heights. σ_v is higher than σ_w up to about $z = 0.8H$ in the two cases with roughness added to the model, and only up to about $z = 0.4H$ in the case with a smooth model surface. Above these heights σ_v and σ_w are approximately equal.

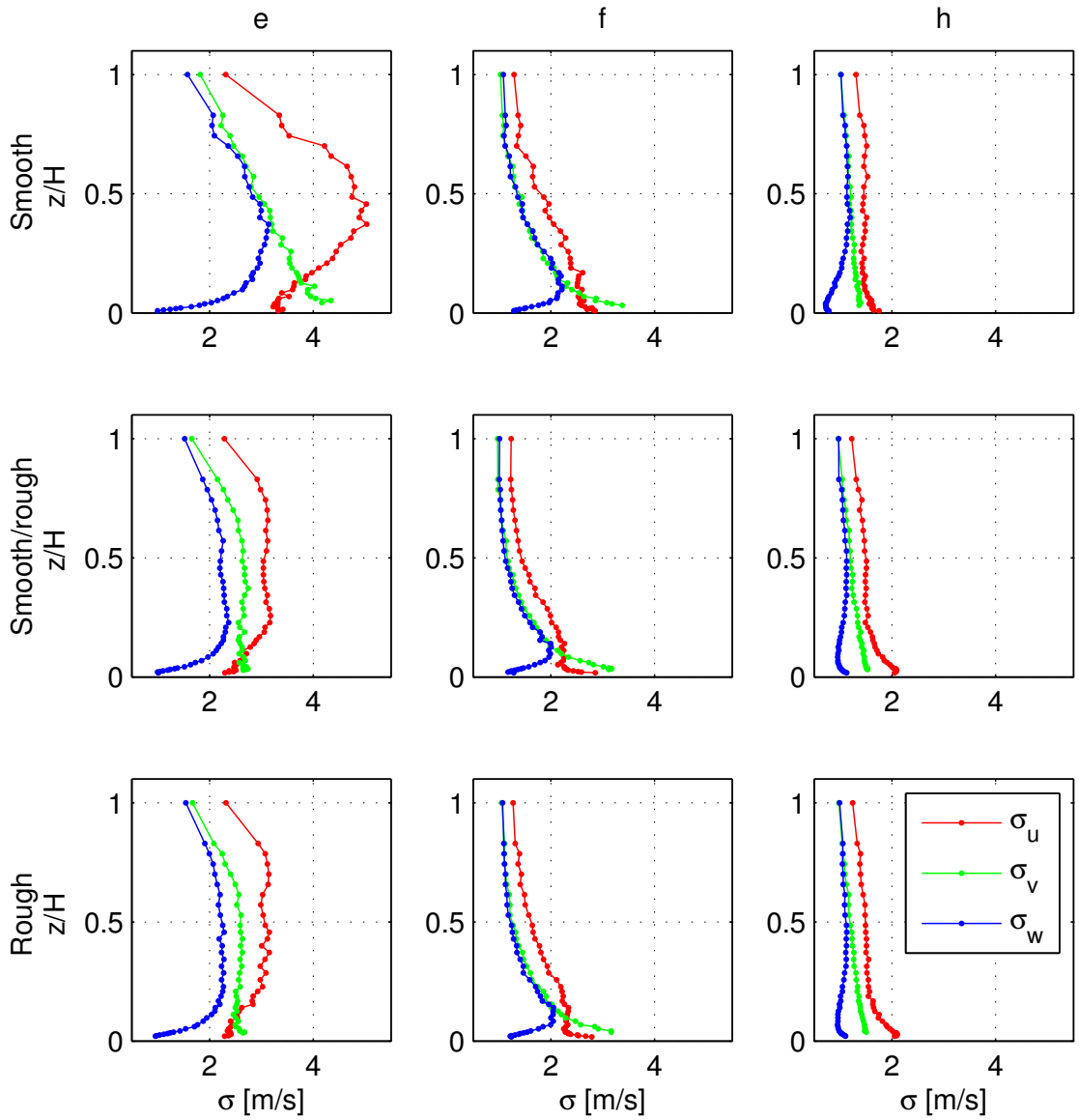

Figure 8.52: Comparison of standard deviations in all three directions. Each column gives results for one measured position (e, f and h in Figure 8.48), and each row contains results for one of the roughness combinations IXa-c.

8.8 Comparison and validation

Most of the estimation methods described in Section 4.3 are not designed for steep hills. It is generally recommended to do experiments, numerical calculations, or both, in the case of such complex terrain. Nevertheless, it was desirable to compare the experimental results in this study with some estimation methods. It is interesting to see if any of the methods can be applicable to steeper hills than they are designed for, since these methods often are applied for parameters out of the intended range (like steeper slopes) after all.

8.8.1 LSD approach

The LSD approach is a simple method used for estimation of speed-up over different types of topography, as described in Section 4.3.2. The minimum and maximum values of $L_{H/2}$ in Case I-IV in the current study are 127.1 mm and 334.8 mm respectively. The corresponding normalized values are $L_{H/2}/z_0 = 31800$ and $L_{H/2}/z_0 = 83700$. These are within the range given by the LSD approach, so it can be assumed that the speed-up is independent of the surface roughness. The thermal stability in the experiment is neutral and the hills in Case I-IV are isolated, as recommended for use of the LSD approach. The length of the plateaus in Case I-IV are from $4.2L_{H/2}$ to $7.2L_{H/2}$, which is larger than $2L_{H/2}$. Hence the LSD approach for the shape defined as "escarpments" can be applied. The parameter $\phi = H/L_{H/2}$ in Case I-IV are 1, 1.7, 1.4 and 2 respectively. Equation 4.6 in the LSD approach is the same for $\phi < 1$ and $\phi \geq 1$, but the parameters are unequal. One difference is that the maximum possible fractional speed-up ratio is limited to 1.3 for the steepest slopes. Despite the fact that $\phi \geq 1$ in all cases in this experimental study, it is also interesting to compare the experimental data to the results for the LSD approach calculated as if $\phi < 1$ for comparison purposes.

The results for the LSD approach are compared to the experimental data in Figure 8.53. Estimates from the ESDU method are also shown, and this will be discussed in Section 8.8.2. The variation of fractional speed-up ratio with height is generally larger for the LSD approach than for the measured data. It is also seen that the estimated fractional speed-up ratios by both LSD options decay much faster along the plateau than the experimental values. The results calculated with $\phi \geq 1$ are too large at the crest and some distance downstream of the crest. As a consequence of the fast decay, the LSD estimate does fit well a distance of about 2-3 hill heights downstream of the crest. Weng et al. (2000) concluded that the maximum values for ΔS_{max} found by the LSD approach were far too high when compared to their more comprehensive numerical calculations which were performed in an attempt to improve the "Guidelines" for estimating variations of wind speed over terrain features. These results were seen for 3D hills and 2D ridges with moderate slopes, but are most likely also representative for embankments and steeper slopes. The results calculated with $\phi < 1$ (which is designed for much more moderate slopes) agree well with the experimental data at the crest, but the fit gets poor quickly as the flow passes the plateau. The speed-up given for $\phi < 1$ decays even faster than for $\phi \geq 1$. At the distances downstream of the crest where the results for $\phi \geq 1$

agrees well with the experimental data, with ΔS in the range 0.5-0.2, the results for $\phi < 1$ are already close to the inflow profile ($\Delta S \simeq 0$).

Separated flow emerge right after the sharp crest in Case IV, as seen in Section 8.2.4. The LSD approach can not catch this consequential detail of the terrain, since the only given information about the slope are the simple length parameters H and $L_{H/2}$ which defines a characteristic slope.

8.8.2 ESDU

The simple ESDU method described in Section 4.3.3 was applied to Case I-IV. The slopes of the superimposed embankments are equal to the maximum slopes in the hills, and the horizontal position was found by graphically trial and error method. The superimposed embankments for Case I-IV were shown in the illustration defining the key parameters in the ESDU method in Figure 4.2. The values for the key parameters are given in Table 8.4, and the value $s_{z=0}$ has to be read from a figure giving values of s at $z = 0$ for two-dimensional embankments in the description of the ESDU method (ESDU, 1993). Both the high hill correction, and the steep slope limitation were applied in the calculations for all four cases. The recommended value for embankments, $\phi_{max,z=0} = 0.4$, was used in Equation 4.8. The values listed in Table 8.4 were used to extract s, and not the values associated with the maximum slope.

Case	I	II	III	IV
H [mm]	350	350	250	250
L_u [mm]	459.4	265.7	240.6	254.4
P [mm]	1599.9	1599.9	973.0	973.0
ϕ_u	0.76	1.32	1.04	0.98

Table 8.4: Values of the parameters used in the ESDU method. Definitions are given in Figure 4.2.

Results calculated by the ESDU method are compared to the experimental data in Figure 8.53. The fractional speed-up ratio calculated by the ESDU method in Case I results in too high values everywhere except close to the ground at the crest, where the experimental fractional speed-up ratio is somewhat higher than the estimates. The results for Case II are approximately the opposite, with too high estimated values close to the ground at the crest. The similarity between the experimental and estimated results is very good at all other elevations and positions along the plateau positions. Case III is somewhere in between these other two cases when it comes to how well the estimates are in accordance with the experimental results. The estimated results decay slightly slower along the plateau than the experimental data.

The best fit is actually seen for the steepest slope and the least good fit occurs for the most gentle slope. This is the contrary of what could be expected, as the assumptions made for the steepest slope ($\phi_u = 1.32$) are even larger than for the

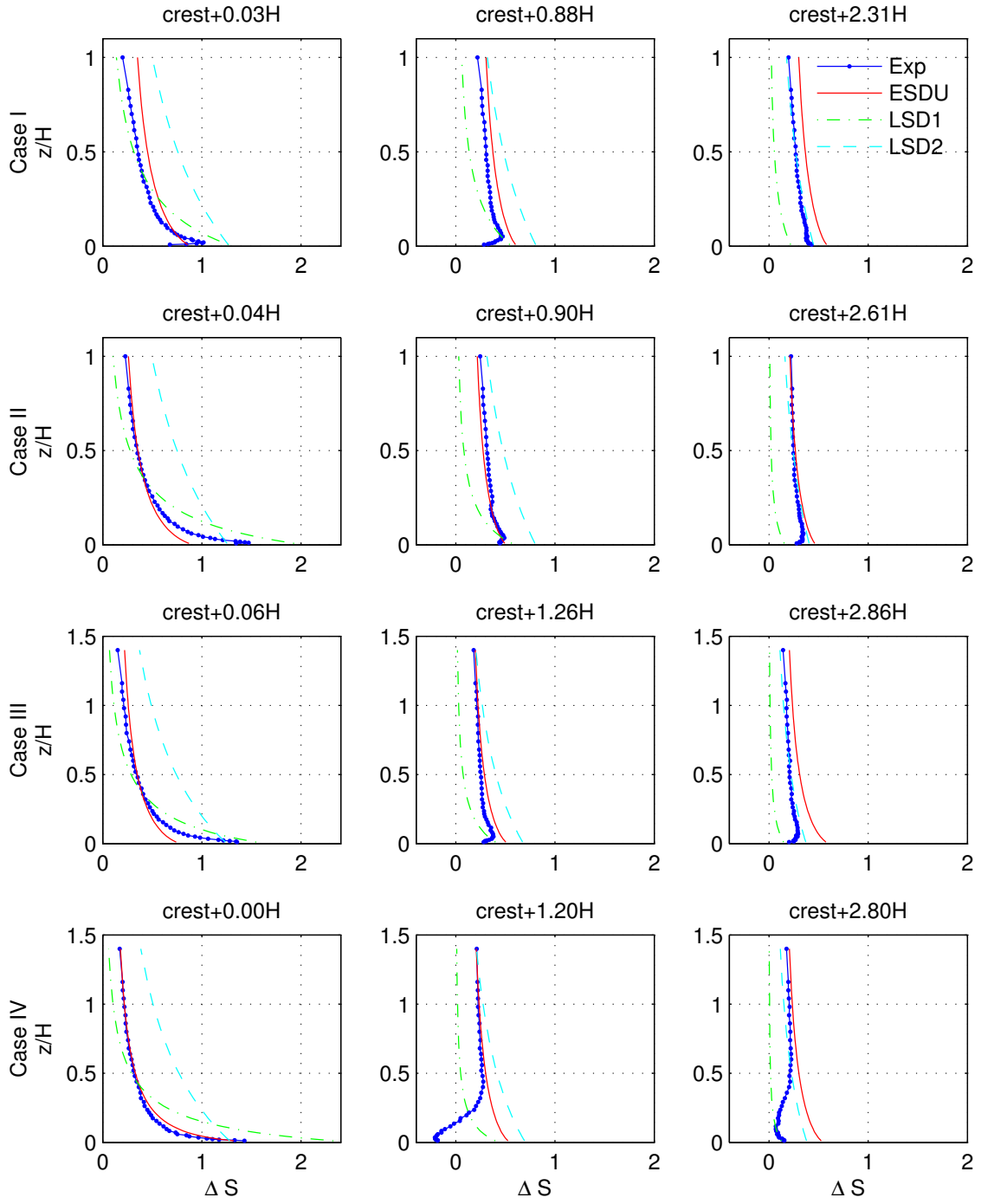

Figure 8.53: A comparison of estimated and observed ΔS for selected positions in Case I-IV. "Exp" is the experimental data and "ESDU" are the results estimated by the ESDU method. "LSD1" are the estimations by the LSD approach with $\phi < 1$, and "LSD2" are the corresponding results when the parameters actually designed for slopes like these are applied ($\phi \geq 1$). The four rows in the figure give results for Case I-IV respectively. The position is given above each frame, where crest is the top of the ascending hill in each case.

most gentle ($\phi_u = 0.76$). This is probably more a coincidence than a rule, as the slopes are much steeper than what the method is developed for. The reason for these results can be due to the combination of the different heights of the models (H), the slopes of the equivalent embankment ϕ_u, the reading of the parameter $s_{z=0}$ and of course uncertainties in the experimental data.

The ESDU method applied to Case IV reveals that it gives a very good match between the model and the experimental results at the very crest. This could be expected since the method is developed for embankments like this. For positions downstream of the crest in Case IV, the results are not in accordance with the measured data in the region closest to the ground. The reason for this is that the ESDU method does not consider separation occurring at the crest, but only separation at the base of the ascending hill and in the descending hill. The separation at the crest influences the flow field far downstream, so the distinct discrepancy between the model and experimental data is still present three hill heights downstream of the crest.

The ESDU method introduces an effective slope which is much more gentle than the actual hill when $\phi_u > 0.4$, and this seems to result in quite good estimates. This is despite the fact that no separation was observed at the base of the hills in the experiments. Profiles were measured 1 m upstream of the model, one profile was measured at the base of the hill, and one profile was measured half way up the hill for each case. None of these profiles actually revealed separated flow, but the profile measured at the base of the hill in some of the cases indicated that there was a probability of separated flow nearby. The profile at the base of the hill in Case II is probably a separation point, as both the streamwise and vertical mean velocities close to the ground are about zero. This is the steepest hill. The velocity slows down upstream of all the other hills measured as well, and $U \approx 1\ m/s$ near the ground in Case III and IV. In addition to the decreased velocities σ_u does also increase in the region near the ground. Ignoring the restriction to ϕ_u results in too high velocity estimates in all positions in all the four cases, so this restriction in the ESDU method is essential.

The boundary layer height $h = u_*/(6f_C)$ constitutes a part of both the equation for the correction factor in the case of high hills, and in the equation for a limiting value of ϕ_u. The Coriolis parameter f_C is about $1.3 \cdot 10^{-4}$ in Norway. This value of f_C and a friction velocity in the incoming flow of $u_* = 0.5\ m/s$ gives a boundary layer height of about 640 m. The generated incoming boundary layer was about 350 m in full-scale, but the velocity was not constant above this height. Hence, setting h to this height is not necessarily correct in the comparison between the ESDU method and measurements above the steep hills. For Equation 4.10 a default value of $h = 1500\ m$ can be assumed. Based on all this, and on some tests with different values of h in the estimates, the constant value $h = 1000\ m$ was utilized in the ESDU method.

As a conclusion, the ESDU method gives quite good results for all the cases in this study, as long as separation only occurs in the areas considered by the method (and not at crests). These successful results are obtained despite the fact that the estimates are found by the simplest ESDU method available. This method is seen

to fit the experimental data much better and more consistently than the estimates given by the LSD approach.

8.8.3 Linearized theories

Linearized theories were described in Section 4.3.1. The theory of Jackson and Hunt (1975) is valid in the limit $L/z_0 \to \infty$ when $H/L < \frac{1}{8}(z_0/L)^{0.1}$ and $\delta/L \gg 2\kappa^2/\ln(\delta/z_0)$. Applying the values $\delta = 350\ mm$, $z_0 = 0.004\ mm$, $\kappa = 0.4$ and the values of H and L given in Table 7.2 yields the numbers listed in Table 8.5.

Case	I	II	III	IV
L/z_0	165250	101700	89000	63550
H/L	0.53	0.86	0.70	0.98
$\frac{1}{8}(z_0/L)^{0.1}$	0.04	0.04	0.04	0.04
δ/L	0.53	0.86	0.98	1.38
$2\kappa^2/\ln(\delta/z_0)$	0.03	0.03	0.03	0.03

Table 8.5: Relevant numbers for consideration of the linearized theory by Jackson and Hunt.

It is seen that all the values of H/L are much larger than $\frac{1}{8}(z_0/L)^{0.1}$. This confirms the well-known fact that the hills in the current study are way to steep for the linearized theory by Jackson and Hunt to be valid. Speed-up values calculated by this theory are listed in Table 8.7 in the next section, and these are much higher than the experimental values.

8.8.4 Comparison of maximum speed-up

Maximum speed-up can be defined in two ways. It is either the maximum value of the fractional speed-up ratio (ΔS_{max}) or the value of the fractional speed-up ratio at the height where the increase in velocity attains its maximum (ΔU_{max}). Both types will be reported here, but estimates based on linearized theories are only available for the latter. The heights where the maximum values occur are also reported when available. All the maximum values listed are approximately at the crest.

Maximum values of the fractional speed-up ratio found in the experiments and those calculated by the LSD approach and the ESDU method are listed in Table 8.6. All the LSD estimates discussed in this context are the results calculated as if $\phi \geq 1$, which is the correct choice for the steep slopes in Case I-IV. The heights where these maximum values occur are the lowest points in the calculations, and the experimental data agree quite well with this. The maximum values found with the LSD approach are in all four cases approximately equal to the maximum possible value with this approach (i.e. 1.3). This is due to the very steep hills. In contrast to the LSD approach, the maximum values for the fractional speed-up ratio found with the ESDU method are quite different for the individual cases. The ESDU method gives lower values than the experimental data in Case I-III, but higher in Case IV.

The agreement between ΔS_{max} found by the ESDU method and the experimental data is best in Case IV, and this is probably due to the fact that Case IV is exactly an embankment like the ones the ESDU method is based on. Even if the steepest slope in Case III and Case IV are approximately equal, the horizontal length scale in the rounded hill in Case III is much longer than for the straight hill in Case IV. This affects the ESDU result considerably.

Case	H/L	$H/L_{H/2}$	Experiment		LSD		ESDU	
			ΔS_{max}	l_{max}/H	ΔS_{max}	l_{max}/H	ΔS_{max}	l_{max}/H
I	0.53	1.05	1.02	0.020	1.27	0.009	0.86	0.009
II	0.86	1.72	1.47	0.011	1.25	0.009	0.87	0.009
III	0.70	1.40	1.35	0.012	1.24	0.012	0.74	0.012
IV	0.98	1.97	1.43	0.012	1.28	0.012	1.32	0.012

Table 8.6: Maximum values of the estimated and observed fractional speed-up ratios, and the height where these occurs, in Case I-IV. All values reported are from a position approximately at the crest.

Table 8.7 lists the values of the fractional speed-up ratio at the heights where the increase in velocity is largest. Results are reported for experimental data, the LSD approach, the ESDU method, the linearized theory of Jackson and Hunt and another simple estimate (Equation 4.5). The percentage deviation of these values from the experimental values are given in Table 8.8. The heights where $\Delta S_{\Delta U_{max}}$ occur are somewhat higher than the height of ΔS_{max} for all the estimation methods. The heights of $\Delta S_{\Delta U_{max}}$ in the experimental results are lower than all the estimated heights in all four cases.

The recommended maximum value in the simple method given by Equation 4.5 is $\Delta S_{\Delta U_{max}} = 1.25$. This is valid for axisymmetric hills, and the maximum for escarpments should be even lower than this, since larger separation bubbles are more likely to form upstream of an escarpment. The results given by Equation 4.5 are said to be generally accurate within ± 15 %, and to have even better agreement on low hills that fit the assumption of linear theory. If the upper recommended value of 1.25 is ignored, the results in Case II-IV are all within this uncertainty range, while the result in Case I is slightly higher than the upper limit. This is quite good for such a simple method considering the very steep slopes in question. It also indicates that the limitation of $\Delta S_{\Delta U_{max}} < 1.25$ is not necessarily correct since the estimated and measured results are higher than this and in good agreement.

The deviations from the experimental values for the fractional speed-up ratio for the LSD approach are -18.9 % (Case IV) to 15.7 % (Case I), for the ESDU method -50 % (Case III) to -14.7 % (Case IV) and for the linearized theory 98 % (Case I) to 178.3 % (Case IV). The poorest agreement between the ESDU method and the experimental data occur close to the ground at the crest, which is also the region with highest speed-up values. This is the reason why the ESDU method seems to give less good results based on Table 8.8. When it comes to these maximum values the LSD approach and the simple proportional relation with the slope given in

Equation 4.5 give the results which fit best with the experimental data. The ESDU method fits less good with these data in the near ground region at the crest. It is clear that the Jackson and Hunt method with linearized theory is not applicable for the steep slopes under consideration. The maximum speed-up values are extremely high, with values of $\Delta S_{\Delta U_{max}}$ up to 4.

Case		I	II	III	IV
H/L		0.53	0.86	0.70	0.98
$\Delta S_{\Delta U_{max}}$	Experiment	1.02	1.43	1.28	1.43
	LSD	1.18	1.17	1.12	1.16
	ESDU	0.78	0.75	0.64	1.22
	0.8ϕ	0.83	1.38	1.12	1.58
	J&H	2.02	3.41	2.80	3.98
l_{max}/H	Experiment	0.020	0.014	0.020	0.012
	LSD	0.069	0.069	0.096	0.096
	ESDU	0.043	0.043	0.060	0.020
	J&H	0.039	0.025	0.031	0.024

Table 8.7: Values of the fractional speed-up ratio ΔS and the corresponding height l_{max}/H where ΔU attains its maximum. All values reported are from a position approximately at the crest. Values from the measured data, LSD approach, ESDU method, Equation 4.5 (0.8ϕ) and linearized theory by Jackson and Hunt (J&H) are reported.

	I	II	III	IV
H/L	0.53	0.86	0.70	0.98
LSD	15.7	-18.2	-12.5	-18.9
ESDU	-23.5	-47.6	-50.0	-14.7
0.8ϕ	-18.6	-3.5	-12.5	10.5
J&H	98.0	138.5	118.8	178.3

Table 8.8: Percentage deviation between the experimental values and the estimates for $\Delta S_{\Delta U_{max}}$ given in Table 8.7.

The results given by the LSD approach were studied thoroughly in Section 8.8.1, and it was seen that this approach for $\phi > 1$ results in larger speed-up values than found in the experiments for all levels and positions near the crest. The only exception is very close to the ground at the crest. This is in accordance with a conclusion by Miller and Davenport (1998) who state that the general trend for methods like the LSD approach is to over-predict the speed-up. All slopes studied by Miller and Davenport were more gentle than the slopes studied here, and the ridges studied have other ridges upstream, as the purpose of the study was to see the effect of complex terrain. The values listed by Miller and Davenport are the maximum values of the fractional speed-up ratio, like the ones in Table 8.6.

Studying only the maximum speed-up can give an incorrect impression of the flow pattern around terrain features. It is clearly seen by the comparison of the LSD approach and the ESDU method with the experimental data (Section 8.8.1 and 8.8.2) that the match of maximum speed-up is not typically representative for the accordance in the rest of the flow. The results in the current section present how much the different methods predict the velocity to increase at the crest, and at which height this typically occurs. This should not be considered as a general measure of how good the experimental data and the different predictions fit.

8.8.5 Potential flow; Case I

Despite the no-slip condition at the wall, the most significant acceleration above the terrain in Case I was found near the ground. This is consistent with the potential flow theory effects found e.g. for the flow over a cylinder or a bump. Although the flow over the hill is viscous and turbulent, most of the flow acceleration along the upstream slope happens so quickly that the flow is mainly dominated by inviscid effects, i.e. by the pressure gradient along the streamline, dP/ds. This can be demonstrated by a simple potential flow calculation. A potential flow source, a sink and a uniform flow can be combined to form a Rankine oval (Section 4.3.5). By suitably spacing the source and sink, a streamline can be found that resembles the shape of the hill, as shown in Figure 8.54(a). The best similarity between a streamline and the terrain in Case I was found for a quite low value of a compared to λ, $\lambda/a = 800$. If $a \to 0$ while λ increases, keeping the product λa constant, a singularity called a doublet is generated. The corresponding body is a circular cylinder. Hence the streamline selected to represent the terrain in Case I is quite similar to a streamline passing some distance above a circular cylinder. The velocity distribution along the streamlines above this surface will then represent the inviscid effects on the flow acceleration above the upstream part of the hill. Obviously the analysis fails on the downstream side due to the flow separation here. From this rather naive calculation the fractional speed-up ratios can be calculated and compared to the ratios from the measurements. It was attempted to fit streamlines above a Rankine oval to the ascending hills in Case II and III as well, but the conformity of the shapes were poor due to the steepness of the hills.

As can be seen from Figure 8.54(b) the agreement at the crest of the hill in Case I is quite good. Experimental data exists for heights up to $z/H_1 = 1$. The potential flow calculation indicates that speed-up effects are also present at higher levels (not shown). The fractional speed-up ratio is 0.095 at the height $z/H_1 = 2$, 0.017 at the height $z/H_1 = 6$ and 0.003 at the height $z/H_1 = 16$. The comparison can be brought a step further by using the estimated fractional speed-up ratio to compute what the upstream reference profile (U_0) would look like at the crest if the acceleration was purely dominated by inviscid effects, as shown in Figure 8.54(c). Again the agreement between the measurement and prediction is seen to be quite good.

According to Freris (1990) potential flow theory is assumed to be valid down to a height level of about $L_{H/2}/10$. Below this the surface roughness becomes more

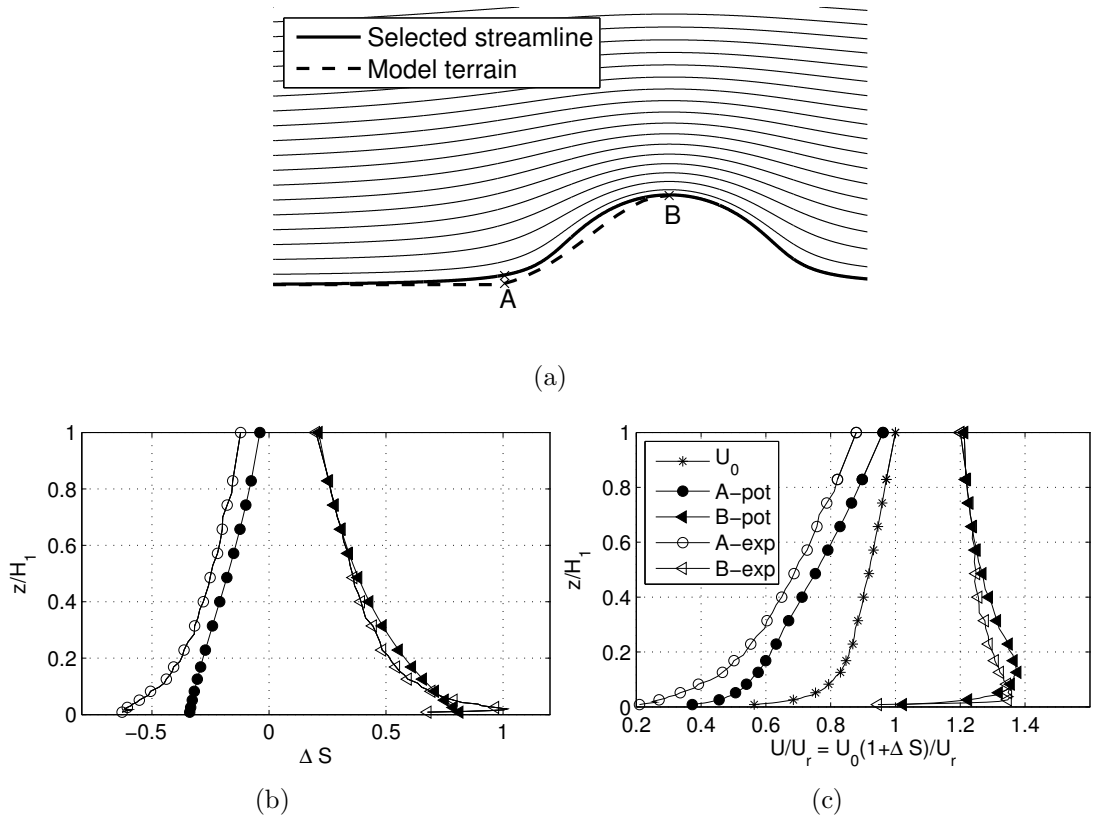

Figure 8.54: Potential flow compared to the experimental results in Case I. Streamlines (a), fractional speed-up ratio (b) and estimated mean velocity profiles (c) at positions A and B from the measured upstream profile $U_0(z)$.

important, so that potential flow theory is no longer applicable. $L_{H/2} = 334.8\ m$ in Case I, so $z/H = L_{H/2}/(10H) = 0.0957 \approx 0.1$. It is clearly seen that the largest discrepancies between the potential flow theory and the measurements are below $z/H_1 = 0.07$. One reason for this comparison with potential theory was to see if the experimental speed-up was larger than this theory, hence indicating an effect of the blocking of the test section in Case I (15 %) . Based on these results, it seems as if the reduction of the test section area caused by the terrain model does not cause a significant increase in velocity.

8.8.6 Numerical calculations

As a part of the Strategic wind energy program 2003-2007 this experimental study was planned to serve as a test case for two numerical flow solvers. These were 3DWind developed by Institute for Energy Technology (IFE), and SIMRA which is developed by SINTEF Energy Research. The calculations by SIMRA were never completed. The results calculated using 3DWind will be summarized below. Karlsen (2008) also did a simple study of Case I and Case IV with the numerical tool

WindSim, but this will not be reported here.

Undheim (2007) carried out 2D simulations with 3DWind for Case III, IV and V. 3D simulations were done for Case III, VIII and IX. 3DWind is a non-linear microscale model. It solves the incompressible Reynolds Averaged Navier Stokes equations on a non-orthogonal grid. The discretisation is based on the finite volum method, and the equations are solved explicitly. Two different turbulence models were used, a one-equation $k-l$ model and a two-equation RNG $k-\epsilon$ model. Both the inflow and the initial conditions were established from measured profiles in an empty tunnel. Since the measured approaching boundary layer only extended outwards to 0.35 m, the profile above this height was tuned to fit the experimental profiles of Case I. This case was chosen since it has the highest terrain model, hence as much as possible of the approaching profile above 0.35 m can indirectly be seen in the measured profiles above the plateau. Periodic boundary conditions were set at the side boundaries, and the top boundary condition was set to a zero-gradient condition in all variables except the vertical velocity. The topography was smoothed towards the side boundaries, instead of vertical cuts as in the physical model.

Undheim studied the results from the numerical calculations thoroughly, and also compared these to the experimental results. The correspondence between the numerical and experimental results at the base of the hill and half-way up the hill in Case III were found to be good. The speed-up estimated by the numerical model at the crest was smaller than in the experiment. Undheim states that this is different from other comparisons with wind tunnel experiments, where the numerical model has tended to overestimate the speed-up at the hilltop. At the end of the plateau, the numerical model predicted a larger speed-up than indicated by the experimental results. This could be due to a numerical instability caused by the sharp crest of the descending hill. The gradient of the numerical results close to the ground was smaller than in the measurements, and this was in accordance with other experiences according to Undheim. This deviation could be caused by numerical diffusion. The turbulence level was found to be generally best matched with the RNG $k-\epsilon$ model. The results for Case IV were found to be quite similar to the results observed for Case III, except that the numerical model overestimated the speed-up at the sharp crest. The numerical model failed to simulate the region with three-dimensional separated flow downstream of the sharp crest.

The numerical model predicted lower rotating velocities in the separated region between the two mountains in Case V than the experiments. The general velocity level above the downstream plateau was similar for the numerical and experimental results, but the speed-up observed closest to the ground in the experiments was not predicted by 3DWind. The simulated recirculation zone in the wake of the downstream mountain in Case V was almost identical to the recirculation zone in Case III, even though the mean velocities above the last hill in Case V was reduced compared to Case III. There are no experimental measurements in this region.

Case VIII was used to evaluate the numerical models ability to predict turning of the flow. The speed-up at the first and low ridge was quite accurately simulated. The velocities downstream of this ridge were similar closest to the ground, but the results predicted by the numerical model further out had a smaller gradient than the

experimental results. This deviation in the velocity gradient was also found above the plateau, and the numerical results were generally lower than the experimental velocities. The simulated turning of the flow was seen to extend further out than in the experimental results.

Case IX was the most complex case, and numerical simulations were only carried out for the smooth case (Case IXa). The agreement between the simulations and the experiments in this case were similar to the other cases. The results at the first ridge were quite similar, and the speed-up at the second ridge and the mean velocities in the recirculation zones were underestimated by 3DWind. The diffusion was overestimated in the simulations, hence leading to smaller gradients in the flow. In general the generation of turbulence was best predicted by the $k - l$ model, but the simulated dissipation of turbulence in both models was lower than in the wind tunnel measurements.

Undheim (2007) concluded that the complexity of the terrain was a demanding test for the flow solver.

Chapter 9

Conclusions and suggestions for further work

9.1 Conclusions

An extensive wind tunnel study of turbulent flow above complex terrain has been carried out. The objective was to generate a test case for numerical models, and to investigate flow above complex terrain with a view to wind turbine siting. A large number of profiles were measured above the model where the flow was characterized by velocity speed-up, separation and flow recovery. Flow conditions that are very favorable from a wind power point of view were found in some cases, and locations that should clearly be avoided for wind farms were observed in other cases.

It was seen that the flow conditions above rounded hills with mean slopes in the range $27.9° - 40.7°$, followed by a plateau, were quite similar.

- The mean velocity profiles showed increased velocities along the entire plateau compared to the incoming velocity profile. Variations for the different slopes were mainly seen closest to the ground. The maximum fractional speed-up ratio, observed closest to the ground at the very crest, increased with increasing slope.

- Starting from a velocity profile typical for flow in coastal regions, the mean velocity was found to become very uniform with height.

- The turbulent energy was only marginally affected by the flow acceleration. Along with significantly increased velocities, this lead to a strong reduction in the turbulence intensity.

Both the flow acceleration, the increased mean velocity uniformity and the reduced turbulence intensity are advantageous for wind turbine operations. The wind energy available is increased, while the loads on the turbines are decreased. One of these rounded hills was compared to a straight slope ending in a sharp crest. The slopes of these two hills were similar.

- The flow conditions at the very crests were quite similar. As expected the sharp crest caused flow separation and severe degradation of the flow conditions at low heights above the plateau.

- Close to the ground, 0.3 hill heights downstream of the sharp crest, the turbulence was increased almost by a factor 6 compared to the inflow.

- While the mean flow and turbulence uniformity was good for $z > 0.2H$ in the rounded case, similar uniformity was only found for $z > 0.6H$ in the sharp crest case, implying that wind turbine rotors must be located considerably higher in this type of terrain to avoid severe dynamic loads.

When two mountains with different heights were combined with a deep valley between, the flow separated at the end of the first plateau and formed a strong vertical motion in the valley. This strongly affected the flow above the downstream plateau.

- With the highest mountain located upstream, the flow above this mountain was unaffected by the mountain downstream. Since the upstream mountain was about 40 % higher than the one downstream, the flow above the downstream plateau was severely affected by the separated region formed in the valley. Very little gain in the mean velocity was evident above the downstream mountain compared to the inflow. However, the increase in turbulence level was significant at all heights in the measurement domain, typically increased by a factor 2.5.

- In the reversed case with the lower mountain upstream, increased velocities were seen at all heights and positions at the higher mountain downstream. This was the case despite the fact that the lower upstream mountain produced separation at the crest, and that a massive separated region was formed in the valley. However, the speed-up was decreased compared to the isolated case. The turbulence levels were increased compared to the isolated case, but the turbulence intensity was still reduced compared to the inflow.

One of the terrain modules (shown in Figure 8.32) was tested with three combinations of two different surface roughnesses in the inflow and on the model. The most striking results were:

- The flow above the first ridge was seen to depend on both the roughness in the inflow and on the model. The flow conditions above the second ridge was quite similar for the cases with the same model roughness, independent of the inflow conditions. Hence, the flow downstream of the second ridge depended on the local surface roughness only.

- Separation occurred at the lee side of the second ridge. The region of separation was larger for the rough surface than the smooth surface, while the resulting turbulent stresses were significantly higher above the smooth than the rough surface.

The results were compared to several simple estimation methods, and the ESDU method was seen to give results which agreed well with the experimental data for the isolated embankments with rounded hills. Undheim (2007) used the experimental results as a test case for the flow solver 3DWind, and concluded that the complexity of the terrain model was a demanding test for the numerical tool.

9.2 Recommendations for further work

Several terrain effects have been investigated in the present study, and this has been done with respect to wind farm siting. An interesting follow-up would be to put wind turbines on the terrain model, to see the combined effect of the flow above the complex terrain and the turbines. Experiments with turbines would have implied that a part of the terrain model was reproduced at a larger scale.

It is obvious that a wind tunnel study of a terrain model with a size as in the present study will suffer from scale effects. This effect is very difficult to quantify. One way of finding out how severely this affects the present study could be to repeat some of the measurements at another, preferably much smaller, scale.

The effect of surface roughness was also studied for one of the cases in the present study. It was seen that the inflow conditions affected the flow only a short distance downstream of the leading edge of the model, while the flow above the terrain model was highly dependent on the local surface roughness. Increased roughness could have been added to the entire model, i.e. all terrain modules, to see how the flow depends on the roughness. Increasing the surface roughness of the terrain model will also generate a flow more similar to atmospheric flows.

Bibliography

H.-E. Albrecht, M. Borys, N. Damaschke, and C. Tropea. *Laser Doppler and Phase Doppler Measurement Techniques*. Springer-Verlag, 2003.

J. Armitt and J. Counihan. The simulation of the atmospheric boundary layer in a wind tunnel. *Atmospheric Environment*, 2(1):49–71, 1968.

S.P.S. Arya. *Introduction to micrometeorology*. Academic Press, Inc., 1988.

S.P.S. Arya, M.E. Capuano, and L.C. Fagen. Some fluid modeling studies of flow and dispersion over two-dimensional low hills. *Atmospheric Environment*, 21(4): 753–764, 1987.

M. Athanassiadou and I.P. Castro. Neutral flow over a series of rough hills: A laboratory experiment. *Boundary-Layer Meteorology*, 101(1):1–30, 2001.

K. Ayotte and D.E. Hughes. Observations of boundary-layer wind-tunnel flow over isolated ridges of varying steepness and roughness. *Boundary-Layer Meteorology*, 112(3):525–556, 2004.

K.W. Ayotte. Computational modelling for wind energy assessment. *Journal of Wind Engineering and Industrial Aerodynamics*, 96(10-11):1571–1590, 2008.

P.H.A. Barbosa, M. Cataldi, and A.P.S. Freire. Wind tunnel simulation of atmospheric boundary layer flows. *Journal of the Brazilian Society of Mechanical Sciences*, 24(3):177–185, 2002.

H.H. Bruun. *Hot-wire Anemometry: Principles and Signal Analysis*. Oxford University Press, 1995.

T. Burton, D. Sharpe, N. Jenkins, and E. Bossanyi. *Wind Energy Handbook*. John Wiley & Sons, 2001.

M.H. Buschmann and M. Gad–el–Hak. Recent developments in scaling of wall-bounded flows. *Progress in Aerospace Sciences*, 42:419–467, 2007.

S. Cao and T. Tamura. Experimental study on roughness effects on turbulent boundary layer flow over a two-dimensional steep hill. *Journal of Wind Engineering and Industrial Aerodynamics*, 94(1):1–19, 2006.

T. Cao and T. Tamura. Effects of roughness blocks on atmospheric boundary layer flow over a two-dimensional low hill with/without sudden roughness change. *Journal of Wind Engineering and Industrial Aerodynamics*, 95(8):679–695, 2007.

P. Carpenter and N. Locke. Investigation of wind speeds over multiple two-dimensional hills. *Journal of Wind Engineering and Industrial Aerodynamics*, 83(1-3):109–120, 1999.

M. Coantic and J.-J. Lasserre. On pre-dissipative bumps and a Reynolds-number-dependent spectral parameterization of turbulence. *European Journal of Mechanics - B/Fluids*, 18(6):1027–1047, 1999.

J. Counihan. An improved method of simulating an atmospheric boundary layer in a wind tunnel. *Atmospheric Environment*, 3(2):197–200, 1969.

J. Counihan. Adiabatic atmospheric boundary layers: A review and analysis of data from the period 1880-1972. *Atmospheric Environment*, 9(10):871–905, 1975.

D.B. DeGraaff and J.K. Eaton. A high-resolution laser Doppler anemometer: design, qualification, and uncertainty. *Experiments in Fluids*, 30(5):522–530, 2001.

ESDU. Mean wind speeds over hills and other topography. Item no. 91043. ESDU International, London, December 1993.

A.D. Ferreira, M.C.G. Silva, D.X. Viegas, and A.G. Lopes. Wind tunnel simulation of the flow around two-dimensional hills. *Journal of Wind Engineering and Industrial Aerodynamics*, 38(2-3):109–122, 1991.

J.J. Finnigan, M.R. Raupach, E.F. Bradley, and G.K. Aldis. A wind tunnel study of turbulent flow over a two-dimensional ridge. *Boundary-Layer Meteorology*, 50: 277–317, 1990.

L.L. Freris. *Wind energy conversion systems*. Prentice-Hall, Inc., 1990.

P.M. Gerhart, R.J. Gross, and J.I. Hochstein. *Fundamentals of fluid mechanics*. Addison-Wesley Publishing Company, Inc., 1992.

M.J. Glanville and K.C.S. Kwok. Measurements of topographic multipliers and flow separation from a steep escarpment. Part II. Model-scale measurements. *Journal of Wind Engineering and Industrial Aerodynamics*, 69-71:893–902, 1997.

W. Gong and A. Ibbetson. A wind tunnel study of turbulent flow over model hills. *Boundary-Layer Meteorology*, 49:113–148, 1989.

N. Hutchins and I. Marusic. Evidence of very long meandering features in the logarithmic region of turbulent boundary layers. *Journal of Fluid Mechanics*, 579:1–28, 2007.

H. Imamura, T. Tsumanuma, J. Kurokawa, and H. Katsuchi. Wind tunnel investigation of flow over various escarpment shapes. In *Proc. of the 7th Asian International Conference on Fluid Machinery*, 2003. No. 20020.

H.P.A.H. Irwin. The design of spires for wind simulation. *Journal of Wind Engineering and Industrial Aerodynamics*, 7(3):361–366, 1981.

T. Ishihara, K. Hibi, and S. Oikawa. A wind tunnel study of turbulent flow over a three-dimensional steep hill. *Journal of Wind Engineering and Industrial Aerodynamics*, 83(1-3):95–107, 1999.

P.S. Jackson and J.C.R. Hunt. Turbulent wind flow over a low hill. *Quarterly journal of the Royal Meteorological Society*, 101:929–955, 1975.

M. Jensen and N. Franck. Model-scale tests in turbulent wind. Part I: Phenomena dependent on the wind speed. Danish Technical Press, Copenhagen, 1963.

T. Jensen and M.L. Fossdal. Vindkraft - Produksjonsstatistikk. Technical report, Norges vassdrags- og energidirektorat, May 2009.

J.C. Kaimal and J.J. Finnigan. *Atmospheric boundary layer flows: their structure and measurement*. Oxford University Press, Inc., 1994.

J.A. Karlsen. Turbulensmodellering i komplekst terreng. En numerisk analyse av strømning over en todimensjonal terrengmodell. Master's thesis, Norwegian University of Science and Technology, 2008.

H.G. Kim, C.M. Lee, H.C. Lim, and N. H. Kyong. An experimental and numerical study on the flow over two-dimensional hills. *Journal of Wind Engineering and Industrial Aerodynamics*, 66(1):17–33, 1997.

P.-Å. Krogstad, R.A. Antonia, and L.W.B. Browne. Comparision between rough- and smooth-wall turbulent boundary layers. *Journal of Fluid Mechanics*, 245: 599–617, 1992.

D.R. Lemelin, D. Surry, and A.G. Davenport. Simple approximations for wind speed-up over hills. *Journal of Wind Engineering and Industrial Aerodynamics*, 28(1-3):117–127, 1988.

W.D. Lubitz and B.R. White. Wind-tunnel and field investigation of the effect of local wind direction on speed-up over hills. *Journal of Wind Engineering and Industrial Aerodynamics*, 95:639–661, 2007.

J.F. Manwell, J.G. McGowan, and A.L. Rogers. *Wind Energy Explained*. John Wiley & Sons Ltd, 2002.

C.A. Miller and A.G. Davenport. Guidelines for the calculation of wind speed-ups in complex terrain. *Journal of Wind Engineering and Industrial Aerodynamics*, 74-76:189–197, 1998.

S. Mochizuki and F.T.M. Nieuwstadt. Reynolds-number-dependence of the maximum in the streamwise velocity fluctuations in wall turbulence. *Experiments in Fluids*, 21(3):218–226, 1996.

D.E. Neff and R.N. Meroney. Wind-tunnel modeling of hill and vegetation influence on wind power availability. *Journal of Wind Engineering and Industrial Aerodynamics*, 74-76:335–343, 1998.

H.A. Panofsky and J.A. Dutton. *Atmospheric turbulence*. John Wiley & Sons, Inc., 1984.

C.C. Pellegrini and G.C.R. Bodstein. The height of maximum speed-up in the atmospheric boundary layer flow over low hills. *Journal of the Brazilian Society of Mechanical Sciences and Engineering*, 26(3):249–259, 2004.

A.E. Perry, K.L. Lim, and S.M. Henbest. An experimental study of the turbulence structure in smooth- and rough-wall boundary layers. *Journal of Fluid Mechanics*, 177:437–466, 1987.

M.R. Raupach, R.A. Antonia, and S. Rajagopalan. Rough-wall turbulent boundary layers. *Applied Mechanichs Reviews*, 44(1):1–25, 1991.

J.A. Rice. *Mathematical Statistics and Data Analysis*. Wadsworth Publishing Company, 1995.

K. Røkenes and P.-Å. Krogstad. A wind tunnel study of neutral flow above complex terrain features. European Wind Energy Conference, Athens, Greece, 2006. Poster Track / Session Code: BL3.

K. Røkenes and P.-Å. Krogstad. A wind tunnel study of flow above complex terrain. The 3rd PhD Seminar on Wind Energy in Europe, Pamplona, Spain, 2007.

K. Røkenes and P.-Å. Krogstad. Wind tunnel simulation of terrain effects on wind farm siting. *Wind Energy*, 12(4):391–410, 2009.

B.-S. Shiau and C.-T. Hsieh. Wind flow characteristics and Reynolds stress structure around the two-dimensional embankment of trapezoidal shape with different slope gradients. *Journal of Wind Engineering and Industrial Aerodynamics*, 90:1645–1656, 2002.

B.-S. Shiau and S.-C. Hsu. Measurement of the Reynolds stress structure and turbulence characteristics of the wind above a two-dimensional trapezoidal shape of hill. *Journal of Wind Engineering and Industrial Aerodynamics*, 91:1237–1251, 2003.

P. Sierputowski, J. Ostrowski, and A. Cenedese. Experimental study of wind flow over the model of a valley. *Journal of Wind Engineering and Industrial Aerodynamics*, 57(2-3):127–136, 1995.

W.H. Snyder and I.P. Castro. The critical Reynolds number for rough-wall boundary layers. *Journal of Wind Engineering and Industrial Aerodynamics*, 90(1):41–54, 2002.

S. Song and J. Eaton. The effects of wall roughness on the separated flow over a smoothly contoured ramp. *Experiments in Fluids*, 33(1):38–46, 2002.

C.J. Strataridakis, B.R White, and A. Greis. Turbulence measurements for wind-turbine siting on a complex terrain. Technical report, American Institute of Aeronautics and Astronautics, 1998. Paper No. AIAA-99-0054.

R.B. Stull. *An introduction to boundary layer meteorology*. Kluwer Academic Publishers, 1988.

T. Takahashi, S. Kato, S. Murakami, R. Ooka, M.F. Yassin, and R. Kono. Wind tunnel tests of effects of atmospheric stability on turbulent flow over a three-dimensional hill. *Journal of Wind Engineering and Industrial Aerodynamics*, 93 (2):155–169, 2005.

O. Undheim. A comparison of CFD simulations with wind tunnel measurements. Technical Report IFE/KR/F-2007/215, Institute for Energy Technology (IFE), 2007.

B. Venås. *Experiments and numerical realisations of complex turbulent flows*. PhD thesis, Norwegian University of Science and Technology, 1998.

Z.Y. Wang, E.J. Plate, M. Rau, and R. Keiser. Scale effects in wind tunnel modelling. *Journal of Wind Engineering and Industrial Aerodynamics*, 61(2-3):113–130, 1996.

W. Weng, P.A. Taylor, and J.L. Walmsley. Guidelines for airflow over complex terrain: model developments. *Journal of Wind Engineering and Industrial Aerodynamics*, 86:169–186, 2000.

B.R. White, R. Coquilla, and J. Phoreman. Existing hillside and proposed building 75 rooftop stacks. A wind-tunnel study of exhaust stack emissions from the National Tritium Labeling Facility (NTLF) located at Lawrance Berkeley National Laboratory, Berkeley, CA. Technical report, University of California, 2001.

F.M. White. *Viscous fluid flow*. McGraw-Hill, Inc., 1991.

Appendix A

The process of generating the incoming boundary layer

It was intended to generate a boundary layer with a power law exponent close to $\alpha = 0.11$, a depth of 350 mm and a turbulence level in accordance with this as in the atmospheric boundary layer. As a first approach in the search for the best setup of turbulence generators, already existing triangular wedge generators were tested. These were 51 cm high, and 8 generators were placed at the entrance to the test section with a centreline spacing of 34-38 cm. The resulting boundary layer, measured at the centreline of the test section about 4-5 meters downstream of the generators, was only 250 mm thick. The mean velocity profile approximately followed a power law and approached the freestream velocity of the tunnel above 250 mm.

New, and higher spires made of wood were constructed in an attempt to generate a thicker boundary layer. These were similar to the ones designed by Irwin (1981), as described in Section 5.2. The splitter plates were slightly lower than the spires, while the one described by Irwin had the same height as the spires. This is probably of minor influence, in accordance with results in the work by Irwin. Irwin also stated that the most important design factor was that the part of the spires facing the main flow direction was of approximately triangular shape. The first version of the wooden spires in the current study had a height of $h_s = 80$ cm, a base-length $b_s = 15$ cm and a centreline distance of $33 - 35$ cm. The reason for the quite high spires was that it was assumed that they should be longer than the tested triangular wedge generators, and the practical fact that it is easier to reduce the height of spires than creating new ones. The resulting mean velocity profile was not even close to a power law profile. Reduced velocities compared to the freestream velocity were observed up to a level as high as the spires. The velocities below $0.1 - 0.2\delta$ could be reasonably well fitted to a logarithmic law or power law, but the velocities in the region $0.2 - 1\delta$ increased almost linearly with height. This was probably due to the significant obstruction of the flow in the lowest part (above 40 % solidity near the surface), hence the flow was struggling to catch up with the freestream velocity at higher levels.

As a consequence of this, 15 cm were cut off the lower part of the spires. The

resulting boundary layer was 600 mm and showed similar characteristics as the previous, although the linear part of the profile was now decreased. For this version, three velocity profiles were measured quite close to each other across the flow, but with different positions relative to one specific spire. This was done to see if the distance from the spires was long enough to achieve a lateral uniformity, i.e. that a wavy lateral velocity profile depending on the positions of the spires was not revealed. These three velocity profiles were seen to be quite similar. The next approach was to add roughness blocks to the floor downstream of the spires. Closest to the spires was a 1.20 m long board covering the width of the tunnel with 186 blocks of size $45 \times 45 \times 86$ mm. This was followed by a 0.8 m long board covering the width of the tunnel with 184 lower blocks of size $45 \times 45 \times 32$ mm. The resulting mean velocity profiles were actually quite similar to the profiles obtained with 15 cm higher spires and no blocks.

Several similar attempts were done, experimenting with even lower wooden spires, the original triangular wedge generators and combinations with roughness blocks. Also, the distance from the spires to the measurement location was increased to 6 meters in the search for a more uniform flow field across the tunnel test section. This was done, despite that the work by Irwin (1981) and others had concluded that a distance of $6h_s$ should be enough to ensure lateral uniformity. The results were not satisfactory, especially due to lack of uniformity across the tunnel. This lead to a more thorough examination of the spanwise velocity variations. This latter experiment revealed surprisingly large and unacceptable discrepancies in mean velocity across the tunnel, indicating a complex and non-homogeneous flow field. The flow in an empty tunnel was seen to be quite homogeneous, hence it seemed as if the spires which were inserted at the entrance to the test section interacted with the flow in a way that resulted in an very inhomogeneous flow field. Further measurements were done at three different heights at a span of 1.5 m across the tunnel. The setup during this tests consisted of the evenly distributed and 51 cm high triangular wedge generators and roughness blocks of two different sizes. A rough image of the flow pattern was as follows: At all height levels, the maximum velocity was found in the region near the centreline of the tunnel. The velocities then decreased outward, before increasing again. The outermost measurement points were at a distance 0.65 m from the sidewalls.

Due to the non-homogeneous results using quite low generators, another approach was taken. Five spires reaching from the floor to the roof were tested as turbulence generators. The shape of the mean velocity profile was not advantageous compared to what was generated by the lower spires, as the mean velocities in the lower parts were too high. An inclined plate was then put at the floor, attempting to slow down the velocities at the lowest levels, but this did not improve the results. The board was then replaced by the largest roughness blocks. Three mean velocity profiles were measured across the tunnel, revealing significant spanwise velocity discrepancies also for these large spires reaching from floor to roof. Another result of the significant blocking of the entrance to the test section with this setup, was that the tunnel had to be run at a maximum to achieve an appropriate velocity at the level above the floor where the terrain model was planned to be. This caused a lot

of noise, and a significant heating of the air in the tunnel. The temperature in the tunnel test section increased by as much as 25 degrees during one hour. Increasing temperature influences the measurements for most measurement methods, causing uncertainties, even if temperature corrections are included.

The method of trial and error was continued, in the search for an acceptable inflow profile. The wooden triangular spires were cut further, attempting to get a fuller velocity profile in the lowest part. Also, since these spires covered a much smaller part of the tunnel area, the extremely high temperature increase was avoided. Eight evenly distributed spires with height 52 cm was found to generate the profile which was closest to the pursued one. As a check, velocities were measured across the tunnel test section to see if the flow was homogeneous. The flow field across the test section was also measured at several distances downstream of the spires to see the development of the flow. At a distance of 1 meter downstream of the spires there were only quite small and regular velocity differences across the flow at each height above the floor. The deficits were of the order of 0.5 m/s, and seemed to depend on whether the measured position was in the shadow of a spire or along a line in between two spires. As the flow passed further downstream, these structures became less distinct and a wavy pattern with larger velocity differences, symmetrical around the centreline and apparently independent of the local flow field downstream of each spire, approached. The flow across the tunnel test section 6 meters downstream of the evenly distributed wooden spires of height 52 cm is shown in Figure A.1. These results were measured with a pitot tube. The standard deviations of the mean velocities at the heights z =10, 110, 210 and 310 mm were 1.1, 1.1, 0.9 and 0.6 m/s respectively. Similar as for the flow generated by triangular wedge generators, large spanwise discrepancies were seen in the mean velocity about 6 meters downstream of the spires. As opposed to the results for triangular wedge generators, the mean velocities were now significantly higher towards the sides of the tunnel compared to along the centreline. This lead to further experimenting with different spires near the sides of the tunnel, as it was suspected that acceleration along the curved part of the contraction could be the explanation for the increased velocities towards at the outermost part of the measured region. An attempt was made with a combination of the 52 cm high spires and large spires at the sides. This variant was discarded, as the turbulent length scales and hence the turbulence profiles could become inhomogeneous across the tunnel.

All in all, a lot of measurements with different variants when it came to type, size, combinations and positioning of turbulence generators were tested. This included triangular wedge generators, wooden spires of different heights, roughness blocks of different sizes, grass covered surface, half spires at the walls, spires from floor to roof, and an inclined plate. A large number of measurements were carried out at a variety of positions in the test section to study the effect of different turbulence generators in all three directions, i.e. the development in the direction of the flow, the homogeneity across the flow, and the flow characteristics with height. High spires from floor to roof caused an unacceptable increase of temperature. These spires, and several combinations of these and other turbulence generating devices, did not give mean velocities with characteristics as aimed at either. All three types of spires failed to

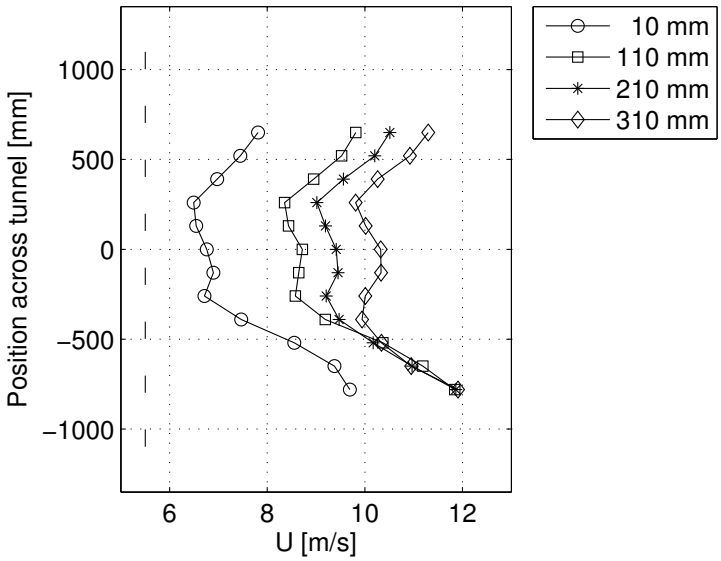

Figure A.1: Mean velocities measured with a pitot tube 6 meters downstream of evenly distributed spires. The positions of the spires are illustrated by the vertical lines to the left.

generate a homogeneous flow field across the tunnel. As the wooden spires without other turbulence generating equipment downstream gave the mean velocity profile closest to the one intended for, new and thorough investigations were done with unevenly distributed spires. The streamwise turbulence characteristics were studied parallel with the mean velocities. The turbulence spectra were also investigated.

Eight unevenly distributed wooden spires were eventually chosen, as described in Section 7.3. The positions of the spires were symmetrical around the centreline, and the centre of the spires were located 44, 57, 70 and 83 *cm* away from the centreline. The large differences between the flow field generated by evenly distributed spires and this final setup with unevenly distributed spires are clearly seen by comparing Figure A.1 with Figure 7.3. For the latter, the standard deviations of the mean velocities at the heights z =10, 110, 210, 310, 410 and 510 mm were 0.13, 0.13, 0.12, 0.13, 0.16 and 0.16 m/s respectively, hence significantly reduced compared to the setup with evenly distributed spires.

Appendix B

Quality of data in more detail

This appendix covers different aspects of data quality, uncertainties and the similarity to atmospheric flows. The effects of blocking due to the narrowing of the test section by the model is also included.

B.1 On the similarity with atmospheric flow

Dimensionless numbers and requirements for validity of wind tunnel experiments were presented in Chapter 5. The model heights are $0.15 - 0.35\ m$ and the approaching velocities at these height levels are $10 - 13\ m/s$. This corresponds to Reynolds numbers in the range 10^5 to $3 \cdot 10^5$ based on U and H. The scale of the experiment is approximately 1:1000. With mean velocities of the same order as relevant atmospheric velocities, the Reynolds numbers are also about an order of 1000 less than in the atmosphere. Charts similar to a Moody chart for pipe flow indicate that some Reynolds number effects will be present. At the same time, Reynolds numbers of the order of some hundred thousand are commonly assumed to be enough to compare experimental flows to real atmospheric flows.

As discussed in Section 8.1 the roughness Reynolds number of the flow is about 0.13, and this indicates that the flow is close to smooth. Hence, the flow in this study differs from most atmospheric flows which are fully rough. This can cause the turbulence near the surface to be incorrectly modelled compared to atmospheric conditions. The roughness Reynolds number in Case IXc, where extra roughness has been added to all surfaces, is 4.74. This makes the surface fully rough, hence the flow near this surface is more representative of atmospheric flows.

Froude number matching can be ignored for neutrally stable conditions, as in the current study. The Prandtl number already matches since the fluid is air. The Eckert number can be ignored due to incompressible flow. It is only recommended to study heights up to 0.15δ if atmospheric flows are simulated in a wind tunnel. This is due to the absence of Coriolis effects in non-rotating wind tunnels. Rossby number similarity can be ignored in this region. The results in this experiment were studied all the way up to a height which was equal to the level taken to be the thickness of the approaching boundary layer.

As pointed out earlier, the current study was carried out with the main perspec-

tive to create a test case for numerical simulations. Flow solvers can be set up to reproduce the experiment. Hence, a comparison between the experimental and numerical results can be carried out, even if the experiment is not fully representative of atmospheric flows.

B.2 Blocking

The maximum blocking of the tunnel cross section caused by any terrain module in the current study was 15 %. The percentage blocking in Case I-IV are listed in Table B.1. Blocking caused by the measuring equipment and the traversing system it was mounted on is not included in these numbers. It is not recommended that the model fills more than $5 - 15$ % of the cross section of the tunnel at any location (see Chapter 5). Hence, blocking is an important issue in this study, and it has been considered both in the theory part and in the discussion of the results.

Case I/II/V/VI	Case III/IV	Case VII	Case VIII	Case IX
15 %	11.5 %	13.5 %	6 %	16 %

Table B.1: Maximum blocking by the terrain model.

B.3 Positioning of terrain model and measurement point

The terrain module which constitutes Case I-II was quite large. The terrain was made out of Styrofoam, and was mounted on a wooden plate. As time passed, the materials changed in different ways. As a result, the underside of the wooden plate became slightly curved. It was attempted to force the large module into the original shape by fixing it to the floor in the wind tunnel with large screws. This was only partly successful. As the main focus in the flow above such terrain often is at the region near the crest, this part was mounted as horizontal as possible. Hence, the largest deviations from the original shape and the theoretical terrain model was at the end of the plateaus in Case I and II. This can have affected the flow by introducing slightly increased vertical velocities above the plateau, but the effect is considered to be unimportant compared to the other and much more significant effects of the terrain in this study.

In general the positioning of the probe was a challenge, as the probe was mounted on a traversing system in the centre of the test section, with few references. When the probe was positioned above the measurement point (seeing the xy-plane), a level could be used to confirm that the probe was normal to the xy-plane. The laser beam was then also seen at the surface, making it easy to find the correct position. When mounting the probe at the side of the measurement point (seeing the xz-plane), no reference was present except the walls in the tunnel. Different methods had to be

applied to find the correct position above ground, dependent on the topography near the measured position. In some locations, the position of the measurement volume in the vertical direction had to be adjusted by the help of equipment like a folding rule. In some other positions, with the probe tilted towards the ground, the zero-level was set at the point of maximum reflections from the ground and then adjusted to the first measuring height by moving the traverse. The surface also often had some unevenness, complicating the determination of the correct vertical positioning of the measurement volume. After this positioning was done, the tilt of the probe in the vertical plane could be measured using a level. The required tilt in the horizontal plane used in a few measurement positions was difficult to quantify.

The LDA probe was used both with and without an expander. The size and weight increased significantly when adding the expander, hence altering both the natural frequency and the drag of the probe. The probe was always shaking to some extent during measurements, despite that the fixing device was strengthened with a supporting rack pushed against the surface in most of the measured positions. The supporting rack and the mounting of the probe are shown in Figure B.1. The shaking varied with the size of the probe, the flow in the region of measurements and whether or not is was possible to utilize the supporting rack. The positioning of the probe was done with zero velocity in the tunnel, so due to the probe drag there was always a probability that the measurement volume was slightly displaced when the tunnel started.

Altogether this gives a positioning uncertainty of the measurement point in the vertical direction of approximately ± 1 mm. The corresponding horizontal uncertainty in the direction of the main flow is approximately ± 2 mm. These positioning errors will have the largest impact near the ground and in regions with separated flow, where the spatial variation of the flow field is largest. The uncertainty in the spanwise direction is about ± 1 mm. This is not of importance in Case I-IV, which are approximately two-dimensional.

The LDA probe was mounted on a traversing mechanism driven by stepper motors. This was used for moving the probe vertical during measurements of each profile. The accuracy of this traverse was estimated to be better than 0.1 mm. This is quite small, and considered to be included in the estimates given above for the positioning of the measurement point.

It is normally desired to make the LDA measurement volume as small as possible to have a good spatial resolution. A small measurement volume is especially important in regions with large mean velocity gradients. Errors due to the size of the measurement volume in the current study were considered negligible compared to other uncertainties, such as the positioning of the measurement volume.

The model scale was chosen to be quite large just to reduce the error related to the measurement positions. It is important to notice that an error of 2 mm in model scale corresponds to only 2 m in full-scale, which is a relatively small distance in the field of atmospheric flows.

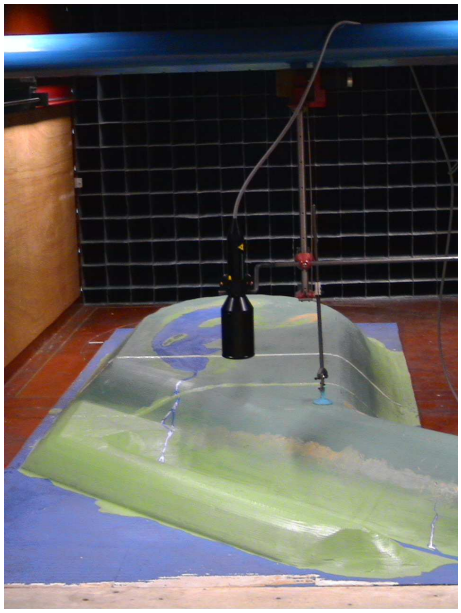

Figure B.1: Fixing device for the LDA equipment. This photo illustrates the probe with an expander, mounted on the traverse and with an additional supporting rack. The terrain is Case VIII.

B.4 Errors due to tilted LDA probe

The LDA probe was tilted by about 7° in several positions in the current study. The theory of how this affects the measured velocities was described in Section 6.5. A tilt of $\beta = 7°$ with $v = 0$ causes an error in the measured instantaneous vertical velocity, w, which is less than 1 % (Equation 6.11). On the other hand, the errors caused by a spanwise velocity deviating from zero may be significant. The latter was considered to mainly influence the results obtained in the region with highly three-dimensional flow near the ridges in Case VIII.

A simple test was done in a position in between the two ridges ($x_m = 3254$ and $y_m = 3185$) in Case VIII. This position was chosen due to a large velocity component along the valley. The measurements were done orthogonal to the ridge, so that the probe was aligned along the valley. Hence, in a tilted position, a part of the horizontal velocity component along the valley was also included as a part of the vertical velocity. Data was obtained at 10 measurement points at height levels $100 - 200\ mm$, both with and without a tilted probe. The horizontal velocities orthogonal to the ridge measured with these two settings were quite similar, indicating that the same points were measured. The horizontal velocity along the valley was measured by mounting the probe above the flow. These measurements were not obtained simultaneously with any of the vertical velocities, and the horizontal velocity normal to the ridge deviated some from the corresponding velocity measured with the probe at the side of the measurement position. It was considered that the velocity along the valley at least was representative enough for this test. Large errors in the vertical velocity measured with a tilted probe were seen at all height levels. The cause of

this was that the measurement points were in a separated flow with vertical mean velocities close to zero, at the same time as the velocities along the probe was high ($\approx 8\ m/s$). It is seen from Equation 6.14 that the errors introduced to w are highly dependent on the fraction v/w (the fraction of the mean values is close to 8/0 in this example). At the uppermost point, $z = 200\ mm$, positive velocities were observed in all three directions. The vertical mean velocity measured in this point with a non-tilted probe was $W = 1.36\ m/s$, and the corresponding velocity with the probe tilted 7° was $W = 2.47\ m/s$. This yields an error caused by the tilting of the probe of 82 %. If Equation 6.11 is applied to the mean velocity measured with a tilted probe (even though it is derived for the instantaneous velocities), the velocity is actually *increased* by 0.02 m/s. This correction assumes that the velocity along the probe is zero, while it really is about 8 m/s. The velocity measured with a tilted probe corrected by Equation 6.14 yields 1.52 m/s, which is 12 % larger than the velocity observed without the tilt. The improvement would probably have been even better if the exact mean velocity along the probe was available. This example emphasize the importance of considering the velocity component along the probe when tilting is introduced, as this is crucial for whether the errors are acceptable or not.

Appendix C

Independent papers

1. Røkenes and Krogstad (2006). A wind tunnel study of neutral flow above complex terrain features. Paper following a poster presentation at the European Wind Energy Conference, Athens, 2006 (EWEC 2006). Published online.

2. Røkenes and Krogstad (2007). A wind tunnel study of flow above complex terrain. Paper following a presentation at The 3rd PhD Seminar on Wind Energy in Europe, Pamplona, 2007. Published online.

3. Røkenes and Krogstad (2009). Wind tunnel simulation of terrain effects on wind farm siting. Published in *Wind Energy*.

A wind tunnel study of neutral flow above complex terrain features

Kjersti Røkenes and Per-Åge Krogstad
Department of Energy and Process Engineering
Norwegian University of Science and Technology (NTNU)
N-7491 Trondheim, NORWAY
Phone: +47 73 59 08 16
Fax: +47 73 59 34 91
E-mail: kjersti.rokenes@ntnu.no

Summary

The turbulent flow above a complex terrain model has been studied in a wind tunnel. The model is generic and based on locations in coastal areas of current interest for wind farms. Several terrain features are represented in the model. It is split up into modules which can be studied both separately and together to cause an even more complex flow. The flow is approximately 2D in some cases, and highly 3D in others. The inflow boundary layer is typical for wind profiles above open sea.

A large number of profiles were measured. These were taken in regions where the flow was characterised by velocity speed-up, separation and flow recovery. Laser Doppler Anemometry was used for the measurements, and quantities like mean values and turbulent stresses were calculated.

Flow conditions that are very favourable from a wind power point of view were found. Rounded hills with various slopes resulted in speed-up and quite homogenous velocities with height above ground, while the stresses were only significantly altered in a thin layer close to the ground. In the case of a sharp ridge instead of a rounded hill, increased turbulence levels and less favourable mean velocity profiles were observed. When the flow passed a higher mountain before it entered a rounded hill, the turbulence level increased up to very high altitudes and the mean velocity was reduced.

1 Introduction

Norway is at the brink of a significant wind energy development. Most of the locations under consideration are in complex terrain along the Norwegian coastal line. These are areas with high mean wind velocities and therefore have great potential for energy production.

A wind tunnel study of a generic terrain model with typical features from this mountainous terrain has been carried out, with an objective to study effects of complex terrain on the wind field at potential turbine sites. This study is also part of a larger project and will serve as a comprehensive test case for calibration and verification purposes in numerical investigations.

2 Experimental setup

2.1 Wind tunnel and generation of inflow boundary layer

The study was carried out in a closed circuit wind tunnel at NTNU. The test section is 2.7m wide, 1.9m high and 11m long. The experimental setup in the tunnel test section is sketched in figure 1. Spires were set up at the entrance to simulate an atmospheric boundary layer. The distance from the spires to the leading edge of the model was 6m. The reference plane of the model was 12mm above the tunnel floor. To compensate for this, a plate was put on the floor and extended 2.4m upstream of the model, and the passage from the floor to this level was shaped as a gentle ramp.

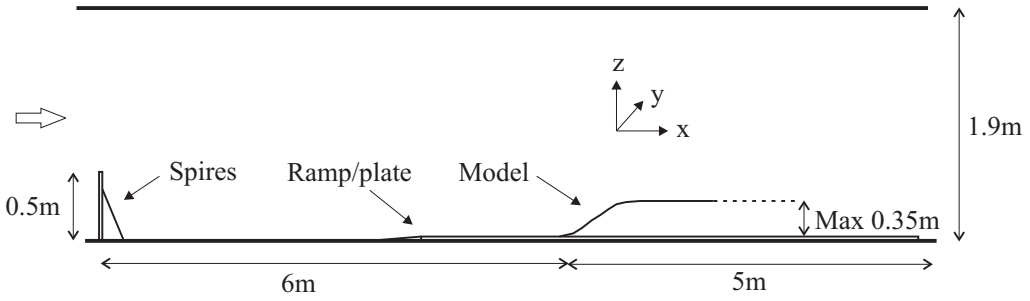

Figure 1: Sketch of wind tunnel test section with spires, plate and model.

2.2 Terrain model

The model is milled out of styrofoam with 5mm contour intervals, then filled in and finally painted. This makes the surface quite smooth. The roughness was considered to be similar to the surface upstream of the model, so effects due to roughness changes were not expected.

The base of the model is about 4m x 4m, and its maximum height is 0.35m (see figures 1 and 2). The model consists of many different features, which are all based on locations of current interest for wind farms in Norway. The model was split into appropriate modules. This division gave the opportunity to study some terrain features separately before modules were put together to produce a more complex flow.

The maximum blocking of the tunnel cross section caused by a module was 15%. This should be taken into consideration when the data are studied. However, one of the main purposes of this experiment was to obtain data to be compared to numerical simulations. This effect can easily be accounted for in the calculations.

2.3 Velocity measurements

Laser Doppler Anemometry (LDA) with a two component fiber optic probe was used for all the measurements reported here. A frequency shift allowed measurement of velocities without directional ambiguity. The probe was mounted on a traversing system 0.5m, and in some cases 0.3m, away from the measurement volume. The flow was seeded with fog particles. The fog was injected continuously through a hole in the floor at the entrance to the test section.

A total of 40 points were measured in every profile. The sampling time was between 45-60 seconds, and the sampling frequency was about 1000Hz. Statistical quantities like mean values (U, V, W) and stresses $(\overline{u^2}, \overline{v^2}, \overline{w^2}, \overline{uw}, \overline{uv})$ were calculated. Two velocity components were measured in all cases, and some profiles were measured a second time with the probe in a perpendicular position to obtain the third velocity component.

2.4 Measurement cases and positions

A total of 9 cases with equal inflow and roughness conditions were studied. Figure 2 shows the 9 different cases with flow directions and measurement positions indicated. Some of the cases consist of a single model module and others of two modules combined. In each case several profiles were measured along a line parallel to the sidewalls of the test section. The number of profiles in the nine different cases varied, as can be seen from the dots in the figure. To avoid the effects of the boundary layers along the sidewalls, measurements were taken as close to the centerline of the test section as possible.

Due to the large amount of measurements, only some of the cases and available data will be presented here. As shown with black lines in figure 2, the cases presented are number 3, 4 and 5. We will focus on the longitudinal mean velocity and longitudinal normal stress component only.

2.4.1 Two-dimensionality

In cases 1-6 the flow was considered to be approximately two-dimensional. This two-dimensionality was confirmed by measurements.

3 Results

3.1 Undisturbed inflow boundary layer

The neutrally stratified undisturbed boundary layer is shown in figure 3. This is the mean value of 4 profiles positioned 0.3m apart across the test section with only spires and plates in the tunnel. The measurements were taken about 6m downstream the spires, which is right in front of the leading edge of the model when it is present (figure 1). The arrangement of the spires was chosen to generate conditions similar to atmospheric wind above open sea with regard to the mean velocity profile, turbulence intensity and turbulence spectra. Homogeneity across the test section was verified by measuring 5 profiles across the flow, both with and without the different model cases in the tunnel.

The wind profile in the atmospheric boundary layer is in micrometeorology often described by a power law, $U(z)/U(z_{ref}) = (z/z_{ref})^{\alpha}$. The velocity profile in the undisturbed boundary layer can be reasonably represented by a power law with an exponent $\alpha = 0.10$ up to the height 0.3m. A fit of the mean velocity in the lower part of the undisturbed boundary layer gives the values $u_* = 0.5$m/s, $z_0 = 0.004$mm and $d_0 = 0.9$mm in the well-known logarithmic velocity profile $U/u_* = \kappa^{-1} ln((z - d_0)/z_0)$. $\kappa = 0.41$ is von Karman's constant, z_0 the roughness length, u_* the friction velocity and d_0 the displacement height. Converted from a model scale of 1:1000 to full-scale conditions, this corresponds to a value of $z_0 = 0.004$m. Both this roughness length, the

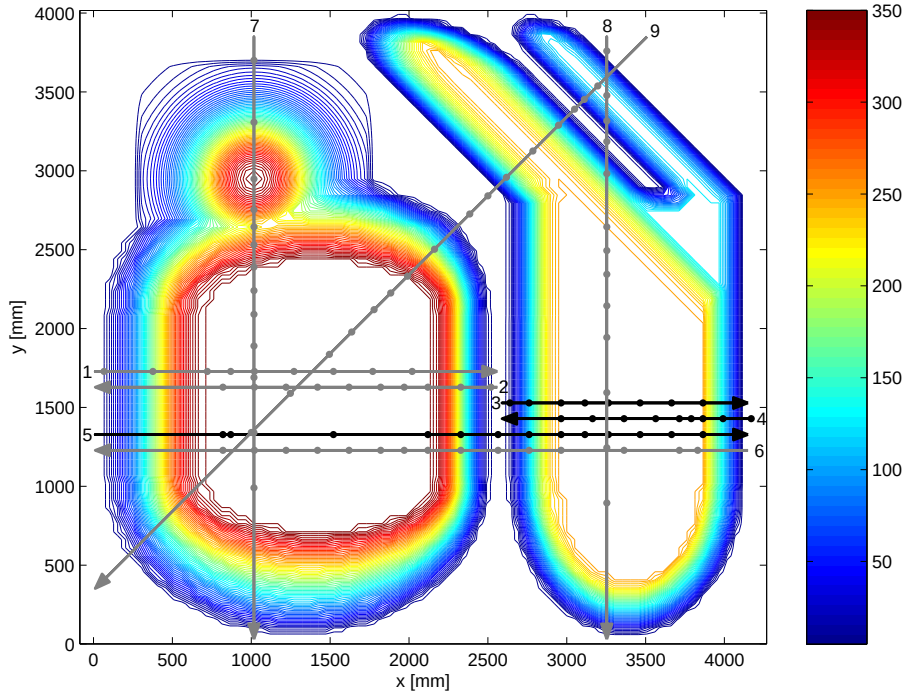

Figure 2: The model with 5mm contour intervals. The measurements were taken along the 9 lines. Arrows point out flow directions. The area under the lines implies the longitudinal part of the model located in the tunnel in each case. Positions for all the measured profiles are marked by dots. Case 1-6 are shown separately in this figure, but were all measured along the same line as case 4. The black lines (3, 4 and 5) are the measured cases for which the results are discussed in the current paper, while measurements along the grey lines are not reported here.

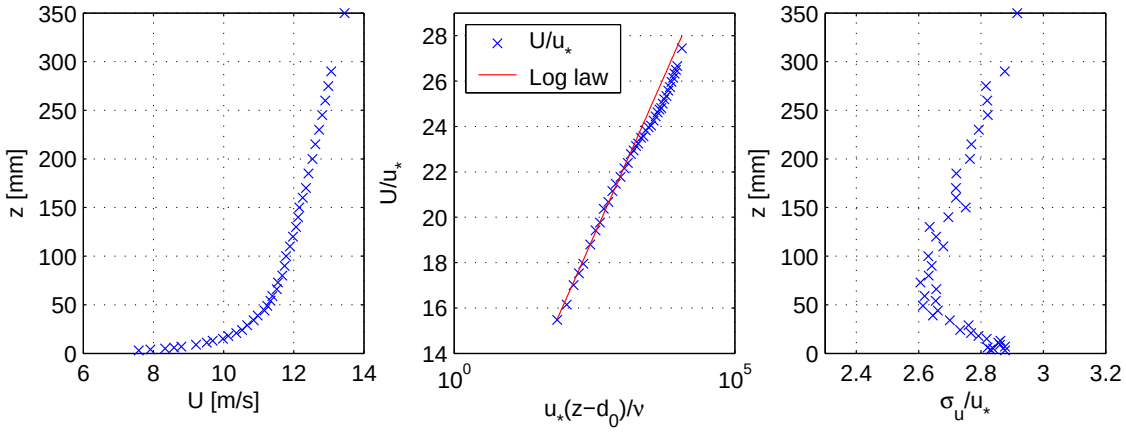

Figure 3: Incoming undisturbed turbulent boundary layer.

adapted α and a full-scale boundary layer height of 300m are values typical for flow above open sea [1].

The ratios of standard deviations to friction velocity near the surface in the longitudinal and vertical directions are $\sigma_u/u_* = 2.8$ and $\sigma_v/u_* = 1.2$ respectively. These values agree reasonably well with corresponding field data and values reported in other wind tunnel experiments[1, 2, 3].

The roughness Reynolds number of the flow, $u_* z_0/\nu$ (ν is the kinematic viscosity), is about 0.13. This is less than typical values about 2.5 given to indicate fully rough flow [4]. But the near-wall area where the flow might be slightly dependent on Reynolds number, is well below the lowest measurement point in the current study.

3.2 Flow above model

3.2.1 Case 3 and 4, a comparison

Figure 5 shows mean values of the longitudinal velocity component above a rounded hill (case 3), compared to the mean value in the undisturbed boundary layer. Almost homogeneous mean velocities with height are observed near the top, even though the incoming flow is quite sheared. Increased velocities are seen at all measured height levels along the entire plateau. As shown in figure 6, the stresses are only altered in a thin layer close to the ground. Hence the turbulence intensity ($I_u = \sigma_u/U$) at the wind turbine impeller plane is reduced considerably. These are beneficial effects in the context of wind power.

The speed-up factor, $S = U/U_0$, can be read from figure 6. It is highest close to the ground at the crest, where it attains a value of 2.4. The factor near the ground decreases as the flow passes along the plateau, while it is more stable at higher levels. At the level above ground corresponding to the hill height, the speed-up factor is about 1.2 along the entire plateau.

The terrain in case 4, as shown in figure 7, is quite similar to case 3. As shown in figure 4 the slopes of the hills are approximately the same, but case 3 is rounded while case 4 is straight with a sharp ridge. The effect of this is clearly seen by comparing figures 5 and 6 with figures 7 and 8. The mean velocity in case 4 is reduced compared to the reference boundary layer and the levels of turbulence are significantly increased near the ground due to separation behind the sharp edge. As seen in the right part of figure 8 the velocity fluctuations are reduced and spreads upwards as the flow passes along the plateau. Both the speed-up factor and the turbulence levels varies significantly with height above ground at typical levels of operation for wind turbine impellers.

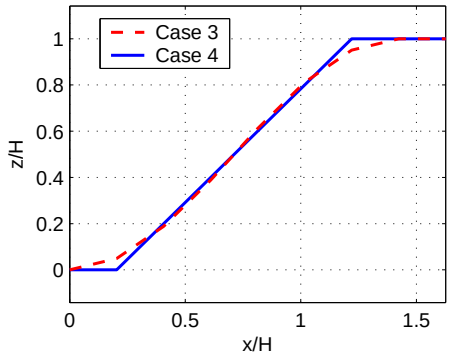

Figure 4: A comparison of upstream hills in case 3 and 4. The rounded hill has a maximum slope of 46°. The straight side has a slope of 44.5° .

3.2.2 Case 5

The effects of letting the flow pass a higher mountain and a valley before it enters the rounded hill can be seen in figures 9, 10 and 11.

The flow above the terrain is compared to the undisturbed boundary layer in figures 9 and 10. Note that the velocity scale for the mean values and the RMS values are not the same. Separation is clearly seen at the downstream side of the highest mountain. The peak of the RMS value appears at the level of maximum velocity differences.

In figure 11, the results above the rounded hill normalised with the inflow boundary layer are shown. The selected positions are the same as in case 3. The mean velocities at the crest of the second mountain are lower than the undisturbed boundary layer, but the velocity deficit is reduced as the flow develops along the plateau. The separation downstream of the large mountain causes highly increased levels of turbulence compared to the undisturbed boundary layer as shown in figure 11. These increased turbulence levels are apparent from the ground and up to levels as high as the upstream mountain. They are still present at the end of the plateau, even if the turbulence has diminished substantially. Compared to case 4 (figure 8), it is seen that the highest level of turbulence is not quite as high as in case 4, but is reached at a higher elevation above ground. This might be more important to consider than the changes to the mean velocity when it comes to wind power, because the increased turbulence level will not just pass under the rotor as it might do in case 4.

The flow above each of the mountains in case 5 was also compared to the flow above each of the two mountains when they were studied separately (case 1 and 3). Both the mean and RMS values above the first (and highest) mountain in case 5 were similar to what was seen in case 1 with the isolated mountain. This confirms that the flow was not affected by the lower mountain downstream, as could be expected. But as can be seen from the results presented in this paper, the flow above the lower mountain downstream was considerably affected by the upstream mountain. All the advantageous effects above the isolated rounded hill (case 3) are absent with a higher mountain upstream (case 5).

4 Final comments and conclusions

A large number of profiles have been measured. These were taken in regions where the flow was characterised by velocity speed-up, separation and flow recovery.

Near the top of the rounded edges almost homogeneous mean velocities with respect to height was found, even though the incoming flow was quite sheared. Speed-up factors at all height levels and all positions along the plateaus are in the range 1.2-2.4. The stresses in these cases were only significantly altered in a thin layer close to the ground and the turbulence intensity was hence considerably reduced compared to the incoming flow. This is very favourable from a wind turbine point of view.

However, in other cases or wind directions, increased shear and turbulence levels were obtained. The flow above a rounded hill was also studied with a higher mountain upstream, and it was compared to the flow above a similar isolated slope with a sharp ridge. All the beneficial effects seen in the case of the rounded hill were then absent.

References

[1] J. Counihan. Adiabatic atmospheric boundary layers: A review and analysis of data from the period 1880-1972. *Atmospheric Environment*, 9(10):871–905, 1975.

[2] M.R. Raupach, R.A. Antonia, and S. Rajagopalan. Rough-wall turbulent boundary layers. *Applied Mechanichs Reviews*, 44(1):1–25, 1991.

[3] H.A. Panofsky and J.A. Dutton. *Atmospheric turbulence*. John Wiley & Sons, Inc., 1984.

[4] W.H. Snyder and I.P. Castro. The critical Reynolds number for rough-wall boundary layers. *Journal of Wind Engineering and Industrial Aerodynamics*, 90(1):41–54, 2002.

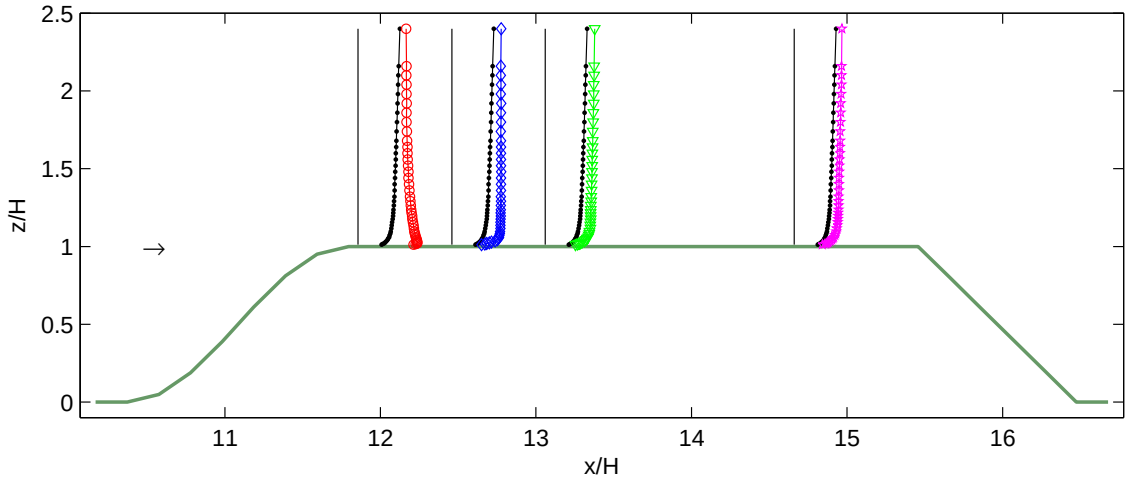

Figure 5: Case 3 (see figure 2), flow from left to right. Profiles of mean longitudinal velocity component (coloured markers), compared to the undisturbed boundary layer (black markers). The black simple lines indicates measurement positions and zero velocity.

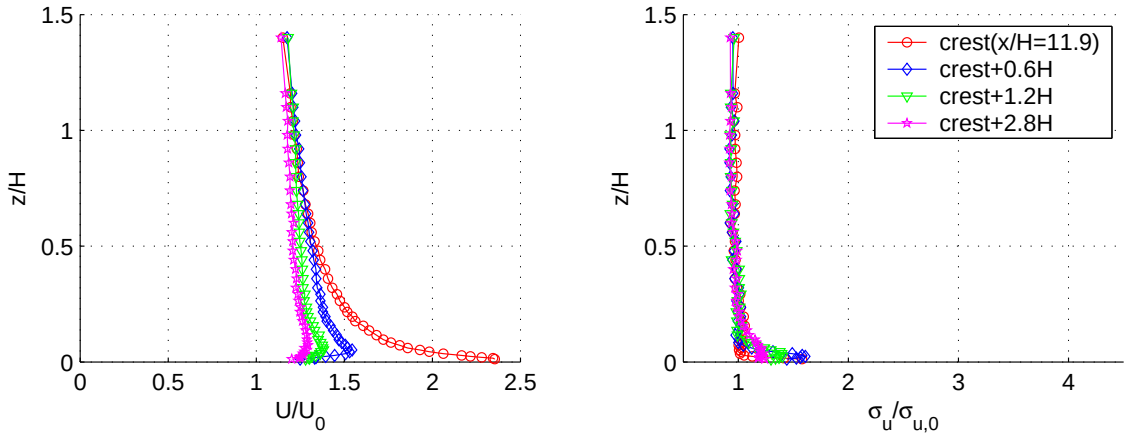

Figure 6: Mean value and RMS profiles in case 3 normalised with the undisturbed boundary layer (figure 3). Colours/markers as in figure 5. Note that all axes are identical to the axes in figures 8 and 11.

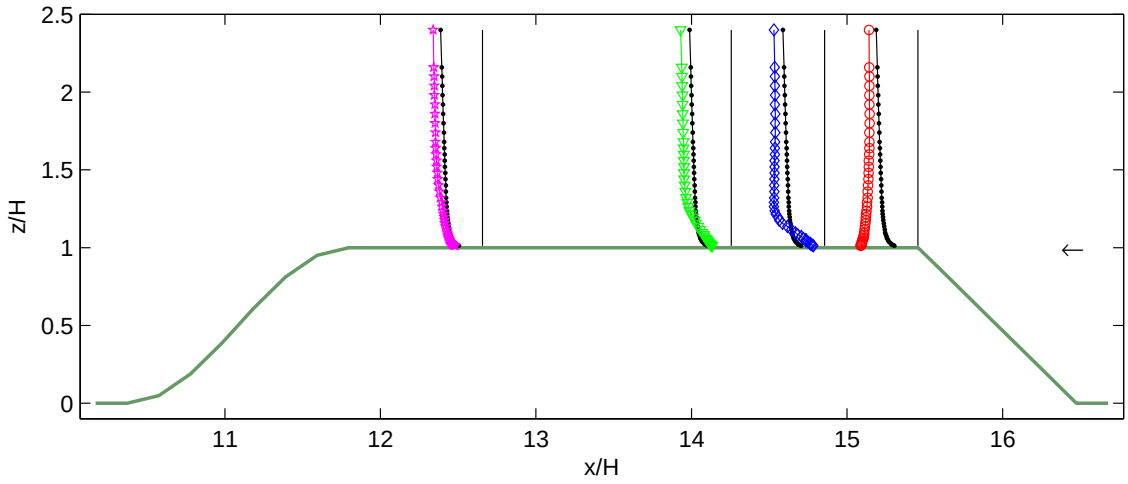

Figure 7: Case 4 (see figure 2), flow from right to left. Profiles of mean longitudinal velocity component (coloured markers), compared to the undisturbed boundary layer (black markers). The black simple lines indicates measurement positions and zero velocity.

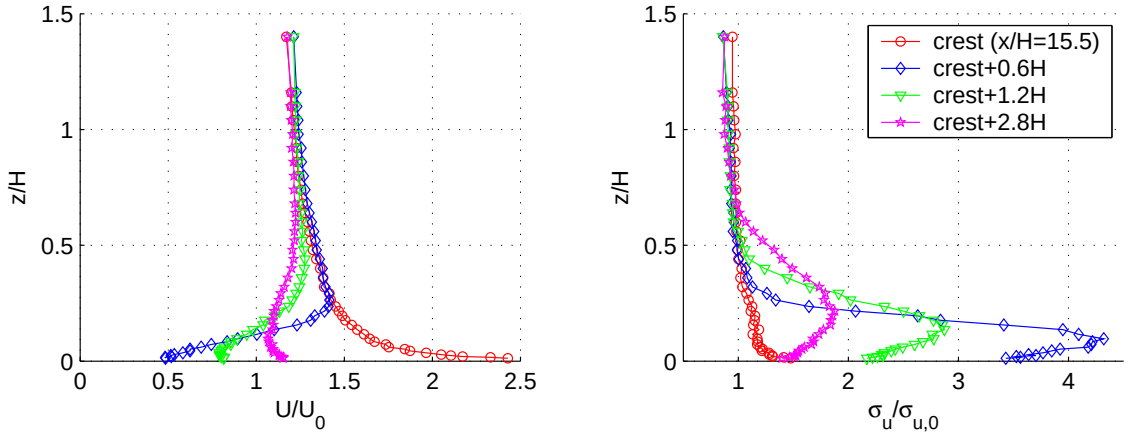

Figure 8: Mean value and RMS profiles in case 4 normalised with the undisturbed boundary layer (figure 3). Colours/markers as in figure 7.

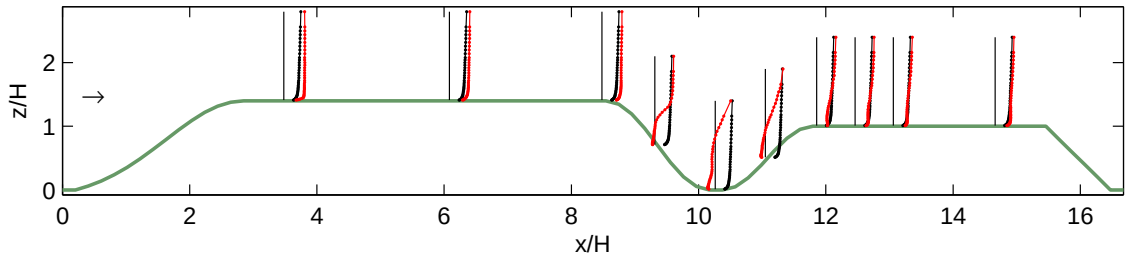

Figure 9: Case 5, flow from left to right. Profiles of mean longitudinal velocity component (red markers), compared to the undisturbed boundary layer (black markers). The black simple lines indicates measurement positions and zero velocity. H is the height of the lowest mountain.

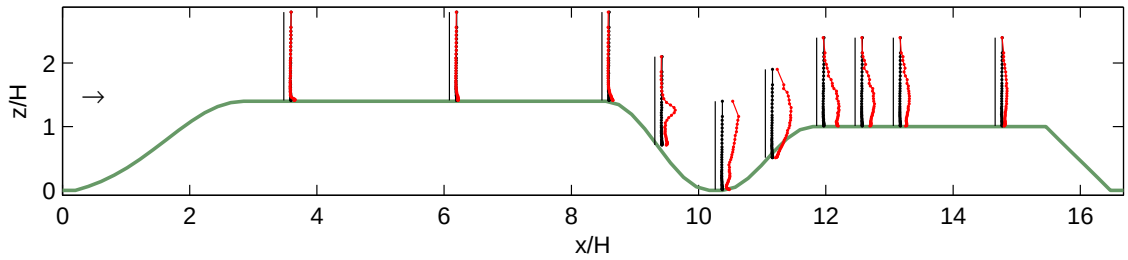

Figure 10: Case 5, flow from left to right. RMS values of longitudinal velocity component (red markers), compared to the undisturbed boundary layer (black markers). The black simple lines indicates measurement positions and zero velocity. H is the height of the lowest mountain.

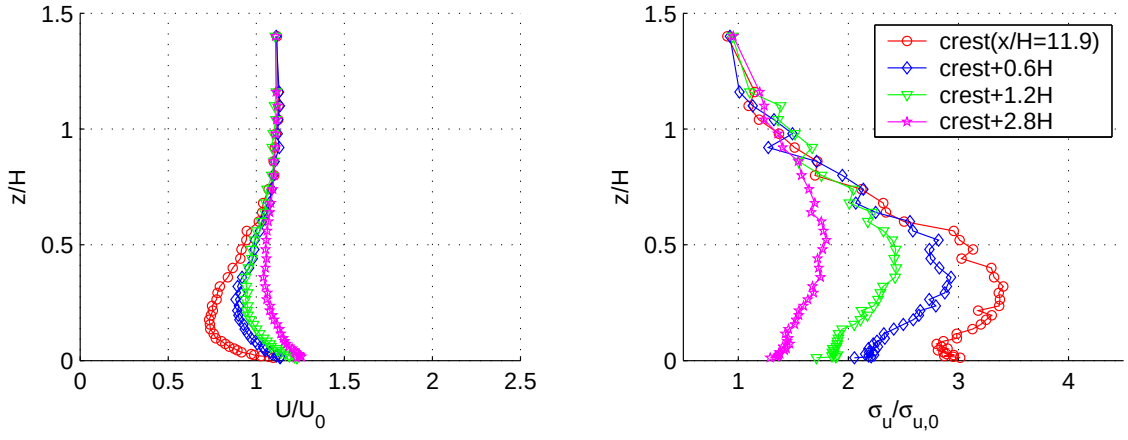

Figure 11: Mean value and RMS profiles in case 5 normalised with the undisturbed boundary layer (figure 3). Terrain as in figures 9 and 10. Measurement positions and colours/markers are identical to case 3 (figure 5).

A wind tunnel study of flow above complex terrain

Kjersti Røkenes and Per-Åge Krogstad
Department of Energy and Process Engineering
Norwegian University of Science and Technology (NTNU)
N-7491 Trondheim, NORWAY
E-mail: kjersti.rokenes@ntnu.no

Abstract

This paper describes the results from an extensive wind tunnel study of the effects of complex terrain on the wind field. The model consists of a number of generic terrain features found for existing and planned wind turbine farms along the Norwegian coastline. Data was obtained using LDA and shows that relatively small changes in the hill geometries may severely change the mean and turbulent velocities at heights typical of large scale turbines. It was also found that surface roughness effects can have a serious effect on the flow even at turbine rotor heights due to its effect on the flow separation characteristics.

1 Introduction

Most of the locations under consideration for wind farms in Norway are in complex terrain along the coastline. These are areas with high mean wind velocities and therefore have great potential for energy production. A wind tunnel study of a generic terrain model with typical features from this mountainous terrain has been carried out, with an objective to study effects of complex terrain on the wind conditions at potential turbine sites.

This study was designed to serve as a comprehensive test case for calibration and verification purposes in numerical investigations.

2 Experimental setup

2.1 Wind tunnel and generation of inflow boundary layer

The study was carried out in a closed circuit wind tunnel at NTNU. The test section is 2.7m wide, about 1.9m high and 11m long. The experimental setup in the tunnel test section is sketched in Figure 1. Spires were set up at the entrance to simulate an atmospheric boundary layer. The distance from the spires to the leading edge of the model was 6m. The reference plane of the model was 12mm above the tunnel floor. To compensate for this, a plate was put on the floor and extended 2.4m upstream of the model, and the passage from the floor to this level was shaped as a gentle ramp.

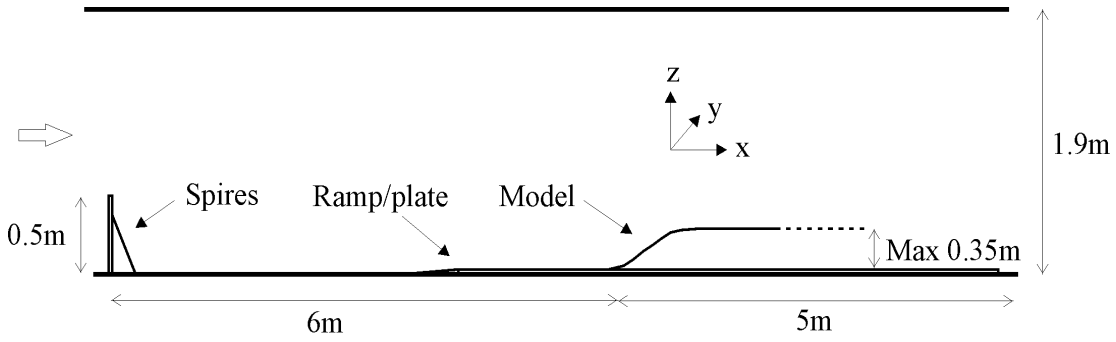

Figure 1. Sketch of wind tunnel test section with spires, plate and model.

2.2 Terrain model

The model is generic, and consists of several features, which are all based on locations of current interest for wind farms in Norway. The model was split into appropriate modules. This division gave the opportunity to study some terrain features separately, before modules were put together to produce a more complex flow. The terrain, and hence the flow, is approximately 2D in some cases, while highly 3D in others. The base of the model is about 4m x 4m, and its maximum height is 0.35m.

This model surface is quite smooth. It was considered to be similar to the wind tunnel wall upstream of the model, so effects due to roughness changes were not expected.

2.3 Velocity measurements

Laser Doppler Anemometry (LDA) with a two component fiber optic probe was used for all the measurements reported here. A frequency shift allowed measurement of velocities without directional ambiguity. The probe was mounted on a traversing system 0.5m, and in some cases 0.3m, away from the measurement volume. The flow was seeded with fog particles which were injected continuously through a hole in the floor at the entrance to the test section. A total of about 40 points were measured in every profile. The sampling time was between 45-60 seconds, and the sampling frequency was about 1000Hz. Statistical quantities like mean values (U , V , W) and turbulent stresses (σ_u^2, σ_v^2, σ_w^2, $\overline{u'w'}$, $\overline{u'v'}$) were calculated. Two velocity components were measured in all cases, and some profiles were measured a second time with the probe in a perpendicular position to obtain the third velocity component.

2.4 Measurement cases and positions

A total of 9 cases with equal inflow and roughness conditions were studied. One of these cases was also studied with varying inflow and roughness conditions. Figure 2 shows the contours of the model with the 9 different cases with flow directions and measurement positions indicated. Some of the cases consist of a single model module, and others of two modules combined. In each case several profiles were measured along a line parallel to the sidewalls of the test section. To avoid the effects of the boundary layers along the sidewalls, measurements were taken as close to the centerline of the test section as possible. The data presented here are from case 3, 4 and 9. We focus on the longitudinal mean velocity and longitudinal normal stress component.

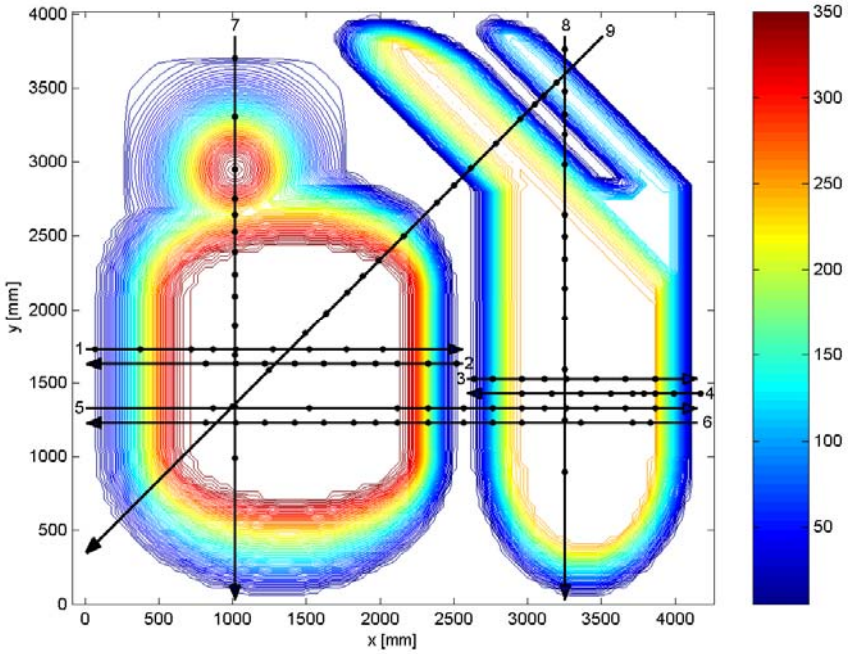

Figure 2. Terrain model with 5 mm contour intervals. Measurements were taken along the 9 lines. Arrows point along the flow directions. Positions for the measured profiles are marked by dots. Case 1-6 were all measured along the same line as case 4. 3, 4 and 9 are discussed in the current paper

.

3 Results

3.1 Undisturbed inflow boundary layer

The neutrally stratified undisturbed boundary layer is shown in Figure 3. This is the mean value of 4 profiles positioned 0.3m apart across the test section with only spires and plates in the tunnel. The measurements were taken about 6m downstream the spires, which is right in front of the leading edge of the model when it is present. The arrangement of the spires was chosen to generate conditions similar to atmospheric wind above open sea with regard to the mean velocity profile, turbulence intensity and turbulence spectra.

The wind profile in the atmospheric boundary layer is in micrometeorology often described by a power law, $U(z)/U(z_{ref}) = (z/z_{ref})^{\alpha}$. The velocity profile in the undisturbed boundary layer can be reasonably represented by a power law with an exponent $\alpha = 0.09$ up to the height 0.3m. Converted from a model scale of 1:1000 to full-scale conditions, the roughness length corresponds to a value of z_0 = 0.004m. This roughness length, the adapted α and a full-scale boundary layer height of 300m are all typical values for flow above open sea [1]. The power spectrum measured in the inflow at a height corresponding to 30m in full-scale is shown in Figure 4, It agrees quite well with Von Karman's model for power spectra when fitted with a characteristic length scale for the large scale motion of L=0.164m at model scale (L=164m at full-scale).

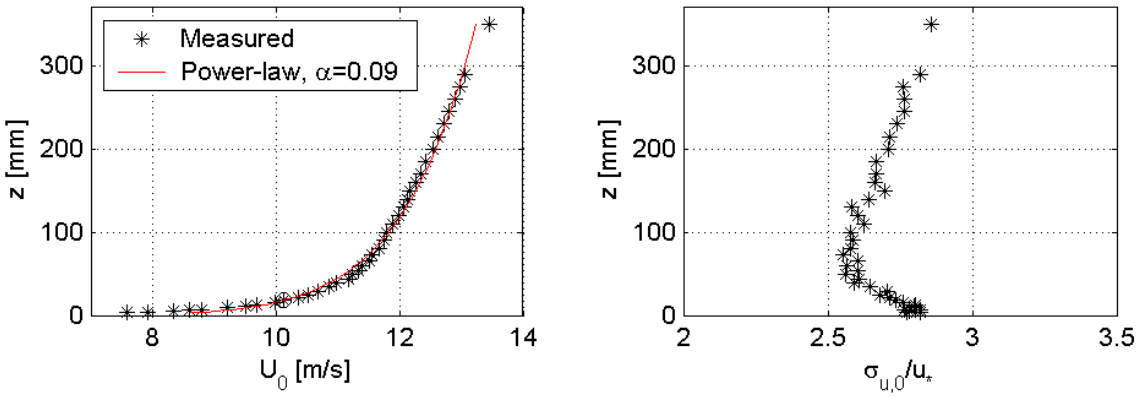

Figure 3. Incoming undisturbed turbulent boundary layer.
The friction velocity is $u_* = 0.5m/s$

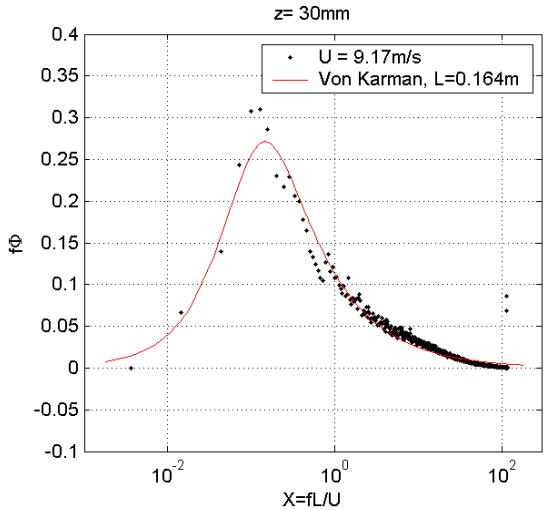

Figure 4. Power spectrum in the inflow boundary layer compared to Von Karman's model.

3.2 Case 3 and 4, a comparison

For case 3, measurements were taken at 8 stations (see Figure 2) for which data will be presented for the 4 stations shown in Figure 5a. In this case the flow is accelerating up a rounded hill before reaching the plateau where the wind turbines will be located. The fractional speed-up ratio is defined as $\Delta S = (U - U_0)/U_0$, and values for the given positions are shown in Figure 6a. Increased velocities are seen at all heights along the entire plateau. ΔS is highest close to the ground at the crest, where it attains a value of 1.4. Near the ground it decreases as the flow passes along the plateau, while it is more stable at higher levels. At the level above ground corresponding to the hill height, the speed-up factor is about 0.2 along the entire plateau. A wind turbine with a rotor plane covering a full-scale height range from 50m to 150m is illustrated. The mean velocities at these heights above the terrain are 20-50% higher than at the corresponding heights in the undisturbed boundary layer. As shown in Figure 6b, the longitudinal normal stresses are only altered in a thin layer close to the ground. Hence the turbulence intensity $I_u = \sigma_u / U$ at the wind turbine rotor plane is reduced considerably. These are beneficial effects in the context of wind power.

The average uphill slopes in case 3 and 4 are approximately the same, but case 3 is rounded while case 4 is straight with a sharp crest. The effect of this is clearly seen by comparing Figure 6 and 7. The mean velocities near the ground in case 4 are reduced compared to the reference boundary layer, and the levels of turbulence are significantly increased. This is due

to a small region of separated flow downstream of the sharp edge. As seen in Figure 7b the velocity fluctuations are reduced, and spreads upwards, as the flow passes along the plateau. Both the fractional speed-up ratio and the turbulence levels vary significantly with height above ground at typical levels of operation for wind turbine rotors.

3.3 Case 9, smooth vs. rough surface

Case 9 was measured with the following three roughness combinations:

- smooth - smooth surface in inflow and smooth model
- smooth/rough - smooth surface in inflow and rough model
- rough - rough surface in inflow and rough model

Results for the longitudinal mean velocities measured in the positions labeled a-h in Figure 8, are shown in Figure 9. The first thing worth noticing is the effect of the inflow compared to the effect of the roughness on the model. The mean velocity in the inflow (a) is similar for the smooth and smooth/rough variant as it should be, while it is decreased in the rough case. The combined effect of inflow and roughness on the model can be seen on the first crest (b). In all following profiles the effect of the different inflow profiles has vanished, the smooth/rough and rough profiles are approximately equal. Hence the only differences seen downstream of the first crest is due to the roughness on the model.

Above the second ridge (c) the velocities are significantly higher in the lower region for the smooth case, than for the cases with a rough surface. As noticed by Cao and Tamura [2] and Song and Eaton [3], the height of zero velocity in the region of separation downstream the second ridge (d) is higher above the ground for the rough case than the smooth. The longitudinal mean velocity is zero at a height 60mm=0.17H above the ground in the smooth case, and 78mm=0.22H in the rough case. H is the maximum height of the terrain in case 9. The difference of height above ground, where zero velocity occurs, increases by 30% from the smooth to the rough case. The height of maximum values for the turbulent stresses ($\sigma_u^2, \sigma_w^2, \overline{u'w'}$) coincides with the height of strongest wind shear dU/dz in separated regions. The height of maximum σ_u^2 and dU/dz is 100mm = 0.29H for the smooth case, and 130mm = 0.37H for the rough case. As for the height levels of zero velocity, the height difference between the smooth and rough case is 30%. All this indicates that the center of the separated shear layer is higher, and with that the flow separates further upstream, for the rough case than for the smooth case.

At the start of the plateau (f and g) the velocities are somewhat higher closest to the ground for the smooth case. Similarly, at the end of the plateau (h) does the rough surface in two of the cases slow down the velocity at heights up to 0.5H compared to the case with a smooth surface.

The normal stresses in the main flow direction are shown in Figure 10. In the inflow (a) the stresses above the rough surface are slightly higher than for the smooth surface, just as intended. Likewise the stresses above the smooth model surface are lower than, or equal to, the stresses above the rough surface in the two following measured positions (b-c). This is altered with the onset of the adverse pressure gradient downstream of the second crest. In the downhill part (d-e) the stresses for the smooth model surface are significantly higher than for the rough case, a stronger peak is developed in the smooth case. This is despite the fact that the separation bubble is thicker in the rough case, and that the mean velocities in the valley (e) are quite similar for all the roughness variants. The highly increased values in the smooth case are present throughout the separation area, and are still slightly visible at the start of the plateau (f-g). At the end of the plateau (h) the stresses in the smooth case have decreased, so that the values are lower than for the two rough model surface cases closest to the ground and equal to the other two cases further up.

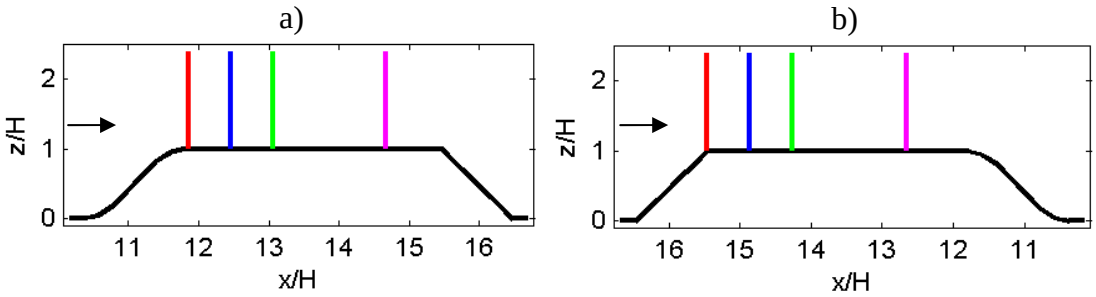

Figure 5. Figure 5a and 5b indicate four of the measured positions in case 3 and case 4 respectively.

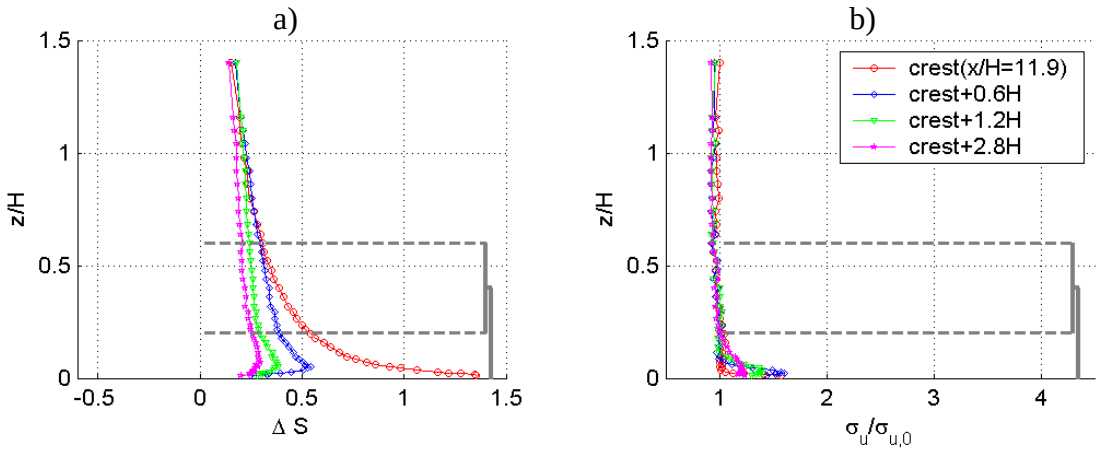

Figure 6. Fractional speed-up ratio and standard deviation of the longitudinal velocity in the main flow direction in case 3. The positions are illustrated in figure 5a.

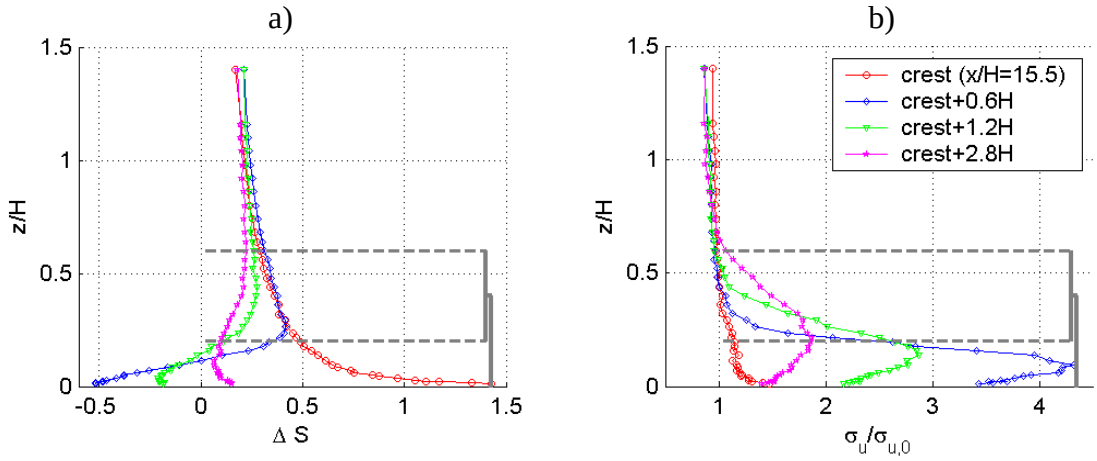

Figure 7. Similar as Figure 6, but for case 4.

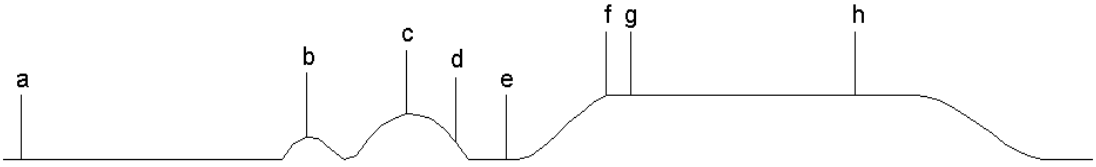

Figure 8. Positions reported in case 9.

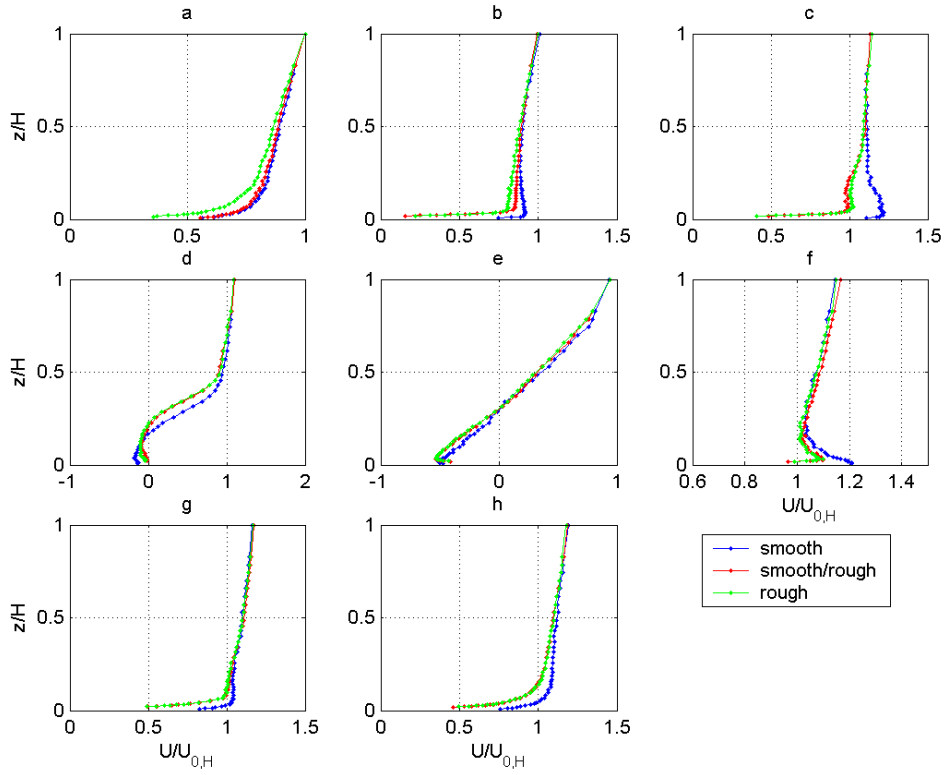

Figure 9. Velocity profiles in the main flow direction in case 9 for different roughness combinations. The mean velocities are nondimensionalized with the velocity at the maximum height of the terrain, H, in the corresponding approaching profile. Positions (a-h) are illustrated in Figure 8.

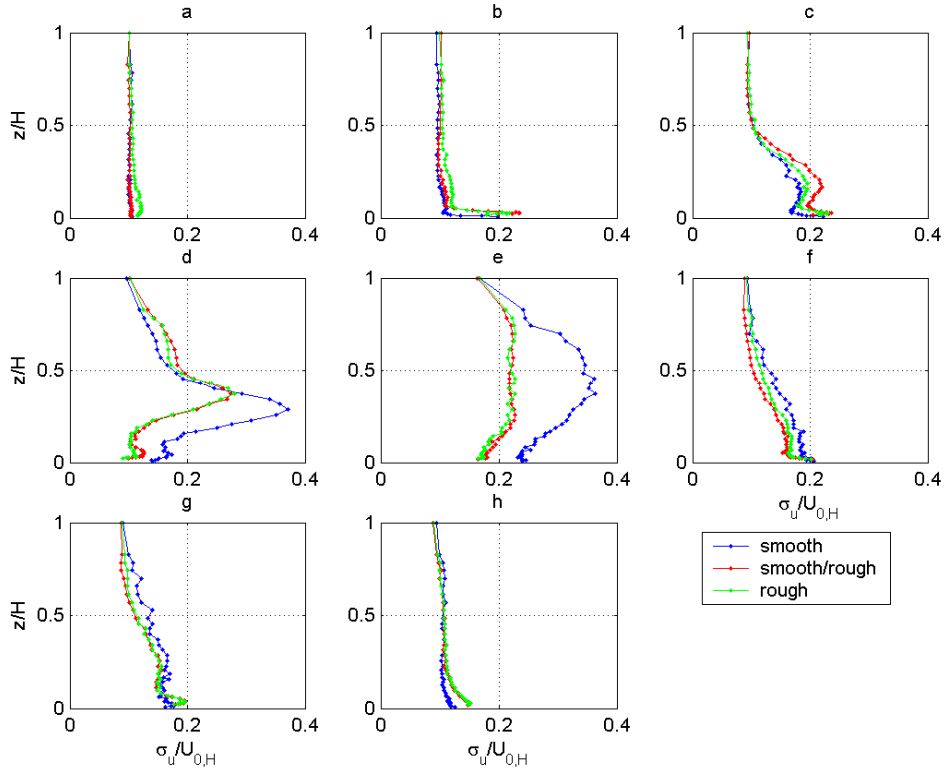

Figure 10. Like Figure 9, but for the standard deviation in the main flow direction. All axes are equal.

4 Conclusions

A large number of profiles have been measured above a complex terrain model. These were taken in regions where the flow was characterized by velocity speed-up, separation and flow recovery.

For all isolated terrain features with rounded crests in the study, maximum fractional speed-up ratios were observed closest to the ground near crests. It was found that this advantageous effect to a certain degree disappears in the case of a sharp crest, due to a separated region downstream the crest. Flow above the same terrain with different roughness conditions resulted in highest speed-up values for the smooth case. All downhill slopes in the terrain model used are steep enough to cause flow separation, and a rough surface resulted in a larger separation bubble than for the smooth surface.

The flow was found to be relatively sensitive to small variations in the terrain, both with respect to orography and roughness. Hence e.g. relatively small changes in surface curvature was found to change flow conditions that are very favorable from a wind power point of view to flow conditions that might cause higher loads on the wind turbines.

References

[1] Counihan, J. Adiabatic atmospheric boundary layers: A review and analysis of data from the period 1880-1972. *Atmospheric Environment*, 9(10), p. 871–905, 1975.

[2] Cao, S. and Tamura, T. Experimental study on roughness effects on turbulent boundary layer flow over a two-dimensional steep hill. *Journal of Wind Engineering and Industrial Aerodynamics*, 94(1), p. 1-19, 2006.

[3] Song, S. and Eaton, J. The effects of wall roughness on the separated flow over a smoothly contoured ramp. *Experiments in Fluids*, 33(1), p. 38-46, 2002.

Is not included due to copyright

Wind tunnel simulation of terraine effects on wind farm siting.

Wind Energ. 2009; **12**:391–410

www.interscience.wiley.com) DOI: 10.1002/we.310